CONTENTS

DE GRUYTER
OPEN

DOI 10.1515/ama-2016-0013

acta mechanica et automatica, vol.10 no.2 (2016)

INFLUENCE OF TEMPERING ON MECHANICAL PROPERTIES OF INDUCTION BENTS BELOW 540°C

Peter JANKEJECH[*], Peter FABIAN[*], Jozef BRONCEK[**], Yuriy SHALAPKO[***]

[*]Faculty of Mechanical Engineering, Department of Technological Engineering,
University of Zilina, Univerzitna 8215/1, 010 26 Zilina, Slovakia
[**]Faculty of Mechanical Engineering, Department of Designing and Machine Components,
University of Zilina, Univerzitna 8215/1, 010 26 Zilina, Slovakia
[***]Institute of Mechanics and Informatics, Chmelnitckiy National University, Str. Institutskaja 11, 29016 Chmelnitckiy, Ukraine

peter.jankejech@fstroj.uniza.sk, peter.fabian@fstroj.uniza.sk, jozef.broncek@fstroj.uniza.sk, shalapko@yahoo.com

received 22 October 2015, revised 1 March 2016, accepted 10 March 2016

Abstract: The article describes basic principles of induction bending and the change of mechanical properties from as received (straight) pipe made from HSLA steel to induction bend. The main purpose of this article is to experiment with tempering temperatures below 540°C. After tempering at 540°C which is the lowest recommended temperature for post bend heat treatment (PBHT) according to CSA specifications (Canadian Standards Association) the induction bend area in many cases does not achieve the minimum required mechanical properties and therefore it is not accepted for usage. In this article mechanical properties such as tensile, toughness, hardness are evaluated. Also the article contains microstructural analyses and comparison of bended and heat treated samples.

Key words: HSLA, Induction, Bending, Tempering

1. INTRODUCTION

Induction bending is a largely automated free forming process. Bends with small bending angles are fabricated on site by means of cold bending. But for smaller radii and bending angles up to 90° hot induction bending is the common manufacturing process. The „transformation" of straight pipe to bent pipe takes place in the heated narrow annular zone which moves continuously along the length of the bend as the bending process advances (Fig. 1). The heating of this zone is affected by means on an induction ring (also Fig. 1) (Muthmann and Grimpe, 2006).

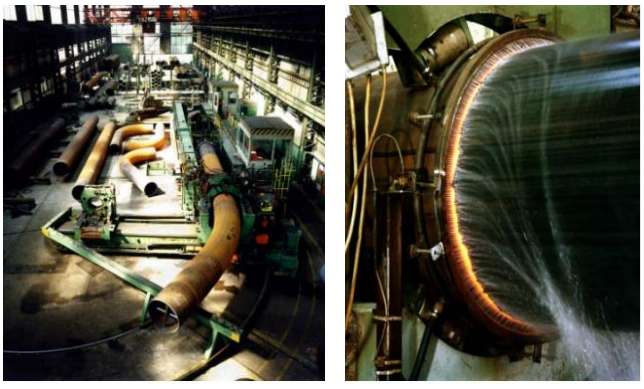

Fig. 1. Description of induction bending machine (left) and the inducted zone where bending takes place (right) (Muthmann and Grimpe, 2006)

An alternating current passes though the inductor and induces a potential which causes an eddy current in the material to be bent. The width of the bending area must be limited to avoid uncontrolled deformation in the bent body. The formed material is cooled by water spray immediately behind the inductor. During bending the temperature of the bending zone is measured continuously and held constant at a predetermined value above Ac3. This results in a short – time austenitizing cycle and a quenched metallurgical structure. The front end of the pipe is clamped to a pivoted arm, the bending force acts axially on the pipe, induced by a hydraulic ram, pushing the pipe through the machine. Set to the desired bending radius, the bending arm then describes a circular arc around its pivot point. As a result of the radial thrust applied to it the pipe automatically follows this curve (Muthmann and Grimpe, 2006; Saga et al.,2010; Tropp et al., 2012). The main advantages of induction bending in comparison to conventional welding of elbows are lower montage costs, lower operational costs, better flow of the transported medium and better corrosion resistance because the whole surface can be uniformly covered by coatings (Fig. 2) (Brezinova et al., 2014; Guzanova et al., 2014).

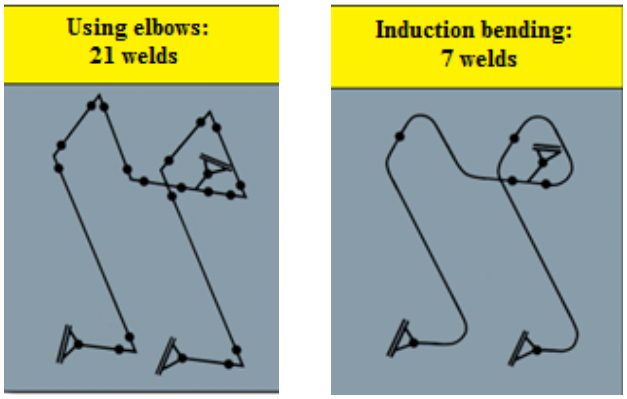

Fig. 2. Advantages of induction bending in comparison with conventional methods of pipeline assembling

DOI 10.1515/ama-2016-0013

2. CHANGES IN MECHANICAL AND STRUCTURAL PROPERTIES OF THE INDUCTION BENTS

Pipes used for induction bending purposes are made from steel manufactured by using controlled rolling technology (large diameter pipes) or by extrusion (low diameter pipes). The goal of controlled rolling is to obtain fine grain microstructure with high tensile properties at a low amount of C (under 0.1%) and other alloying elements. When this kind of material is heated above the transformation temperature the microstructure changes and the mechanical properties mostly drop (approximately 100-150 MPa). That is why pipes made from HSLA steels aren´t able to retain their mechanical properties after induction bending. This drop of after induction bending is also described in Fig. 3. (Broncek et al., 2015; Shome and Mohanty, 2006; Sampath, 2006).

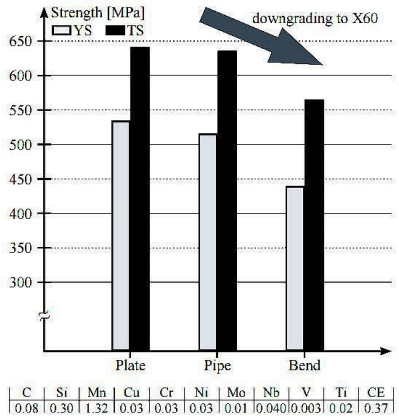

Fig. 3. Changes in tensile properties after induction bending of Gr. X65 steel (Muthmann and Grimpe, 2006)

Fig. 3 represents mechanical properties of pipeline steel grade X65 before and after induction bending. Because of low carbon and alloy content the material after heating and subsequent cooling is not able to retain its mechanical properties. It is important to notice that even the little amount of carbon in this type of steels plays significant role when it comes to mechanical properties after induction bending. (Vervynckt et al., 2012; Fernandez et al., 2014). In the case of microstructural properties the initial microstructure contains a mixture of fine ferrite grains, pearlite and in some cases bainte (depends on the chemical composition, rolling parameters and heat treatment) (Fig. 4). After induction bending in many cases the microstructure contains ferrite grains with a small amount of pearlite. The change in microstructure is shown in Fig. 5. (Broncek et al., 2015; Jun et al. 2006; Chandra et al. 2007).

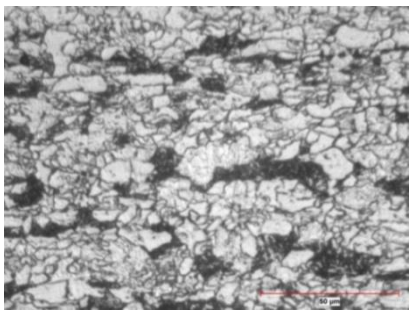

Fig. 4. Microstructure of HSLA steel (Gr.483) before induction bending, Nital 2%, 400x (Broncek et al., 2015)

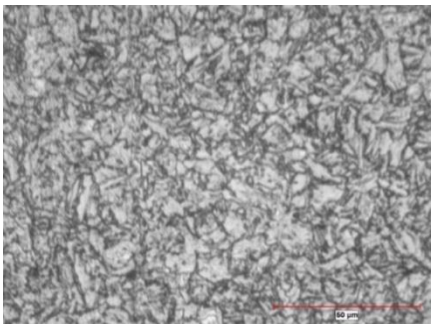

Fig. 5. Microstructure of HSLA steel (Gr.483) after induction bending, Nital 2%, 400x (Broncek et al., 2015)

3. EXPERIMENTAL PART

The examined material is thermo-mechanically rolled HSLA API 5L Gr. X70 steel which mechanical properties ale listed in Tab. 2 and chemical composition in Tab. 1.

Tab. 1. Chemical composition of examined steel

C	Si	Mn	P	S	Ni	Cu
0.08	0.23	1.69	0.009	0.002	0.02	0.01
Cr		**Mo**	**Nb**	**V**	**Ti**	**B**
0.17		0	0.04	0	0.01	0

Tab. 2. Mechanical properties and dimension of examined pipe before induction bending

Size OD x t (mm)	0,5% Yield Strength (MPa)	Tensile strength (MPa)
762 x 19.1	550	667
Elongation (%)	**Toughness (J)**	**Avg. Hardness (HV)**
36	200(1) 237(2)	213

(1) At 0°C; (2) At -40°C

The minimum mechanical property requirements that the induction bend needs to achieve after induction bending are described in Tab. 3.

Tab. 3. Minimum requirements for API 5L X70 steel according to CSA Z245.11-13

Grade	Yield Strength (MPa)	Tensile Strength (MPa)	Y/T Ratio (-)
483 (X70)	483	565	Max. 0.93(1)
Elongation	**Toughness**	**Hardness (HV)**	
min. 20	27(2)(3)	248(4)	

(1) According to CSA Z245.1 Code for straight pipe; (2) Full size specimen (55 x 10 x 10 mm); (3) Toughness of the weld can have a minimum value of 18J (full size specimen); (4) This value is for sour service, induction bend described in the article is for sweet service (302 HV max)

After induction bending the samples for destructive testing were cut in transverse orientation from six locations (Fig. 6).

DOI 10.1515/ama-2016-0013

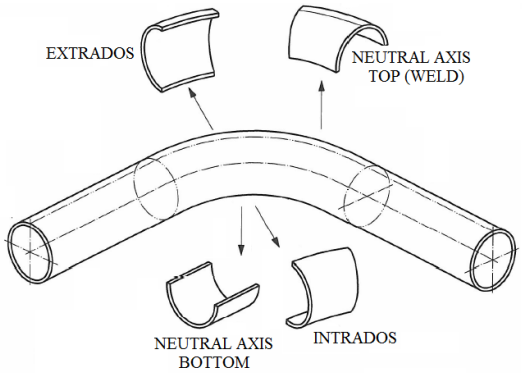

Fig. 6. Drawing of locations in the tested induction bend

These locations were tested in as received condition (no heat treatment) and after providing two experimental post bend heat treatments, one at 540°C for 30 minutes and 420°C for 30 minutes. After providing two experimental heat treatments the samples for tensile and toughness tests were machined according to ASMT A370. Metallographic samples were made according to ASTM E3-11. For hardness measurement nine indents were made in transverse orientation in the extrados, intrados and neutral axis location (Fig. 7a).

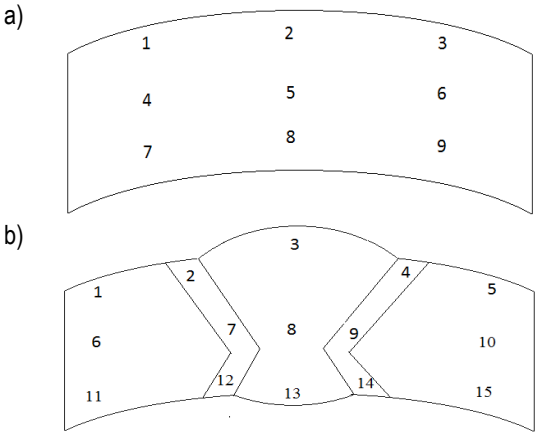

Fig. 7. Drawings of samples for hardness measurement; a. seamless, b. with weld

Neutral axis weld consisted of fifteen indents (Fig. 7b). Heat treatment was provided in a draw (annealing/tempering) furnace Cress 162012. After finishing soaking the samples were unloaded from the furnace and cooled on air.

4. RESULTS AND DISCUSSION

The yield strength (0.5% extension under load) in as bent condition compared with the values stated in Tab. 2 decrease significantly, below the minimum requirements. After applying 540°C/30 min. regime the yield strength in the bend zone increases, especially in the extrados and intrados location and slightly decreases in neutral axis location. However this increase of yield strength isn't sufficient enough and extrados location doesn't meet the minimum requirements stated in Tab. 3 (Fig. 8). When applying the 420°C/30 min. regime the yield strength in all locations increases. According to the values stated in Tab. 5 it is possible to assume that tempering below 540°C has positive impact on yield strength. All the locations after applying 420°C/30 min. regime meet the minimum requirements for yield strength. Yield strength of neutral axis weld isn't recorded because according to the CSA specification it is not recommended.

Tab. 4. Measured values of tensile strength

Location (Orientation)	No PBHT		540°C/30 min.		420°C/30min.	
	UTS (MPa)	EUL 0.5% (MPa)	UTS (MPa)	EUL 0.5% (MPa)	UTS (MPa)	EUL 0.5% (MPa)
Extrados (Transverse)	617	427	542	463	611	518
Intrados (Transverse)	630	475	574	489	645	557
Neutral Weld (Transverse)	670	-	603	-	670	-
Neutral Axis (Transverse)	666	531	612	529	664	573

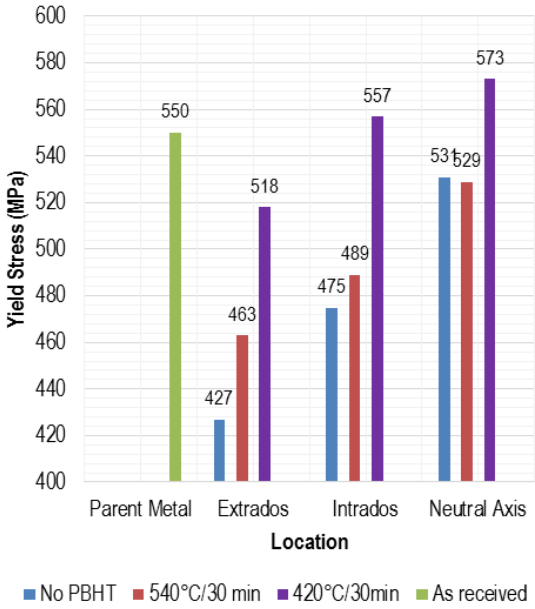

Fig. 8. Values of yield strength in the bend zone

In as bent condition (no PBHT) the tensile strength meets the criteria for minimum tensile strength (see Tab. 3). After applying PBHT 540°C/30 min. tensile strength of the received test bend in all locations decreases (Tab. 4). Here is important to notice that in the extrados location the tensile strength decreases rapidly, below the minimum criteria. However after applying 420°C/30 min. regime the drop of tensile strength is less significant (Fig. 9). In the intrados location slightly increases. According to the values listed in Tab. 5 it is possible to assume that tempering bellow 540°C has a smaller negative impact on tensile strength.

After applying PBHT the Y/T ratio of the received test bend in all locations is approximatelly the same (Fig. 10). Y/T ratio from neutral axis weld location wasn't measured because it is not required in the specification. The values of Y/T ratio in as bent and PBHT condition meet the requirements listed in Tab. 3. The elongation of the received test bend in all locations slightly increases, and also meets the requirements (Fig. 11). Elongation from neutral axis weld location wasn't provided because it was not required.

Peter Jankejech, Peter Fabian, Jozef Broncek, Yuriy Shalapko
DOI 10.1515/ama-2016-0013

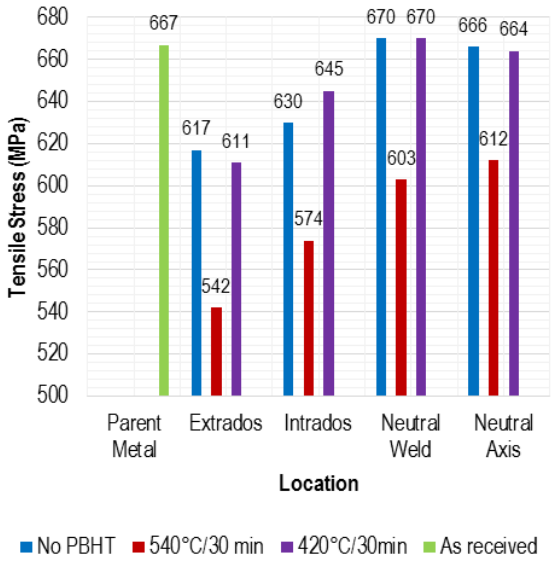

Fig. 9. Values of tensile strength in the bend zone

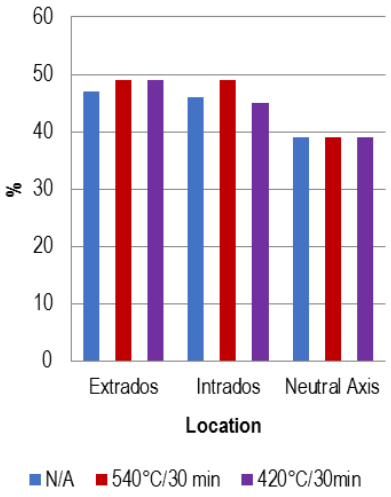

Fig. 10. Values of Y/T ratio in as bend and PBHT condition

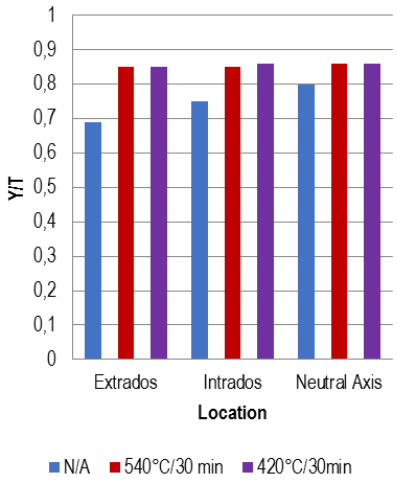

Fig. 11. Elongation values of locations in as bent and PBHT condition

Induction bends also must meet the minimum requirements for toughness. That's why an appropriate temperature, and amount of quenching, must be chosen to provide the induction bend with good toughness properties. According to Tab. 3 the minimum absorbed energy for this grade is 27 J (seamless locations), and 18 J for locations containing welds. In as bend condition the toughness values listed in Tab.5 meet these minimum requirements.

After applying PBHT the toughness in all locations increases (Fig. 12). This means that tempering at temperatures from 540°C and below has positive effect on toughness properties for steel with the chemical composition listed in Tab. 1.

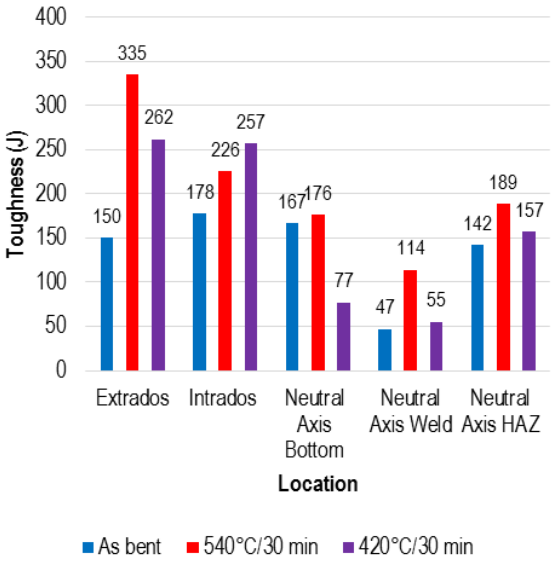

Fig. 12. Toughness values of the bend zone

Single hardness values of induction test bend do not exceed 302 HV10 and therefore meet the requirements for sweet condition. Sweet condition means that the pipe can be used only for transportation of natural gas that does not contain significant amounts of hydrogen sulfide. Again due to increased toughness properties the hardness after PBHT decreases thanks to the softening processes during tempering. The average hardness value of each location is stated in Tab. 5.

Tab. 5. Average values of harness in each location

	Hardness HV10 (Average)		
	No PBHT	**540°C/30min.**	**420°C/30min.**
Extrados (Transverse)	216	180	207
Intrados (Transverse)	213	193	215
Neutral axis bottom (Transverse)	227	211	217
Neutral axis weld (Transverse)	240	201	226

As mentioned above, temperature used in the induction bending process exceeds the Ac3 transformation temperature and therefore a new microstructure is obtained. Instead of a mixture of elongated ferrite grains with upper bainite (or pearlite) (Fig. 13a.), the microstructure in Fig. 13b. contains a mixture of ferrite grains with (probably) small islands of pearlite.

DOI 10.1515/ama-2016-0013

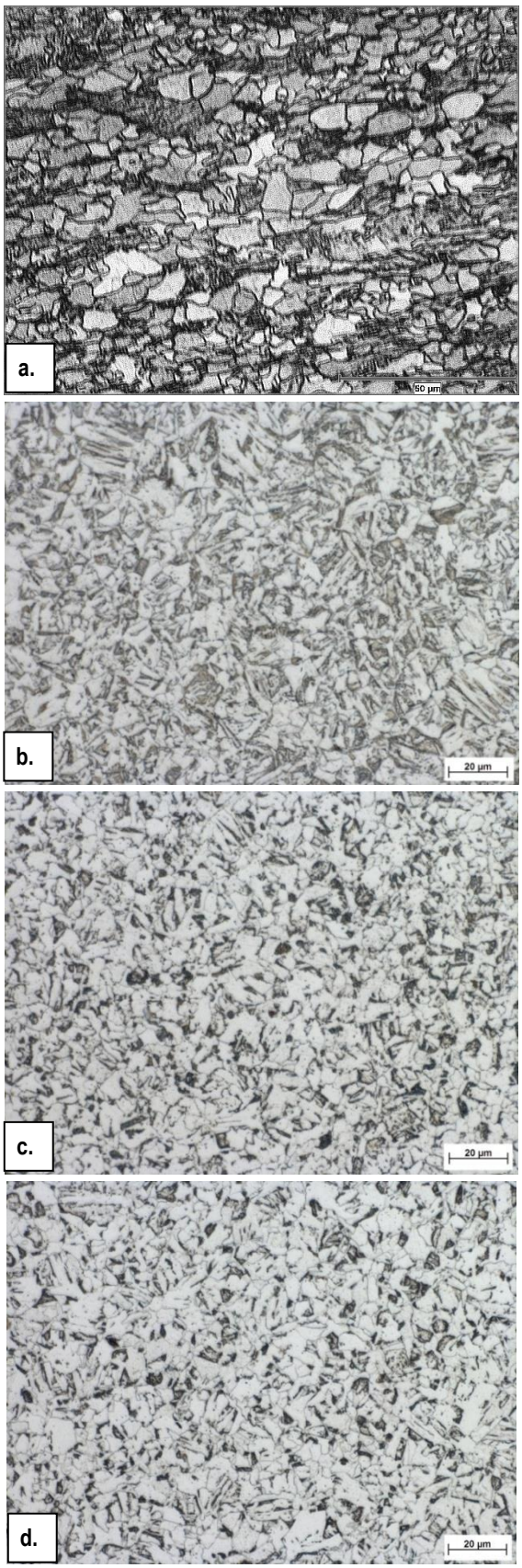

Fig. 13. Microstructure of parent material (a.), extrados location after induction bending (b.), after PBHT 540°C/30 min (c) and after PBHT 420°C/30 min. (d.); etched nital 2%, 400x (a.) 500x (b.c.d.)

Fig. 13c. represents the microstructure of extrados location after applying PBHT 540°C/30 min. As one can see during tempering on this temperature the grains get coarser which can explain the loose of tensile strength stated in Tab.5. The increase of yield strength can be due to precipitation strengthening mechanism mostly because of niobium carbide (NbC) particles or free nitrogen contained in the steel.

Fig. 13d. represents microstructure of the same location after applying PBHT 420°C/30min where the grain coarsening is less pronounced due to lower temperature. That's why the loss of tensile strength isn't that significant as in the previous heat treatment. Also the secondary precipitation takes place which can explain the increase of yield strength.

5. CONCLUSION

Because the requirements for heat treatment of induction bents have not been revised for years and the procedures for thermo-mechanical controlled rolling as well as the chemical composition of the material have improved, the purpose of this article was to refer that temperatures below 540°C could be also considered as a part of post bend heat treatment in the future. After destructive testing of induction bended pipe and provided experimental heat treatments it is possible to assume that both regimes increase the yield strength and decrease the tensile strength, decrease hardness, and increase toughness. However when applying lower tempering temperature (420°C) the decrease of tensile strength is not that significant as it is when applying 540°C. The most important thing is that when tempering at 420°C the yield strength increases more than at 540°C. After taking to account the measured values after applying 540°C tempering temperature, the test bend would not meet the minimum requirements because it would fail in the extrados location on low yield and tensile strength. But after applying 420°C tempering temperature all locations in the bend zone would meet the minimum requirements. Of course these conditions can be related only to the material with such (or approximate) chemical composition as stated in Tab. 1. However the CSA specification for pipe fittings requires PBHT also for tangent body and weld location (straight part of the pipe). In this case additional tests must be done to assure that PBHT below the minimum recommended temperature stated in CSA specification doesn't have negative influence on mechanical properties of this location.

REFERENCES

1. **Brezinova, J. - Guzanova, A. - Spisak, E**. (2014), Assessment of properties thermal sprayed coatings realised using cermet blend powder, *Metalurgija*, 53(4), 661-664.
2. **Broncek J., Jankejech P., Fabian P., Radek N.** (2015), Influence of mechanical anisotropy in low carbon microalloyed steel, *Communications : scientific letters of the University of Žilina*, 17(3), 25-30.
3. **Chandra T., Tsuzaki K., Militzer M., Ravindran C.,** (2007), Optimization of Nb HSLA microstructure using advanced thermo mechanical processing in a CSP plant, *Materials Science Forum,* 539-543, 28-35.
4. **Fernandez J., Illescas S., Guilemany J.M.,** (2014), Effects of microalloying elements on the austenitic grain growth in a low carbon HSLA steel, *Materials Letters* , 61(11-12), 2389-2392.
5. **Guzanova, A., Brezinova, J., Draganovska, D., Jas, F**. (2014), A study of the effect of surface pre-treatment on the adhesion of coatings, *Journal of Adhesion Science and Technology*, 28(17), 1-18.

DOI 10.1515/ama-2016-0013

6. **Jun H.J., Kang J.S., Seo D.H., Kang K.B., Park C.G.,** (2006), Effects of deformation and boron on microstructure and continuous cooling transformation in low carbon HSLA steels , *Materials Science and Engineering: A*, 422(1-2), 157 – 162.
7. **Muthmann E.**, **Grimpe F.** (2006), *Fabrication of hot induction bends from LSAW large diameter pipes manufactured from TMCP plate*, Microalloyed Steels for the Oil and Gas Industry International Symposium, Araxá, Brazil.
8. **Saga M., Handrik P., Kopas P**. (2010). Contribution to computer simulation of induction bending of large diameter pipes. *Metalurgija = Metallurgy*, 49, 498-502.
9. **Sampath K.** (2006), An Understanding of HSLA-65 Plate Steels, *Journal of Materials Engineering and Performance,* 15, 32-40.
10. **Shome M., Mohanty O.N.** (2006), Continuous Cooling Transformation Diagrams Applicable to the Heat-Affected Zone of HSLA-80 and HSLA-100 Steels, *Metallurgical and Materials Transactions*, 37A, 2159-2169.
11. **Tropp M., Handrik M., Kopas P., Saga M.** (2012), Computer simulation of induction bending process, *Pipeline & Gas Journal*, 239(11), 3.
12. **Vervynckt S., Verbeken K., Lopez B., Jonas J.J.,** (2012), Modern HSLA steels and role of none-recrystallization temperature, *International Materials Reviews,* 57(4), 187-207.

Acknowledgment: Authors would like to thank Triple D Bending for material providing (induction bending) and Prooftest Consulting Inc. for providing laboratory equipment and space for sample machining and destructive testing.

DE GRUYTER
OPEN

DOI 10.1515/ama-2016-0014

acta mechanica et automatica, vol.10 no.2 (2016)

TYPE SYNTHESIS, MODELLING AND ANALYSIS OF THE MANIPULATOR FOR WHEEL-LEGGED ROBOT

JAROSŁAW SZREK*, ARTUR MURASZKOWSKI*, PRZEMYSŁAW SPERZYŃSKI*

*Faculty of Mechanical Engineering, Department of Biomedical Engineering, Mechatronics and Theory of Mechanisms, Wroclaw University of Technology, Wybrzeże Wyspiańskiego 27, 50-370 Wrocław, Poland

jaroslaw.szrek@pwr.edu.pl, artur.muraszkowski@pwr.edu.pl, przemyslaw.sperzynski@pwr.edu.pl

received 11 December 2014, revised 14 March 2016, accepted 21 March 2016

Abstract: The aim of this article is to present the concept of wheel-legged mobile manipulator, which is a combination of mobile platform with specially selected suspension system and a manipulator. First, a literature review was performed and own solution proposed. The kinematic structure of manipulator, selected simulation results, physical model and the concept of the control system has been presented. Geometry synthesis was used to design basic dimension. Structural synthesis was performed according to the intermediate chain method. Simulations were performed using the multibody dynamics simulation software. New approach in the field of the mobile manipulators was presented as a result.

Key words: Mobile Manipulator, Multibody Dynamics Analysis, Wheel-Legged Platform

1. INTRODUCTION

A wheel-legged manipulator consists of mobile platform with special suspension system carrying a manipulator arm. Thanks to this solution the machine obtains additional functionality and offers new possibilities of application, such as remote manipulation in field with obstacles, exploration of unknown or contaminated areas (even other planets) and counter-terrorism task (Gronowicz et al., 2009; Szrek et al., 2010; Trojnacki et al., 2008).

There are numerous designs of mobile manipulators. The Inspector seen in Fig. 1a, Ibis (Fig. 1c), and PIAP Scout (Fig. 1d) were designed in the Industrial Research Institute for Automation and Measurements (PIAP, Poland) (http://www.antyterroryzm.com /product/pl/inspektor, http://www.antyterroryzm.com/product/pl/scout). The robot Inspector has tracked chassis and manipulator with 5 degrees of freedom. Its main features are large weight and large payload of manipulator. The PIAP Scout platform uses different type of the drive system – wheel-track, which has better performance while overcoming obstacles.

The Ibis is a six-wheel platform equipped with a manipulator which has seven degrees of freedom and an impressive range of over 3 meters.

Each of the robots described above has a system of 4 cameras used for observation. Time of initialization from power off to standby is approx. 2 sec.

Another example of mobile robot is Seekur Jr (http://www.mobilerobots.com/Research Robots/SeekurJr_with_Outdoor_Manipulator.aspx), presented in Fig. 2a. This platform has four non-swivel wheels and a manipulator with 5 degrees of freedom. An interesting feature is the use of a pneumatic actuator, as an additional support during the operation of the manipulator. Perpendicular to wheel motor placement suggests that worm gear has been used. Manipulator has approximately 1 meter range, weight 10kg, and maximum payload is dependent on the scope and varies from 3 to 15kg.

Another mobile manipulator is Herb (Srinivasa et al., 2009), shown in Fig. 2c. A class 2.0 mobile platform with additional support wheel is a moving module. The manipulator is equipped with an effector for picking various objects.

Interesting solution of manipulator (Fig. 2b) is used by GWAM robot designers (http://www.ams.com/eng). The manipulator has a modular construction and can be customized according to the needs. It can achieve up to seven degrees of freedom. This mobile platform moves on wheels, and additionally has track support, which is significant when driving in the rough terrain. The robot weights 139kg, and its payload is 9kg. The maximum speed of the robot is 3 m/s.

Another example is the KUKA robot (Fig. 2d). Mobile platform, which uses Mecanum wheels for omni-direction movement is equipped with a light industrial manipulator. Drive system used in this robot allows it to move mainly on hard and flat surfaces.

The main task for mobile manipulators is primarily to drive to a specific location and provide visual information to the operator. More complex task may consist of manipulation of the camera for more accurate analysis, provide additional sensory data or use of additional tools (eg. gripper, milling head). Further action may include grasping objects and loading on the platform.

To ensure that all the requirements are satisfied, the platform should have a chassis adapted to the task. If the action of the robot takes place on uneven terrain with obstacles task becomes much more difficult. A special case is when it is not possible to bypass obstacles and robot has to face it. In such a situation track drive system do well, especially equipped with an additional system lifting the front of the robot. However, the major disadvantage of solution is poor stability when moving over rough terrain. In this case, the wheel-legged suspension has the advantage.

Manipulators integrated with moving platform should have appropriate number of degrees of freedom to ensure correct manipulation during the task. Based on performed analysis, five degrees of freedom were assumed to be enough for manipulator performing most types of inspection tasks.

DOI 10.1515/ama-2016-0014

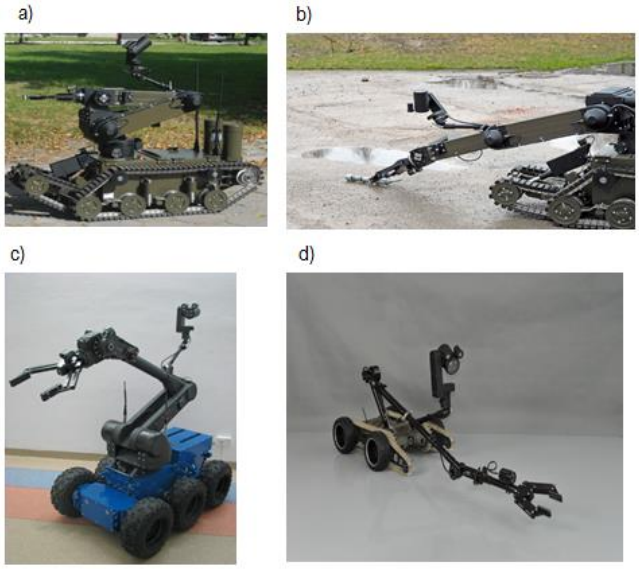

Fig. 1. Mobile robots produced by PIAP. a – Inspector manipulator when moving, b – Inspector manipulator performing task, c –Ibis, d – PIAP Scout

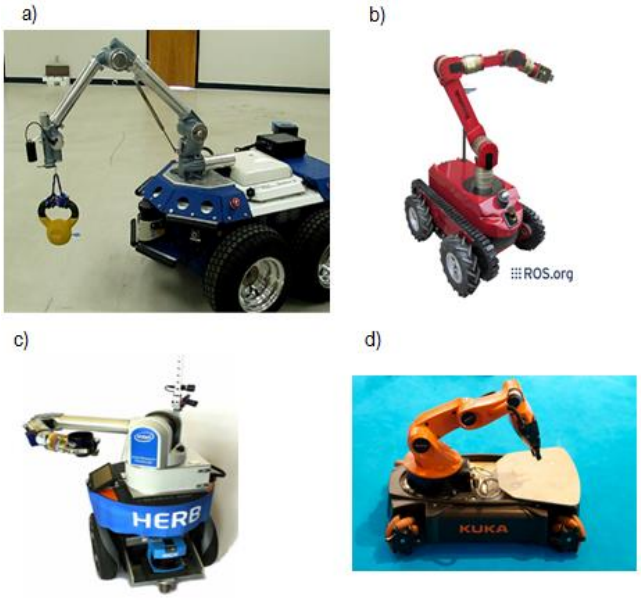

Fig. 2. Selected examples of mobile manipulators. a – Seekur Jr, b – Herb, c- GWAM, d – KUKA robot

2. CONCEPT OF WHEEL-LEGGED MANIPULATOR

Mobile manipulator designing started with identification of the overall assumptions and purposes. First, working area of the manipulator and its assumed location on the mobile platform – the wheel-legged robot (Bałchanowski et al., 2012a; Bałchanowski, 2012b; Gronowicz et al., 2009a; 2009b; 2012; Szrek et al., 2010), which view is shown in Fig. 3, were defined.

Overall analysis of the construction of the manipulator due to the number of degrees of freedom and its structure was performed. In addition, types and location of joints were considered. The choice of the structure was performed using the method of intermediate chain (Gronowicz, 2003; Miller, 1988; Szrek, 2006) and the location of joints was dictated by practical considerations.

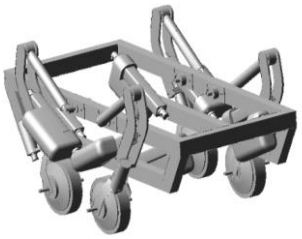

Fig. 3. Spatial model of mobile platform with wheel-legged suspension system

Next, the basic dimensions of elements were selected to ensure assumed range of movement and working area of manipulator. Each dimension was chosen for appropriate manipulator movements with regard to its mounting location on platform (the possibility of manipulation in front of the platform and below the mounting point).

2.1. Kinematic Structure

Kinematic scheme of manipulator is shown in Fig. 4a. It is assumed that the first joint of manipulator is placed in the geometric center of the platform. It will be a revolute joint (A) with vertically oriented axis of rotation, which will turn the whole manipulator. Rest of manipulator's elements forms partially closed structure. A mechanism consisting of the elements 2, 3, 4, 5 has been selected due to the possibility of providing a determined trajectory (Buśkiewicz, 2014; Szrek, 2006; Sperzyński et al., 2010) with a single drive (the drive in joint B).

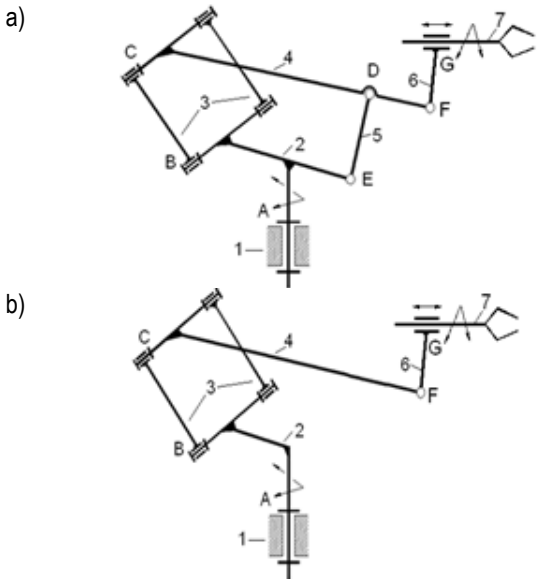

Fig. 4. Manipulator kinematic scheme: a) structure with four-bar linkage; b) serial structure

Similar principle is applied in the motion of the wheel-legged robot limbs, which resulted in reducing the number of drives needed for leveling function from eight to four (Gronowicz et al, 2009a). Moreover, in such a structure load is transferred via joints B and E, and partially closed kinematic chain structure provide additional stiffness of the manipulator.

DOI 10.1515/ama-2016-0014

The rest of the manipulator has a serial structure and consists of rotary joint F and cylindrical joint G (elongation and rotation of the effector).

During the selection process, the serial structure of the kinematics has been considered, shown in Fig. 4b. This solution simplifies the construction of the manipulator – less parts are needed, but they require one more drive.

2.2. Computational model

After selecting the structure and dimensions of the manipulator, model computing was performed. Figure 5a and 5b shows the view of the manipulator along with examples of trajectories - straight and circular.

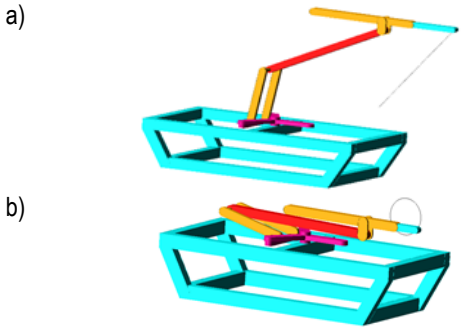

Fig. 5. Computational model of manipulator with platform: a) linear trajectory performance; b) circular trajectory performance

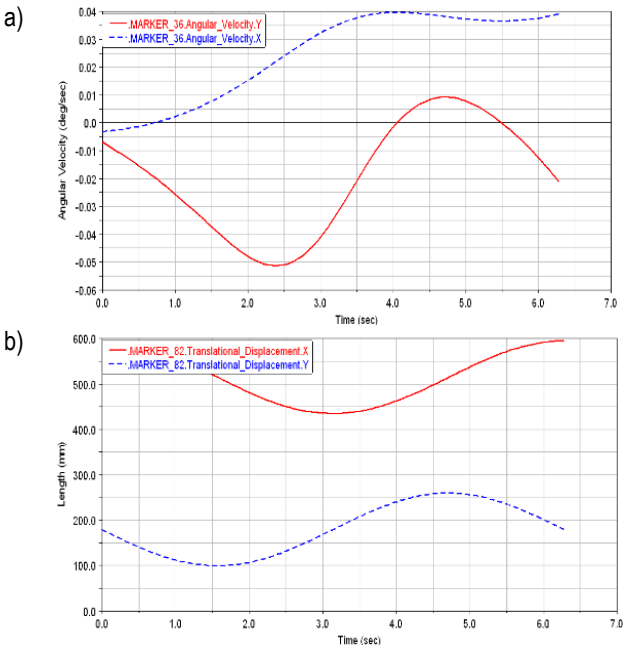

Fig. 6. Exemplary plots of circular trajectory simulation: angular velocity of element 3; b) displacement of element 7; component x and y

In the next step, series of simulation tests was performed. Using appropriate software, both the kinematic and dynamic parameters were determined, such as range of motion, velocity, acceleration (linear, angular), forces and torque in kinematic joints and drives.

Exemplary plots are shown in Fig. 6. First plot (Fig. 6a) shows the components of the angular velocities of element 3 during executing circular trajectory. The waveforms of displacement along x and y axes of global coordinate system of element 7 is shown in Fig. 6b.

2.3. Prototype

After simulation tests, construction of the basic prototype of the manipulator was performed. Prototype was made according to previously determined kinematic structure and dimensions. The selected elements was made of steel and aluminium profiles. All revolute joints are mounted on bearings, and linear joint was made of two linear guideways with ball bearing arrangement. Fig. 7a shows the manipulator arm in the initial position where linear joint is arranged parallel to the arm 4. Fig. 7b shows the last element with the axis on which a gripper will be mounted.

Fig. 7. Selected views of manipulator prototype: a) initial configuration view; b) linear and revolute joints of effector

Fig. 8. Prototype of the manipulator on mobile wheel-legged platform

Manipulator was attached to wheel-legged mobile platform, shown in Fig. 10, and preliminary experimentally tested, where mechanical part correlations was studied.

2.4. Control system

The proposed manipulator has six degrees of freedom. The control system of the whole wheel-legged manipulator is responsible for the movement of the platform (drive module, leveling, stepping) and for the movement of the manipulator. Block diagram of the control system of the whole robot is shown in Fig. 8 with marked block responsible for the control of the manipulator.

DOI 10.1515/ama-2016-0014

Due to the high complexity of the object, the control system is divided into functional blocks, and one of these blocks responsible for controlling the manipulator. Fig. 9 shows a more detailed structure diagram of the manipulator control system. Individual motors MOT 1-6 are driven by motor driver amplifiers (motor controllers) with PWM signal generated in the timers block located in modules with microcontroller MOD uC 1-3. The feedback loop is made with the quadrature signals from incremental encoders, which is mounted on each motor axle.

Motor controllers are determined as local modules in the structure - subordinate to the PC-Server placed on the platform. Communication between the computer and the modules is carried out using the RS485 standard in accordance with communication protocol developed by authors.

Surveillance system is connected to two independent modules with higher performance required for image processing. Another reason to separate parts responsible for handling drive control from vision was to avoid interference. The software of the control system is based on the URBI package which has modules for task synchronization, which is necessary for controlling this type of device. The software is run and tested on a standard operating system, and ultimately will be set on the real-time system.

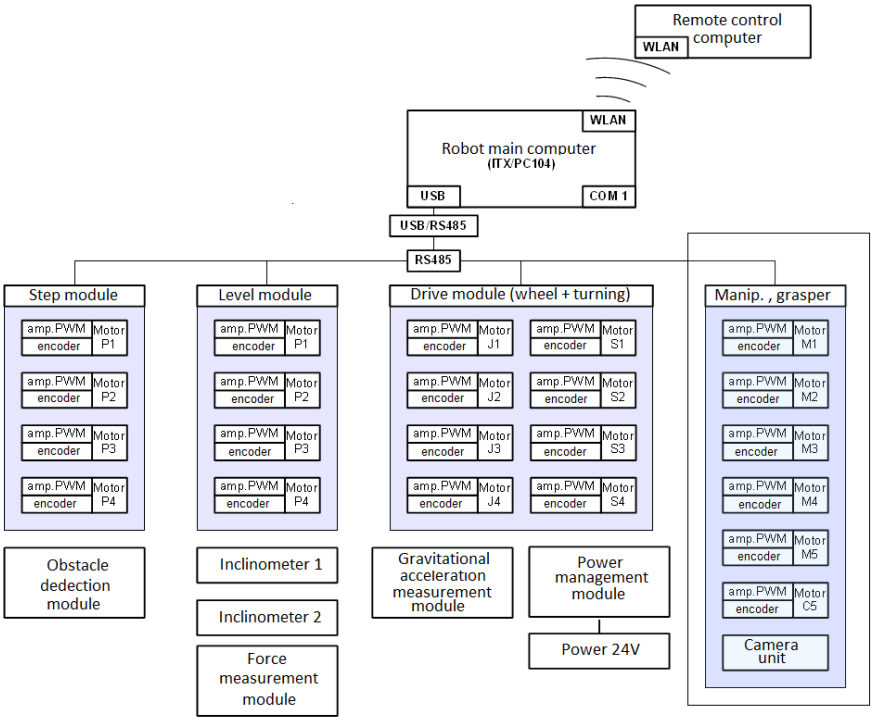

Fig. 9. Diagram of wheel-legged manipulator control system

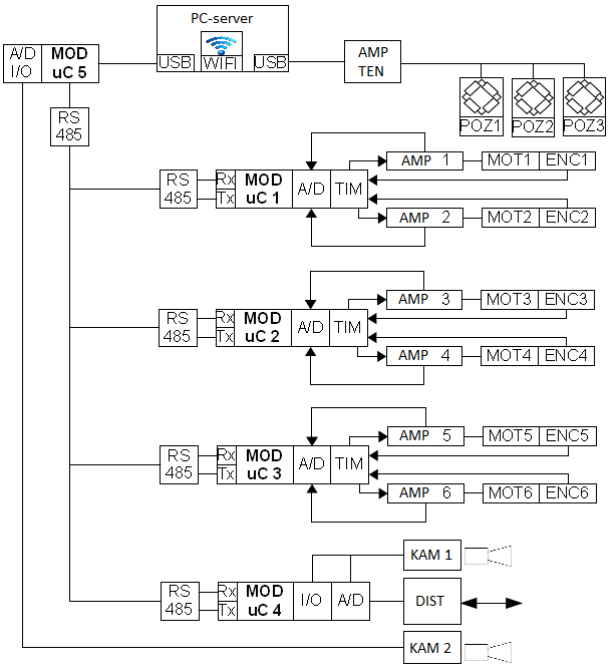

Fig. 10. Manipulator control system structure

DOI 10.1515/ama-2016-0014

3. SUMMARY

Introduction to mobile manipulators and comparison of selected platforms was performed. Afterwards, own design was presented. Two kinematic structures shown in article were taken into account for later consideration. One of them was chosen and developed in prototype.

Design of four degree of freedom manipulator was presented. Construction of prototype of the manipulator was performed. Manipulator was preliminary tested for compatibility with wheel-legged platform including work area, maximum range, dead zone and collisions. It has the ability to work witch different tools like graspers or electric tools, depending on the task. In the next step, it will be mounted on real wheel-legged platform and will become a base for the study of wheel-legged mobile manipulator.

Control system was also designed and presented in this paper. It has modular architecture for easy expansion and numerous comunication ports for attaching different sensors.

Furthermore, the idea of control system of wheel-legged mobile platform with attached manipulator was presented. Controlling such device is quite complex, due to the need of synchronization a large number of drives and cope in difficult robot environment - uneven terrain with obstacles.

Designed control system has a modular structure, which allows adding new modules for both measurement and control of multiple DC electric motors.

Presented manipulator and wheel-legged platform integration is the new approach in the field of the mobile manipulators. The article proves, that this kind of integration is achievable. The main construction assumption of the manipulator, such as ability to reach objects from the surface on which the platform is moving, are sustained regardless of the platform kinematic configuration.

REFERENCES

1. **Bałchanowski J.** (2012b): Mobile wheel-legged robot: researching of suspension leveling system, *Advances in mechanisms design* / eds. Jaroslav Beran, Dordrecht, Springer.
2. **Bałchanowski J., Gronowicz A.** (2012a), Design and simulations of wheel-legged mobile robot, *Acta Mechanica et Automatica*, 6(2), 11-16.
3. **Buśkiewicz J.** (2014), Design of a feeder with the use of the path synthesis method – New Advances in Mechanisms, *Transmissions and Applications Mechanisms and Machine Science*, 17, 251-259.
4. **Gronowicz A.** (2003), *Basis of kinematics systems analysis (in Polish)*, Oficyna wydawnicza PWr., Wrocław.
5. **Gronowicz A., J. Szrek** (2009b), Design of LegVan wheel-legged robot's mechanical and control system, *SYROM 2009 Red. Ion Visa*, Springer Netherlands, 145–158.
6. **Gronowicz A., Szrek J.** (2009a), Idea of a quadruped wheel-legged robot, *Archive of Mechanical Engineering*, 56(3), 263–278.
7. **Gronowicz A., Szrek J., Wudarczyk S.** (2012), A rig for testing the leg of a wheel-legged robot, *Acta Mechanica et Automatica*, 6(2), 48-52.
8. **Miller S.** (1988), *Kinematic systems. Design basis* (*in Polish),* WNT 1988, Warszawa.
9. **Sperzyński P., Szrek J. Gronowicz A.** (2010), Geometric synthesis of mechanism implementing linear trajectory (in Polish), *Acta Mechanica et Automatica*, 4(2), 124-129.
10. **Srinivasa S. S., D. Ferguson, C. J. Helfrich, D. Berenson, Avaro Collet, R. Diankov, G. Gallagher, G. Hollinger, J. Kuffner, M. VandeWeghe** (2009), HERB: a home exploring robotic butler*, Auton Robot*, 28, 5–20, Springer Science+Business Media.
11. **Szrek J.** (2006), Synthesis method of wheel-legged mobile robot suspension (in Polish), *XX Konferencja Naukowo – Dydaktyczna Teorii Maszyn i Mechanizmów*, Zielona Góra.
12. **Szrek J., Wójtowicz P.** (2010), Idea of wheel-legged robot and its control system design, *Bulletin of the Polish Academy of Sciences. Technical Sciences*, 58(1), 43-50.
13. **Trojnacki M., Szynkarczyk P., Andrzejuk A.** (2008): Trends of mobile land robots development (in Polish), *Pomiary Automatyka Robotyka,* 6.
14. http://www.ams.com/eng
15. http://www.antyterroryzm.com /product/pl/inspektor
16. http://www.antyterroryzm.com/product/pl/scout
17. http://www.mobilerobots.com/ResearchRobots/ SeekurJr_with_Outdoor_ Manipulator.aspx
18. http://www.robotnik.es/en/contact/

DOI 10.1515/ama-2016-0015

MULTI-UAV FLIGHT USING VIRTUAL STRUCTURE COMBINED WITH BEHAVIORAL APPROACH

Cezary KOWNACKI*

*Faculty of Mechanical Engineering, Bialystok University of Technology, Wiejska 45C, 15-351 Bialystok, Poland

c.kownacki@pb.edu.pl

received 8 June 2015, revised 15 March 2016, accepted 21 March 2016

Abstract: Implementations of multi-UAV systems can be divided mainly into two different approaches, centralised system that synchronises positions of each vehicle by a ground station and an autonomous system based on decentralised control, which offers more flexibility and independence. Decentralisation of multi-UAV control entails the need for information sharing between all vehicles, what in some cases could be problematic due to a significant amount of data to be sent over the wireless network. To improve the reliability and the throughput of information sharing inside the formation of UAVs, this paper proposes an approach that combines virtual structure with a leader and two flocking behaviours. Each UAV has assigned different virtual migration point referenced to the leader's position which is simultaneously the origin of a formation reference frame. All migration points create together a virtual rigid structure. Each vehicle uses local behaviours of cohesion and repulsion respectively, to track its own assigned point in the structure and to avoid a collision with the previous UAV in the structure. To calculate parameters of local behaviours, each UAV should know position and attitude of the leader to define the formation reference frame and also the actual position of the previous UAV in the structure. Hence, information sharing can be based on a chain of local peer-to-peer communication between two consecutive vehicles in the structure. In such solution, the information about the leader could be sequentially transmitted from one UAV to another. Numerical simulations were prepared and carried out to verify the effectiveness of the presented approach. Trajectories recorded during those simulations show collective, coherence and collision-free flights of the formation created with five UAVs.

Key words: Multi-UAV, Virtual Structure, Formation, Flocking Behaviors

1. INTRODUCTION

In the last few years, technology development in the area of unmanned aerial vehicles (UAV) is reflected in a high number of commercial flying robots, which became widely available for even inexperienced users. Therefore, taking photos or making movies from the air becomes commonplace and just popular. The main reason is a simplicity of controlling of such kind of vehicles, whose autonomy is based mainly on the use of GPS (Global Positioning System) assisted by a simple AHRS (Attitude and Heading Reference System). Hence, the autonomous flight of single UAV through the sequence of waypoints is just a trivial task in present days. But frequently, a flight of single UAV is insufficient especially, if a mission requires collecting lots of information in a short time. If we consider a relatively short flight time of electrical vehicles, multi-UAV missions seem to be the best way to achieve this. However, coordinated and collective flights are no longer so easy to prepare by the use of commonly available UAVs. Autonomous control of multi-UAV systems is much more complex and it requires applying of additional mechanisms of control and sharing of navigational parameters, which are crucial for position coordination in 3D. Those issues are not supported yet by any commercial UAV system, as that multi-UAVs systems are still under development and they are not ready to be used even for a military purpose. Therefore, there is a wide area to conduct research in this field to achieve coordinated flight of a group of UAV.

Most of known algorithms designed for the formation control could be classified to three separate subsets of approaches to multi-UAV systems, namely, bio-inspired behavioural methods (Kownacki and Ołdziej, 2015; Virágh Cs. et al., 2014, Quintero et al., 2013), virtual structure methods (Norman et al., 2008; Ren and Beard, 2004; Cai et al., 2012; Shao et al., 2014; Low et al, 2011; Askari et al., 2015; Shan et al., 2005) and leader-follower methods (Ambroziak and Gosiewski, 2014; Yun et al. 2008; Xingping et al., 2003). The first approach treats a group of UAVs like a flock of birds that behaves according to four major behaviours formulated by C. Reynolds, i.e. cohesion, repulsion, migration and alignment (Reynolds, 1987). The advantage of that approach is a decentralised control, which makes possible to self-organize a structure of the swarm through local interactions between vehicles. But the structure of the flock is not rigid, but even it has random nature. The weakness arises from the necessity of information sharing between all or at least most of flock members, which is essential to estimate parameters of flocking behaviours, especially if cohesion and migration are acting globally. The second approach allows creating a formation in the form of a virtual rigid structure, where relative locations of each vehicle should be continuously constant as it is possible (Norman et al., 2008). The advantage of the approach is that a relative location of UAV can be coupled with a specific role in the formation of UAVs or with a different setup of the field of view of on-board sensors. Also it can be used to reconFig. geometric relationships among UAVs in the formation. On the other hand, the approach of virtual structure requires precise position tracking and it synchronisation and this makes it susceptible to external disturbances. This is also related with high requirements of communication quality, which

DOI 10.1515/ama-2016-0015

is crucial in computing desired positions. The precision of position tracking should be limited by placing dead zones around desired relative positions of UAVs in the structure, to avoid excitations of vibrations of control signals, when UAV is nearby its desired relative position. Then even small displacement of UAV position can generate high errors in angles of heading or pitch. The last approach uses only a peer-to-peer relation between a leader and a follower, or between two consecutive followers (Ambroziak and Gosiewski, 2014). In such case, this is relatively the simplest approach because interactions between UAV and information sharing are limited only to a pair of vehicles. The control algorithm in the leader-follower method is similar, but also simpler than this one used in the approach of the virtual structure. It comes from the fact that it is easier to control a distance and a heading angle than a relative position in the structure.

Other approaches in the field of multi-UAV systems are usually combinations of elements of these three basic approaches (Cai et al., 2012; Kownacki and Ołdziej, 2015). Each time, the main aim is to create an algorithm which will eliminate weaknesses of each of mentioned approaches. Therefore, also in this paper, we propose a method combining all three approaches: flocking behaviours, leader – follower and virtual structure. The main result of such combination is the increment of the formation stiffness, in respect to our previous work (Kownacki and Ołdziej, 2015). In the method, the leader of a UAVs formation still will be the one and only UAV that is controllable by the ground station. Hence, management of the formation should be easier and more convenient for the operator. Position and attitude of the leader determine also the origin and the orientation of a reference frame of the formation required to determine current positions of virtual migration points (nodes in the structure), which are assigned to each UAV. To make a UAV tracking its individual migration point as a relative position in the virtual structure, individual cohesion behaviours based on birds' flocks (Reynolds, 1987) can be applied. The second flocking behaviours, which are used in the method, are repulsion behaviours which help to prevent collisions with a vehicle located in the preceding node of the structure. Such combination of decentralised behaviours with the virtual structure makes possible to create coordinated, collective and coherent flights based on a simple information flow inside the formation. Scheme for information flow can be based on peer-to-peer transmission between pairs of radio modems. It is a simpler approach to information sharing in contrast to the position errors synchronisation, where UAVs must know positions errors of other UAVs (Norman et al., 2008). The case of two vehicle does not show this issue, which probably could occur during algorithm implementation. Moreover, as it was proved in (Ambroziak and Gosiewski, 2014), tracking of reference positions based on the minimization of positions errors will fail when those and headings errors are relatively large. Then UAVs will be unable to track their desired positions, which move in accordance with the leader or a virtual leader. The usage of flocking behaviours eliminates this problem and simultaneously it does not require applying two-stage switching control as it was in Ambroziak and Gosiewski, (2014). In the proposed method, UAV uses set-point values of pitch and heading, which arise from the orientation of the UAV position relative to the assigned position in the structure, and position error as displacement is minimised by the control of airspeed. An idea of combining virtual structure with behaviours is also presented in Cai et al., (2012), but in contrast to our conception, it applies only single behaviour of obstacle avoidance.

The remainder part of this paper is split into three sections. In the section titled "model of UAVs formation", we define the virtual structure of the formation and next describe relations between UAVs. We formulate also rules of local behaviours and present the way of information sharing which is essential for tracking of relative positions. In the next section, we present results of numerical simulations and a discussion on it. The last section offers conclusions and summarises the paper.

2. STRUCTURE OF UAVS FORMATION

Similarly to other research on the methods of virtual structure, the formation is treated as a rigid body. The position of each UAV inside the virtual structure is typically defined in a local frame, with respect to a reference point in the structure, which could be also the origin of the frame. In our case, the relative positions of the vehicles inside the virtual structure are defined in a reference frame L whose the origin is located at the leader's position. Hence, the leader becomes a reference point for each UAV in the formation. In accordance to the trajectory of the leader, the virtual structure evolves in time and the desired relative positions for each UAV are determined by pre-set offsets from the current position of the leader. The diagram of the virtual structure and relations between desired positions P_{iR}^{L} and P_{iL}^{L} in the reference frame L is presented in Fig. 1.

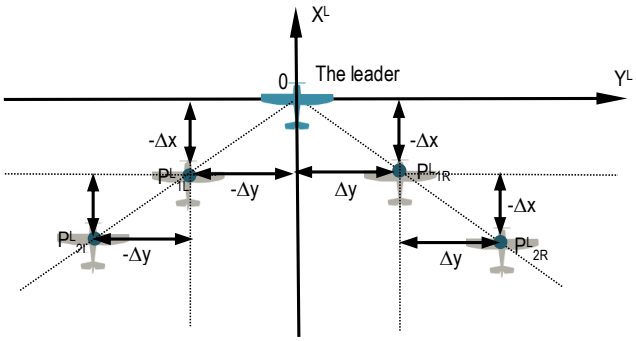

Fig. 1. A diagram of virtual structure in the reference frame L. Δx, Δy – spacings between UAVs inside the virtual structure, $P_{iR(L)}^{L}$ – the position of the i-the UAV on the right or on left side of the leader

The proposed structure of the formation is identical as in a herd of ducks. We have two chains of UAVs as branches on both sides of the leader. In such structure, the position of each UAV in the formation frame L (superscript) is defined by equations:

$$P_{iR}^{L} = \begin{bmatrix} x_{iR}^{L} \\ y_{iR}^{L} \\ z_{iR}^{L} \end{bmatrix} = \begin{bmatrix} -i \cdot \Delta x \\ i \cdot \Delta y \\ 0 \end{bmatrix} \qquad P_{iL}^{L} = \begin{bmatrix} x_{iL}^{L} \\ y_{iL}^{L} \\ z_{iL}^{L} \end{bmatrix} = \begin{bmatrix} -i \cdot \Delta x \\ -i \cdot \Delta y \\ 0 \end{bmatrix} \quad (1)$$

where: i – the order of UAVs in chain L or R with respect to the leader, Δx, Δy – spacings between UAVs, respectively in x and y axes.

Because the structure of the formation is treated as a rigid body and the origin of the formation frame L is located at the leader's position, any rotation of the leader should be reflected in rotations of the virtual structure in respect to the inertial frame. Therefore, the equations defining the relative positions of UAVs

DOI 10.1515/ama-2016-0015

inside the virtual structure, given in inertial frame G, are:

$$P_{iR}^{G} = P_{LD}^{G} + D_{G}^{L} \cdot P_{iR}^{L} \quad P_{iL}^{G} = P_{LD}^{G} + D_{G}^{L} \cdot P_{iL}^{L} \tag{2}$$

where: D_g^L – rotation matrix defining rotations between the formation frame L and the inertial frame G, P_{LD}^G - the position of the leader in the inertial frame G, P_{iR}^G - the desired position of the i-th UAV on the right side of the leader (R) in the inertial frame G, P_{iL}^G - the desired position of the i-th UAV on the left side of the leader (L) in the inertial frame G.

According to equation (2), to determine in time its own desired relative position, each UAV must collect information about the leader's position and its orientation.

If each UAV knows its current position from the GPS system and its own desired relative position in the inertial frame G, the UAV will able to minimize its position error defined as the distance between the desired and the current position. The simplest way is to use PID or PI regulators (Norman et al., 2008). But, as it was found in (Ambroziak and Gosiewski, 2014), position tracking, which is based only on position errors is ineffective, especially when position errors are high and the reference trajectory has a lot of turns. In that case, due to limited turn radius and the misalignment between the heading of UAV and the reference heading of the leader, position error will grow again even if it was zero. Therefore, we propose an algorithm which combines the position error control with the heading angle control, to direct UAV towards its desired relative position in the structure.

3. CONTROL ALGORITHM

One of the methods, which can be applied to achieve an effective position tracking, is the cohesion behavior in birds flocks (Reynolds, 1987). This behavior, named differently as the attraction rule, is frequently used in robotics to concentrate agents around the centroid of a swarm. But instead of the centroid, we are able to apply this rule to any virtual point. Moreover, the point of aggregation can be different for each UAV in the formation. Hence, the nodes in the virtual structure defining desired relative positions of UAVs can be treated as virtual points which attract only their assigned agent. This also means that every agent implements its individual cohesion behavior. The idea of adapting cohesion behaviors of birds' flocks, as separate cohesion behaviors for every UAV in the formation, in the proposed approach is explained in Fig. 2.

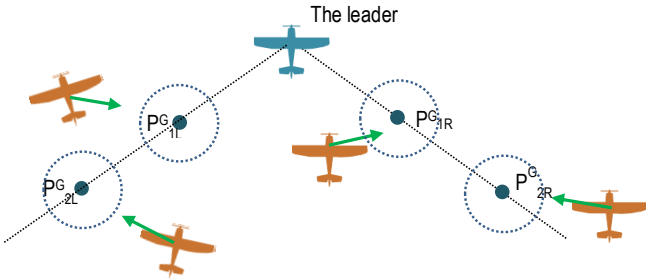

Fig. 2. An idea of position tracking in the virtual structure using individual cohesion behaviors, inspired by the theory of birds flocking. Green arrows define directions of cohesion. Each UAV has its assigned virtual point, which should attract it. Circles around virtual points in the structure define dead zones where cohesion behavior and speed control are not active

The principle of cohesion behavior is identical for every UAV (Fig. 3). To calculate the direction of cohesion that is defined jointly by desired heading and desired pitch angles, the knowledge about both the current position of the node and the current position of a UAV is required. The current position of every UAV is measured by GPS, and the current position of the node is the result of equation (2). Hence, the leader's position and his orientation in the inertial frame G should be broadcasted to other UAVs through wireless communication network inside the formation. This issue will be discussed later. But back to the definition of the cohesion direction, it can be simply defined for the i-th UAV as a normalized vector $\overrightarrow{K^C}_{iL(R)}$, which is given by equation (3). The vector can be named as a cohesion vector (Kownacki and Ołdziej, 2015).

$$\overrightarrow{K^C}_{iL(R)} = \frac{1}{\left|\overrightarrow{AP_{iL(R)}^G}\right|} \cdot \overrightarrow{AP_{iL(R)}^G} \quad \overrightarrow{AP_{iL(R)}^G} = \overrightarrow{P_{iL(R)}^G} - \overrightarrow{P_{UAV_{iL(R)}}^G} \tag{3}$$

where: $\overrightarrow{AP_{iL(R)}^G}$ – the cohesion vector is defined as a difference between the coordinates of the i-th UAV ($\overrightarrow{P_{UAV_{iL(R)}}^G}$) in the inertial frame G and the coordinates of assigned node in the virtual structure $\overrightarrow{P_{iL(R)}^G}$, $\left|\overrightarrow{AP_{iL(R)}^G}\right|$ – is a distance between the i-th UAV and the assigned node in the structure. This is also the displacement error.

The idea of cohesion behavior is illustrated in Fig. 3.

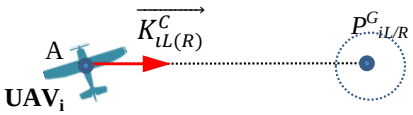

Fig. 3. An illustration of cohesion behavior. $P_{iL(R)}^G$ – the desired position in the structure for the i-th vehicle, $\overrightarrow{K_i}$ – the direction of cohesion

However, determining the direction of cohesion is not enough to achieve the effective position tracking, because it does not take into account one important parameter i.e. the displacement error. A separate control loop of airspeed is required to minimize this error. The easiest way to implement this is the usage of standard PID regulator, which will determine a desired airspeed to minimize the displacement error. The displacement error is defined as distance $\left|\overrightarrow{AP_{iL(R)}^G}\right|$. Therefore, the desired airspeed for the i-th UAV is defined by equation:

$$S_{iL(R)}^{d} = K_p \cdot \left[\left|\overrightarrow{AP_{iL(R)}^G}\right| + K_I \cdot \int_0^t \left|\overrightarrow{AP_{iL(R)}^G}\right| d\tau + K_D \cdot \frac{d\left|\overrightarrow{AP_{iL(R)}^G}\right|}{dt}\right] \tag{4}$$

where: K_p, K_D, K_I – gains of PID terms, $\left|\overrightarrow{AP_{iL(R)}^G}\right|$ – the distance between the i-th UAV and the assigned node in the structure (the displacement error), $S_{iL(R)}^d$ – the desired airspeed of the i-th UAV.

To avoid instability, i.e. fluctuations of values of desired heading and desired pitch, which can be generated by rapid changes in the relative orientation between the current position of a UAV and the current position of the assigned node. This could happen while the displacement error is nearly zero. Therefore, dead zones should be defined as spheres around each node in the structure of the formation (Fig. 2). Inside dead zones, each UAV aligns its airspeed to the airspeed of the formation, i.e. to the airspeed of leader. Thus, a modified definition of the desired airspeed can be given by:

DOI 10.1515/ama-2016-0015

$$S^d_{iL(R)} = \begin{cases} PID\left(\left|\overrightarrow{AP^G_{iL(R)}}\right|\right) & \left|\overrightarrow{AP^G_{iL(R)}}\right| \geq R \\ S_i & \left|\overrightarrow{AP^G_{iL(R)}}\right| < R \end{cases} \quad (5)$$

where: S_i – the airspeed of the entire formation (the leader's commanded airspeed), R – a radius of dead zones around the nodes in the virtual structure, $S^d_{iL(R)}$ – the desired airspeed of the i-th vehicle, $\left|\overrightarrow{AP^G_{iL(R)}}\right|$ – the distance between the i-th vehicle and its assigned node.

Gains of PID terms should be adjusted in the way ensuring that the desired speed will be greater than the speed S_i if UAV is outside the area of related dead zone. In that way, a UAV will be able to catch its assigned node in the structure with tolerance about R.

Collision avoidance between different UAVs in the formation should be also considered in the algorithm. It is necessary because of the fact that even wider spacing between the nodes in the virtual structure is not able to exclude a risk of collisions. Making maneuvers by the entire formation is related with a problem of intersections of trajectories that could be caused by inertia in dynamics of the position tracking. To prevent this, we propose a simple mechanism that is based on another flocking behavior, i.e. repulsion. This behavior is also implemented by the local control of a UAV, and its task is to repulse a UAV only from the preceding UAV in the structure. This way, the amount of information, which should be shared in the formation, is limited, and repulsion behaviors related with each pair of closest UAVs create a sequence of interactions, which will increase spacing between UAVs sequentially. The implementation of repulsion behaviors in the proposed algorithm is presented in Fig. 4.

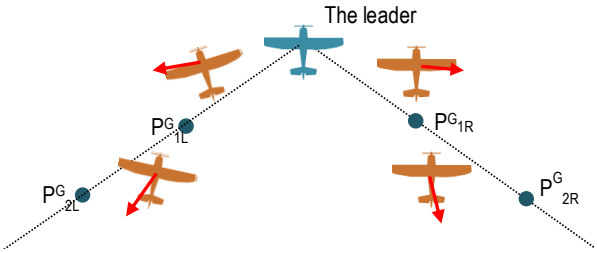

Fig. 4. Individual repulsion behaviors in the formation. Each vehicle is repulsed from the vehicle, which is preceding in the structure. It results in a chain of reactions. Red arrows represent directions of repulsion

The direction of the repulsion behavior is defined as it is shown in Fig. 5.

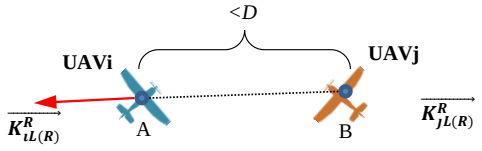

Fig. 5. An illustration of repulsion behavior. $\overrightarrow{K^R_{iL(R)}}$ – the direction of repulsion

In Fig. 5, a normalized vector $\overrightarrow{K^R_{iL(R)}}$ defines the direction of repulsion which is indispensable to keep a distance between two UAVs above the value of D. The repulsion vector is defined together by equations 6 and 7.

$$\overrightarrow{K^R_{iL(R)}} = \begin{cases} \frac{1}{\left|\overrightarrow{P^G_{iL(R)}P^G_{jL(R)}}\right|} \cdot \overrightarrow{P^G_{iL(R)}P^G_{jL(R)}} & \left|\overrightarrow{P^G_{iL(R)}P^G_{jL(R)}}\right| \leq D \\ 0 & \left|\overrightarrow{P^G_{iL(R)}P^G_{jL(R)}}\right| > D \end{cases} \quad (6)$$

$$\overrightarrow{P^G_{iL(R)}P^G_{jL(R)}} = \overrightarrow{P^G_{iL(R)}} - \overrightarrow{P^G_{jL(R)}} \quad (7)$$

where: $\overrightarrow{P^G_{iL(R)}}, \overrightarrow{P^G_{jL(R)}}$ – positions respectively of the i-th and the j-th vehicle, where $j < i$, $\left|\overrightarrow{P^G_{iL(R)}P^G_{jL(R)}}\right|$ – a distance between UAVs, D – the minimum permissible distance between two UAVs.

A combination of the repulsion vector and the cohesion vector gives a resultant direction satisfying goals of both tasks of control, i.e. the position tracking and the collision avoidance. This resultant direction is given by vector $\overrightarrow{K_i}$.

$$\overrightarrow{K_{iL(R)}} = \overrightarrow{K^R_{iL(R)}} + \overrightarrow{K^C{}_{iL(R)}} \quad (8)$$

When the resultant vector $\overrightarrow{K_{iL(R)}}$ would be already calculated, the set-points for low-level control loops, i.e. the desired heading angle and the desired pitch angle, can be easily determined from following equations:

$$\overrightarrow{K_{iL(R)}} = \begin{bmatrix} x_{iL(R)} \\ y_{iL(R)} \\ z_{iL(R)} \end{bmatrix}, \quad (9)$$

$$\Psi^d_{iL(R)} = arctan\left(\frac{x_{iL(R)}}{y_{iL(R)}}\right), \quad (10)$$

$$\Theta^d_{iL(R)} = arctan\left(\frac{z_{iL(R)}}{\sqrt{{x_{iL(R)}}^2 + {y_{iL(R)}}^2}}\right) \quad (11)$$

where: $\overrightarrow{K_{iL(R)}}$ – a vector which defines the resultant direction of flight, $\Psi^d_{iL(R)}$ – the desired heading angle, $\Theta^d_{iL(R)}$ – the desired pitch angle.

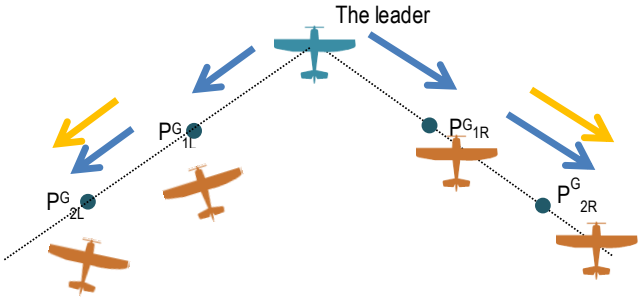

Fig. 6. Information flow inside the structure of the formation of UAVs, which is essential for the control. Blue arrows represent information about the leader; orange arrows represent information about the preceding UAV in the structure

Finally, we can formulate a control vector $\overrightarrow{u_i}$, which is composed with three parameters that are applied as set-points to the low-level control loops.

$$\overrightarrow{u_i} = \begin{bmatrix} \Psi^d_{iL(R)} \\ \Theta^d_{iL(R)} \\ S^d_{iL(R)} \end{bmatrix} \quad (12)$$

As it was mentioned earlier, the algorithm requires information sharing between UAVs in the structure. Every UAV must collect

DOI 10.1515/ama-2016-0015

data about the leader's position and its orientation in the inertial frame G and about the position of the preceding UAV in the structure, also in the inertial frame G. Thus, we propose the information flow inside the structure of the formation of UAVs as it is shown in Fig. 6.

The presented idea of information flow inside the formation, assumes that data about the leader are forwarded from one UAV to another, attaching only its own actual position to the leader's data. This means that the communication is based on a tree of peer-to-peer one-way transmission, starting at the leader as the root and next flowing accordingly with the increment of the node index. Such model of wireless networking can use simple radio modems, which are paired in couples of the transmitter and the receiver. Hence, there is no need for transmission synchronization between each pair of modems. Each node of the tree transmits data when it has already received data from the previous node. Random delays are a disadvantage of asynchronous communication which can destabilize the structure. But if we assume that the leader can broadcast its data with a higher rate, those delays would be relatively small and they could be ignored.

4. NUMERICAL SIMULATION

Numerical simulations are performed with the use of different the trajectories of the leader which goes through a sequence of four waypoints. Four UAVs fly behind the leader with predefined spacing between them, and all UAVs together create a formation which looks like a flock of ducks, i.e. it is in the shape of character "V". Spacings between UAVs in the formation respectively in x-axis and y-axis of the local frame L, i.e. Δx and Δy are the same and equal 10 meters. the radius R of dead zones around nodes in the structure is 5 meters. The leader's airspeed is set to 10 m/s. For each UAV in the formation, maximum roll angle was limited to ±30° and maximum pitch angle was limited to ±15°. These values are typical for small sized UAVs. The four waypoints, used to generate the leader's trajectories, are located at different altitudes to make able to observe behaviors of the formation during maneuvers of climbing or descending. Delays related with the information sharing (Fig. 6) are implemented by a number of unit delays, which is set adequately for each UAV, considering relative location of the assigned node.

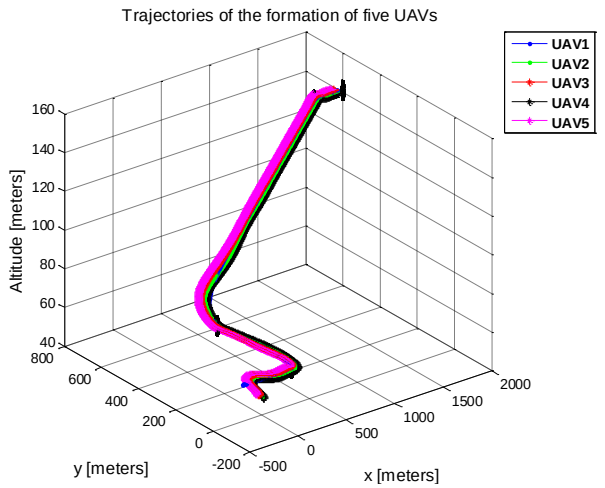

Fig. 7. Simulated trajectories of five UAVs creating the formation

Fig. 7 presents parallel trajectories of five UAVs creating the formation in "V" shape. While Fig. 8 shows horizontal projections of these trajectories. Positions of the UAVs at the end of the trajectories indicate clearly the shape of the formation.

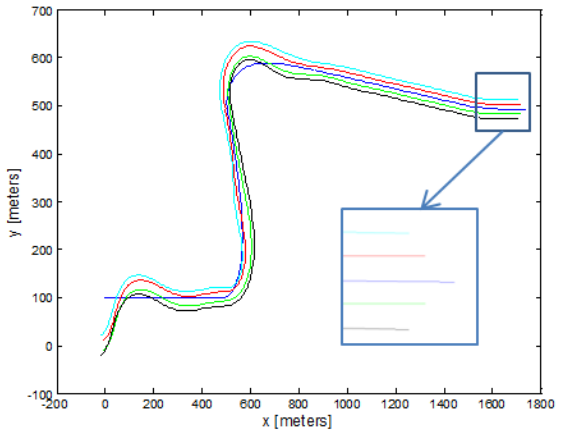

Fig. 8. Horizontal projections of the trajectories from Fig. 7

In next Figs. 9-12, there are respectively graphs of airspeeds, heading angles and pitch angles of all UAV, and finally distances between UAVs and their assigned nodes in the structure. The airspeed, the pitch and the heading of the leader are given in blue color.

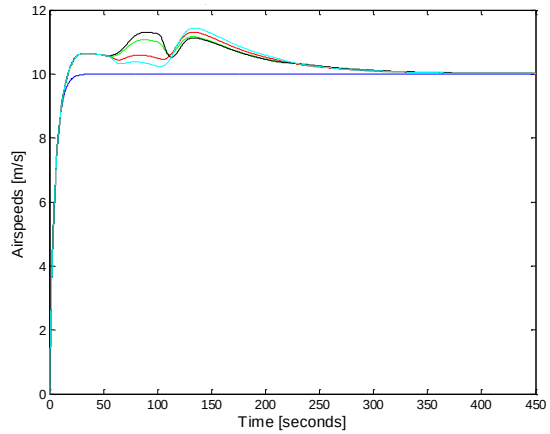

Fig. 9. Airspeeds of five UAVs in the formation. The airspeed of the leader is in blue

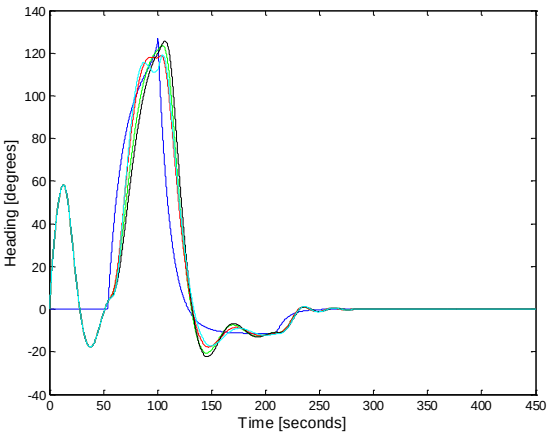

Fig. 10. Headings of five UAVs in the formation. The heading angle of the leader is in blue

DOI 10.1515/ama-2016-0015

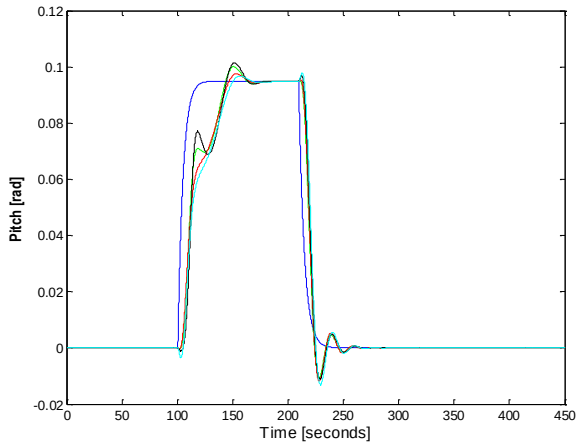

Fig. 11. Pitch angles of five UAVs in the formation. The pitch angle of the leader is in blue

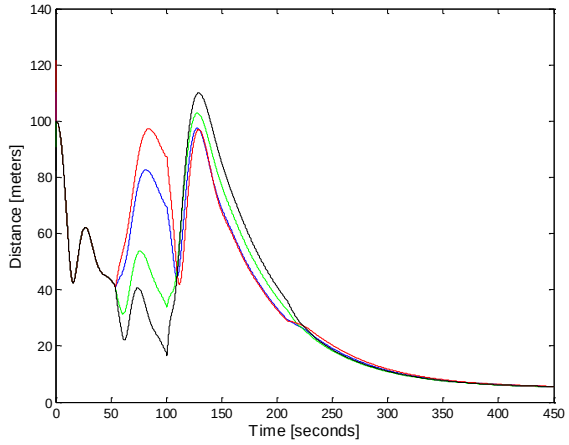

Fig. 12. Distances between UAVs and their assigned positions in the structure of the formation (Fig. 7 and 8)

Basing on Figs. 9 to 11, it can be found that all four UAVs align their trajectories to the leader's trajectory pretty well. Of course, inertia in responses of followers is noticeable, especially in situations when the leader changes its flight direction (Fig. 10 and 11). Moreover, it can be noticed that the trajectory of the leader and the trajectories of the rest of formation are not parallel during manoeuvres. This is a synergistic result of the limited turning radius of fixed-wing UAVs, which is a square function of airspeed (Eq. 13), and depends on delays of information sharing and rotations of the local frame L around the leader's position in reference to the inertial frame G.

$$R = \frac{V^2}{g \cdot \tan(\phi)} \tag{13}$$

where: V – airspeed, g – gravity acceleration, ϕ – limited roll angle.

Thus, if the leader turns to the right, the desired positions of the followers are shifted to the left in reference to their current positions and therefore, those UAVs turn to the left, oppositely to the leader. To minimize increased displacements in the positions (Fig. 12), the airspeeds of the followers should grow in reference to the leader (Fig. 9). Increased airspeeds result in longer turning radiuses, what can be visible as wider arcs of trajectories in comparison to the leader. At the ends of the sections of the trajectories, which are straight lines, UAVs manage to achieve the minimum displacement error that equals the radius of the dead zones. Not parallel trajectories can be observed regardless to the airspeed of UAVs and to the radius of the dead zones, what is shown in Fig. 13 and 14. This time, the airspeed is only 5 m/s and the radius of dead zones is 2 meters.

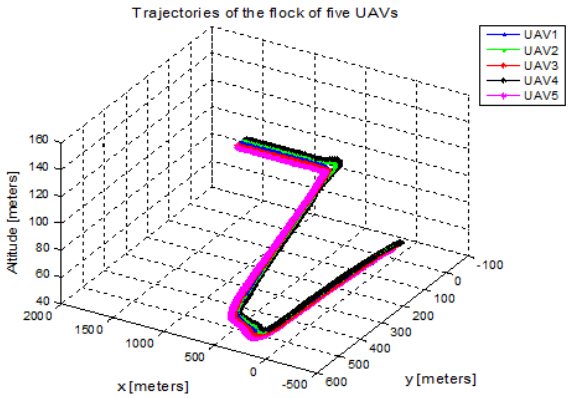

Fig. 13. Trajectories of simulated flight of the formation of five UAVs

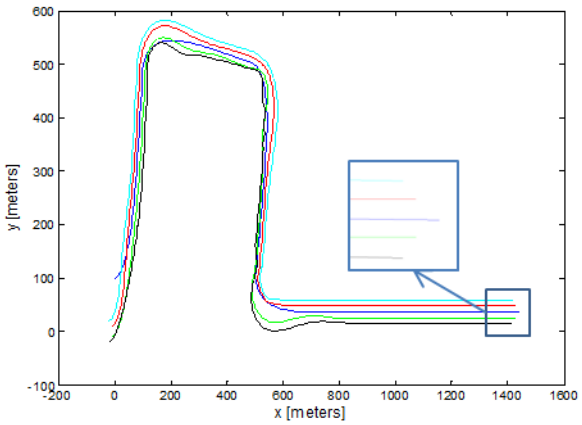

Fig. 14. Horizontal projections of the trajectories from Fig. 13

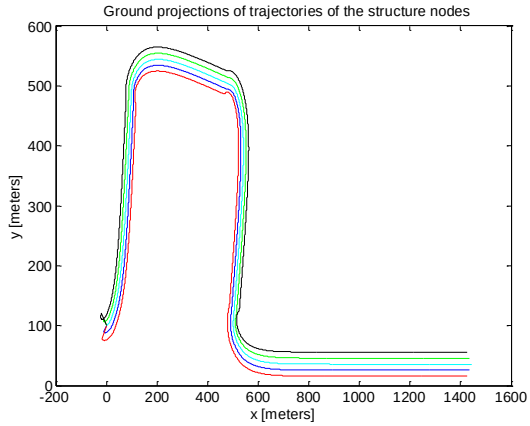

Fig. 15. Horizontal projections of the trajectories of the structure nodes which are related to the trajectories from Fig. 14

In Fig. 15, the trajectories of the nodes, i.e. desired positions, in the structure present an evidence for the effect of rotations of the virtual structure in reference to the inertial frame G, which are related with the leader's manoeuvres. Trajectories of the followers are bent in the reverse direction in respect to the trajectory of the leader, only later they go in the same direction. The effect is more visible for UAVs whose desired positions are located at longer distances from the leader. Spacing between vertical

DOI 10.1515/ama-2016-0015

sections of trajectories of the nodes look different than those between horizontal sections due to different scales of x-axis and for y-axis.

In Fig. 14, we can observe how trajectories intersect and overlap, what could mean that there are collisions. To dispel concerns associated with this issue, Fig. 16 presents graphs of distances between all UAVs in the formation. All distances are always greater than zero and this excludes definitely the possibility of collisions. The closeness of the trajectories lines is only an illusion also caused by different scales for x-axis and for y-axis.

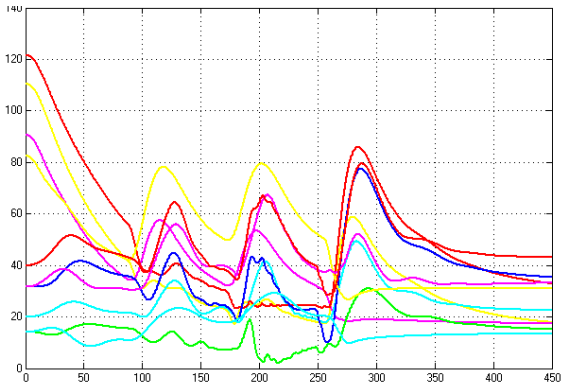

Fig. 16. Distances between all UAVs in the formation related with the trajectories from Fig. 13

Thus, the conclusion is that a simple collision avoidance rule, based on the repulsion behaviour is sufficient to provide safe flights of several UAVs in the proposed approach. The combination of behaviours of cohesion and repulsion offers a coherent and safe flight of the formation of UAVs.

The last issue, which should be discussed here, are delays in information flow between UAVs. If we take into account the fact that a UAV requires information from the leader to determine a current location of the node in the structure assigned to it, we will find that any delay in delivery of this information should impact only on relations between nodes. In other words, delays will increase real distances between nodes, but does not make local control unstable. To prove this argument, we prepared two simulations with different delays in the communication between two neighbours in the formation. In the second simulation, a value of delay is about 5 seconds, and it is greater hundred times than in the first case. Distances between UAVs and distances between UAVs and assigned nodes for each case are compared in Fig. 17 and Fig. 18.

In both Figs., UAV1 is the leader, UAV2 and UAV3 are just behind the leader respectively on its left and right side, UAV4 and UAV5 are behind UAV2 and UAV3, also respectively on the left and the right side of the leader. Basing on these results, it can be noticed that distances between pairs of UAVs in Fig. 17(2) are relatively greater than distances in Fig. 17(1), and this is the effect of increased delay. Simultaneously, distances between UAVs and their assigned positions in the formation look similarly on both sub Figs. of Fig. 18. It means that position errors used in the local control of UAV are insensitive to delays in communication. The problem is typical and common for all methods of formation flight of UAV, where positions of UAVs are synchronized in respect to a real or virtual reference point.

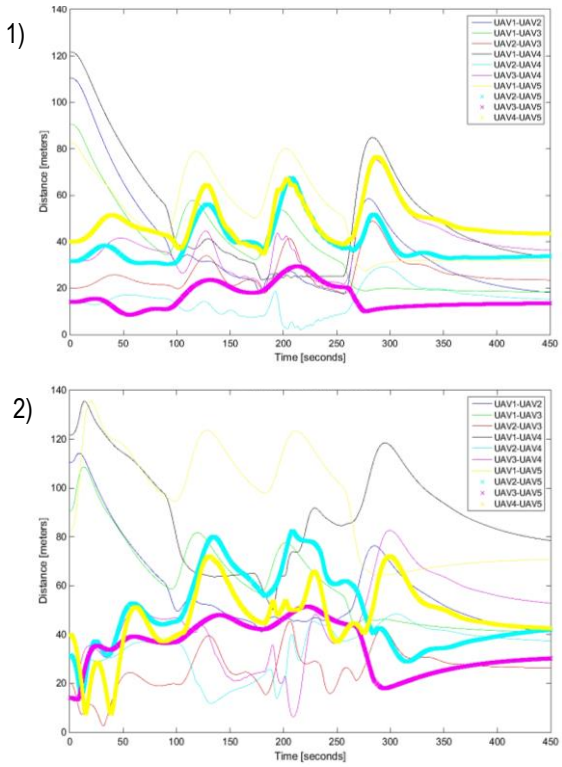

Fig. 17. Distances between all UAVs in the formation. 1) delay is about 0.05s, 2) delay is about 5s.

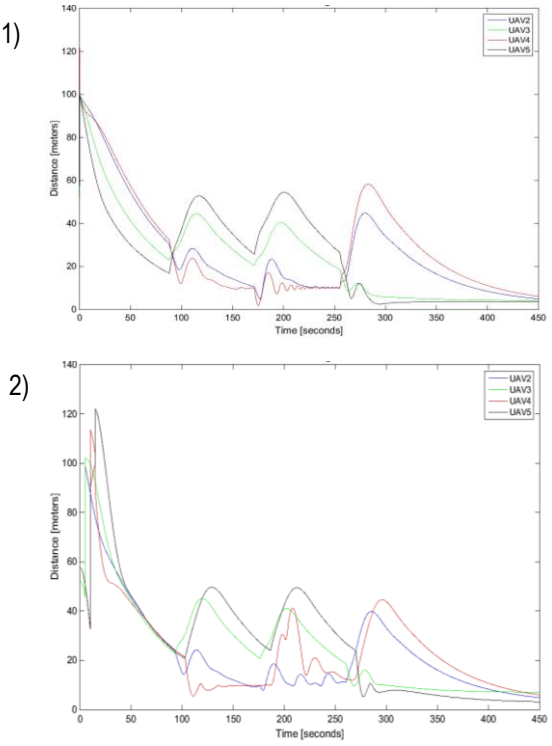

Fig. 18. Distances between UAVs and their assigned positions in the formation. 1) delay is about 0.05s, 2) delay is about 5s

5. CONCLUSIONS

In conclusion, the results of the simulations demonstrate the possibility of achieving a coherent formation flight by the combina-

DOI 10.1515/ama-2016-0015

tion of following approaches: virtual structure, leader-follower and flocking behaviours. Presented approach can be an attractive way to implement formations of the UAVs in the real applications. Applying the real leader offers a convenient way to control formation flight missions by an operator. The behaviour of cohesion provides effective tracking of UAVs positions in the formation with the acceptable level of positions errors. Simultaneously, the simple implementation of the repulsion behaviour protects the structure of the formation against collisions between UAVs inside it, even if a UAV is repulsed only from the UAV which is preceding in the structure. Such implementation of the repulsion behavior reduces also the amount of information which should be shared between UAVs in the formation. Also in contrast to other approaches, information sharing in the proposed conception of formation control uses a simple communication method which could be based on a chain of peer-to-peer connections composed with standard radio modems. This approach to information sharing inside the formation increases the span of the formation because a spacing between two UAVs is limited only by the range of\ a single radio modem.

The found problem of trajectories, which are not parallel, is related with the inertia of dynamics of UAV, delays in the control and the communication, and also with rotations of the virtual structure around the reference point i.e. the leader. The problem can be solved in two ways, by resizing the structure during manoeuvres or alternatively by adjusting airspeeds of UAVs flying at the inner and outer side of a turn. This will be a subject of future research.

REFERENCES

1. **Ambroziak L., Gosiewski Z.** (2014), Two stage switching control for autonomous formation flight of Unmanned Aerial Vehicles, *Aerospace Science and Technology*, 46, 221-226.
2. **Askari A., Mortazavi M., Talebi H.A.** (2015), UAV Formation Control via Virtual Structure Approach, *Journal of Aerospace Engineering*, 28(1).
3. **Cai D., Sun J., Wu S.** (2012), UAVs Formation Flight Control Based on Behavior and Virtual Structure, AsiaSim 2012, *Communications in Computer and Information Science*, 325, 429-438.
4. **Kownacki C., Ołdziej D.** (2015), Flocking Algorithm for Fixed-Wing Unmanned Aerial Vehicles, Third CEAS Specialist Conference on Guidance, Navigation and Control, *Advances in Aerospace Guidance, Navigation and Control*, 415-431.
5. **Low Ch. B., Ng Q.S.** (2011), A flexible virtual structure formation keeping control for fixed-wing UAVs, *9th IEEE International Conference on Control and Automation*, 621-626.
6. **Norman H. M. Li, Hugh H.T. Liu** (2008)**,** Formation UAV Flight Control using Virtual Structure and Motion Synchronization, *American Control Conference*, 1782-1787.
7. **Quintero S.A.P., Collins G.E., Hespanha J.P.** (2013), Flocking with Fixed-Wing UAVs for Distributed Sensing: A Stochastic Optimal Control Approach, *American Control Conference*, 2025-2031.
8. **Ren W., Beard R. W.** (2004)**,** Decentralized scheme for spacecraft formation flying via the virtual structure approach, *Journal of Guidance, Control and Dynamics*, 27(1), 73–82.
9. **Reynolds, C.W.** (1987), Flocks, herds and schools: a distributed behavioral model, ACM SIGGRAPH Computer Graphics*, Proceedings of ACM SIGGRAPH '87*, 25-34.
10. **Seo J., Ahn Ch., Kim Y.** (2009), Controller Design for UAV Formation Flight Using Consensus based Decentralized Approach, *AIAA Infotech@Aerospace Conference Unmanned Unlimited Conference*, 248-259.
11. **Shan J., Liu H.T.** (2005), Close-formation flight control with motion synchronization, *Journal of Guidance, Control and Dynamics*, 28(6), 1316–1320.
12. **Shao Z., Zhu X., Zhou Z., Wang Y.** (2014), A Nonlinear Control of 2-D UAVs Formation Keeping via Virtual Structures, Intelligent Robotics and Applications, *Lecture Notes in Computer Science*, 8917, 420-431.
13. **Virágh Cs., Vásárhelyi G., Tarcai N., Szörényi T., Somorjai G., Nepusz T., Vicsek T.** (2014), Flocking algorithm for autonomous flying robots, *Bioinspiration & Biomimetics*, 9(2).
14. **Xingping Ch., Serrani A., Ozbay H.** (2003), Control of leader-follower formations of terrestrial UAVs, *Proceedings of 42nd IEEE Conference on Decision and Control*, 498-503,
15. **Yun B., Chen B.M., Lum K.Y., Lee T.H.** (2008), A leader-follower formation flight control scheme for UAV helicopters, *IEEE International Conference on Automation and Logistics*, 1-3, 39-44.

DOI 10.1515/ama-2016-0016

THE USE OF SPECTRAL METHOD FOR FATIGUE LIFE ASSESSMENT FOR NON-GAUSSIAN RANDOM LOADS

Adam NIESŁONY[*], Michał BÖHM[*], Tadeusz ŁAGODA[*], Filippo CIANETTI[**]

[*]Faculty of Mechanical Engineering, Department of Mechanics and Machine Design, Opole University of Technology,
ul. Mikołajczyka 5, 45-271 Opole, Poland
[**]Department of Engineering, University of Perugia, via G. Duranti, 93, Perugia, 06125 Italy

a.nieslony@po.opole.pl, m.bohm@po.opole.pl, t.lagoda@po.opole.pl, filippo.cianetti@unipg.it

received 4 May 2015, revised 10 May 2016, accepted 12 May 2016

Abstract: The well-known problem with the fatigue lifetime assessment of non-Gaussian loading signals with the use of spectral method has been presented in the paper. A correction factors that transform the non-Gaussian signal into an equivalent Gaussian signal proposed by Bracessi et al. (2009) has been used for the purpose of lifetime calculations together with Palmgren-Miner Hypothesis. The calculations have been performed for the 10HNAP steel under random non-Gaussian load with four dominating frequencies. The signal has been generated on the test stand SHM250 for random tension-compression tests. The results with zero and non-zero mean stresses have been used to calculate the fatigue life with the frequency domain method based on Dirlik's model and with a time domain method with the use of the rainflow cycle counting algorithm. The obtained calculation results have been compared with experimental results.

Key words: Spectral Method, Fatigue Life, Random Loading, Non-Gaussian

1. INTRODUCTION

Fatigue life assessment is an important issue nowadays, and is strongly related with the reliability of components. It gains importance if we are dealing with random loading conditions or vibrations (Benasciutti et al. 2006, 2010, 2013). Some scientists have noticed that most stochastic natural forces as e.g. the wind or sea waves have a Gaussian distribution. When we try to record real life stress histories, they usually have also an almost ideal Gaussian characteristic. For the purpose of calculations we assume that the almost ideal signals are Gaussian. It doesn't affect the calculations if we filter the histories correctly (Pawliczek and Kluger 2013). We are dealing with serious issues when we are working with signals that are not nearly Gaussian and we have to calculate the fatigue life. There are some fresh solutions related to that problem presented by Bracessi et al (2009) or Wolfsteiner and Sedlmair (2013, 2015). The solutions have the intention to either correct the Gaussian damage degree or to filter the non-Gaussian signal into an equivalent Gaussian signal (when it comes to statistical information) with the use of correction factors. We can assess the life interval of a structural component related to its fatigue with the use of either standard stand tests or computation methods. These methods can be divided into two groups defined in the time domain which are based on cycle counting procedures, or those defined in the frequency domain which are using the statistic information of the load. That are so called spectral methods. They use the power spectral density (PSD) to describe the stress amplitudes. The spectral method for fatigue life assessment has many advantages such as the computation time. But the main drawback consists in calculation methods applied in the case of a non-Gaussian random loads. It works perfectly on signals with Gaussian load characteristic, but when we try to calculate non-Gaussian characteristics we often obtain fatigue lives that are overestimated a few times. The paper deals with fatigue life assessment of the 10HNAP steel under non-Gaussian loading condition with and without the influence of the mean stress effect. To compensate the mean stress effect a procedure proposed by Niesłony and Böhm (2012, 2015) has been used. The non-Gaussianity of a signal has been corrected by the correction factor by Braccesi et al (2009). The fatigue lives estimated on the basis of combination of spectral method and the Dirlik model have been compared with results obtained when the rainflow cycle counting method and experimental data were applied. Damage accumulation for both cases has been calculated with the use of the Palmgren-Miner hypothesis.

2. FATIGUE STAND TESTS

The fatigue stand tests have been performed by Łagoda for the 10HNAP steel. Basic material constants can be found in the paper by Łagoda et al. (2001) and are presented in Tab. 1. The samples were tested on the fatigue test stand SHM250 for random tension-compression. A signal has been generated that has a non-Gaussian probability distribution with four dominating frequencies for the case of zero mean stress and non-zero mean stress. The tests with non zero mean stress have been performed for a large influence of the negative stress value. The Probability distribution function of the signal has been presented in Fig. 1. The rainflow matrix of the stress history has been presented in Fig. 2.

DOI 10.1515/ama-2016-0016

Tab. 1. Mechanical properties of 10HNAP steel

R_e, MPa	R_m, MPa	A_{10}, %	Z, %	E, GPa	ν
414	556	31	35	215	0.29

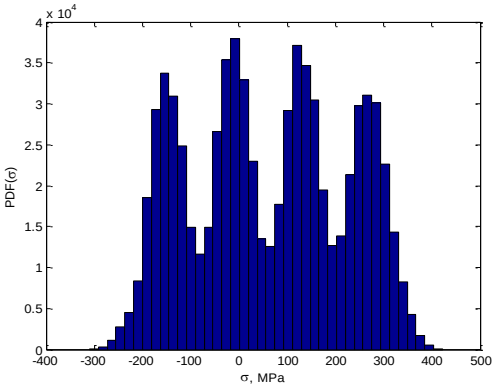

Fig. 1. Probability distribution function (PDF) of the non-Gaussian stress signal

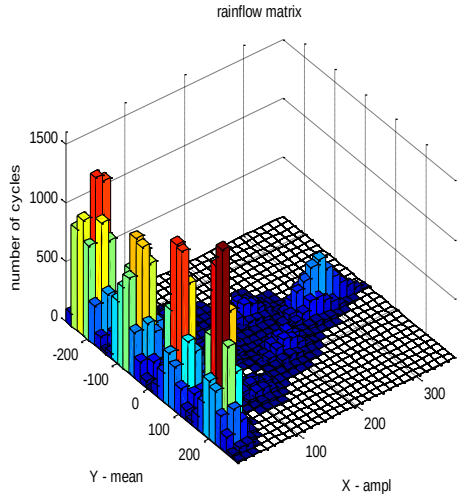

Fig. 2. Rainflow matrix of the stress history

3. FATIGUE LIFE CALCULATION

The fatigue life has been calculated with the use of spectral method with the Dirlik model and with the cycle counting method with the use of rainflow cycle counting procedure. The mean stress effect has been compensated with the use of the procedure proposed by Niesłony and Böhm. This one is based on the transformation of a zero mean stress PSD with a correction factor according to the equation:

$$G_{\sigma T}(f) = K_i{}^2(\sigma_m) \cdot G_\sigma(f), \tag{1}$$

where: $G_\sigma(f)$ is the PSD function of a centered stress course, f is the frequency, K_i is the mean stress correction factor according to a used compensation model, which can be defined exemplary as K_G for the Gerber mean stress compensation model as:

$$K_G = \frac{1}{1-\left(\frac{\sigma_m}{R_m}\right)^2}, \tag{2}$$

where: σ_m – mean value of the stress course, R_m – ultimate tensile strength.

The transformed PSD is used to calculate its first five moments ξ_k:

$$\xi_k = \int_0^\infty G_{\sigma T}(f) f^k df, \tag{3}$$

that are needed to calculate the probability distribution function (PDF). We can find many proposals in the literature that are used for the PDF calculations. These solutions have found their place in certain areas of the industry:

For the marine industry:

Rice (1944) PDF:

$$p(\sigma) = \frac{1}{\sqrt{2\pi\xi_0}}(1-\gamma^2)^{\frac{1}{2}}\exp\left[\frac{-\sigma^2}{2\mu^2(1-\gamma^2)}\right] + \\ + \frac{\sigma}{2\mu^2}\left[1+\operatorname{erf}\left(\frac{\sigma}{\xi_0\sqrt{2\gamma^{-2}-2}}\right)\right]\exp\left(-\frac{\sigma^2}{2\mu^2}\right), \tag{4}$$

where: μ – variance, and γ can be calculated with the use of spectral moments ξ_i:

$$\gamma = \frac{\xi_2}{\sqrt{\xi_0\xi_4}}, \tag{5}$$

and the function $\operatorname{erf}(u)$ is the error function of stress signal value finding in [0,u] interval:

$$\operatorname{erf}(u) = \frac{2}{\sqrt{\pi}}\int_0^u e^{-t^2}\,dt. \tag{6}$$

Chadbury and Dover (1985) have used the Rice formula and proposed the weighted amplitude PDF:

$$\sigma_{aw} = \left(2\sqrt{2\xi_0}\right)\left[\left(\frac{\left(\sqrt{1-\gamma^2}\right)^{m+2}}{2\sqrt{\pi}}\right)\Gamma\left(\frac{m+1}{2}\right) + \frac{\gamma}{2}\Gamma\left(\frac{m+2}{2}\right) + \right. \\ \left. + \operatorname{erf}(\gamma)\frac{\gamma}{2}\Gamma\left(\frac{m+2}{2}\right)\right]^{\frac{1}{m}} \tag{7}$$

Hancock (1985):

$$\sigma_{aw} = \left(2\sqrt{2\xi_0}\right)\left[\gamma\cdot\Gamma\left(\frac{m}{2}+1\right)\right]^{\frac{1}{m}}, \tag{8}$$

where Γ is the gamma function.

For the aviation industry:

Lallane (2013):

$$p(\sigma) = \sqrt{\frac{1-\gamma^2}{2\pi\xi_0}}\exp\left(\frac{-\sigma^2}{2\xi_0(1-\gamma^2)}\right) + \\ + \frac{\gamma\sigma}{2\xi_0}\exp\left(\frac{-\sigma^2}{2\xi_0}\right)\left(1-erf\left(\frac{\gamma\sigma}{\sqrt{2\xi_0(1-\gamma^2)}}\right)\right). \tag{9}$$

Electronic industry:

Steinberg (2000):

$$\sigma_{aw} = \left[0{,}683\left(2\sqrt{\xi_0}\right)^m + 0{,}271\left(4\sqrt{\xi_0}\right)^m + \right. \\ \left. + 0{,}043\left(6\sqrt{\xi_0}\right)^m\right]^{\frac{1}{m}}. \tag{10}$$

Railway industry:

Tunna (1986)

$$p(\sigma) = \frac{\sigma}{4\gamma\xi_0}\exp\left(\frac{-\sigma^2}{8\gamma\xi_0}\right). \tag{11}$$

We can also find universal solutions:

By Rayleigh (Bendat 1964):

$$p(\sigma) = \frac{\sigma}{\xi_0}\exp\left(\frac{-\sigma^2}{2\xi_0}\right), \tag{12}$$

and later deviation of Rayleigh's formula by Bendat (1964):

$$p(\sigma) = \frac{\sigma}{4\xi_0}\exp\left(\frac{-\sigma^2}{8\xi_0}\right). \tag{13}$$

DOI 10.1515/ama-2016-0016

According to the Dirlik's (1985) distribution function:

$$p(\sigma_a) = \frac{1}{2\sqrt{\xi_0}} \cdot \left[\frac{K_1}{K_4} \cdot e^{\frac{-Z}{K_4}} + \frac{K_2 \cdot Z}{R^2} \cdot e^{\frac{-Z^2}{2 \cdot R^2}} + K_3 \cdot Z e^{\frac{-Z^2}{2}} \right], \quad (14)$$

where: Z, K_1, K_2, K_3, K_4, R – factors which are functions of the first five moments of the transformed PSD.
Zhao and Baker (1992):

$$p(\sigma) = w \cdot \alpha \cdot \beta \cdot \sigma^{(\beta-1)} \exp(-\alpha\sigma^b) + (1-w)\sigma \exp\left(\frac{-\sigma^2}{2}\right), \quad (15)$$

where w, α, β are factors described as:

$$w = \frac{1-\gamma}{1-\sqrt{\frac{2}{\pi}}\Gamma\left(1+\frac{1}{\beta}\right)\alpha^{\frac{-1}{\beta}}}, \quad (16)$$

$$\alpha = 8 - 7\gamma, \quad (17)$$

$$\beta = \begin{cases} 1.1; & \gamma < 0.9 \\ 1.1 + 9(\gamma - 0{,}9); & \gamma \geq 0{,}9 \end{cases} \quad (18)$$

Benasciutti and Tovo (2005) proposed a direct damage function:

$$E(D_{RFC}) = \nu_p C - 1\gamma\left(\sqrt{2\xi_0}\right)^m \Gamma\left(1+\frac{m}{2}\right)[b + (1-+b)\gamma^{m-1}], \quad (19)$$

where: C and m are constants from the Basquin curve, b is weight function dependant from the PSD, νp is calculated with the formula:

$$\nu_p = \frac{1}{2\pi}\sqrt{\frac{\xi_4}{\xi_2}}. \quad (20)$$

Lutes and Sarkani (1996):

$$p(\sigma) = \frac{\sqrt{1-\gamma^2}}{\sqrt{2\pi\xi_0}} \exp\left(\frac{\sigma^2}{2\mu^2(1-\gamma^2)}\right) + + \frac{\gamma\sigma}{\mu^2} \exp\left(\frac{\sigma^2}{2\mu^2}\right) \Phi\left(\frac{\gamma\sigma}{\xi_0\sqrt{1-\gamma^2}}\right). \quad (21)$$

A plot of some of these functions has been presented in Fig.3.

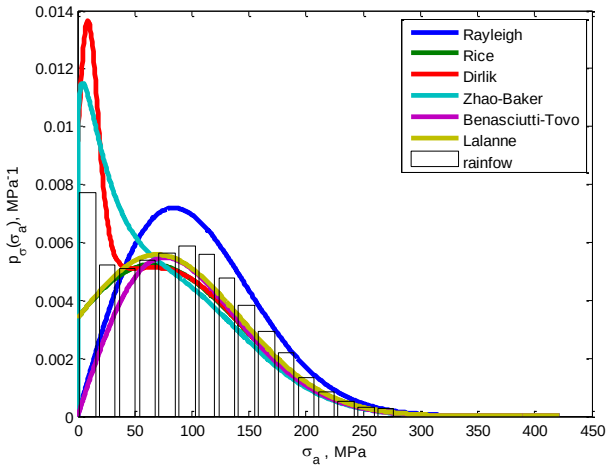

Fig. 3. Chosen probability distribution function shapes for random data in comparison with rainflow amplitude distribution

Fatigue life is calculated using the selected hypotheses of fatigue damage accumulation, e.g. for a linear Palmgren-Miner hypothesis with the amplitude below the fatigue limit we obtain:

$$T_{cal} = \frac{1}{E[P]\int_0^\infty \frac{p(\sigma_a)}{N(\sigma_a)} d\sigma_a} \cdot \frac{1}{\lambda_{ng}}, \quad (22)$$

where $E[P]$ is the expected number of peaks, and non-Gaussianity is corrected with a corrective factor according to Braccesi et al. (2009):

$$\lambda_{ng} = \exp\left(\frac{m^{\frac{2}{3}}}{\pi}\left(\frac{K-3}{5} - \frac{S^2}{4}\right)\right), \quad (23)$$

where m – slope of Wöhler curve, K – kurtosis and S – skewness (asymmetry of PDF).

4. RESULTS AND DISCUSSION

The calculation of fatigue lifetime has been performed with three calculation methods according to rainflow cycle counting method and with the use of Dirlik's model for spectral method. For the case of non-zero mean stress all methods used the Gerber mean stress compensation model. Calculations according to spectral method have been modified with a corrective coefficient. The obtained power spectrum density has been presented in Fig. 4: The calculations have been compared with experimental results and have been illustrated in a comparison graphs presented in Fig. 5 and Fig. 6

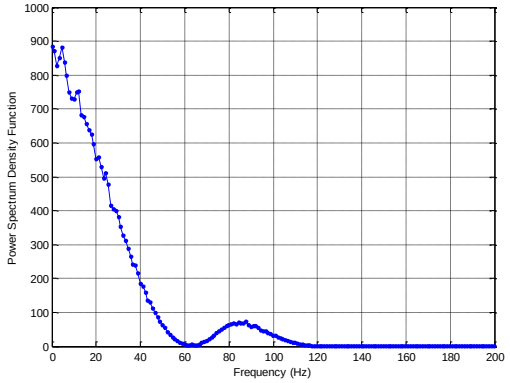

Fig. 4. Course of power spectrum density of the non-Gaussian stress signal versus signal frequency

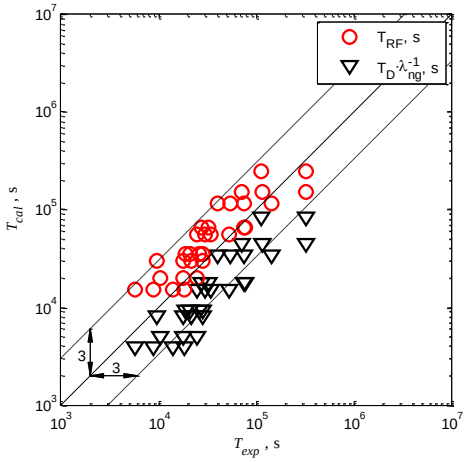

Fig. 5. Comparison of experimentally recorded lifetimes with the calculated results on the basis of rain-flow cycle counting method T_{RF} and the Dirlik model T_D for zero-mean stress signal

DOI 10.1515/ama-2016-0016

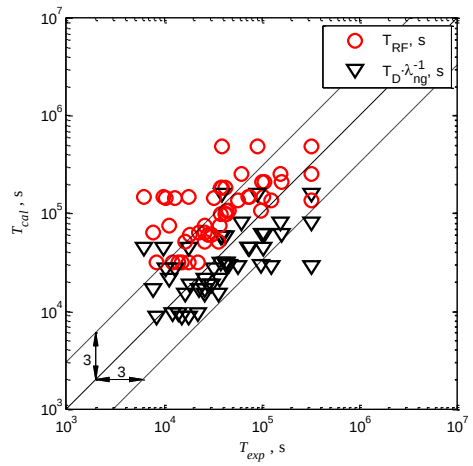

Fig. 6. Comparison of lifetime experimental results with the calculated onces on the basis of rain-flow cycle counting method T_{RF} and the Dirlik model T_D with mean stress correction factor

5. CONCLUSIONS AND OBSERVATIONS

The fatigue lifetime assessment for the case of non-Gaussian loading histories with four dominating frequencies gives satisfied results after the use of the corrective factor λ_{ng}. It is possible to use the correction coefficient for such loading cases. It can be awaited that this method will be possible to use for such loading cases. The results indicate that in the case of non-zero mean stress non-Gaussian loading histories the use of spectral method with the correction factor can be applied with the success. Calculations of fatigue lifetime with the use of the Gerber compensation model allow to obtain satisfied results and take into account the impact of compression, when the tests are proceeded with a large influence of negative mean stress value.

REFERENCES

1. **Banvillet A., Łagoda T. , Macha E., Niesłony A., Palin-Luc T., Vittori J.-F.** (2004), Fatigue life under non-Gaussian random loading from various Models, *International Journal of Fatigue*, 26, 349–363.
2. **Benasciutti D., Cristofori A.,Tovo R.** (2013) Analogies between spectral methods and multiaxial criteria in fatigue damage evaluation, *Probabilistic Engineering Mechanics*, 31, 39–45.
3. **Benasciutti D., Tovo R.** (2005), Spectral methods for lifetime prediction under wide-band stationary random processes, *International Journal of Fatigue*, 27 867–877.
4. **Benasciutti D., Tovo R.** (2006) Comparison of spectral methods for fatigue analysis of broad-band Gaussian random processes, *Probabilistic Engineering Mechanics*, 21(4), 287–299.
5. **Benasciutti D., Tovo R.** (2010) On fatigue cycle distribution in non-stationary switching loadings with Markov chain structure, *Probabilistic Engineering Mechanics*, 25(4), 406-418.
6. **Bendat J.S.** (1964)., M.A. Corporation, U.S.N.A. and S. Administration, *Probability functions for random responses: prediction for peaks, fatigue damage, and catastrophic failures*, National Aeronautics and Space Administration.
7. **Braccesi C., Cianetti F., Lori G., Pioli D.** (2009), The frequency domain approach in virtual fatigue estimation of non-linear systems: The problem of non-Gaussian states of stress, *International Journal of Fatigue*, 31(4), 766–775.
8. **Chaudhury G., Dover W.** (1985), Fatigue analysis of offshore platforms subject to sea wave loadings, *International Journal of Fatigue*, 7, 13–19.
9. **Dirlik T.** (1985), *Application of computers in fatigue analysis*, phd thesis, University of Warwick.
10. **Hancock J., D. Gall** (1985), *Fatigue under narrow and broad band stationary loading*, Marine Technology Directorate Ltd.
11. **Łagoda T., Macha E., Pawliczek R.** (2001),The influence of the mean stress on fatigue life of 10HNAP steel under random loading, *International Journal of Fatigue*, 23, 283–291.
12. **Lalanne C.** (2013), *Mechanical Vibration and Shock Analysis*, Fatigue Damage, John Wiley & Sons.
13. **Lutes L.D.** (1996), *Stochastic Analysis of Structural and Mechanical Vibrations*, 1st edition, Prentice Hall, Upper Saddle River, N.J.
14. **Niesłony A., Böhm M**. (2012), Mean Stress Value in Spectral Method for the Determination of Fatigue Life, *Acta Mechanica et Automatica*, 6, 71–74.
15. **Niesłony A., Böhm M**. (2015), Mean Stress Effect Correction in Frequency-domain Methods for Fatigue Life Assessment, *Procedia Engineering*,12(101), 347-354.
16. **Pawliczek R., Kluger K.** (2013) Influence of the irregularity coefficient of loading on calculated fatigue life, *Journal of Theoretical and Applied Mechanics*, 51(4), 791-798.
17. **Rice S.O.** (1944), Mathematical Analysis of Random Noise, *Bell SystemTechnical Journal*, 23 282–332.
18. **Steinberg D.S.** (2000), *Vibration Analysis for Electronic Equipment*, 3 edition, Wiley-Interscience, New York.
19. **Tunna J.M.** (1986), Fatigue Life Prediction for Gaussian Random Loads at the Design Stage, F*atigue & Fracture of Engineering Materials & Structures*, 9, 169–184.
20. **Wolfsteiner P., Breuer W.** (2013) Fatigue assessment of vibrating rail vehicle bogie components under non-Gaussian random excitations using power spectral densities, *Journal of Sound snd Vibration*, 332(22), 5867-5882.
21. **Wolfsteiner P., Sedlmair S.** (2015), Deriving Gaussian Fatigue Test Spectra from Measured non Gaussian Service Spectra, *Procedia Engineering*, 101, 543 – 551.
22. **Zhao W., Baker M.** (1992), On the probability density function of rainflow stress range for stationary Gaussian processes, *International Journal of Fatigue*, 14 (2), 121–135.

Acknowledgements: The Project was financed from a Grant by National Science Centre (Decision No. 2013/09/N/ST8/04332).

DOI 10.1515/ama-2016-0017

INFLUENCE OF CORRUGATION DEPTH ON LATERAL STABILITY OF COLD-FORMED STEEL BEAMS OF CORRUGATED WEBS

Viorel UNGUREANU*, Dan DUBINA*

*Department of Steel Structures and Structural Mechanics, Politehnica University of Timisoara, Romania
Laboratory of Steel Structures, Romanian Academy – Timisoara Branch, Romania

viorel.ungureanu@upt.ro, dan.dubina@upt.ro

received 6 September 2015, revised 10 May 2016, accepted 12 May 2016

Abstract: The beams of thin corrugated web afford a significant weight reduction compared with hot-rolled or welded ones. In the initial solutions, the flanges are made of flat plates, welded to the sinusoidal web sheet, requiring a specific welding technology. A new solution is proposed by the authors, in which the beam is composed by a web of trapezoidal cold-formed steel sheet and flanges of back-to-back lipped channel sections. For connecting flanges to the web self-drilling screws are used. The paper summarizes the experimental and numerical investigations carried out at the CEMSIG Research Centre (www.ct.upt.ro/centre/cemsig/) of the Politehnica University of Timisoara and, at the end, presents the influence of corrugation depth of web on the lateral stability of the beams.

Key words: Corrugated Web Beam, Cold-Formed Steel Solution, Discrete Fasteners, Self-Drilling Screws, Experimental Investigation

1. INTRODUCTION

Corrugated web girders represent a relatively new structural system emerged in the past two decades in Europe, particularly in Germany and Austria. Increased interest for this solution was observed for the main frames of single-storey steel buildings and in steel bridges. The technical solution consists in using a sinusoidal web sheet which is welded to the flat plates used for flanges, a specific welding technology being applied.

The main benefits of this type of elements are that the corrugated webs increase the beam's stability against local buckling and also against lateral-torsional buckling, which may result in a more economical design if compares with flat web with stiffeners. Furthermore, the use of thinner webs results in lower material cost, with an estimated cost savings of 10-30% in comparison with conventional fabricated sections and more than 30% compared with standard hot-rolled beams. The buckling resistance of the sinusoidal corrugated steel sheet used for webs, which is very thin (1.5-3 mm), is comparable with plane webs of 12 mm thickness or more.

A new technological solution composed by webs made of trapezoidal cold-formed steel sheets and flanges of built-up cold-formed steel profiles (e.g. back-to-back lipped channel sections or angles with turn lips) has been proposed by the authors Dubina et al., (2013, 2015). The connections between flanges and web can be done with self-drilling screws or by spot welding. Compared with the traditional solution, where the sinusoidal web sheet is continuous, in this case the width of corrugated sheets that compose the web is approximately 1000 mm. Consequently, seam connections are needed for providing the continuity of the web. This ensemble, i.e. seam connections – two overlapped corrugated sheets, acts as web stiffeners, increasing resistance under transverse loads, of particular interest in the locations of purlin supports.

Also, it is easy to be observed that the new solution, as a whole, is 100% composed by cold-formed steel elements, avoiding the combination of two types of steel products, i.e. cold-formed for webs and hot-rolled for flanges as presented before (www.zeman-steel.com). Moreover, high protection to corrosion due to the fact that all components are galvanized is a major advantage.

Thin new solution can be used as roof girders, frame bearing structures (also multi-span and multi-storey) and short span pedestrian bridges. It is expected from this solution to cover medium spans up to 24 m length. They also can be a reliable alternative to purlins and secondary beams where these have to cover large bays, instead of using steel trusses.

A beam with corrugated web behaves similarly to a lattice girder, in which the bending moments and applied forces are transferred via flanges only, while the transverse forces are transferred through the diagonals and verticals of the lattice girder, in this case the corrugated web. The dimensioning of corrugated web beams is ruled by Annex D of the EN 1993-1-5:2006, together with specific aspects of EN 1993-1-1 and EN 1993-1-3.

The main aim of present study is to complete the previous studies of authors with an investigation of sensitivity of webs to distortion of corrugations when the size of corrugations increases.

2. LITERATURE REVIEW

Several types of built-up cold-formed steel beams prepared for industrialised fabrication have been experimentally investigated. For these beams, bolts, screws or spot/laser welding are used as fastening technologies.

In 2000, BEN-VAUTIER S.P.A., Italy (WO 00/17463), patented a modular H-beam comprises one or more modules, each formed of two half-structural parts of two pieces of structural steel,

DOI 10.1515/ama-2016-0017

forming each a thin sheet, comprising a central part or core and lateral half-flanges. The half-flanges form gaps, inside which plates are introduced in order to strengthen the flanges of the beam, which constitute the regions more subjected to bending stresses.

Zhao (2005) at Queensland University of Technology initiated a research program to investigate the structural behaviour and design of hollow flange beam sections as compression members. He used rectangular hollow flanges and various manufacturing methods such as spot welding, self-pierced riveting and screw fastening to form Rectangular Hollow Flange Beam (RHFB) sections from a single steel strip. It was observed that the type of fastening and spacing does not affect the member compression capacity significantly. However, the structural behaviour and design of RHFB as flexural members will be different and therefore further investigations are needed to identify their failure modes and develop suitable design rules.

Wanniarachchi (2005) extended the work of Zhao (2005) and developed a new cold-formed steel beam with two rectangular hollow flanges rigid in torsion and a slender web formed using intermittent screw fastening to enhance the flexural capacity while maintaining a minimum fabrication cost. His research was focused on the flexural behaviour and design of cold-formed steel beams with rectangular hollow flanges (RHFB) made of separately formed flanges and web connected by simple screw fastening. He has found that intermittent screw fastening method appears to be structurally adequate and minimises the fabrication cost.

Landolfo et al. (2008) evaluated the applicability of built-up cold-formed steel beams assembled by laser welding and assessed the load bearing capacity of the assembled beams. The I-section with hollow flanges is fabricated from two back-to-back special C-profiles. The two profiles are joined with connections which are located on the web and on the flanges. Two reinforcing plates are placed inside the top and bottom hollow flanges of the I-section, providing an additional connection system between the two C-profiles.

A very important aspect related to the cold-formed steel is the connecting technique. Briskham et al. (2006) performed a comparative study on of self-pierce riveting, resistance spot welding and spot friction joining for aluminium automotive sheet. Quantitative comparisons have been made on the basis of tensile strength (shear and peel), process time, equipment price and running cost. The results identified resistance spot welding as a more economically favourable option than self-pierce riveting or spot friction joining for the task of producing the majority of the joints. The analysis indicates that it is the ongoing cost of the rivets that makes self-pierce riveting the most expensive process. For resistance spot welding, the largest cost factors identified were energy consumption and frequency of electrode replacement. Although the material is aluminium, similar conclusions can be drawn for steel too.

Guenfoud et al. (2010) tested welded specimens fabricated through one, two or four layers of steel sheets with thicknesses ranging from 0.76 mm to 1.52 mm. A total of 72 tension tests and 107 shear tests were completed. The idea was the initiation of a research program on the shear resistance and tension resistance of multi-layer arc spot welds. They found that the type of electrode, high current setting and proper welding technique affect the quality of arc-spot welds in multi-layer connections, and a lower limit for the net effective weld diameter was proposed.

Snow (2008) conducted a similar research in order to establish a relationship between arc spot weld shear strength and the arc time used while forming the weld. In this case the arc times were broken down into three separate categories. The first category consisted of full-time welds, the second 2/3-time welds, and the third 1/3-time welds. Testing was performed on steel gauge sheets of 0.85 mm, 1 mm, 1.3 mm and 1.6 mm. Each gauge material was tested in single-, double- and four-layer configurations. Two types of diameter arc spot welds were tested. Comparisons were made between shear strength and weld geometry, including average diameter, effective diameter and penetration. The research has proven that arc time has a tremendous influence on arc spot weld shear strength.

A wide experimental investigation on laser welded connections based on both lap-shear and tension tests were performed at the University of Naples (2009). The experimental programme was designed in order to evaluate the effects of different parameters on the strength and ultimate displacement of the selected connections. The results of the experimental tests were compared with the predicted resistance values according to Eurocode 3, with the aim of validating for laser welding the mechanical models provided for spot welds.

A lot of work has been done to study the shear capacity (Yi et al., 2008; Moon et al., 2008; Sause and Braxtan, 2011) and the behaviour under patch loading of steel beams with corrugated web (Abbas et al., 2006, 2007). In what concerns the bending behaviour it was observed that the contribution of the web to the ultimate moment capacity of a beam with corrugated web is negligible, and the ultimate moment capacity is based on the flange yield stress. The effect of the corrugation profiles of the web on the lateral-torsional buckling strength of I-girders was also studied (Kazemi et al., 2010; Jiho et al., 2009; Moon et al., 2013; Kövesdi, 2012). Pasternak et al. (2010) presented a new proposal for Annex D of EN 1993-1-5:2006.

Probably, the first built-up steel girder using corrugated sheets as web elements and cold-formed sections for flanges is the Macomber Panlweb girder appeared on the market around the ’70s. The Macomber Panlweb girder consists of 1.9 mm to 3.8 mm thickness of the corrugated web for depths of 0.51 to 1.02 m (US3444664). This solution applies shallow VV-section for flanges, which make difficult enough the installing of flange-to-web fasteners.

The first attempt of the authors of this paper related to this type of beams 100% composed by cold-formed steel elements was a numerical study (Neagoie et al., 2005) in order to prove the efficiency of such solution against cold-formed steel trusses.

A similar solution has been proposed and analysed in the frame of PRECASTEEL project (RFSR-CT-2007-00038), but using blind rivets as seam fasteners for the corrugated web and bolts for web-to-flange connections. For flanges, back-to-back lipped channel or two types of hat-sections have been used. Deep corrugation web sheeting of longitudinal intermediate stiffeners have been applied in this solution. However, looking to the test results, one observes the sensitivity to distortion of corrugation still remain high.

3. EXPERIMENTAL TESTS

3.1. Specimens, test procedure and test results

The experimental program was carried out at the CEMSIG Research Centre (http://www.ct.upt.ro/en/centre/cemsig) of the Politehnica University of Timisoara. Five beams with corrugated

Viorel Ungureanu, Dan Dubina
DOI 10.1515/ama-2016-0017

webs (CWB) with a span of 5157 mm and a height of 600 mm have been tested (see Tab. 1), considering different arrangements for self-drilling screws and shear panels [1,2].

Fig. 1(a) presents the components of the CWB-1 beam with corrugated web (standard solution), i.e.:

- back-to-back lipped channel sections for flanges 2×C120/2.0;
- corrugated web with the corrugation depth of 43 mm and the thickness of 0.7 mm – A45/0.7;
- reinforcing shear panels – plates of 1 mm thickness and 830 mm length, at the beam ends where the shear force is maximum;
- reinforcing U150/2.0 profiles used under the load application points, to avoid excessive local deformations;
- self-drilling screws for flange-to-web connection – STP-6.3×25;
- self-drilling screws for shear plates to end support – STP-5.5×25;
- self-drilling screws as seam fasteners for corrugated webs – STT-4.8×20;
- bolts M12 class 8.8 for flanges to the end support connection.

Tab. 1. Types of specimens

Code	Description
CWB-1	Standard solution: flange-to-web connection in every corrugations and uniformly distributed seam fasteners
CWB-2	Standard solution + supplementary lipped channel sections under the load application points
CWB-3	Optimized solution by adapting the flange-to-web connections according to the distribution of shear stresses (connections at each second corrugations where the shear force decreases)
CWB-4	Optimized solution by eliminating shear panels and doubling of corrugated webs in the zones with high shear forces
CWB-5	Optimized solution by adapting both the flange-to-web connections and seam fasteners to the distribution of shear stresses

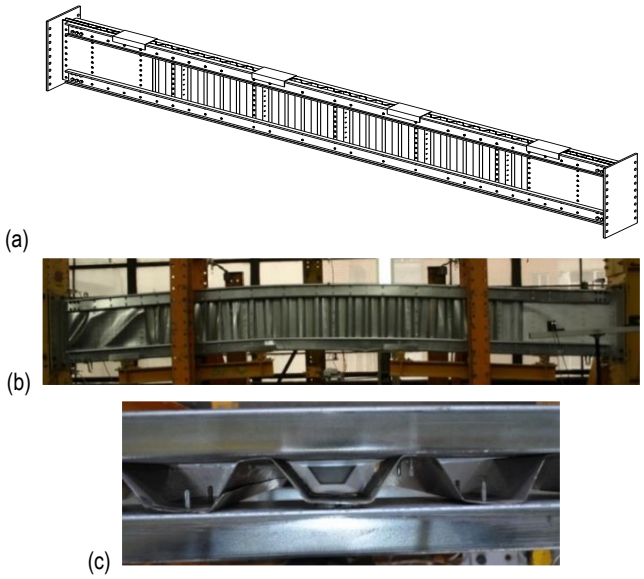

Fig. 1. (a) Configuration of the specimens; (b) Deformed shape of CWB-5 beam at failure; (c) Distortion of the web corrugation

Fig. 2 presents the experimental arrangement. Six points bending tests, monotonically conducted, were applied for each specimen with a loading velocity of 2 mm/min.

Dubina et al. (2013, 2015) show detailed information related to the behaviour of each tested specimen, including the initial stiffness, K_{0-Exp} and maximum load F_{max}, as well as the failure mode. These values are summarised in Tab. 4. Fig. 1 (b,c) show, as an exemplification, the deformed shape of the CWB-5 beam at collapse and the distortion of the web corrugation in the region with the reduced number of screws.

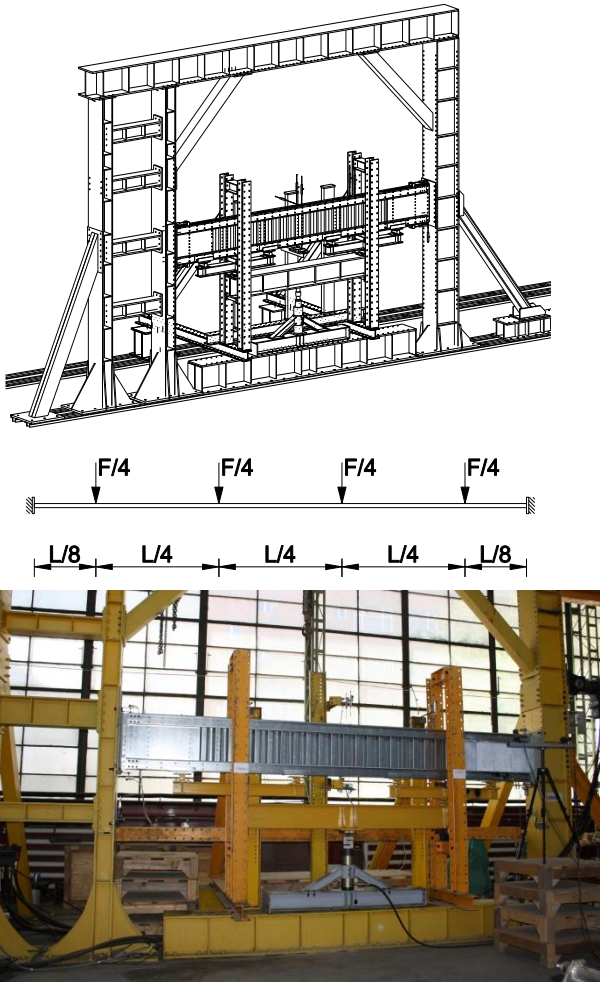

Fig. 2. Experimental arrangement

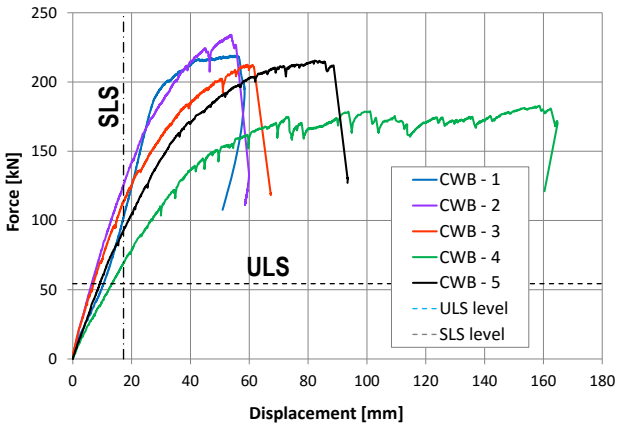

Fig. 3. Load-displacement curves for the tested specimens

DOI 10.1515/ama-2016-0017

Finally, Fig. 3 shows, comparatively, the load-displacement curves for all five specimens, together with the ultimate (ULS) and serviceability limit state (SLS) levels.

The full-scale testing program was completed with tensile tests to determine both the material properties for beam components and the behaviour of connections.

3.2. Material properties and connections behaviour

In order to determine the mechanical properties of the CWB components, a set of samples were cut out from the lipped channels, corrugated sheet, both from the flat regions and corners and reinforcing shear panels, according to EN ISO 6892-1:2009 specifications, as shown in Fig. 4. Tab. 2 presents the mean values, standard deviations and the characteristic values for yield and ultimate strengths for the above samples. The following abbreviations for coupons have been used: BM-CF coupon cut from the flange of the lipped channel; BM-CW coupon cut from the web of the lipped channel; CM-CF coupon cut from the flange-web corner of the lipped channel; CM-CW coupon cut from the flat region of the corrugated web; BM-SP coupon cut from the shear panel.

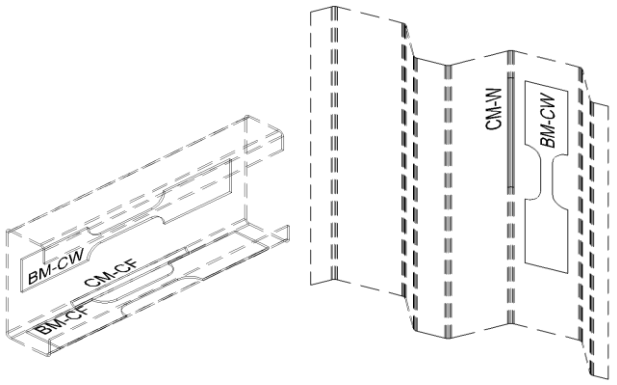

Fig. 4. Samples cut from flat regions and corners

Tab. 2. Yield and ultimate strengths of coupons cut from lipped channels, corrugate sheet and shear panel

Type	f_{yM} [MPa]	f_{uM} [MPa]	s_{fy}	$s_{f\backslash u}$	f_{yk} [MPa]	f_{uk} [MPa]
BM-CF	438.74	517.06	5.69	2.46	425.48	511.33
BM-CW	441.65	521.86	25.53	3.48	382.16	513.05
CM-CF	521.64	585.07	9.89	9.69	498.6	562.49
CM-CW	358.42	419.59	4.09	2.48	348.9	413.81
BM-SP	349.41	394.75	12.67	10.89	319.89	369.37

Six types of connections were tested according to Publication 124 of ECCS [29], at a loading velocity of 1 mm/min, i.e.:

- T1-1.4 seam fasteners for corrugated sheets;
- T2-1.7, seam fasteners for shear plates and corrugated sheets;
- T3-3.7, self-drilling screws for shear plates and flanges;
- T4-9.0, self-drilling screws for shear plates and end supports;
- T5-11.0, bolts for flanges to end-supports;
- T6-2.7, self-drilling screws for flanges to corrugated webs at mid-span,

in order to determine the behaviour of all types of connections found in the beam (see Tab. 3 and Fig. 5) (Abbas et al., 2007).

Tab. 3. Types of tested connections

Name	t_1 [mm]	t_2 [mm]	No. of tests	d_{nom} [mm]	Name
T1-1.4	0.7	0.7	6	4.8	T1-1.4
T2-1.7	1.0	0.7	5	4.8	T2-1.7
T3-3.7	2.0+1.0	0.7	6	6.3	T3-3.7
T4-9.0	1.0	8.0	5	5.5	T4-9.0
T5-11.0	2.0+1.0	8.0	5	M12	T5-11.0
T6-2.7	2.0	0.7	10	6.3	T6-2.7

4. NUMERICAL MODEL CALIBRATION AND VALIDATION

Numerical models applied to simulate the behaviour of members experimentally tested have been created using the commercial FE program ABAQUS/CAE v.6.7.1. Rectangular 4-noded shell elements with reduced integration (S4R) were used to model the thin-walled components. CONN3D2 element types, with 2 nodes and 6 DOF per node, have been used to model the self-drilling screws and bolts. RB3D2 elements were used as rigid body for load transfer and multi-point constrain beam (MPC-Beam) for DOF coupling between groups of specified nodes.

The material behaviour used for numerical modelling was in accordance with the recorded curves from tensile tests from coupons cut over the cross-section of component elements (see Tab. 2). Self-drilling screws and bolts were introduced using CONN3D2 element type according to the mean values recorded from tests of each type of connection (see Fig. 5).

General contact with the following parameters have been used, i.e. (1) on normal direction – hard contact; (2) on transversal direction – a friction coefficient of μ=0.1. Finally, as initial imperfections, the first 3 eigen modes from a linear bucking analysis have been used.

Fig. 6 presents comparatively the FEM and experimental load-displacement curves for the five beams, while Tab. 4 shows comparatively, for each specimen, the initial stiffness and ultimate load obtained experimentally and via numerical simulations. Significant work on girders with corrugated web has been done. An extended literature review will be presented on the following.

Tab. 4. Initial stiffness and ultimate load: FEM vs. experimental results

Beam type	$K_{0\text{-}Exp}$ (N/mm)	$K_{0\text{-}FEM}$ (N/mm)	$F_{max\text{-}Exp}$ (kN)	$F_{max\text{-}FEM}$ (kN)
CWB-1	6862.2	7721.1	218.9	225.9
CWB-2	7831.5	7834.6	231.3	229.5
CWB-3	7184.9	6819.3	209.5	205.8
CWB-4	3985.0	4932.0	181.9	223.5
CWB-5	5516.2	6594.9	214.6	216.0

The results obtained via numerical simulations show that the behaviour and maximum load accurately replicate the experimental tests. In case of CWB-4 beam the numerical results are 23% higher than experimental one. The reason could be the higher contribution of shear in the end panels; in this case there are no stiffening shear plates.

Viorel Ungureanu, Dan Dubina
DOI 10.1515/ama-2016-0017

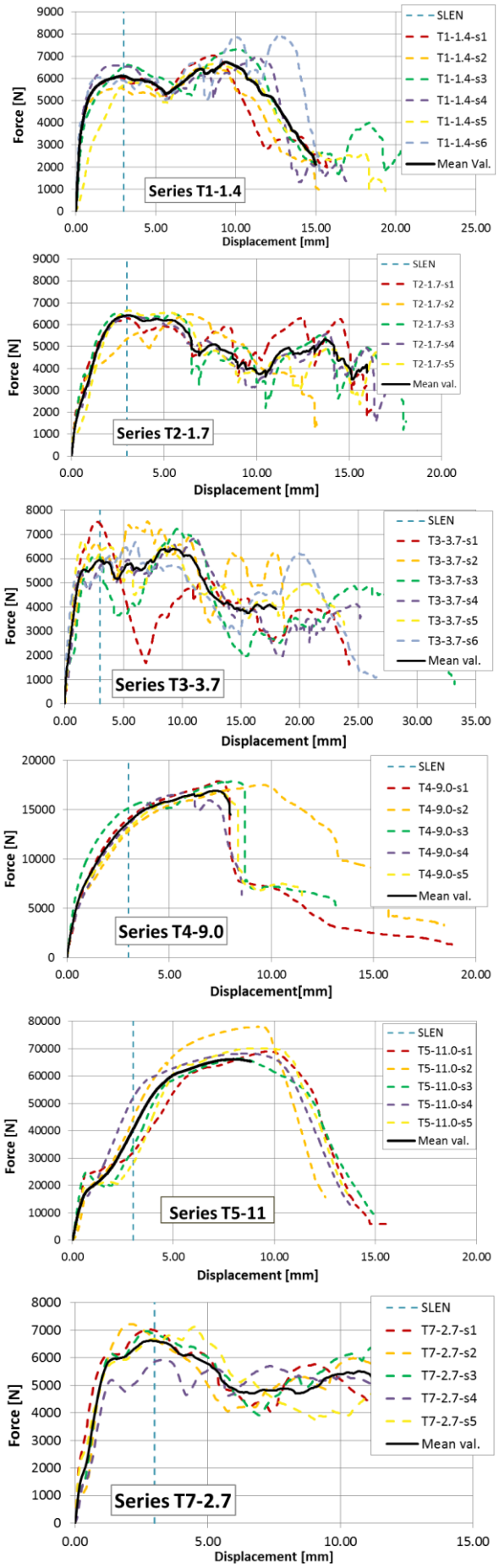

Fig. 5. Force-displacement curves for the tested connections

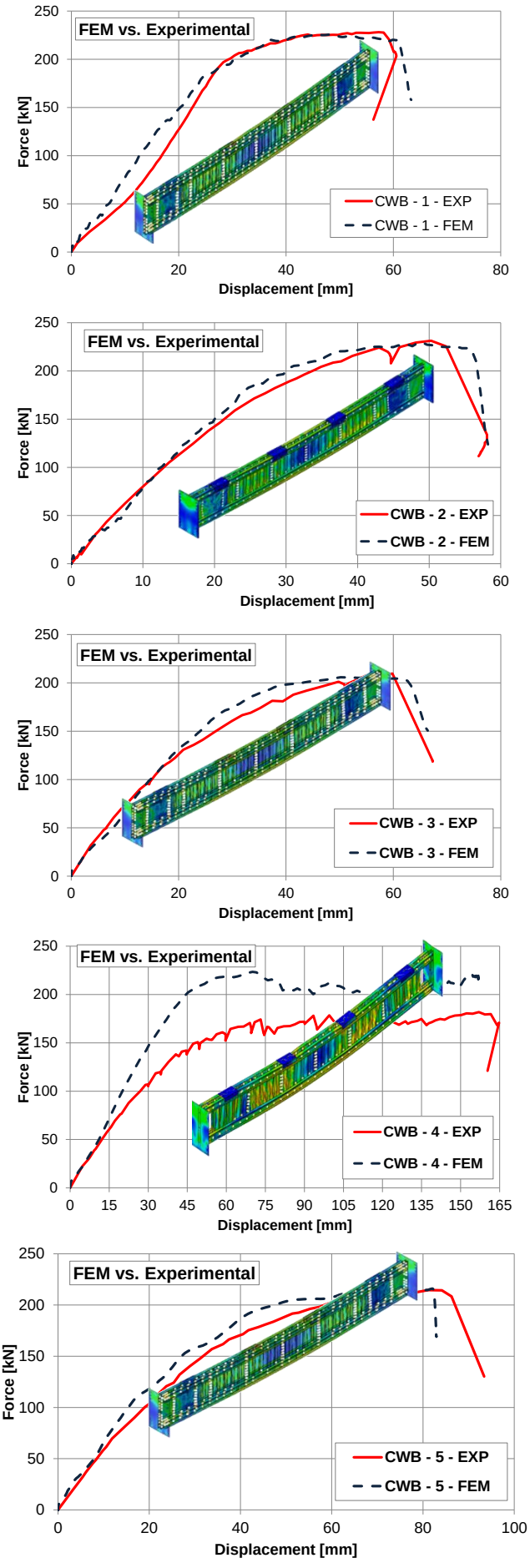

Fig. 6. FEM / Experimental load – displacement curves

DOI 10.1515/ama-2016-0017

Based on the presented results, the FEM model can be considered as validated. Further, it has been applied to evaluate the behaviour and capacity of a beam of 12 m span, with trapezoidal shape, as shown in Fig. 7. The height of the beam at ridge was considered 900 mm, while at eaves 1700 mm. Details concerning the beam components are presented in Dubina et al. (2014). The lateral-torsional bucking has been prevented. Similar failure modes have been obtained as in case of the tested beams. Fig 7 presents the stress distribution and the load-displacement curve for this beam with trapezoidal shape. The maximum capacity is achieved at 389.12 kN (i.e. corresponding to 5.4 kN/m2, considering a spacing of 6 m) for 35 mm displacement.

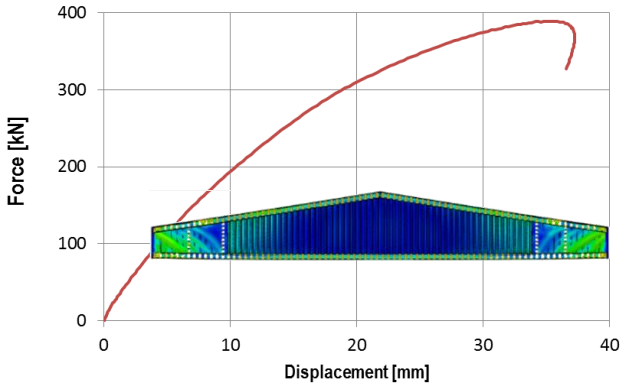

Fig. 7. Stress distribution and load-displacement curve for a 12 m span beam with corrugated web

Even good capacities can be obtained for larger spans, i.e. 16-18 m or more, the disadvantage of these trapezoidal beams is the height at the eaves and the difficulties in tailoring the corrugated sheets at the top flanges. In order to overcome these deficiencies, an alternative solution of parallel flanges sloped beams (e.g. pitched roof beams) was considered.

FEM model, correspondingly adapted, has been applied to evaluate the behaviour and capacity of these beams, taking as reference a pitched roof portal frame of 16 m span, with a 10° slope, as shown in Fig. 8 (Dubina et al., 2014)).

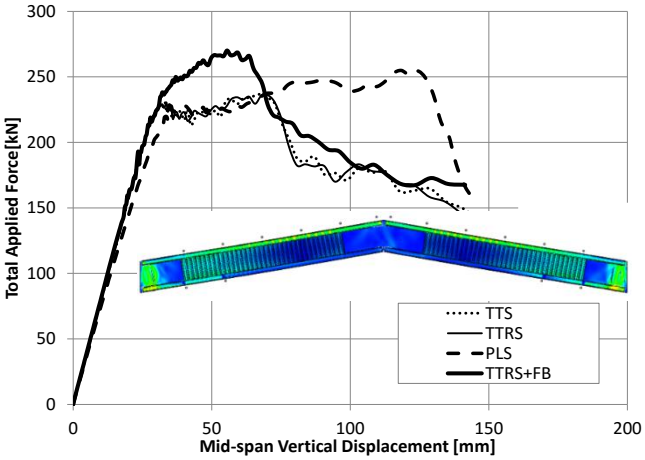

Fig. 8. Stress distribution and load-displacement curve for a 16 m span beam with corrugated web

The beam components are:

- back-to-back lipped channel sections for flanges – 2×C150/2.0, steel grade S350GD+Z;
- corrugated web with the corrugation depth of 43 mm and the thickness of 0.7 mm – A45/0.7, steel grade S320GD+Z;
- reinforcing shear panels – plates of 2 mm thickness and 1300 mm length, at the beam ends (ridge and eaves), steel grade S320GD+Z;
- self-drilling screws for flange-to-web connection – STP-6.3×25 (3 self-drilling screws per height of the profile);
- self-drilling screws for shear plates to end support with a nominal diameter – STP-5.5×25;
- self-drilling screws as seam fasteners for corrugated webs with a nominal diameter – STT-4.8×20 (16 self-drilling screws per height of the profile);
- M16 bolts class 8.8 for flanges to the end support connection (6 bolts for each flange); (8) the height of the beam was constant along the length, i.e. 1000 mm.

Four types of lateral restraints have been considered in the analysis, i.e.

- pinned lateral supports at the top flange in the position of purlins (PLS);
- transversal translational springs at the top flange in the position of purlins, corresponding to axial rigidity of a Z200/2 purlin (TTS);
- transversal translational and rotational springs at the top flange in the position of purlins, corresponding to axial and bending rigidities of a Z200/2 purlin (TTRS);
- case no. 3 including fly bracings corresponding to the first purlin adjacent to the ridge (TTRS+FB). Fig. 9 presents the load-displacement curves for this beam with trapezoidal shape.

The maximum capacity for TTRS+FB beam is achieved at 270.16 kN (i.e. corresponding to 2.81 kN/m2, considering a frame spacing of 6 m) for 55.51 mm displacement.

5. INFLUENCE OF CORRUGATION DEPTH ON THE LATERAL STABILITY OF BEAMS

Based on the conclusions of the second beam, of 16 m span with parallel flanges, on the following, the influence of the depth of corrugation on the global behaviour is studied. In this sense, three different depths for the corrugated web have been chosen, i.e. 30 mm, 43 mm (presented above) and 85 mm, in all the cases the thickness being 0.7 mm. Case number (4) from the chapter above has been analysed and presented below. Also, it should be mention that in case of screws, the optimized solution used for beam CWB-5 was adopted, i.e. by adapting both the flange-to-web connections and seam fasteners to the distribution of shear stresses. Fig. 9 presents the force-displacement curve for the 30 mm depth of corrugation and the points 1-2-3 corresponding to the appearance of local failures.

Tab. 5. Force and displacements for characteristic points

Point	30 mm corr.		45 mm corr.		85 mm corr.	
	F (kN)	Δ (mm)	F (kN)	Δ (mm)	F (kN)	Δ (mm)
1	258.1	29.5	275.5	32.7	263.4	36.7
2	291.2	41.1	279.8	46.3	293.3	43.4
3	279.7	53.8	286.7	59.8	287.2	46.5

Viorel Ungureanu, Dan Dubina
DOI 10.1515/ama-2016-0017

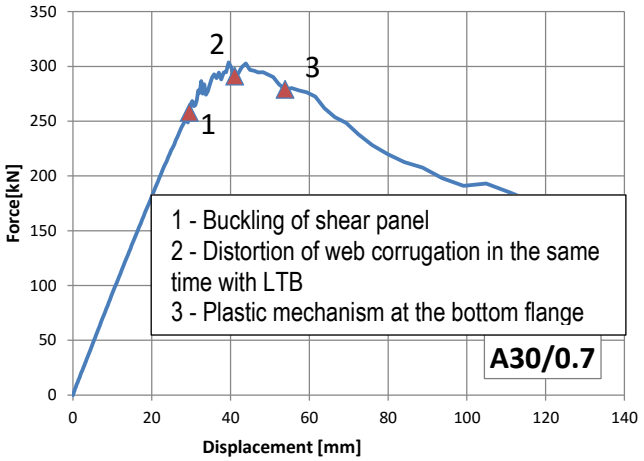

Fig. 9. Force-displacement curve for 30 mm depth of corrugation

Fig. 10 presents the distribution of stresses for the three characteristic points.

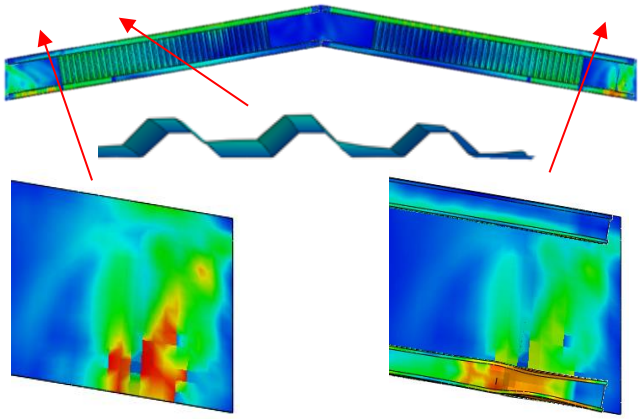

Fig. 10. Distribution of stresses for the three characteristic points

Fig. 11 and Fig. 12 present the force-displacement curves for the 43 mm and 85 mm depths and the corresponding points 1-2-3. The subsequences of appearance are the same as in the first case, but for different values of force/displacement (see Tab. 5). The distribution of stresses presented in Fig. 10 is almost the same as for the beam with 30 mm depth of corrugation.

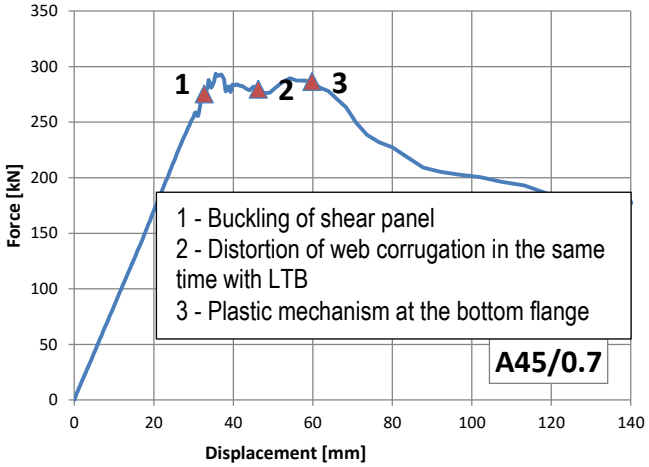

Fig. 11. Force-displacement curve for 45 mm depth of corrugation

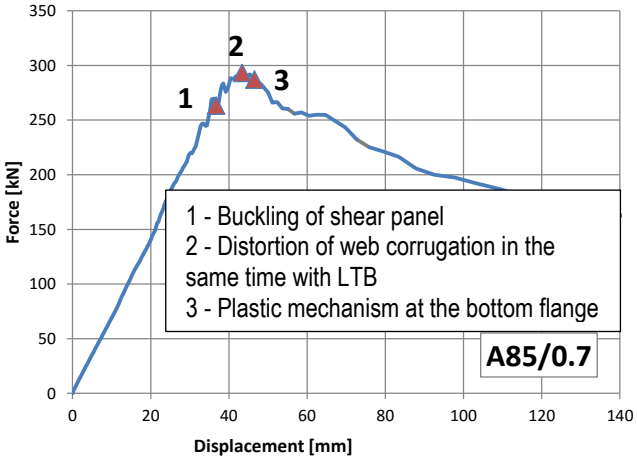

Fig. 12. Force-displacement curve for 85 mm depth of corrugation

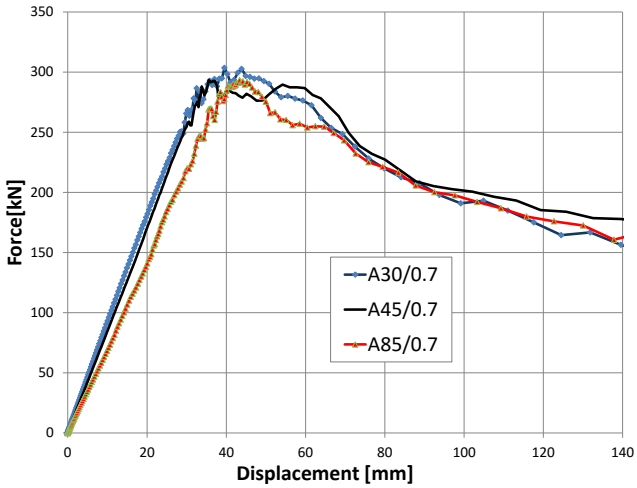

Fig. 13. Force-displacement curve for the three different depths of corrugated web

Plotting all three curves on the same graph, it is easy to see that curve for corrugation A85 has a reduced stiffness compared to the other two due to the fact the depth of the corrugations is more sensible to the end distortion of the corrugations. More, after reaching the maximum load the curve drop suddenly and a stable path can be seen due to the buckling coming from in-plane loading of the web. The curves for corrugation A30 and A45 have the same stiffness, but the maximum force is lower in case of A45 and a "plateau" can be seen between points 1-2-3 (see Fig. 13 and Tab. 5).

Another aspect is related to the optimisation of screws used both as seam fasteners and for connecting the web to the flanges. A better distribution of self-drilling screws together with reduced thicknesses for the web will put better in evidence the influence of the sheeting.

6. CONCLUSION

A large experimental program carried out at the CEMSIG Research Centre (www.ct.upt.ro/centre/cemsig/) of the Politehnica University of Timisoara on five beams with corrugated webs with different arrangements for self-drilling screws and shear panels was presented. Very good agreement between numerical models

DOI 10.1515/ama-2016-0017

and experimental ones have been obtained, in both failure modes and load-displacement curves.

A beam with parallel flanges, coming from a pitched roof portal frame of 16 m span, considering 4 types of lateral restraints have been numerically tested, in order to observe the potential for practical application of proposed technical solutions. The influence of corrugation depth has been particularly investigated in present study, by using three different depths, i.e. of 30, 45 and 85 mm. It can be observed that the capacity of these beams is almost the same, but for deeper corrugations, as effect of distortion, the deflection increases, while stiffness decreases. It is expected for thinner sheeting, the differences might be even more significant. The increase of ratios between pitch of seem fasteners and of flange-to-sheeting connectors vs. thickness of the web must be other parameters contributing to increase the influence of corrugation depth. On the aim of optimizing the technical solution for a mass production of such beams, the further investigations will focus on these aspects.

REFERENCES

1. **Abbas H.H., Sause R., Driver R.G.** (2006), Behavior of corrugated web I-girders under in-plane loads, *Journal of Engineering Mechanics, ASCE*, 132(8), 806-814.
2. **Abbas H.H., Sause R., Driver R.G.** (2007), Analysis of flange transverse bending of corrugated web I-girders under in-plane loads, *Journal of Structural Engineering*, 133(3), 347-355.
3. **Briskham P., Blundell N., Han L., Hewitt R., Young K., Boomer D.** (2006), Comparison of self-pierce riveting, resistance spot welding and spot friction joining for aluminium automotive sheet, SAE Technical Paper 2006-01-0774, doi:10.4271/2006-01-0774.
4. **Dubina D., Ungureanu V. and Gîlia L.** (2014), Cold-formed steel beams of corrugated web and built-up section chords, *Proceedings of the 7th European Conference on Steel and Composite Structures - EUROSTEEL 2014*, 10-12/09, 429-430.
5. **Dubina D., Ungureanu V., Gîlia L.** (2015), Experimental investigations of cold-formed steel beams of corrugated web and built-up section for flanges, *Thin-Walled Structures*, 90, 159–170.
6. **Dubina D., Ungureanu V., Gîlia, L.** (2013), Cold-formed steel beams with corrugated web and discrete web-to-flange fasteners, *Steel Constructions – Design and Research*, 6(2), 74–81.
7. **Guenfoud N., Tremblay R., Rogers C.A.** (2010), Arc-Spot Welds for Multi-Overlap Roof Deck Panels, *Twentieth International Specialty Conference on Cold-Formed Steel Structures*, 535-549.
8. **Jiho M., Jong W., Byung H.C., Hak-Eun L.** (2009), Lateral-torsional buckling of I-girder with corrugated webs under uniform bending, *Thin Walled Structures*, 47(1), 21-30.
9. **Kazemi Nia Korrani H.R., Molanaei S.** (2010), The Effects of the Corrugation Profiles of the Web on the Lateral-Torsional Buckling Strength of the Inelastic I-Girder, *World App. Sci. Journal*, 8(5), 527-530.
10. **Kövesdi B., Jáger B., Dunai L.** (2012), Stress distribution in the flanges of girders with corrugated webs, *Journal of Constructional Steel Research*, 79, 204–215.
11. **Landolfo R., Mammana O., Portioli F., Di Lorenzo G., Guerrieri M.R.** (2009), Experimental investigation on laser welded connections for built-up cold-formed steel beams, *Journal of Constructional Steel Research*, 65, 196–208.
12. **Landolfo R., Mammana O., Portioli F., Di Lorenzo G., Guerrieri, M.R.** (2008), Laser welded built-up cold-formed steel beams: Experimental investigations, *Thin-Walled Structures*. 46(7-9), 781-791.
13. **Moon J., Yi J., Choi B.H., Lee H.-E.** (2008), Shear strength and design of trapezoidally corrugated steel webs, *Journal of Constructional Steel Research*, 65(5), 1198–1205.
14. **Moon, J., Lim, N.H., Lee, H.E.** (2013), Moment gradient correction factor and inelastic flexural–torsional buckling of I-girder with corrugated steel webs, *Thin-Walled Structures*, 62, 18–27.
15. **Neagoie B., Ungureanu V., Dubina D.** (2005), Beams with cold-formed steel sections for flanges and corrugated web (in Romanian), *Stability and Ductility of Steel Structures – Recent research*, Academic Days, Timisoara, Romania, 27/05, 57-70.
16. **Pasternak H., Robra J., Kubieniec G.** (2010), *New proposals for EN 1993-1-5, Annex D: Plate girders with corrugated webs*, Codes in Structural Engineering, Joint IABSE-fib Conference, Dubrovnik, Croatia, 2, 1365-1372.
17. **Sause R., Braxtan T.N.** (2011), Shear strength of trapezoidal corrugated steel webs, *Journal of Constructional Steel Research*, 67(2), 223–236.
18. **Snow G.** (2008), *Strength of arc spot welds made in single and multiple steel sheets*, MSc Thesis, Blacksburg, Virginia, USA.
19. **Wanniarachchi S.** (2005), Flexural Behaviour of Cold-formed Steel Beams with Rectangular Hollow Flanges, PhD Thesis, School of Civ. Eng., Queensland University, Brisbane, Australia.
20. **Yi J., Gil H., Youm K., Lee H.** (2008), Interactive shear buckling behavior of trapezoidally corrugated steel webs, *Engineering Structures*, 30(6), 1659–1666.
21. **Zhao W.** (2005), *Behaviour and design of cold-formed steel hollow flange sections under axial compression*, PhD Thesis, School of Civ. Eng., Queensland Univ., Brisbane, Australia.
22. **ABAQUS/CAE v6.7.1** [Computer software]. ABAQUS Inc., Pawtucket, RI.
23. **ECCS 2008**, The Testing of connections with mechanical fasteners in steel sheeting and sections, Publication 124, ECCS, Brussels, Belgium.
24. **EN ISO 6892-1:2009**. Metallic materials - Tensile testing - Part 1: Method of test at room temperature. CEN, Brussels.
25. **EN1993-1-1:2005**, Eurocode 3: Design of steel structures – Part 1-1: General rules and rules for buildings, CEN, Brussels.
26. **EN1993-1-3:2006**, Eurocode 3: Design of steel structures. Part 1-3: General Rules. Supplementary rules for cold-formed thin gauge members and sheeting, CEN, Brussels.
27. **EN1993-1-5:2006**, Eurocode 3: Design of steel structures – Part 1-5: Plated structural elements, CEN, Brussels.
28. **RFSR-CT-2007-00038**, Prefabricated steel structures for low-rise buildings in seismic areas (Precasteel), Final report, Research Fund for Coal and Steel, 2013.
29. **US3444664A** Patent, Ribbed web girder, Macomber Inc, Fink Jr. H. R., Scott V. P., http://www.google.com/patents/US3444664, 1967.
30. **WO 00/17463**, International Patent Classification E04C 3/07 (2000). Modular H-beam, BEN-VAUTIER S.P.A., Italy.
31. **Zeman & Co GmbH**, Corrugated Web Beam, Technical Document, 2013 (www.zeman-steel.com/).

DE GRUYTER
OPEN

THE PARAMETER CORRELATION OF ACOUSTIC EMISSION AND HIGH-FREQUENCY VIBRATIONS IN THE ASSESSMENT PROCESS OF THE OPERATING STATE OF THE TECHNICAL SYSTEM

Petr BARON*, Jozef DOBRÁNSKY*, Martin POLLÁK*, Marek KOČIŠKO*, Tomáš CMOREJ*

*Faculty of Manufacturing Technologies, Department of Computer Aided Manufacturing Technologies,
Technical University of Košice, Štúrova 31, 080 01 Prešov, Slovakia

petr.baron@tuke.sk, jozef.dobransky@tuke.sk, martin.pollak@tuke.sk, marek.kocisko@tuke.sk, tomas.cmorej@tuke.sk

received 23 October 2015, revised 10 May 2016, accepted 13 May 2016

Abstract: The article describes application of selected methods of technical diagnostics for assessing the operating status of precision gearboxes. Within the confines of experimental measurements in the field of physical metallurgy materials of diagnosed system were being examined while taking into account the process of degradation of material properties during operation of monitored gearboxes. Measurements and collecting of dynamic data were realized on 4 selected gearboxes where a high-frequency vibrations and acoustic emission (noise) measurements were carried out. Retrieved values were subsequently used for mutual correlation and verification of applied methods. Results of both selected methods underlined unsatisfactory operation status with 3 inspected gearboxes. Measured values were identified as being above suggested caution limit of Alarm 2, representing a level of danger.

Key words: Technical Diagnostics, Vibrodiagnostics, Analysis of Dynamic Signal

1. INTRODUCTION

The most important role of technical diagnostics lies in predicting the technical condition of the system being assessed. One of the objectives of technical diagnostics is predicting of duration of flawless operation, i.e. time interval between observed moment up to occurrence of failure. The failure prediction is based on identification of deterioration in the condition of assessed systems and determining the moment when it is necessary to implement appropriate measures in order to prevent failures and undesired damage (Janoušek et al, 1988; Valent et al., 2010; Panda and Prislupčák, 2014).

Basic tasks of diagnostics is to determine the diagnosis characterizing the technical state of the object in terms of failures and this diagnosis must be usable for optimizing the servicing (maintenance) actions in order to bring the object to normal state. Monitored features of diagnosed object are vital for the success of the diagnostic system. One of the most important properties is diagnosability, i. e, feature that allows you to obtain information about the technical condition using diagnostic tools; in other words it presents the capacity of the object for the use of diagnostic equipment. The machine is sufficiently diagnosable if it is possible to perform all diagnostic tasks easily with required accuracy and, if possible, low cost (Valent et al., 2010; Hreha et al., 2010; Michalik et al., 2014; Šebo et al., 2013).

In the process of technical diagnosis variety of techniques is applied to diagnose machines but it often happens that the measurements are not interpreted or interpretation is not correct. Within the frame of vibration diagnostics there are occurrences of realizing the very collecting and recording of the vibrations signals while ignoring the force and energy that causes fatigue damage to machine parts and thusly shortens their lifespan. It means that twice the force shortens durability of the bearings to 1/8 of technical serviceability and device's lifespan is reduced from 5 – 10 years to only several months. Bearing diagnostics is a very demanding field and if technical diagnostician relies only on "their" method, the results of their work can even be fatal. Bearing damage can be caused by unsuiTab. lubricant, contaminated lubricant, water, excessive force, oxidation and degradation of the lubricant additives. The human factor can cause that bearing is installed with a larger overlap, overheated during installation or it is over-lubricated, insufficiently lubricated or without oil. These difficulties can shorten the bearing lifespan by a few hours up to several months (Valent et al., 2010; Šebo et al., 2013; Stejskal et al., 2013; Šoltésová and Baron, 2013; Jurko et al., 2011).

Based on cooperation of our department with practice the demand arose for accurate assessment of the operating condition of gearboxes. Four selected gearboxes were analyzed. In the context of diagnostic it was applied measurement of high-frequency vibration and acoustic emission. The measured values were used for the cross-correlation and verification of selected methods.

2. DESCRIPTION OF THE MEASURING - CHARACTERISTICS OF THE MACHINES AND MEASURING METHODS

In the process of diagnostic activities for the purpose of vibration measurement, process data collection and subsequent analysis the following diagnostics systems were used:

- the frequency analyzer and Data Collector Microlog GX,
- the software interface of Aptitude Analyst,
- vibration sensor, accelerometer Wilcoxon Research Model

DOI 10.1515/ama-2016-0018

SKF786M, sensitivity 100 mV/g, frequency range from 1 to 20 000 Hz.

Used measuring method based on recommendations of the technical standard STN ISO 10816-3 – Mechanical oscillation. Evaluation of machine oscillation by measuring on non-rotating parts of machine.

For purpose of vibration assessment in the low frequency area the following were applied:

- The measurement method Velocity (vibration velocity), unit mm/s, RMS detection.
- According to the recommendations of ISO 10816-3, FFT (Fast Fourier Transform) frequency spectrum for the area from 10 to 800 Hz.
- The measurement method Enveloping Acceleration (method of measuring the vibration acceleration in the high frequency range to 10 - 20 kHz through which assessment is carried out in particular for the state of the rolling bearings and gear ratio), unit Eg, detection of PtP, the frequency area from 50 to 1000 Hz, FFT spectrum and time record.

For the assessment of vibration in the high-frequency area the following methods were used:

- The measurement method Acceleration (vibration acceleration), unit g, detection of PtP, frequency range up to 16 kHz, the FFT spectrum and time record.
- The measurement method Acceleration Enveloping, unit Eg, detection of PTP, Frequency range up to 10 kHz to 20 kHz, the FFT spectrum and time.

Diagnostic methods for the assessment of acoustic emission and ultrasound:

- The measurement method See (Spectral Emitted Energy) – acoustic emissions (SKF), a unit See, detection of PtP, frequency range up to 600 kHz, the FFT spectrum and time record.
- The measurement method HFD – High Frequency detection method (SKF), analysis of vibration (acceleration) in frequencies 40 kHz.
- Method for assessment of the state of lubrication, resistance of the oil film, metallic contact, sticking, abrasion of contact surfaces (bearings and gear).

3. RECORDING AND RUNNING OF OPERATING PARAMETERS - REALIZATION OF THE EXPERIMENTAL MEASUREMENTS

Tab. 1 contains a summary of the measured values of the exposure of noise and vibrations of the individual gearboxes marked A, B, C, D.

Tab. 1. Measured exposure values for noise and vibrations of gearboxes A, B, C, D

Gearbox	HF vibrations - oscillations			Sound - noise			Evaluation
	Acc	Acc	EnvAcc	LAeq	LASmax	LAImax	
	[g]	[g]	[gE]	[dB]	[dB]	[dB]	
	To 20 kHz	Zone 1 - 6 kHz	To 10 kHz				
A	8.09	6.87	3.67	79.5	81.0	84.6	A2
B	5.30	4.49	2.45	73.6	74.7	78.0	A2
C	4.43	3.07	1.58	72.5	73.8	75.5	A2
D	3.20	1.37	0.92	72.4	73.5	74.6	SUITAB.
ALARM 1 (A1)	3.30	2.20	1.00	-	-	-	
ALARM 2 (A2)	4.30	3.00	1.50	75.0	75.0	75.0	

Explanatory notes: Acc – acceleration of vibration displacement, EnvAcc – envelope of vibration acceleration, Laeq – value of the equivalent level of acoustic pressure A, LASmax – the maximum level of acoustic pressure using the weighting filter type A and the time constant "Slow", LAImax – the maximum level of acoustic pressure using the weighting filter type A and the time constant "Impulse".

The measured acceleration values were obtained by diagnostic system with the application of accelerometer Wilcoxon Research, SKF786M in cooperation with the PorTab. Data Collector/FFT Analyzer SKF Microlog Analyzer (Fig. 3). The gearboxes were measured at one measuring point (acceleration).

The values of alarm levels (primarily for noise limits, sound pressure, acoustic emission and high frequency acceleration) are determined by the following ways:

- by agreement between a supplier (manufacturer) and customers,
- when the signal increase over 200% compared to the reference (agreed) level measured on the normal product quality and design,
- by comparing the dynamic characteristics of competing manufacturers - suppliers), respectively by comparing the measured values with the normal level of the same products in the local market.

In the specific case of defined alarm set points were based on an analysis of signal levels of 95% of the measured values of controlled amount of the same types of mechanisms (see. Tab. 1).

From the diagram of the measured values of the gearbox "A" (Fig. 4) it is seen that the value of the frequency about 2700 Hz achieved the level of noise 81 dB, respectively 84,6 dB.

FFT spectrum of a vibration signal confirmed the statement as with value about 2700 Hz measured signal value was: EnvAcc – 3.67 (gE), Acc – 6.87 (g), Acc – 8.09 (g). Time record of signal points to the unsatisfactory operating condition of the gearbox (Fig. 5). In both cases the measured values are set above the limit of alarm A2 (see Tab. 1).

Petr Baron, Jozef Dobránsky, Martin Pollák, Marek Kočiško, Tomáš Cmorej DOI 10.1515/ama-2016-0018

Fig. 1. The sound pressure measurement

Fig. 2. The contactless measuring of vibration by the laser vibrometer

Fig. 3. Accelerometer model Wilcoxon Research, SKF786M and PorTab. Data Collector/FFT Analyzer SKF Microlog Analyzer

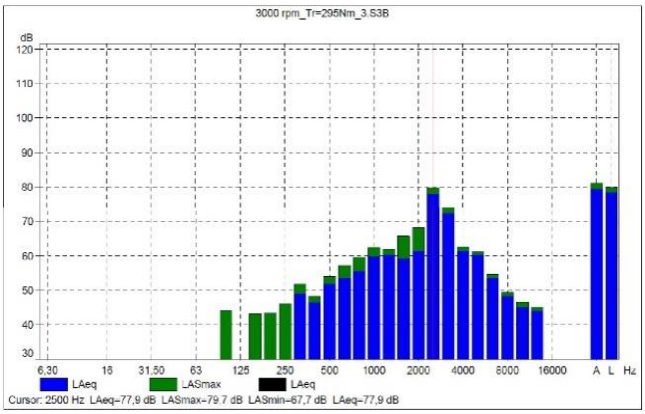

Fig. 4. Graphic record of acoustic emission for gearbox "A"

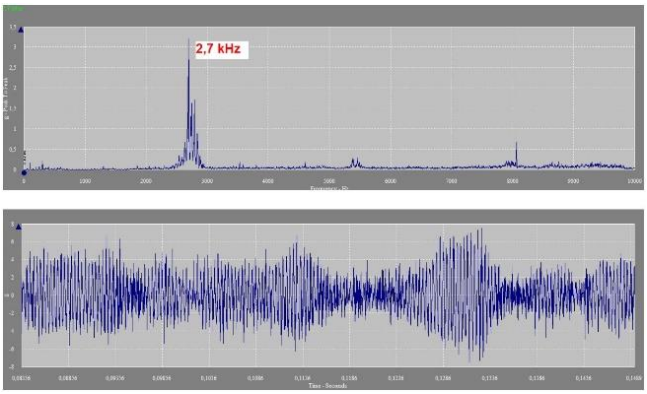

Fig. 5. FFT spectrum and recording TIME of gearbox „A“

In the case of the gearbox marked by the symbol "B" it is possible to record the state from the diagram when the vibration value about 4000 Hz is equal to the noise level of 74,7 dB and 78 dB (Fig. 6).

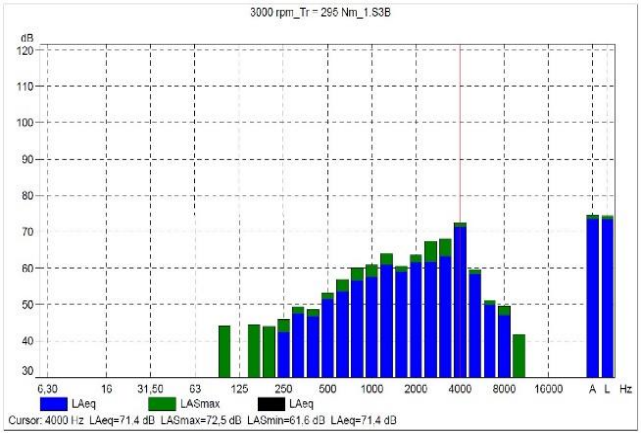

Fig. 6. The graphic record of acoustic emission for gearbox "B"

FFT spectrum of a vibration signal confirms the state where with value about 4200 Hz the measured signal value was: EnvAcc – 2.45 (gE), Acc – 4.49 (g), Acc – 5.30 (g). Time record of signal points to the unsatisfactory operating condition of the gearbox “B” (Fig. 7). In both cases the measured values are set above the limit of alarm A2.

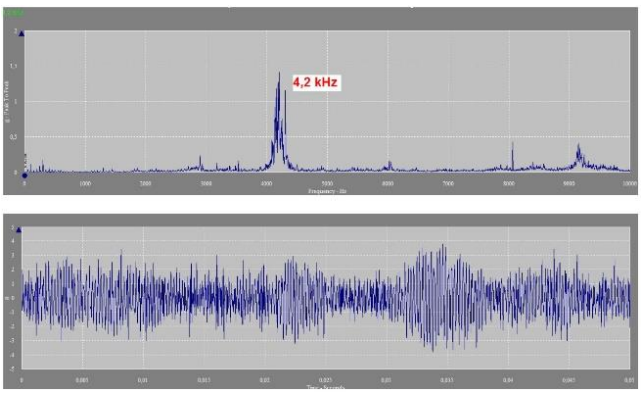

Fig. 7. FFT spectrum and recording TIME of gearbox „B“

DOI 10.1515/ama-2016-0018

For the third case – gearbox "C" in the vibration value about 4000 Hz had a vibration sound emission moving at the level of 73.8 and 75.5 dB (Fig. 8). FFT spectrum of a vibration signal confirmed that with value around 4150 Hz the measured signals value was: EnvAcc – 1.58 (gE), Acc – 3.07 (g), Acc – 4.43 (g). Time record of signal points to the unsatisfactory operating condition of the gearbox "C" (Fig. 9). In both cases the measured values are set above the limit of alarm A2.

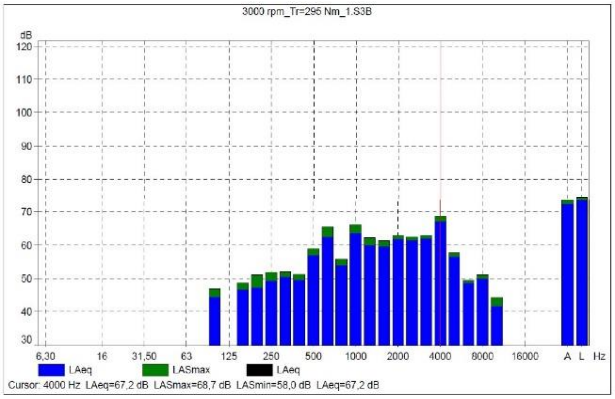

Fig. 8. The graphic record of acoustic emission for gearbox "C"

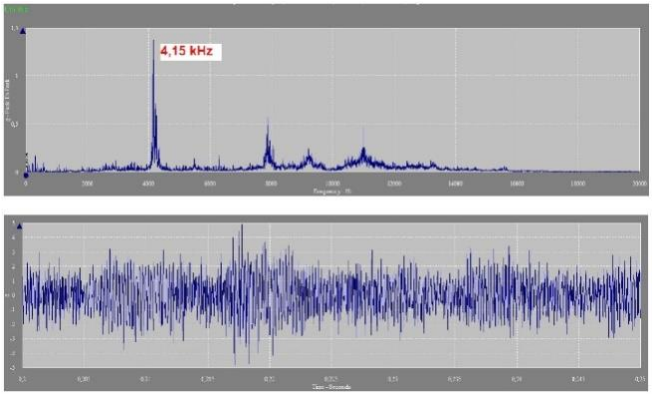

Fig. 9. FFT spectrum and recording TIME of gearbox „C"

In the case of the last gearbox marked by the symbol "D" was recorded a state where the all zones were located below level of 70 dB without dominant frequencies across the whole monitored zone.

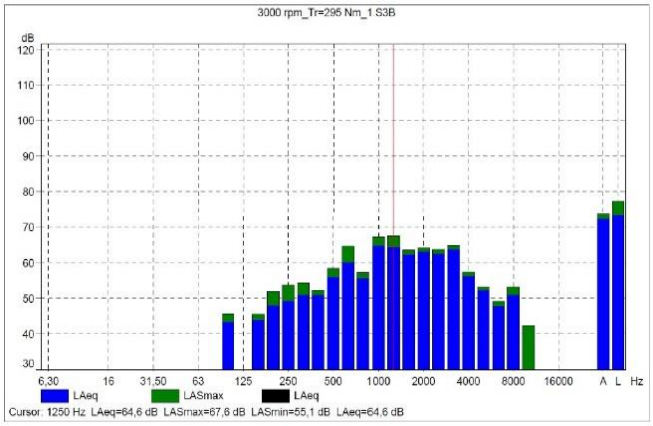

Fig. 10. Graphic record of acoustic emission for gearbox "D"

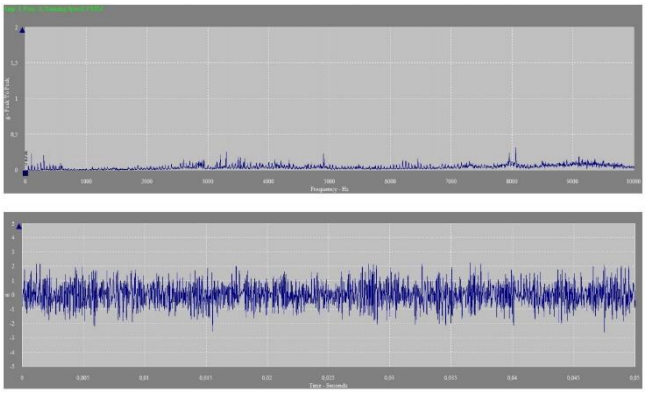

Fig. 11. FFT spectrum and recording TIME of gearbox „D"

FFT spectrum of the vibration signal also confirms that within measurement area there is not a state of increased signal. The measured signal value was: EnvAcc – 0,92 (gE), Acc – 1,37 (g), Acc – 3,20 (g). Time record points to the satisfactory operating condition of the gearbox (Fig. 11). The measured values of both cases are within the defined limits, i.e. condition is satisfactory.

4. CONCLUSION

Noise and vibrations are closely related since in many cases the oscillating bodies are the cause of secondarily created noise and vice versa - air-transmitted acoustic energy can create interfering oscillation of constructions, worsening of workplace conditions etc. (Jurko et al., 2010; Dobránsky et al., 2015; Balthazar et al., 2013). The causes of vibration in technical practice are alternate forces that arise from the clearance and inaccuracies in rotating movements of machines, in vehicles movement and their parts, at work with the various machine tools, etc. Primary task of vibration diagnostics is early identification of moment of required maintenance or possibly changing the segment in assessed system before end of its working life. This type of diagnostics increases security, reliability and durability, the period between two repairs respectively. Finally, thereby reducing maintenance costs (Warminski et al., 2013; Hyung-Deok and Hun Lee, 2014; Wereley and Meinhart, 2010; Gallagher et al., 2012).

In respect to case of diagnostics of assessed precision gearboxes described in the article it is possible, based on realized measurements and analysis of dynamic signal by means of correlation of two methods, to state the following conclusion:

- operating state of gearboxes "A", "B" and "C" is unsatisfactory. The measured values are identified above the recommended limit of warning Alarm 2 (A2 – danger),
- gearbox "D" is in satisfactory working condition for all measured parameters and measurement methods.

After the realized repair of gearboxes "A" to "C" it is recommended to re-diagnose their operating status by measuring high-frequency vibrations. Consequently it is desirable, by measuring the microgeometry of contact surfaces, to assign the measured value of high dynamic signal for specific gearbox component, and define its eventual production inaccuracy (Asiri, 2007).

REFERENCES

1. **Asiri S.** (2007) Tunable mechanical filter for longitudinal vibrations, *Shock and Vibration*, 14(5), 377-391.
2. **Balthazar J. M., Gonçalves P.B., Fenili A.** (2013) Nonlinear vibrations in elastic structures:Dynamics and control, *Shock and Vibration*, 20(6), 1031-1032
3. **Dobránsky J., Baron P., Simkulet V., Kočiško M., Ružbarský J., Vojnová E.** (2015) Examination of material manufactured by direct metal laser sintering (DMLS), *Metalurgija*, 54(3), 477-480.
4. **Gallagher K. S., Grübler A., Kuhl L., Nemet G., Wilson Ch.** (2012) The Energy Technology Innovation System, *Annual Review of Environment and Resource*, 37, 137-162.
5. **Hreha P., Hloch S., Valíček J., Monková K., Monka P., Harničárová M., Fusek M., Konjatić P.** (2010), Impact of abrasive mass flow rate when penetrating into a material on its vibration, *Tehnički vjesnik - Technical Gazette*, 17(4), 475-479.
6. **Hyung-Deok S.**, **Hun L.** (2014) Disentangling the role of knowledge similarity on the choice of alliance structure, *Journal of Engineering and Technology Management*, 30(4), 350-362.
7. **Janoušek I., Kozák J., Taraba J.** (1988), *Technical Diagnostics*. SNTL Praha.
8. **Jurko J., Džupon M., Panda A., Gajdoš M., Pandová I.** (2011), The deformation under the machined surface material in the production of drilling holes into the austenitic stainless steel, *Chemické listy,* 105(16), 600-602.
9. **Jurko J., Gajdoš M., Panda A.** (2010) Study of changes under the machined surface and accompanying phenomena in the cutting zone during drilling of stainless steels with low carbon content, *Metalurgija*, 50(2), 113-117.
10. **Michalik P., Zajac J., Hatala M., Hutyrová Z., Mitaľ D., Olhova J.** (2014), Comparison Measurement of the Distance between Axes of Holes with the Roundtest RA-120 and Thome Präzision-Rapid, *Applied Mechanics and Materials*, 616, 284-291.
11. **Panda A., Prislupčák M.** (2014), Analysis of technological factors, *Studia i materialy*, 34(1), 13-16.
12. **Šebo J., Buša J., Demeč P., Svetlík J.** (2013), Optimal replacement time estimation for machines and equipment based on cost function, *Metalurgija*, 52(1), 119-122.
13. **Šoltésová S., Baron P.** (2013), The Operation Monitoring Condition of the Production Machinery and Facilities Using the Tools of Technical Diagnostics, *Applied Mechanics and Materials*, 308, 105-109.
14. **Stejskal T., Kováč J., Valenčík Š.** (2013), Mechanism of randomness in vibration signals of machinery, *Applied Mechanics and Materials*, 282, 257-262.
15. **Valent O., Galád M., Kačmár Ľ.** (2010), Technical Diagnostics, 1, Condition Monitoring and Maintenance Systems, CMMS, Prague
16. **Warminski J., Cartmell M.P.**, **Mitura A.**, **Bochenski M.,** (2013) Active vibration control of a nonlinear beam with self- and external excitations, *Shock and Vibration*, 20 (6), 1033-1047.
17. **Wereley S. T., Meinhart C. D.,** (2010) Recent Advances in Micro-Particle Image Velocimetry, *Annual Review of Fluid Mechanics*, 42, 557-576.

Acknowledgements: Ministry of Education, Science, Research and Sport of SR supported this work, contract VEGA No. 1/0032/12 and ITMS project 26220220125.

DE GRUYTER
OPEN

DOI 10.1515/ama-2016-0019 acta mechanica et automatica, vol.10 no.2 (2016)

ACCURACY OF SPINDLE UNITS WITH HYDROSTATIC BEARINGS

Dmytro FEDORYNENKO*, Serhii SAPON*, Sergiy BOYKO*

*Chernihiv National University of Technology, Mechanical Engineering Department, Shevchenko Street, 95, Chernihiv, Ukraine

fdy1974@gmail.com, s.sapon@gmail.com, svboyko.cstu@gmail.com

received 2 March 2015, revised 11 May 2016, accepted 13 May 2016

Abstract: The work is devoted to the research ofprecision regularities in a spindle unit by the trajectory of the spindle installed on hydrostatic bearings.The mathematical model of trajectories spindle with lumped parameters that allows to define the position of the spindle with regard the simultaneous influence of design parameters, geometrical deviations ofform, temperature deformation bearing surfaces, the random nature of operational parameters and technical loads of hydrostatic bearings has been developed. Based on the results of numerical modeling the influence of shape errors of bearing surface of hydrostatic bearing on the statistical characteristics of the radius vector trajectories of the spindle by varying the values rotational speed of the spindle and oil pressure in front hydrostatic bearing has been developed. The obtained statistical regularities of precision spindle unit have been confirmed experimentally. It has been shown that an effective way to increase the precision of spindle units is to regulate the size of the gap in hydrostatic spindle bearings. The new design of an adjustable hydrostatic bearing, which can improve the accuracy of regulation size gap has been proposed.

Key words: Spindle, Hydrostatic Bearing, Spindle Unit, Adjustable Hydrostatic Bearing, Machining Accuracy, Trajectory, Bearing Surface Imperfection

1. INTRODUCTION

One of the most important formative units of any machine tool is the spindle unit (SU) the output accuracy parameters of which are strongly dependent on the type of spindle bearings. An efficient way to increase the accuracy of machine tools is to use as spindle bearings hydrostatic bearings (HB) adjustable type. It will provide the expansion of technological capabilities of machine tools by combining roughing and finishing, the increase of efficiency of processing based on high speed bearings and structural designs and reducing operating costs by adjusting geometric and operating parameters of HB depending on the nature of technological load (Savin, 2006; Shen et al., 2010; Solomin, 2007; Wardle, 2015; Perovic, 2012).

The main parameter of the precision of a SU is the trajectory of spatial movement of fixed points located on the auxiliary spindle bases that determine the position of the cutting tool or the device with fixed workpiece (Fedorynenko et al., 2015; Savin, 2006; Strutynsky and Fedorynenko, 2011). The trajectory of the spindle motion is formed under the influence of totality variables in magnitude and the direction of the external and internal efforts with determined and stochastic components: cutting force, reaction in HB, the efforts from the main motion, static and dynamic unbalance from rotating of workpiece in the spindle, technological equipment, which is fixed in (on) spindles, etc. The analysis of regularities of formation of spindle trajectories under such system of forces with taking into account the shape errors at the same time, elastic and temperature deformations of bearing surfaces is an actual scientific problem. Solving of this problem will determine rational design and operating parameters of spindle units, which will improve the accuracy of machine tools and expand their technological capabilities.

2. MATHEMATICAL MODEL TRAJECTORIES OF SPINDLE WITH HYDROSTATIC BEARINGS

The basic method for the theoretical analysis of the spatial movement of the spindle with HB is a method of trajectories (Fedorynenko et al., 2015; Xiaodong and Huaimin, 2006; Xiaodong et al., 2007), based on the numerical integration of the system equations of hydrodynamics lubricant layer and the equations of the spindle motion to simulate a real dynamic behavior of the spindle, considering the influence of nonlinear reactions of lubricant layer, operating parameters of HB, technological power loads etc.

The object of the modeling is a SU of the precision lathe UT16A (Fig. 1), which spindle 3 is mounted on two radial HB 1 and 6 and thrust bearing, formed between the ends of bushings 5 and 7 and housing of front radial HB.

Spindle position in the space under loading force and reactions in HB is described by the trajectory of its axis. Taking into account that the axial displacement of the spindle lathe does not affect the accuracy of forming a radial direction, the study a spindle precision unit has been carried out by its performance trajectories of motion in the plane perpendicular to the geometrical axis.

The offset of the spindle under the power loads and reactions of lubricant layer are represented as an equivalent single-mass dynamic model (Fig. 2), which includes the resulted mass m, which is displaced in the vertical Δy and horizontal Δx directions under force loads and resultant reactions in HB reduced to the cutting area projections. As a result of a limited impact of characteristics of rear HB on machining precision, the reactions of a lubricant layer, that arise in rear HB were not considered.

Dmytro Fedorynenko, Serhii Sapon, Sergiy Boyko

DOI 10.1515/ama-2016-0019

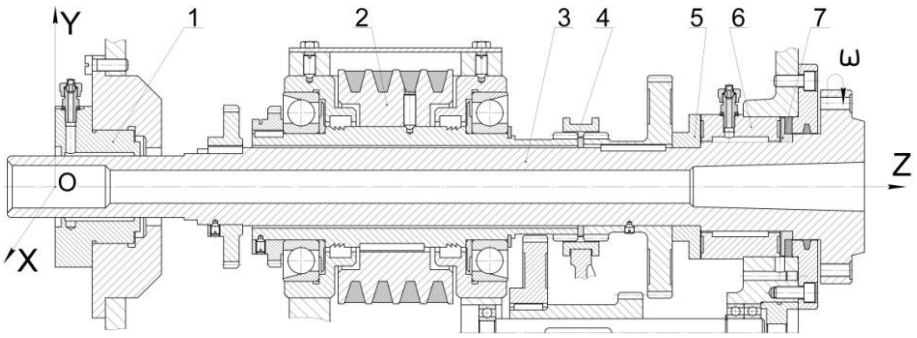

Fig. 1. Constructive scheme of spindle lathe UT16A: 1, 6 – radial HB; 2 – pulley drive; 3 – spindle; 4 – gear coupling; 5, 7 – bushings of axial HB

In the drive of main machine tool UT16A motion belt transmission unloaded from efforts tension of belts, is used and efforts of the drive are represented by a random component, which is caused by shock processes in gears in gear couplings 4 (see Fig. 1).

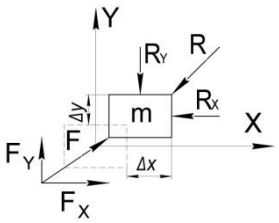

Fig. 2. The equivalent single-mass dynamic model of the spindle

Taking into account all previously made assumptions the system of differential equations that describe the displacement of the spindle in the plane perpendicular to its geometrical axis will look like:

$$\begin{cases} m\frac{d^2x}{d\tau^2} = F_x - R_x \\ m\frac{d^2y}{d\tau^2} = F_y - R_y \end{cases} \quad (1)$$

where: m – bringing mass of the spindle; F_x , F_y , R_x , R_y – projection on the axis OX and OY respectively resultant power loads on the spindle and the resultant reactions in HB.

Projections F_x , F_y resultant power loads on the spindle, bringing to the cutting area, are defined as follows:

$$F_x = \chi_c F_{Cx} + \chi_R F_{prx} + \chi_P P_x, \quad (2)$$

$$F_y = \chi_c F_{Cy} + \chi_R F_{pry} + \chi_P P_y + \chi_G mg \quad (3)$$

where: $\chi_c, \chi_R, \chi_P, \chi_G$ – coefficients of bringing forces and the mass to the cutting area; F_{Cx}, F_{Cy} , P_x, P_y, F_{pry}, F_{prx} – projections on the axis OX and OY respectively centrifugal force of the inertia, constituting cutting force and effort on the part of the main drive motion.

It should be noted that virtually all components of resultant power loads (formula (2) and (3)) are random to determine them generally the dependency was used:

$$f(\tau) = \bar{m}_f + \Delta f \cdot \xi(\tau) \quad (4)$$

where: $\bar{m}_f$, Δf – mathematical expectation and a range of deviation of its mean value; $\xi(\tau)$ – positioning centered random process of magnitude fluctuation.

Thus, when modeling a random process of fluctuations of angular velocity, its absolute value at a certain time τ was defined:

$$\omega(\tau) = \omega_n + \Delta\omega_n \cdot q(\tau) \quad (5)$$

where: ω_n, $\Delta\omega_n$ – nominal values and deviation range of the angular velocity; $q(\tau)$ – random process fluctuations of the angular velocity.

Ranges of the angular velocity were determined on the basis of a priori information about the statistical characteristics of the random change of the spindle angular velocity, which was obtained by a series of additional experiments.

Projections of inertia centrifugal force caused by static unbalance of rotating elements spindle unit, taking into account fluctuations of the angular velocity value were determined by the relationships:

$$F_{Cx}(\tau) = m \cdot \Delta \cdot \left(\omega_n + \Delta\omega_n \cdot q(\tau)\right)^2 cos(\omega_n\tau + \varepsilon), \quad (6)$$

$$F_{Cy}(\tau) = m \cdot \Delta \cdot \left(\omega_n + \Delta\omega_n \cdot q(\tau)\right)^2 sin(\omega_n\tau + \varepsilon) \quad (7)$$

where: Δ – the displacement of the mass center caused by static unbalance; ε – the initial phase of static unbalance.

In the presence of static unbalance of rotating elements of a SU absolute value of the depth of cut at time τ was defined:

$$t(\tau) = t_n + \Delta \cdot cos(\omega_n\tau + \varepsilon) + \Delta t_n \cdot \xi(\tau) \quad (8)$$

where: t_n– nominal depth of cut; Δt_n – magnitude of the changes allowance; $\xi(\tau)$ – random process fluctuations of cut depth.

Random fluctuations in the process of cutting depth can be realized in the form of "white noise", similar to the angular speed of the spindle rotation, or a harmonic function with random amplitude and initial phase (Rubinstein, 2007; Sapon, 2013):

$$\xi(\tau) = a(\tau)cos(\omega_n\tau + \alpha_n) \quad (9)$$

where: $a(\tau)$ – amplitude coefficient which takes random values from the interval [-1; 1] with the relevant distribution law; α_n – random phase of harmonic function with uniform distribution in the interval [0; 2π].

Instant value of approach $S_0(\tau)$ depend on the nominal value of S_0, as well as a random variable that takes into account the uneven movement of slide as a result of kinematic errors of the drive navigating shaft:

$$S_0(\tau) = S_0 + \Delta S_0 \cdot \eta(\tau) \quad (10)$$

where: S_0, ΔS_0 – nominal deviation and range of approach; $\eta(\tau)$ – random process fluctuations of approach.

Taking into account the random component of the depth

DOI 10.1515/ama-2016-0019

of cut, feed, speed spindle, the absolute values of the projections P_x, P_y cutting force at a time τ were determined by the dependencies:

$$\mathrm{P}_x(\tau) = 10C_{Px}(t_n + \Delta \cdot cos(\omega_n\tau + \varepsilon) + \Delta t_n \cdot \xi(\tau))^x \times \left(S_0 + \Delta S_0 \cdot \eta(\tau)\right)^y \left(\frac{3D\cdot(\omega_n+\Delta\omega_n q(\tau))}{100}\right)^n \cdot K_{Px}(\tau), \quad (11)$$

$$\mathrm{P}_y(\tau) = 10C_{Py}(t_n + \Delta \cdot sin(\omega_n\tau + \varepsilon) + \Delta t_n \cdot \xi(\tau))^x \times \left(S_0 + \Delta S_0 \cdot \eta(\tau)\right)^y \times \left(\frac{3D\cdot(\omega_n+\Delta\omega_n q(\tau))}{100}\right)^n \cdot K_{Py}(\tau) \quad (12)$$

where: C_{Px}, C_{Py}, n, x, y – coefficients and exponents, which take into account the type of processing, physical and mechanical properties of the workpiece material and tool, D – diameter of workpiece, mm; $K_{Px}(\tau)$, $K_{Py}(\tau)$ – correction factors which take into account the actual processing conditions.

Correction factors K_{Px}, K_{Py}, were defined as the product of the instantaneous values of coefficients that take into account the influence of the parameters of the cutting tool and the physical and mechanical properties of the material.

Effort which is caused by shock loads in tooth gearings drive the main spindle movement, is presented in the form of "white noise" the model of which is formed like a random sequence of delta impulse $\delta(\tau i)$ with random amplitude values of $a(\tau)$:

$$F^c_{prx}(\tau) = a(\tau)sin\alpha \cdot \delta(\tau - \tau_i), \quad (13)$$

$$F^c_{pry}(\tau) = a(\tau)cos\alpha \cdot \delta(\tau - \tau_i), \quad (14)$$

where: a – angle of applying shock pulse; τ_i – random time of occurrence disturbance;

$$\delta(\tau - \tau_i) = \begin{cases} 1, & if \ \ \tau = \tau_i \\ 0, & if \ \ \tau \neq \tau_i \end{cases}$$

The main influence on parameters of machining precision have the parametrs of front spindle HB. Ignoring the part of reactions, which is caused by friction in the lubricant layer, projection resultant reactions of lubricant layer in front HB in function of the polar angle φ is presented by a part of reactions caused by hydrostatic pressure grease on the bearing neck of the spindle:

$$R_x = \frac{D_0}{2}\int_0^{2\pi} p(\varphi)cos\varphi d\varphi, \quad R_y = \frac{D_0}{2}\int_0^{2\pi} p(\varphi)sin\varphi d\varphi, \quad (15)$$

where: D_0 – diameter of the supporting part in HB; $p(\varphi)$ – distribution function of the pressure on the supporting part of HB.

The distribution function of pressure $p(\varphi)$ on the supporting part of regulated HB is determined by double integration of the Reynolds equation and depends in the dynamic radial clearance $p(\varphi)$, which at simultaneous taking into account the errors of form and displacement of support surfaces due to their elastic deformation and temperature, is determined by the dependencies:

$$h(\phi) = \delta_0 - m\left(\Delta r^b_{\mathrm{T}}\right) - m(\Delta r^s_{\mathrm{T}}) + \frac{T^b_r}{2} + \frac{\mathrm{T}^s_r}{2} + \\ + \sum_{k=1}^{N} A^b_k sin\left(k\varphi + \psi^b_{0k}\right) - \sum_{k=1}^{Q} A^s_k sin(k\varphi + \chi^s_{0k}), \quad (16)$$

where: $m\left(\Delta r^b_{\mathrm{T}}\right)$, $m(\Delta r^s_{\mathrm{T}})$ – mathematical expectation displacement of radial coordinate profile hydrostatic support surfaces bushings and the spindle caused by temperature deformation in a particular temperature; δ_0 – static radial clearance in the support; T^b_r, T^s_r – roundness tolerances of support surfaces in the bearing; A^b_k, ψ^b_{0k}, A^s_k, χ^s_{0k} – amplitude and initial phase of harmonic Fourier series which describe the deviation hydrostatic support surfaces bushings and the spindle respectively; N and Q – the number of important harmonics profile of hydrostatic support surfaces bushings and the spindle at a certain temperature.

Details question of the function of the pressure distribution $p(\varphi)$ considering non-ideal geometry and thermal deformation of the bearing support surfaces are considered in the monograph (Fedorynenko et al., 2014; Junpeng et al., 2008; Strutynsky and Fedorynenko, 2011; Yu and Zhang, 2008; Zhao et al., 2007).

Mathematical expectations of displacement of radial coordinate $m\left(\Delta r^b_{\mathrm{T}}\right)$ and profile $m(\Delta r^s_{\mathrm{T}})$ of support surfaces were determined by the results of numerical modeling tools of CAE-system SolidWorks Simulation (Fig. 3) (Junpeng et al., 2007; Yang et al., 2008).

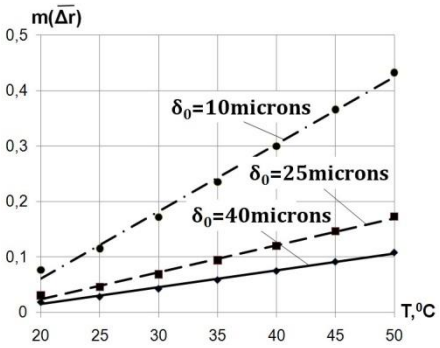

Fig. 3. Dependence of the mathematical expectation $m(\overline{\Delta r})$ value to temperature of support surface

Number N, Q and harmonic A^b_k, A^s_k amplitudes of HB profile support surfaces, were defined by spectral analysis of contour built by the results of numerical simulations of displacement radial coordinate profile support surfaces as a result of temperature (Fig. 4) and elastic deformation means by CAE-system SolidWorks Simulation (Yaun et al., 2008).

a)

b)

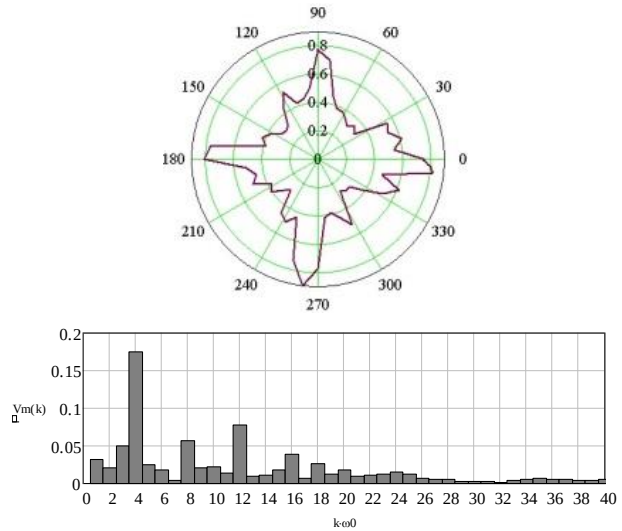

Fig. 4. Temperature displacement ($\mathrm{T} = 35°\mathrm{C}$) of profile hydrostatic bearing surface of the bushing which approximated in package MathCAD by cubic splines a) and typical spectrum b) amplitudes $V_m(k)$ of harmonics profile $k{\cdot}\omega_0$

Taking into account all previous assumptions, simplifyings

DOI 10.1515/ama-2016-0019

and calculations, the system of differential equations that describe the displacement of the spindle in the plane perpendicular to its geometrical axis, will look:

$$\begin{cases} m\frac{d^2x}{d\tau^2} = \chi_c F_{Cx}(\tau) - \chi_F R_x + \chi_R F_{prx}(\tau) + \chi_P P_x(\tau), \\ m\frac{d^2y}{d\tau^2} = \chi_c F_{Cy}(\tau) - \chi_F R_y + \chi_R F_{pry}(\tau) + \chi_P P_y(\tau) + \chi_G mg, \end{cases} \quad (17)$$

The components included in the right part of the equation system (17) are determined by the dependencies (6), (7), (11) - (15).

In general case, given the nonlinearity and the random nature of the components included in the right parts of equations, the system (17) has no analytical solution. This necessitates the use of numerical methods to solve it.

3. THE RESULTS OF NUMERICAL SIMULATION TRAJECTORIES SPINDLE WITH HYDROSTATIC BEARINGS

For numerical simulation of trajectories spindle is used statistical modeling by Monte Carlo (Rubinstein, 2007; Yu and Zhang, 2008). Description of spindle movements was carried out by means of radius vector in polar coordinates:

$$R(\varphi_j) = \sqrt{x^2(\tau_j) + y^2(\tau_j)} \quad (18)$$

It was established that the workflow fluctuations in HB spindle is stationary and ergodic process that has a pronounced stochastic character in all ranges of variation of operating parameters and technological loads. Moreover the distribution law of a random variable spindle oscillations is close to normal. Therefore, the estimation of trajectories spindle parameter was performed using the statistical characteristics of the radius vector: m_R mathematical expectation and standard deviation σ_R, which determine the displacement and dispersion of the spindle regulations and affect the accuracy of the nominal size of the treated surface.

According to the results of numerical simulations it was found that the increase of pressure in HB pockets from 1 MPa to 3 MPa enhances the precision machining that was shown in reducing the expectation of m_R radius vector trajectories of the spindle with idealized form bearing surfaces – 30%, with the errors of form bearing surfaces – 20%. Mathematical expectation of the value of the radius vector spindle trajectories with ideal form of bearing surfaces in 1.2-1.4 times less compared to the spindle, HB of which have geometric deviation bearing surfaces (Fig. 5, b). The deviation form bearing surfaces of spindle in HB have little impact on the medium-deviation of radius vector trajectories (Fig. 5, b).

It was defined that for HB with idealized form of bearing surfaces expectation m_R radius vector in the range n = 1500-2400 min^{-1} increases 1.85 times, while taking into account the forms errors of bearing surfaces in HB m_R increases in 1.4 times (Fig. 6,a).

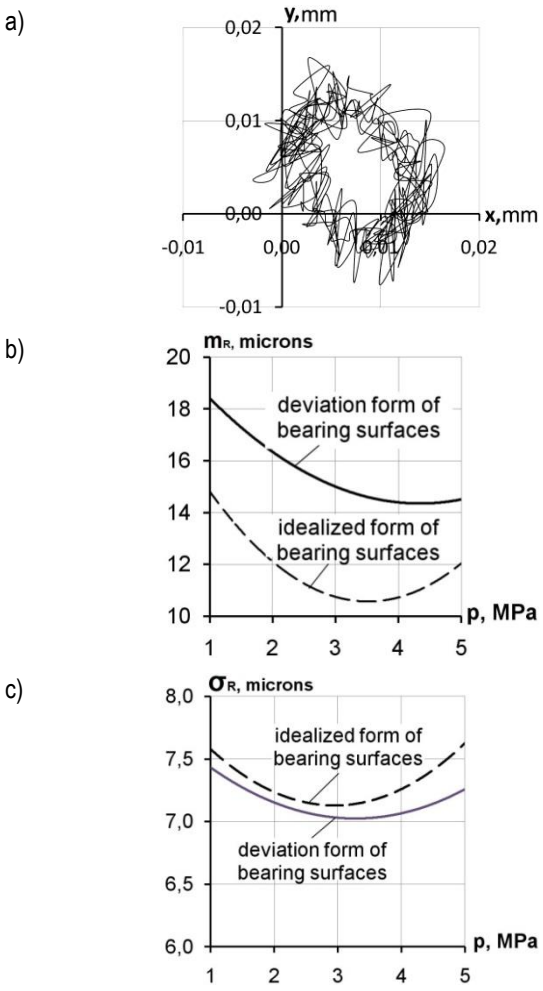

Fig. 5. Typical trajectory of 5 spindle turns: a) mathematical expectation; b) medium-square deviation; c) value of the radius vector trajectories in regulating of pockets pressure in HB (n = 1500 min^{-1}, Dst = 4360·10^{-6} kg·m)

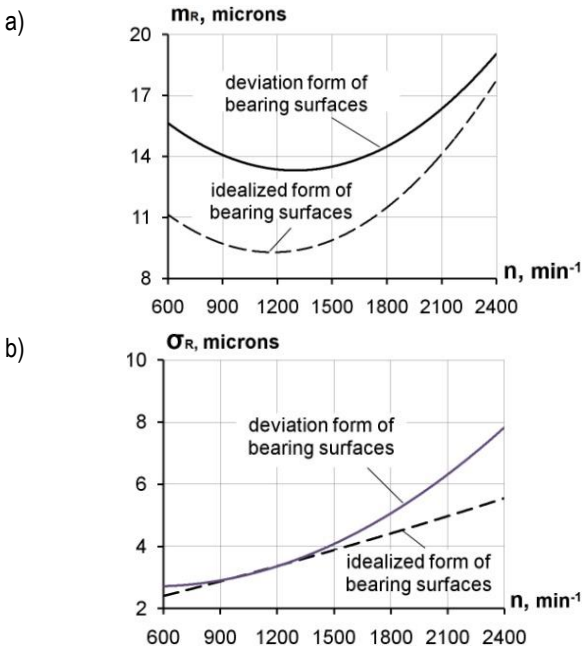

Fig. 6. Mathematical expectation a) and medium-square deviation b) of radius vector trajectories by varying frequency of spindle rotation

DOI 10.1515/ama-2016-0019

4. EXPERIMENTAL RESEARCH TRAJECTORIES OF THE SPINDLE WITH HYDROSTATIC BEARINGS

Experimental studies were conducted to test the adequacy of the results obtained by numerical simulation. For this purpose, it was developed a set for experimental studies, implemented as a experimental stand based on precision lathe model UT16A (Sapon, 2013) (Fig. 7).

With increasing frequency of rotation the difference between the values of mathematical expectation m_R of radius vector of trajectories spindle for HB with deviations and ideal form of bearing surfaces decreases from 40% for n = 600 min^{-1} to 8% for n = 2400 min^{-1}. The deviation form bearing surfaces HB affects the value of standard deviation σ_R of radius vector at frequency of rotation over 1500 min^{-1} (Fig. 6, b), at the same time with increasing frequency of rotation the influence of bearing surfaces forms on the precision of the spindle becomes more significant.

The tendency for increasing of the statistical characteristics of spindle precision with increasing rotation frequency is due to the influence of centrifugal force of inertia, which is proportional to the square of the angular velocity ω spindle. Reducing the value of m_R in the range n = 600-1200 min^{-1} is due to the reduction of size cutting force with increasing cutting speed and constant t_n and S_0.

As a result of spectral analysis of the frequency composition trajectories it is showed that the amplitude of harmonic spectra trajectories with deviation form of bearing surfaces in HB are at 15-60% more than harmonic trajectories with idealized form of bearing surface, confirming a significant impact on the accuracy of formative movements of spindle accuracy of the bearing surfaces.

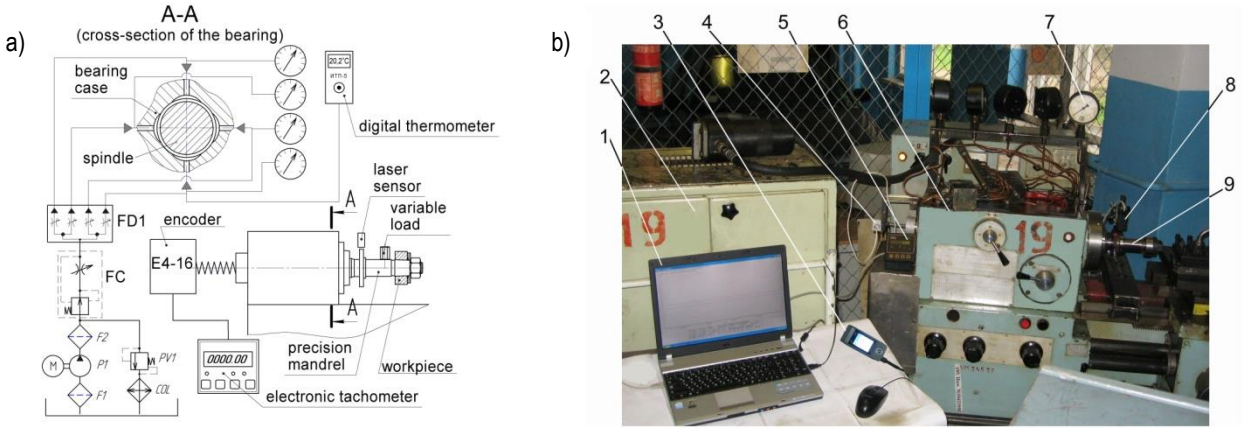

Fig. 7. Structural diagram (a) and general view (b) information-measuring complex for experimental studies of spindle accuracy with adjustable HB: 1 – laptop; 2 – stations; 3 – thermometers; 4 – encoder; 5 – electronic tachometer; 6 – lathe UT16A; 7 – manometer; 8 – laser sensor; 9 – precision mandrel; FD1 – flow divider; FC – control flow valve; P1 – pump; F1, F2 – filters rough and fine cleaning; PV1 – relief valve; COL – oil chiller

The frequency of spindle rotation was fixed on the testimony of specialized electronic tachometer with accuracy of ± 0,05 min^{-1}. The pressure in the HB pockets was defined by means of the flow regulator throttle type, and controlled pressure gauge with an accuracy of 0.1 MPa.

To determine the spindle displacements Δx and Δy in a plane perpendicular to the axis of rotation were used triangulation laser sensors model RF603.2-10/ 2-485-U-IN-AL-CG (Fig. 8, a), the working range of which is 2 mm, the resolution is – 0.2 mkm, the maximum sampling frequency f_d = 9.4 kHz.

Two sensors were installed at 90º on a rack 3 and in the measurements interacted with the control surface of precision mandrel 1 (Fig. 8, b), which was installed in a conical hole spindle machine.

The registration of signals from laser sensors were carried out by the analog-to-digital converter (ADC) based on a digital oscilloscope (Fig. 8, c). ADC connection with PC was carried out using usb interface.

The developed software on the basis of the Windows operating system provides registration, storage, conversion of input signals and then output to the display PC graphics as time dependencies in real time. To minimize the systematic error of the spindle rotation caused by deviations form the control surface of precision mandrels, fine finish control surface was carried out on this machine tool, and after processing mandrel was remained invariably fastened in the spindle for the entire series of experimental studies. It made it possible to provide radial deviation of control surface within the limits of 1.0 microns.

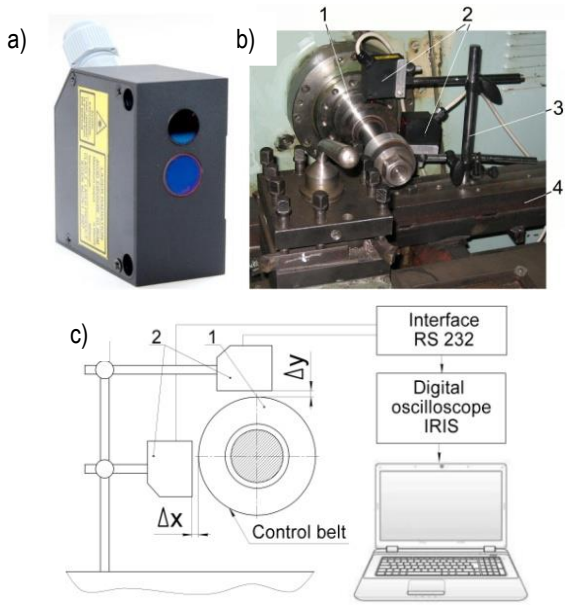

Fig. 8. Triangulation laser sensor a) general view b) schemes of fixing and block diagram measurement of spindle trajectories c): 1 – precision mandrel; 2 – laser sensors; 3 – stand; 4 – stove

DOI 10.1515/ama-2016-0019

To ensure the same number of measurements per rotation of the spindle during the experiments sampling frequency ADC signal to change the proportion to the frequency spindle within f_d = 200–2500 Hz so as to ensure each sensor 50 measurements per rotation of the spindle. This accuracy allows to set statistical characteristics of the trajectories by varying operating parameters HB and discover new patterns in the test process.

Fig. 9 shows experimental trajectories of three spindle rotations, that are built on the results of measurements with sampling rates f_d = 200 Hz and f_d = 2000 Hz and static imbalance Dst = 6525·10^{-6} kg·m. The resulting shape of the trajectories in Fig. 9 indicates the advisability of providing high sample rate ADC during the measurement.

It allowed to establish a discrepancy existing ideas about the ellipticity of the trajectory of the spindle on hydrostatic bearings terms of precision machining (Fig. 9). As shown in Fig.9, the trajectory of the spindle at HB have a pronounced stochastic character, indicating that the complicated nature of processes in lubricant layer of HB. This is explained by the influence of random errors of form, elastic and thermal strains bearing surfaces. The presence of the loop-shaped trajectories of movement is caused by the nonlinear properties of lubricating layer in resisting by the action unsteady external load.

a)

b)

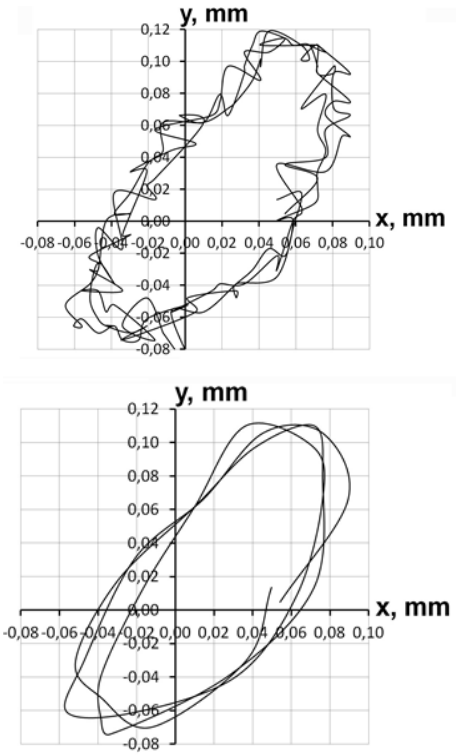

Fig. 9. The experimental trajectory of spindle lathe: a – f_d=2000 Hz; b – f_d=200 Hz

By the measurement results of experimental trajectories were defined their statistical value. The comparison of experimental and theoretical dependences of mathematical expectation and mean-square deviation of the radius vector of trajectories (Fig.10 a, b) and frequency spindle rotation (Fig. 10 c, d) shows their qualitative consistency.

The maximum difference between the experimental and theoretical values of mathematical expectation of a radius vector, regarding deviations form of bearing surfaces does not exceed 16.7% with regulating pressure in the pockets and 18.8% – by varying the rotation speed of the spindle. Compared with the values of mathematical expectation radius vector trajectories obtained by mathematical model with an idealized bearing surface, experimental values differ on average in 1.5 times, it shows the importance of taking into account the forms of bearing surfaces in the study of HB precision spindle.

a)

b)

c)

d)

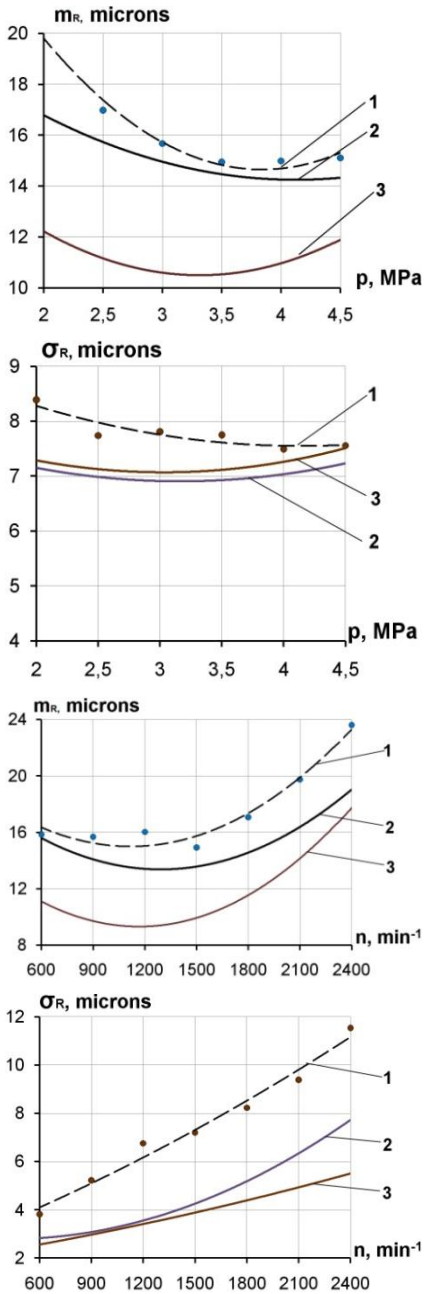

Fig. 10. Comparison of experimental and theoretical dependences of mathematical expectation and mean-square deviation of the radius vector of trajectories a), b) at n = 1500 min^{-1} and the rotational speed of the spindle c) and d) at p=3 MPa: 1 – experimental dependence; 2 – theoretical dependence considering deviations form the supporting surfaces; 3 – theoretical dependence with idealized bearing surface

The maximum difference between the experimental and theoretical values mean-square deviation of the radius vector trajectories obtained taking into account the deviation form bearing sur-

DOI 10.1515/ama-2016-0019

faces does not exceed 14.3% - with regulating pressure in pockets of HB and 43% - by varying the rotation speed of the spindle. The difference between the experimental and theoretical values mean-square deviation of spindle trajectories by varying the rotation speed of the spindle is due to the influence of centrifugal force of inertia caused by the presence of static imbalance, on vibration spindle unit which parameters are quite difficult to describe analytically in a mathematical model.

5. CONSTRUCTION OF ADJUSTABLE HYDROSTATIC BEARING

One of the most perspective directions to improve the accuracy of machine tools is to develop new and upgrade existing structures spindle units by applying in them hydrostatic bearings adjustable type.

Adjusting the operating and design parameters of hydrostatic bearings allows to expand technological capabilities of machines, increase processing performance, reduce operating costs, allows accurate control of formative movement tools, from which to perform the accuracy of the size, shape and relative position of parts of machined surfaces are dependent.

In Chernihiv National University of Technology a new design adjustable hydrostatic bearing has been developed (Fig. 11).

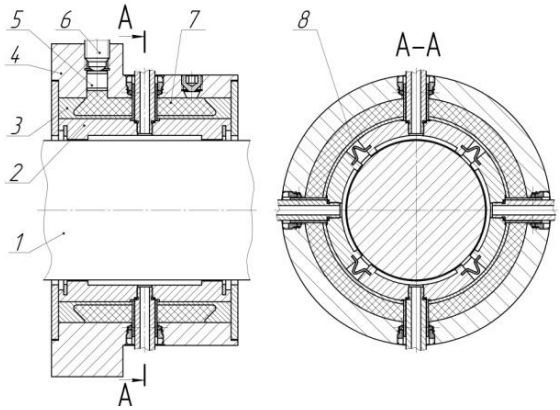

Fig. 11. Adjustable hydrostatic bearing 1 – spindle; 2 – segment; 3 – elastic sleeve; 4 –housing; 5 – plunger; 6 – screw; 7 – hydro-plastic; 8 – springs

In the basic design of the adjustable hydrostatic bearing was assigned the task of improving the uniformity of the adjustment radial clearance, maintenance of repair capability and technological design of the bearing.

The adjusting of the radial clearance in the bearing is made by turning the screw 6, spherical end face of which presses the plunger 5, creating hydrostatic pressure in the cavity filled with hydro-plastic 7.Under the influence of hydrostatic pressure of hydro-plastic theuniform deformation of a thin-walled sleeve 3, takes place resulting in 2 segments movement radially decreasing radial clearance between the bearing surface of the spindle 1 and segments.The deflection of segments is regulated by hydrostatic pressure that is created in the cavity with hydro-plastic.

The benefits of the design: the surface of the hydrostatic bearing is made of 4 individual segments 2, connected by springs 8 of special shape and the regulation of radial clearance in the bearing is provided by simultaneous radial displacement of 4 segments due to uniform deformation of elastic thin-walled sleeve 3 under hydro-plastic pressure.

Built-up construction of hydrostatic bearing surface, connected by springs of special shape allows to increase adaptability, ability to repair bearing and expand the range of structural materials for the manufacture of the bearing. The minimum anisotropy of physical and mechanical properties, precision of shapes and sizes of springs 8 of special shape is achieved by using a calibrated rolled metal sheets as the original piece and finish shaping pressure. Named design and technological options will provide uniform radial displacement of segments 2, which will increase to 1.3-1.5 times control the amount of precision radial clearance in the bearing.

6. CONCLUSIONS

It was developed the mathematical model ofspindle trajectories on hydrostatic bearings, which takes into account the influence of design parameters, geometrical deviations form deformation temperature bearing surfaces of the bearing, random and deterministic operating parameters hydrostatic bearings and technological loads, it allows to increase by 30-60% the accuracy of the spindle position.

It was defined that accounting errors of shape in transverse direction and temperature strain bearing surfaces of the hydrostatic bearing in modeling trajectories spindle leads to an increase in the statistical characteristics of the radius vector paths: the mathematical expectation – by 30%, mean-square deviation – 12.5% compared to idealized bearing surface of the bearing.

As a result of numerical modeling was defined and statistical patterns of precision of the lathe by terms of precision spindle movement trajectories in hydrostatic bearings, the results were verified experimentally:

- increasing the rotational speed of the spindle in the range of 600-2400 min^{-1} in the presence of static imbalance of the spindle unit causes increase in 1.6-2.1 times the mathematical expectation and 2.5-3.4 times the mean-square deviation radius-vector of trajectories spindle;
- rational value of hydrostatic pressure in bearing pockets in which the minimum value provided by the mathematical expectation and mean-square deviation of the radius vector trajectories is in the range of 3-3.5 MPa.

It was developed a new design of adjustable hydrostatic bearing, which can increase to 1.3-1.5 times the precision control of the radial clearance, bearing manufacturing technology and expand the range of structural materials for the manufacture of bearing elements.

REFERENCES

1. **Fedorynenko D., Boyko S., Sapon S.** (2015), The search of the spatial functions of pressure in adjustable hydrostatic radial bearing, *Acta Mechanica et Automatica,* 9(1), 23-26.
2. **Fedorynenko D., Sapon S., Boyko S.**(2014), Considering of the thermal strains in determining the function of the radial clearance in hydrostatic bearing in high-speed spindle node, *Technological systems*, 2(10), 154-159.
3. **Fedorynenko D., Sapon S., Boyko S., Kosmach A.** (2015), Information-measuring complex for research of spindle trajectories on hydrostatic bearings, *Scientific Bulletin of National Mining University: scientific journal,* 6(150), 42-48.

DOI 10.1515/ama-2016-0019

4. **Junpeng S., Guihua H., Yanqin Z., Yuhong D.** (2008), Hardware-in-the-loop Simulation on Controllable Hydrostatic Thrust Bearing, *IEEE International Conference on Automation and Logistics (ICAL 2008)*, 1095-1099.
5. **Junpeng S., Yanqin Z., PengchengL.** (2007), Static flow simulation of hydrostatic bearing ellipse and sector curve based on fluent, *Lubrication Engineering*, 1, 93−95.
6. **Perovic B.** (2012), Hydrostatic guides and bearings: basic principles, calculation and design of hydraulic plans (in German), *Springer-Verlag Berlin Heidelberg*.
7. **Rubinstein R.Y.** (2007), Simulation and the Monte Carlo Method, *Kroese – 2nd edition, Wiley*.
8. **Sapon S.P.**(2013), Methodology of experimental determination precisionspindle, *Bulletin of Chernihiv State Technological University, A series of technical sciences*, 1(63), 66-74.
9. **Savin L.A.** (2006), *Simulation of rotor systems with fluid friction bearings*, Moscow: Engineering.
10. **Shen C.G., Wang G.C., Wang S.L.** (2010), Computation and Analysis of Unbalancing Responses of High Speed Machining Tool System, *Advanced Materials Research*, 148-149(1), 40-46.
11. **Solomin O.V.**(2007), *Development of methods and tools of dynamic analysis of rotor systems with fluid friction bearings,* phd thesis, Orel State University.
12. **Strutynsky V., Fedorynenko D.** (2011), *Statistical dynamics of spindle units for hydrostatic bearings*, Nizhin: LLC "Publishing" Aspect-Polygraph.
13. **Wardle F.** (2015), *Ultra Precision Bearings*, Cambridge: Elsevier.
14. **Xiaodong Y., Huaimin L.** (2006), Computerized Simulation of Lubricating Characteristics of Circular Tilting Pad Thrust Bearing, *Lubrication Engineering*, 3, 84-87.
15. **Xiaodong Y., Huaimin L., Xiurong G.** (2007), Numerical Analysis of Lubricating Characteristics of Sector Thrust Bearing Pad, *Lubrication Engineering*, 1, 123-125.
16. **Yu X.D., Zhang Y.Q.** (2008), Numerical Simulation of Gap Flow of Sector Recess Multi-pad Hydrostatic Thrust Bearing, Proc. 2008 Asia Simulation Conference-7th Int. Conf. *Simulation and Scientific Computing (ICSC 08),* 675–679.
17. **Yuan S., Lin J., Liu Q.** (2008), Finite Element Analysis of Machine Tool as a Whole, *Machine Tool & Hydraulics*,36(4):17-18,49.
18. **Zhao H., Yang J., Shen J.**(2007), Simulation of thermal behaviour of a CNC machine tool spindle, *International Journal of Machine Tool & Manufacture*, 47(6), 1003-1010.

Acknowlegement: The presented results are part of projects 0113U000503 "Development of the Precision-Controlled Hydraulic Bearings of High-Speed Spindle Units" and 0115U002362 "Development of Energy-Efficient High-Speed Spindles with the Adaptive Journal Bearings" funded by the Government of Ukraine.

DE GRUYTER
OPEN

DOI 10.1515/ama-2016-0020 acta mechanica et automatica, vol.10 no.2 (2016)

CONSTITUTIVE MODELLING OF DAMAGE EVOLUTION AND MARTENSITIC TRANSFORMATION IN 316L STAINLESS STEEL

Maciej RYŚ*

*Institute of Applied Mechanics, Faculty of Mechanical Engineering,
Cracow University of Technology, Al. Jana Pawla II 37, 31-864 Cracow, Poland

maciej_rys@o2.pl

received 4 May 2015, revised 11 May 2016, accepted 13 May 2016

Abstract: In this work, the constitutive model, derived with the use of thermodynamic of irreversible processes framework is presented. The model is derived under the assumption of small strains. Plastic strain induced martensitic phase transformation is considered in the austenitic matrix where the volume fraction of the martensite is reflected by a scalar parameter. The austenitic matrix is assumed as the elastic-plastic material and martensitic phase is assumed as randomly distributed and randomly oriented inclusions. Both phases are affected by damage evolution but there is no distinction in the model between damage in austenite and martensite.

Key word: Constitutive Modelling, Dissipative Materials, Phase Transformation, Damage Evolution

1. INTRODUCTION

In this work a material that is susceptible to several coupled dissipative phenomena: plasticity, damage, and phase transformation, that are formalized on the macroscopic level by the use of a proper set of state variables, is considered. Other phenomena, like discontinuous yielding are not taken into account here (Egner and Skoczeń 2010, Skoczeń et al., 2014).

Among metallic materials, that are characterized by the mentioned above dissipative phenomena, we can find austenitic stainless steels. These materials preserve ductility practically down to 0K, thus they are applied for components of superconducting magnets and cryogenic transfer lines: tubes, cylinders, thin walled shells (like bellows expansion joints) or massive parts like vacuum barriers (Ryś, 2015). In the present paper 316L stainless steel is chosen as a field of application of the constitutive description.

The first model of plastic strain induced austenite to martensite ($\gamma \rightarrow \alpha'$) phase transformation was proposed by Olson and Cohen (1975). The authors, on the basis of micromechanical observations, developed a three parameter model capable of describing the experimentally verified sigmoidal curve that represents the volume fraction of martensite as a function of plastic strain. Later on, this model was widely used by others (Stringfellow et al., 1992; Tomita and Iwamoto, 2001; Iwamoto, 2004). Moreover, Stringfellow et al., (1992) expanded on Olson and Cohen's law by incorporating the effect of stress triaxiality on the phase transformation. Tomita and Iwamoto (1995) generalized the model proposed by Stringfellow et al., (1992) by taking into account the effect of strain rate. Micromechanical model was developed by Diani et al. (1995) and later on Cherkaoui et al. (1998) proposed a micromechanical model of martensitic transformation induced plasticity in austenitic single crystal. Another micromechanical model was proposed by Fischer and Schlögl (1995), the Authors investigated the local stress state in a martensitically transforming micro-region including plastic anisotropy. In the paper published by Fischer et al. (2000) the authors devoted their attention to explanation of the martensitic transformation in polycrystalline materials subjected to non-proportional loading paths. A simple phenomenological stress independent transformation law to describe the deformation – induced martensite formation in stainless steel was also proposed by Santacreu et al. (2006). Santacreu's et al. model was further generalized by Beese and Mohr (2011) who proposed a stress-state-dependent transformation kinetics law that incorporates the effect of the Lode angle parameter in addition to the stress triaxiality. However, in the present work the Santacreu's et al. (2006) model in his basic form is chosen to use.

Other constitutive models of materials undergoing phase transformation are due to: Narutani et al. (1982); Cherkaoui et al. (2000); Fischer and Reisner (1998); Diani and Parks (1998); Levitas et al. (1999); Heung Nam Han et al. (2004); Kubler et al. (2011); Ziętek and Mróz (2011), and many others.

In contrast to the beneficial properties, martensitic transformations may also have a detrimental effect on the thermomechanical response of a material. This occurs if the martensitic product phase is relatively hard and brittle, and provides nucleation sites for crystalline damage. Moreover, crystalline damage eventually may lead to crack formation at a higher length scale.

There exists some evidence for the presence of micro-damage fields within the martensite sites (cf Baffie et al., 2000; Le Pecheur, 2008). It seems that the bain strain, associated with formation of the martensite inclusions, can promote local development of damage fields. Also, the martensite platelets are supposed to be carriers of the short cracks that contribute to the general state of damage (see Fig. 2). For this reason the evolution of damage fields has been postulated both in the matrix and in the inclusions. However, there is no distinction between the type of damage in austenite and martensite in the model. Thus, the average content of damage in the RVE (representative volume element) is described by one single scalar parameter. This simpli-

DOI 10.1515/ama-2016-0020

fication is strong because martensitic phase is hard and behaves rather like rock-like material (Egner et al. 2015a, Stolarz 2001). However, it is very difficult to estimate damage content in each phase separately, what justifies the above assumption. On the other hand, as the boundaries between the inclusions and the matrix are coherent, the micro-damage related to some sort of delamination or decohesion within the boundaries has not been taken into account.

For other approaches of damage modeling in austenitic steels see Suiker and Turteltaub (2006, 2007); Egner et al., (2015a, b); Garion and Skoczeń (2003).

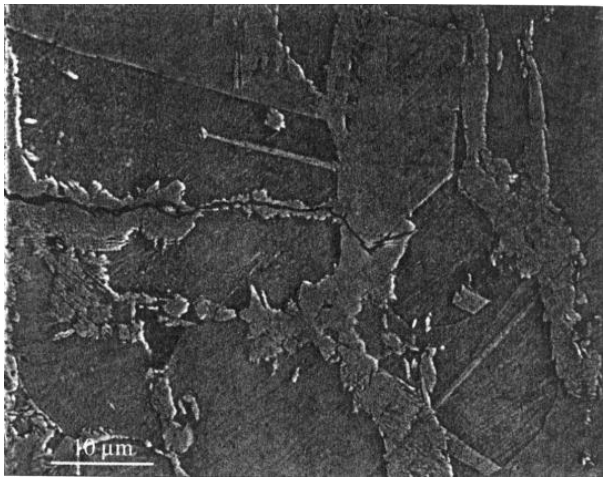

Fig. 1. Propagation of a short crack across an island of martensite (Baffie et al., 2000)

As was mentioned above, the scalar damage parameter, D (with condition: $D = 0$ – initial undamaged state, $D = 1$ – final fractured state), is used to reflect the damage state in the RVE. This concept was proposed first by Kachanov (1958) and then modified by Rabotnov (1968, 1969), and may be interpreted as the fraction of decrease in the effective area due to damage development (Murakami, 2012). In the constitutive modelling damage parameter is used to take into account the influence of voids and cracks accumulation in material on the stress concentration and reduction of the stiffness of the material.

The classical laws of kinematic and isotropic hardening are postulated in the present work. Since the phase transformation has strong influence on hardening process during the plastic deformation, the volume fraction of martensite affects the parameters of both kinematic and isotropic hardening. The kinetic laws for state variables are derived from the normality rule applied to the plastic potential, while the consistency multiplier is obtained from the consistency condition applied to the yield function (Chaboche 2008).

2. CONSTITUTIVE DESCRIPTION OF THE ELASTIC-PLASTIC-DAMAGE TWO PHASE MATERIAL

The author considers a material that is susceptible to three coupled dissipative phenomena: plasticity, damage evolution and phase transformation. The motions within the considered thermodynamic system obey the fundamental laws of continuum mechanics (conservation of mass, conservation of linear momentum, conservation of angular momentum) and two laws of thermodynamics, written here in the local form:

— conservation of energy

$$\rho\dot{u} - \dot{\epsilon}_{ij}\sigma_{ij} - r + q_{i,i} = 0 \tag{1}$$

— Clausius-Duhem inequality

$$\pi = -\rho\left(\dot{\psi} + s\dot{\theta}\right) + \dot{\epsilon}_{ij}\sigma_{ij} - q_i\frac{\theta_{,i}}{\theta} \geq 0 \tag{2}$$

where π denotes the rate of dissipation per unit volume, ρ is the mass density per unit volume; σ_{ij} are the components of the stress tensor; u stands for the internal energy per unit mass; ϵ_{ij} denote the components of the total strain tensor; r is the distributed heat source per unit volume; q_i is the outward heat flux; s denotes the internal entropy production per unit mass, ψ stands for Helmholtz' free energy and θ is the absolute temperature.

The RVE based constitutive model presented in the paper is based on the following assumptions (see also Egner et al. 2015 a,b; Ryś, 2014):

— the martensitic platelets are randomly distributed and randomly oriented in the austenitic matrix,
— both phases are affected by damage,
— rate independent plasticity is assumed,
— small strains are assumed,
— mixed isotropic/kinematic plastic hardening affected by the presence of martensite fraction is included,
— isothermal conditions are considered.

Applying infinitesimal deformation theory to elastic – plastic – damage - two phase material the total strain ϵ_{ij} can be expressed as a sum of the elastic part, ϵ_{ij}^e plastic, ϵ_{ij}^p and Bain strain $\epsilon^{bs} = 1/3\Delta v I$, denoting the additional strain caused by phase transformation.

$$\epsilon_{ij} = \epsilon_{ij}^e + \epsilon_{ij}^p + \xi\epsilon_{ij}^{bs} \tag{3}$$

In order to include in the model variation of the material properties caused by the damage development the mechanical behavior of a damaged material is usually described by using the notion of the effective state variables, together with the hypothesis of mechanical equivalence between the damaged and undamaged configuration.

The current state in representative volume element (RVE) of a real, damaged configuration, $\mathrm{B_t}$, (Fig 1a) is specified by the pairs of state variables:

$$\left(\sigma_{ij}, \epsilon_{ij}^e\right), \left(R^p, r^p\right), \left(X_{ij}^p, \alpha_{ij}^p\right), (Z, \xi), (-Y, D) \tag{4}$$

It is also assumed the exisctence of the fictitious undamaged configuration, B_f, (Fig 1b) which has the identical total strain energy W_T to that of B_t and hence is mechanically equivalent to B_t (Saanouni et. al, 1994, Murakami, 2012).

It is assumed further that the mechanical state of the RVE in fictitious undamaged configuration is described by the set of the effective variables corresponding to Eq. 7.

$$\left(\tilde{\sigma}_{ij}, \tilde{\epsilon}_{ij}^e\right), \left(\tilde{R}^p, \tilde{r}^p\right), \left(\tilde{X}_{ij}^p, \tilde{\alpha}_{ij}^p\right), (Z, \xi), (Y = 0, D = 0) \tag{5}$$

Thus, the hypothesis of total energy equivalence employed in the present work can be formulated as: The mechanical behaviour of a damaged material in the current damaged configuration B_t (Fig 2a) is derived from state and dissipation potentials defined in the fictitious undamaged configuration B_f (Fig 2b) by repleacing the state variables in them by the corresponding effective state

DOI 10.1515/ama-2016-0020

variables (Saanouni et al., 1994; Murakami, 2012; Saanouni, 2012).

Accordingly, the application of this energy equivalence principle leads to:

$$W_T\left(\epsilon_{ij}^e; \alpha_{ij}^p, r^p, \xi, D\right) = W_T(\tilde{\epsilon}_{ij}^e; \tilde{\alpha}_{ij}^p, \tilde{r}^p, \xi, D = 0) \tag{6}$$

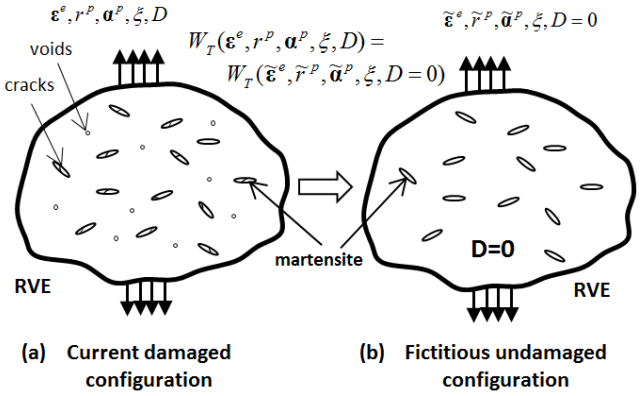

Fig. 2. Hypothesis of total energy equivalence

Since the total energy W_T can be devided into elastic part W_E and parts corresponding to kinematic W_K and isotropic W_I hardening the following relations should be satisfied (Murakami, 2012, Saanouni, 2012):

$$W_E\left(\epsilon_{ij}^e, D\right) = W_E\left(\tilde{\epsilon}_{ij}^e, D = 0\right) = \frac{1}{2}\sigma_{ij}\epsilon_{ij}^e = \frac{1}{2}\tilde{\sigma}_{ij}\tilde{\epsilon}_{ij}^e \tag{7}$$

$$W_K\left(\alpha_{ij}^p, D\right) = W_K\left(\tilde{\alpha}_{ij}^p, D = 0\right) = \frac{1}{2}X_{ij}^p\alpha_{ij}^p = \frac{1}{2}\tilde{X}_{ij}^p\tilde{\alpha}_{ij}^p \tag{8}$$

$$W_I(r^p, D) = W_I(\tilde{r}^p, D = 0) = \frac{1}{2}R^p r^p = \frac{1}{2}\tilde{R}^p\tilde{r}^p \tag{9}$$

It is worth to point it out that phase transformation is assumed here not affected by the damage evolution.

The above relations (Eq. 7 - 9) are always satisfied if the effective state variables are defined as follows (Murakami, 2012, Saanouni, 2012):

$$\tilde{\sigma}_{ij} = \frac{\sigma_{ij}}{\sqrt{(1-D)}}, \tilde{\epsilon}_{ij}^e = \sqrt{(1-D)}\epsilon_{ij}^e \tag{10}$$

$$\tilde{X}_{ij}^p = \frac{X_{ij}^p}{\sqrt{(1-D)}}, \tilde{\alpha}_{ij}^p = \sqrt{(1-D)}\alpha_{ij}^p \tag{11}$$

$$\tilde{R}^p = \frac{R^p}{\sqrt{(1-D)}}, \tilde{r}^p = \sqrt{(1-D)}r^p \tag{12}$$

The presented model is based on the framework of thermodynamics of irreversible processes with internal state variables, where Helmholtz free energy ψ is postulated as a state potential. The state potential depends on the elastic part ϵ_{ij}^e of the total strain ϵ_{ij}, and set of internal state variables $\{\alpha_{ij}^p, r^p, \xi, D\}$, which define the current state of the material:

$$\psi = \psi(\epsilon_{ij}^e; \alpha_{ij}^p, r^p, \xi, D) \tag{13}$$

where $\alpha_{ij}^p, r^p, \xi, D$ are variables related to the kinematic hardening, isotropic hardening, volume fraction of martensite and damage parameter, respectively. Moreover, the damage parameter, D, reflects the average state of damage in whole RVE. There is also the assumption of the existence of thermodynamic forces corresponding to the internal variables

$$\{X_{ij}^p, R^p, Z, -Y\} \tag{14}$$

where $X_{ij}^p, R^p, Z, -Y$ denote, respectively, kinematic and isotropic hardening conjugated forces, thermodynamic conjugated force associated to phase transformation and the associated thermodynamic conjugated force with the isotropic damage variable D.

The Helmholtz free energy of the material can be written as a sum of elastic (E), inelastic (I) and chemical (CH) terms (Abu Al-Rub and Voyiadjis, 2003; Egner et al., 2015a):

$$\psi = \psi^E + \psi^I + \psi^{CH} \tag{15}$$

In the present paper the Helmholtz free energy (Eq. 6) is a quadratic function of all of the strain-like variables and in the fictive configuration it is formulated as (Saanouni, 2012, Besson et. al, 2010):

$$\psi^E = \frac{1}{2}\tilde{\epsilon}_{ij}^e E_{ijkl}\tilde{\epsilon}_{kl}^e = \frac{1}{2}(1-D)\epsilon_{ij}^e E_{ijkl}\epsilon_{kl}^e \tag{16}$$

$$\psi^I = \frac{1}{3}C^p(\xi)\tilde{\alpha}_{ij}^p\tilde{\alpha}_{ij}^p + \frac{1}{2}R_\infty^p(\xi)(\tilde{r}^p)^2 = \frac{1}{3}(1-D)C^p(\xi)\alpha_{ij}^p\alpha_{ij}^p + \frac{1}{2}(1-D)R_\infty^p(\xi)(r^p)^2 \tag{17}$$

Term ψ^{CH} in Eq. 15 represents the chemically stored energy:

$$\psi^{CH} = (1-\xi)\psi_\gamma^{CH} + \xi\psi_{\alpha'}^{CH} \tag{18}$$

The terms ψ_γ^{CH} and $\psi_{\alpha'}^{CH}$ are the chemical energies of the respective phases, cf. Hallberg et al. (2010), Mahnken and Schneidt (2010). This internally stored energy is different for the two phases and it will affect the generation of heat during phase transformation, as well as the transformation itself.

Using the Clausius-Duhem inequality for isothermal case, one obtains:

$$\pi^{mech} = \sigma_{ij}\dot{\epsilon}_{ij} - \dot{\psi} \geq 0 \tag{19}$$

where π^{mech} is defined as mechanical dissipation.

The time derivative of Helmholtz free energy (Eq. 15) as a function of internal state variables is given by:

$$\dot{\psi} = \frac{\partial\psi}{\partial\epsilon_{ij}^e}\dot{\epsilon}_{ij}^e + \frac{\partial\psi}{\partial\alpha_{ij}^p}\dot{\alpha}_{ij}^p + \frac{\partial\psi}{\partial r^p}\dot{r}^p + \frac{\partial\psi}{\partial\xi}\dot{\xi} + \frac{\partial\psi}{\partial D}\dot{D} \tag{20}$$

Substituting the rate of the Helmholtz free energy into Clausius-Duhem inequality the following thermodynamic constraint is obtained:

$$\left(\sigma_{ij} - \frac{\partial\psi}{\partial\epsilon_{ij}^e}\right)\dot{\epsilon}_{ij}^e + \sigma_{ij}\dot{\epsilon}_{ij}^p - \frac{\partial\psi}{\partial\alpha_{ij}^p}\dot{\alpha}_{ij}^p - \frac{\partial\psi}{\partial r^p}\dot{r}^p - \frac{\partial\psi}{\partial\xi}\dot{\xi} - \frac{\partial\psi}{\partial D}\dot{D} \geq 0 \tag{21}$$

Eq. 21 results in the following thermodynamic state laws for the conjugate thermodynamic forces:

$$\sigma_{ij} = \frac{\partial\psi}{\partial\epsilon_{ij}^e} = (1-D)E_{ijkl}^0\left(\epsilon_{kl} - \epsilon_{kl}^p - \xi\epsilon_{kl}^{bs}\right) \tag{22}$$

$$X_{ij}^p = \frac{\partial\psi}{\partial\alpha_{ij}^p} = \frac{2}{3}(1-D)C^p(\xi)\alpha_{ij}^p \tag{23}$$

$$R^p = \frac{\partial\psi}{\partial r^p} = (1-D)R_\infty^p(\xi)r^p \tag{24}$$

$$Z = \frac{\partial\psi}{\partial\xi} = \rho\frac{\partial\psi^I}{\partial\xi} + \left(\rho\psi_{\alpha'}^{CH} - \rho\psi_\gamma^{CH}\right) \tag{25}$$

$$Y = -\frac{\partial\psi}{\partial D} = Y^E + Y^{IN} = \frac{1}{2}\epsilon_{ij}^e E_{ijkl}^0\epsilon_{kl}^e + \frac{1}{3}C^p(\xi)\alpha_{ij}^p\alpha_{ij}^p + \frac{1}{2}R_\infty^p(\xi)(r^p)^2 \tag{26}$$

DOI 10.1515/ama-2016-0020

Thermodynamic force, Y, conjugated to the damage parameter, D, is the strain energy density release rate and in the case when the hypothesis of total energy equivalence is employed represents the contribution from elasticity, kinematic hardening, and isotropic strain hardening.

It is assumed here that all dissipative mechanisms are governed by plasticity with a single dissipation potential F (Lemaitre 1992):

$$F = F^p\left(\sigma_{ij}, X_{ij}^p, R^p, \xi\right) + F^{TR}(Q,\xi) + F^D(-Y, D) \tag{27}$$

Plastic potential $\mathrm{F^p}$ has the following form:

$$F^p = f^p + \frac{1}{2}\frac{b}{R_\infty^p(\xi)}\left(\tilde{R}^p\right)^2 + \frac{1}{2}\frac{\gamma}{C^p(\xi)}\frac{3}{2}\tilde{X}_{ij}^p\tilde{X}_{ij}^p \tag{28}$$

where, $\mathrm{f^p}$ is von Mises yield function:

$$f^p = J_2\left(\tilde{\sigma}_{ij} - \tilde{X}_{ij}^p\right) - \sigma_y - \tilde{R}^p = \sqrt{\frac{3}{2}\left(\tilde{\sigma}_{ij}^D - \tilde{X}_{ij}^p\right)\left(\tilde{\sigma}_{ij}^D - \tilde{X}_{ij}^p\right)} - \sigma_y - \tilde{R}^p \tag{29}$$

where, $\mathrm{\tilde{\sigma}_{ij}^D}$ is the deviatoric part of the Cauchy stress tensor.

The phase transformation dissipation potential is assumed here in the following form:

$$F^{TR} = \frac{1}{\sqrt{1-D}}(\xi^{max} - \xi)mA(Ap)^{m-1}Q^{TR} - B^{TR} \tag{30}$$

The quantity $\mathrm{Q^{TR} = \sigma_{ij}\epsilon_{ij}^{bs} - Z}$ is conjugated to the transformation rate $\dot{\xi}$ and can be treated as a thermodynamic force that drives the phase front through the material (cf. Hallberg et al., 2007, 2010), p is accumulated plastic strain, A, m, $\mathrm{\xi^{max}}$ are the model parameters that have to be found through experimental validation of the model, and $\mathrm{B^{tr}}$ is the barrier force for phase transformation (cf. Mahnken and Schneidt, 2010; Fisher et al., 2000).

Damage dissipation potential is as follows (Bonora, 1997):

$$F^D = \frac{1}{2}\frac{S}{\sqrt{1-D}}\left(\frac{Y}{S}\right)^2\frac{(D_C - D)^{(\alpha-1)/\alpha}}{p^{(n+2)/n}} \tag{31}$$

where $\mathrm{D_C}$ is the critical value of damage variable for which ductile failure occurs, S is a model parameter, n is the material hardening exponent, while α is an exponent characterizing the damage development.

Normality rule involves only one plastic multiplier, determined from the consistency condition. The equations involving the dissipation potentials take the form:

$$\dot{\epsilon}_{ij}^p = \dot{\lambda}^p\frac{\partial F^p}{\partial \sigma_{ij}} = \frac{\dot{\lambda}^p}{\sqrt{1-D}}\frac{3}{2}\frac{\left(\sigma_{ij}^D - X_{ij}^p\right)}{J_2\left(\sigma_{ij}^D - X_{ij}^p\right)} \tag{32}$$

$$\dot{p} = \sqrt{\frac{2}{3}\dot{\epsilon}_{ij}^p\dot{\epsilon}_{ij}^p} = \frac{\dot{\lambda}^p}{\sqrt{1-D}} \tag{33}$$

$$\dot{\alpha}_{ij}^p = -\dot{\lambda}^p\frac{\partial F^p}{\partial X_{ij}} = \dot{\epsilon}_{ij}^p - \gamma\dot{\lambda}^p\alpha_{ij}^p = \dot{\epsilon}_{ij}^p - \gamma\dot{p}\sqrt{1-D}\alpha_{ij}^p \tag{34}$$

$$\dot{r}^p = -\dot{\lambda}^p\frac{\partial F^p}{\partial R^p} = \frac{\dot{\lambda}^p}{\sqrt{1-D}}\left(1 - b\sqrt{1-D}r^p\right) = \dot{p}\left(1 - b\sqrt{1-D}r^p\right) \tag{35}$$

$$\dot{\xi} = \dot{\lambda}^p\frac{\partial F^{TR}}{\partial Q^{TR}} = (\xi^{max} - \xi)mA(Ap)^{m-1}\dot{p} \tag{36}$$

It has to be mentioned here that the phase transformation dissipation employed in the form of Eq. 30 allows to obtain kinetic law of phase transformation orginally proposed by Santacreu et al. (2006).

The choice of the damage potential (Eq. 31) leads to the following damage kinetic evolution with the effective accumulated plastic strain (Bonora, 1997):

$$\dot{D} = \frac{\dot{\lambda}^p}{\sqrt{1-D}}\left(\frac{Y}{S}\right)\frac{(D_C - D)^{(\alpha-1)/\alpha}}{p^{(n+2)/n}} = Y\frac{(D_C - D)^{(\alpha-1)/\alpha}}{S}\frac{\dot{p}}{p^{(n+2)/n}} \tag{37}$$

Bonora in his works used the strain energy equivalence hypothesis which results, in accordance with symbols in the present article, that $\mathrm{Y = Y^E}$. In the case of isotropic material elastic part of Y can be expressed as a function of the von Mises equivalent stress $\mathrm{\sigma_{EQ}}$ and the stress triaxiality (defined as a ratio of the hydrostatic stress and von Mises stress, $\mathrm{\sigma_H/\sigma_{EQ}}$) (Lemaitre, 1992; Murakami, 2012):

$$Y^E = \frac{(\sigma_{EQ})^2}{2E(1-D)^2}\left(\frac{2}{3}(1+\upsilon) + 3(1-2\upsilon)\left(\frac{\sigma_H}{\sigma_{EQ}}\right)^2\right) = \frac{(\sigma_{EQ})^2}{2E(1-D)^2}f\left(\frac{\sigma_H}{\sigma_{EQ}}\right) \tag{38}$$

Moreover, Bonora proposed to use the Ramberg – Osgood relation

$$p = \left(\frac{\sigma_{EQ}}{(1-D)K}\right)^n \tag{39}$$

what gives

$$\dot{D} = \frac{K^2}{2ES}f\left(\frac{\sigma_H}{\sigma_{EQ}}\right)(D_C - D_0)^{(\alpha-1)/\alpha}\frac{\dot{p}}{p} \tag{40}$$

It can be shown (Murakami, 2012) that integration of this relation under uniaxial tenstion with the initial condition of $\mathrm{p = \epsilon_D}$ and $\mathrm{D = D_0}$, and then applying the fracture condition $\mathrm{\epsilon = \epsilon_R}$, $\mathrm{D = D_C}$ one can obtain the reliation:

$$\frac{K^2}{2ES} = \alpha\frac{(D_C - D_0)^{1/\alpha}}{\ln(\epsilon/\epsilon_D)} \tag{41}$$

Finally, we can obtain the following kinetic equation of the damage evolution:

$$\dot{D} = \alpha\frac{(D_C - D_0)^{1/\alpha}}{\ln(\epsilon_f) - \ln(\epsilon_{th})}f\left(\frac{\sigma_m}{\sigma_{EQ}}\right)(D_C - D)^{(\alpha-1)/\alpha}\frac{\dot{p}}{p} \tag{42}$$

where, $\mathrm{D_0}$ is the initial damage state in the material microstructure, $\mathrm{\epsilon_{th}}$ and $\mathrm{\epsilon_f}$ are threshold strain at which damage process starts and the strain to failure in the uniaxial state of stress, respectively.

The use of the total energy equivalence, in the present work, imply that $\mathrm{Y = Y^E + Y^{IN}}$. Moreover, as denoted by Saanouni et al. (1994) the contribution of the inelastic part, $\mathrm{Y^{IN}}$, in the total damage energy release rate, Y, is significant and should not be neglected. Hence, in the present work, the basic form (Eq. 37) of the kinetic equation of the damage evolution is used in which the relation $\mathrm{Y = Y^E + Y^{IN}}$ is applied.

The consistency multiplier $\mathrm{\dot{\lambda}^p}$ is obtained from the consistency condition:

$$\dot{f}^p = \frac{\partial f^p}{\partial \sigma_{ij}}\left(\dot{\sigma}_{ij} - \dot{X}_{ij}^p\right) + \frac{\partial f^p}{\partial R^p}\dot{R}^p + \frac{\partial f^p}{\partial D}\dot{D} + \frac{\partial f^p}{\partial \xi}\dot{\xi} = 0 \tag{43}$$

The evolution equations for thermodynamic conjugated forces are obtained by taking time derivatives of quantities defined by equations 22 - 24. In particular, the force rates appearing in consistency condition (Eq. 43) are given by the following formulae:

DOI 10.1515/ama-2016-0020

$$\dot{\sigma}_{ij} = E_{ijkl}(D)\left(\dot{\epsilon}_{kl} - \dot{\epsilon}^{p}_{kl} - \dot{\xi}\epsilon^{bs}_{kl}\right) - E^{0}_{ijkl}\left(\epsilon_{kl} - \epsilon^{p}_{kl} - \xi\epsilon^{bs}_{kl}\right)\dot{D} \quad (44)$$

$$\dot{X}^{p}_{ij} = \frac{2}{3}(1-D)C^{p}(\xi)\dot{\alpha}^{p}_{ij} - \left(\frac{\dot{D}}{1-D} - \frac{1}{C^{p}(\xi)}\frac{\partial C^{p}(\xi)}{\partial \xi}\dot{\xi}\right)X^{p}_{ij} \quad (45)$$

$$\dot{R}^{p} = (1-D)R^{p}_{\infty}(\xi)\dot{r}^{p} - \left(\frac{\dot{D}}{1-D} - \frac{1}{R^{p}_{\infty}(\xi)}\frac{\partial R^{p}_{\infty}(\xi)}{\partial \xi}\dot{\xi}\right)R^{p} \quad (46)$$

In the present work, the simplest, linear form of functions $C^{p}(\xi)$ and $R^{p}_{\infty}(\xi)$ is assumed, namely:

$$C^{p}(\xi) = C^{p}_{0}(1 + h_{C}\xi), \quad (47)$$

$$R^{p}_{\infty}(\xi) = R^{p}_{\infty,0}(1 + h_{R}\xi) \quad (48)$$

3. LOCAL INTEGRATION SCHEME

In the present work elastic predictor – plastic corrector procedure is used where the Newton-Raphson scheme is adopted to solve all nonlinear equations. Applying the forward Euler scheme, equations of time-independent plasticity, Eq. 32, 34-37 and 29 can be written in the following residual form:

$$R^{\epsilon}_{ij} = \epsilon^{p,n+1}_{ij} - \epsilon^{p,n}_{ij} - \frac{\Delta\lambda^{p}}{\sqrt{1-D^{n+1}}}\frac{3}{2}\frac{\left(\sigma^{D,n+1}_{ij} - X^{p,n+1}_{ij}\right)}{J_{2}\left(\sigma^{D,n+1}_{ij} - X^{p,n+1}_{ij}\right)} \quad (49)$$

$$R^{\alpha}_{ij} = \alpha^{p,n+1}_{ij} - \frac{1}{1+\gamma\Delta\lambda^{p}}\left(\alpha^{p,n}_{ij} + \Delta\epsilon^{p}_{ij}\right) \quad (50)$$

$$R^{r} = r^{p,n+1} - \frac{1}{1+b\Delta\lambda^{p}}\left(r^{p,n} + \frac{\Delta\lambda^{p}}{\sqrt{1-D}}\right) \quad (51)$$

$$R^{D} = D^{n+1} - D^{n} - \frac{\Delta\lambda^{p}}{\sqrt{1-D}}\left(\frac{Y^{n+1}}{S}\right)\frac{(D_{C} - D^{n+1})^{(\alpha-1)/\alpha}}{p^{(n+2)/n}} \quad (52)$$

$$R^{\xi} = \xi^{n+1} - \xi^{n} - (\xi^{max} - \xi^{n+1})mA(Ap)^{m-1}\frac{\Delta\lambda^{p}}{\sqrt{1-D}} \quad (53)$$

$$R^{f} = f^{p,n+1} = \frac{1}{\sqrt{1-D^{n+1}}}\sqrt{\frac{3}{2}\left(\sigma^{D,n+1}_{ij} - X^{p,n+1}_{ij}\right)\left(\sigma^{D,n+1}_{ij} - X^{p,n+1}_{ij}\right)} - \sigma_{y} - \frac{R^{p,n+1}}{\sqrt{1-D^{n+1}}} = 0 \quad (54)$$

The stress – like variables involved in the above equations are given by:

$$\sigma^{n+1}_{ij} = (1-D^{n+1})E^{0}_{ijkl}\left(\epsilon^{n+1}_{kl} - \epsilon^{p,n+1}_{kl} - \xi^{n+1}\epsilon^{bs}_{kl}\right) \quad (55)$$

$$X^{p,n+1}_{ij} = \frac{2}{3}(1-D^{n+1})C^{p}_{0}(1 + h_{C}\xi^{n+1})\alpha^{p,n+1}_{ij} \quad (56)$$

$$R^{p,n+1} = (1-D^{n+1})R^{p}_{\infty,0}(1 + h_{R}\xi^{n+1})r^{p,n+1} \quad (57)$$

$$Y^{E,n+1} = \frac{1}{2}\left(\epsilon^{n+1}_{ij} - \epsilon^{p,n+1}_{ij} - \xi^{n+1}\epsilon^{bs}_{ij}\right)E^{0}_{ijkl}\left(\epsilon^{n+1}_{kl} - \epsilon^{p,n+1}_{kl} - \xi^{n+1}\epsilon^{bs}_{kl}\right) \quad (58)$$

$$Y^{IN} = \frac{1}{3}C^{p}_{0}(1 + h_{C}\xi^{n+1})\alpha^{p,n+1}_{ij}\alpha^{p,n+1}_{ij} + \frac{1}{2}R^{p}_{\infty,0}(1 + h_{R}\xi^{n+1})(r^{p,n+1})^{2} \quad (59)$$

3.1. Elastic predictor – plastic corrector scheme

There is assumed that the total strain at the end of the time step, ϵ^{n+1}_{kl}, is known and defined as follows:

$$\epsilon^{n+1}_{kl} = \epsilon^{n}_{kl} + \Delta\epsilon_{kl} \quad (60)$$

Moreover, in the elastic – predictor step, the incremental strains are assumed to be elastic with no damage such that an initial trial stress can be computed as:

$$\sigma^{n+1,trial}_{ij} = (1-D^{n})E^{0}_{ijkl}\left(\epsilon^{n+1}_{kl} - \epsilon^{p,n}_{kl} - \xi^{n}\epsilon^{bs}_{kl}\right) \quad (61)$$

The trial state $\left(\sigma^{n+1,trial}_{ij}, \epsilon^{p,n}_{ij}, \alpha^{p,n}_{ij}, r^{p,n}, D^{n}, \xi^{n}\right)$ is used to check the yield criterion, Eq. 29.

If $f^{p,n+1\,trial}\left(\sigma^{n+1,trial}_{ij}\epsilon^{p,n}_{ij}\alpha^{p,n}_{ij}, r^{p,n}, D^{n}, \xi^{n}\right) \leq 0$ then $\sigma^{n+1}_{ij} = \sigma^{n+1,trial}_{ij}$ and the increment is completed.

Alternatively, if the yield function for trial stress is positive

$$f^{p,n+1\,trial}\left(\sigma^{n+1,trial}_{ij}\epsilon^{p,n}_{ij}\alpha^{p,n}_{ij}, r^{p,n}, D^{n}, \xi^{n}\right) > 0,$$

it means that current state lies outside of the yield surface. Plasticity has occurred and the state has to be returned to the yield surface. Thus, the system of equations from 49 to 54 is linearized and has to be solved with respect to the following unknowns

$$\mathbf{u} = \left\{\epsilon^{p,n+1}_{ij}, \alpha^{p,n+1}_{ij}, r^{p,n+1}, D^{n+1}, \xi^{n+1}, \Delta\lambda^{n+1}\right\}$$

with the initial condition

$$\epsilon^{p,n+1}_{ij} = \epsilon^{p,n}_{ij};\ \alpha^{p,n+1}_{ij} = \alpha^{p,n}_{ij};\ r^{p,n+1} = r^{p,n};$$

$$D^{n+1} = D^{n};\ \xi^{n+1} = \xi^{n};\ \Delta\lambda^{n+1} = 0;$$

The linearized system of six equations can be solved with the use of the Newton-Raphson scheme at iteration (s) what can be written in the following general form

$$\{\mathbf{R}\}^{s}_{n+1} + \left[\frac{\partial \boldsymbol{R}}{\partial \boldsymbol{u}}\right]^{s}_{n+1}\{\delta\boldsymbol{u}\}_{n+1} + \cdots = \{\mathbf{0}\} \quad (62)$$

where, $\{\mathbf{R}\}^{T} = \{R^{\epsilon}_{ij}, R^{\alpha}_{ij}, R^{r}, R^{D}, R^{\xi}, R^{f}\}^{T}$, $[\partial\mathbf{R}/\partial\mathbf{u}]$ is the Jacobian defined as:

$$\left[\frac{\partial \mathbf{R}}{\partial \mathbf{u}}\right] = \begin{bmatrix} \frac{\partial R^{\epsilon}_{ij}}{\partial \epsilon^{p,n+1}_{kl}} & \frac{\partial R^{\epsilon}_{ij}}{\partial \alpha^{p,n+1}_{kl}} & \frac{\partial R^{\epsilon}_{ij}}{\partial r^{p,n+1}} & \frac{\partial R^{\epsilon}_{ij}}{\partial D^{n+1}} & \frac{\partial R^{\epsilon}_{ij}}{\partial \xi^{n+1}} & \frac{\partial R^{\epsilon}_{ij}}{\partial \Delta\lambda^{n+1}} \\ \frac{\partial R^{\alpha}_{ij}}{\partial \epsilon^{p,n+1}_{kl}} & \frac{\partial R^{\alpha}_{ij}}{\partial \alpha^{p,n+1}_{kl}} & \frac{\partial R^{\alpha}_{ij}}{\partial r^{p,n+1}} & \frac{\partial R^{\alpha}_{ij}}{\partial D^{n+1}} & \frac{\partial R^{\alpha}_{ij}}{\partial \xi^{n+1}} & \frac{\partial R^{\alpha}_{ij}}{\partial \Delta\lambda^{n+1}} \\ \frac{\partial R^{r}}{\partial \epsilon^{p,n+1}_{kl}} & \frac{\partial R^{r}}{\partial \alpha^{p,n+1}_{kl}} & \frac{\partial R^{r}}{\partial r^{p,n+1}} & \frac{\partial R^{r}}{\partial D^{n+1}} & \frac{\partial R^{r}}{\partial \xi^{n+1}} & \frac{\partial R^{r}}{\partial \Delta\lambda^{n+1}} \\ \frac{\partial R^{D}}{\partial \epsilon^{p,n+1}_{kl}} & \frac{\partial R^{D}}{\partial \alpha^{p,n+1}_{kl}} & \frac{\partial R^{D}}{\partial r^{p,n+1}} & \frac{\partial R^{D}}{\partial D^{n+1}} & \frac{\partial R^{D}}{\partial \xi^{n+1}} & \frac{\partial R^{D}}{\partial \Delta\lambda^{n+1}} \\ \frac{\partial R^{\xi}}{\partial \epsilon^{p,n+1}_{kl}} & \frac{\partial R^{\xi}}{\partial \alpha^{p,n+1}_{kl}} & \frac{\partial R^{\xi}}{\partial r^{p,n+1}} & \frac{\partial R^{\xi}}{\partial D^{n+1}} & \frac{\partial R^{\xi}}{\partial \xi^{n+1}} & \frac{\partial R^{\xi}}{\partial \Delta\lambda^{n+1}} \\ \frac{\partial R^{f}}{\partial \epsilon^{p,n+1}_{kl}} & \frac{\partial R^{f}}{\partial \alpha^{p,n+1}_{kl}} & \frac{\partial R^{f}}{\partial r^{p,n+1}} & \frac{\partial R^{f}}{\partial D^{n+1}} & \frac{\partial R^{f}}{\partial \xi^{n+1}} & \frac{\partial R^{f}}{\partial \Delta\lambda^{n+1}} \end{bmatrix}$$

Solving the general equation Eq. 62 allows to obtain the corrections $\{\delta\mathbf{u}\}^{T} = \left\{\delta\epsilon^{p,n+1}_{ij}, \delta\alpha^{p,n+1}_{ij}, \delta r^{p,n+1}, \delta D^{n+1}, \delta\xi^{n+1}, \delta\Delta\lambda^{n+1}\right\}^{T}$ for the current iteration. Accordingly, the values of the unknowns for the next iteration are deduced from:

$$\left(\epsilon^{p,n+1}_{ij}\right)^{s+1} = \left(\epsilon^{p,n+1}_{ij}\right)^{s} + \delta\epsilon^{p,n+1}_{ij}$$

$$\left(\alpha^{p,n+1}_{ij}\right)^{s+1} = \left(\alpha^{p,n+1}_{ij}\right)^{s} + \delta\alpha^{p,n+1}_{ij}$$

$$(r^{p,n+1})^{s+1} = (r^{p,n+1})^{s} + \delta r^{p,n+1}$$

$$(D^{n+1})^{s+1} = (D^{n+1})^{s} + \delta D^{n+1}$$

$$(\xi^{n+1})^{s+1} = (\xi^{n+1})^{s} + \delta\xi^{n+1}$$

$$(\Delta\lambda^{n+1})^{s+1} = (\Delta\lambda^{n+1})^{s} + \delta\Delta\lambda^{n+1}$$

DOI 10.1515/ama-2016-0020

The iteration proceeds until convergence is achieved based on an appropriate criterion of type $\{R\}_{n+1}^{s} < ERROR$.

Obtaining final values of unknowns the values of stress – like variables can be easily calculated by using the equations 55-59.

4. VALIDATION OF THE MODEL

The constitutive model of coupled phenomena has been validated by means of loading/unloading test performed at the temperature of liquid helium (4.2 K) (Egner and Skoczeń, 2010, Egner et al., 2015a). The experimental stress-strain curve for 316L stainless steel subjected to uniaxial tension is shown in Fig. 3. The evolution of micro-damage was measured by introducing unloading procedure and tracing variations of the unloading modulus. Parameters included in the evolution equations for thermodynamic forces (isotropic/kinematic hardening laws) and kinetic laws of evolution of internal variables (damage and phase evolution equations) were found with the use of ISIGHT program.

Accounting for three dissipative phenomena: plasticity, damage evolution and phase transformation in the present constitutive model allows to obtain a satisfactory reproduction of the experimental stress-strain curve for 316L stainless steel subjected to uniaxial tension at the temperature of 4.2K (see Fig. 3). Hardening effect due to phase transformation combined with softening effect due to damage evolution enables to model the initially nonlinear plastic hardening, followed by plastic plateau and strong nonlinear hardening in the final stage of plastic flow.

To show influence of the particular dissipative phenomena (damage evolution and phase transformation) on the model, three cases are presented (see Fig. 3): (a) only softening effect of damage was accounted for (no phase transformation); (b) only hardening effect of phase transformation was considered (damage development was neglected) and (c) both effects of damage evolution and phase transformation are included.

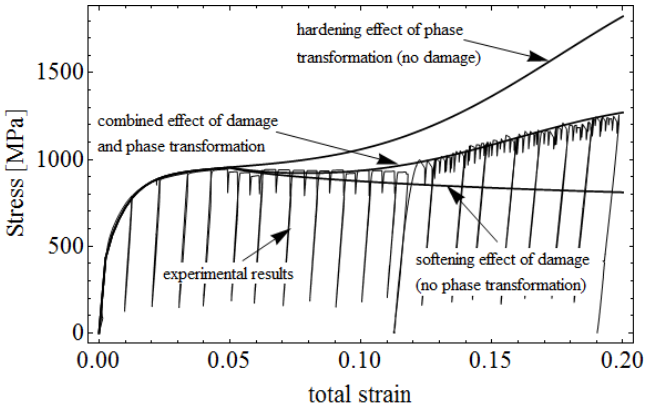

Fig. 3. Stress-strain curve for 316L stainless steel

The use of Bonora's law of damage evolution and Santacreu's kinetic model of phase transformation allows to obtain a very good agreement of the numerical results with experimental data (see Fig. 4). As was mentioned before, the use of total energy equivalence priciple imply that the damage energy release rate contains two terms: Y^E is the (classical) contribution of elastic energy and Y^{IN} represents the release of the stored energy due to the damage growth (Saanouni, 1994). It is worth to point it out that for some materials Y^{IN} represents more than 50% of the overall Y (Saanouni, 1988; Ju, 1989). The significant influence of Y^{IN} on damage evolution can be observed in Fig. 4 where using only classical term Y^E ($Y = Y^E$) in Eq. 37 caused about 50% drop of damage content in the RVE. The contribution of particular terms (Y^E and Y^{IN}) in Y is shown in Fig. 5.

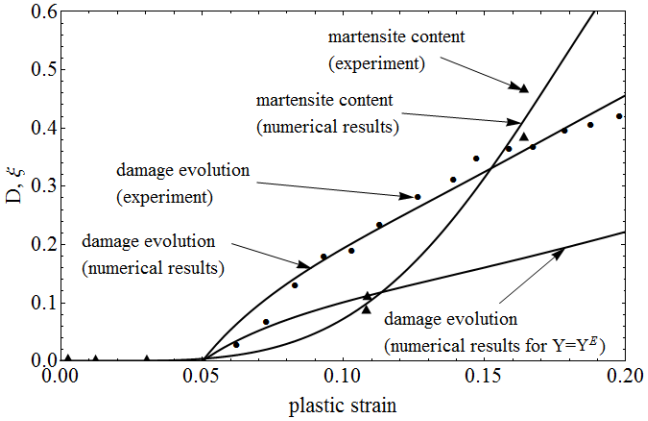

Fig. 4. Numerical and experimental results of damage evolution and martensite content versus plastic strain

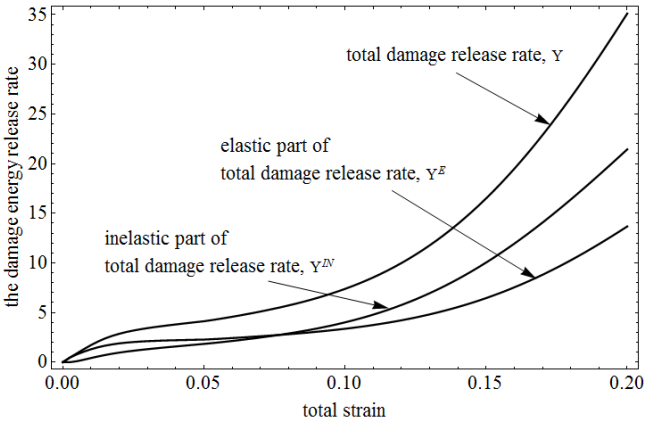

Fig. 5. The contribution of terms: Y^E and Y^{IN} in the total damage energy release rate Y

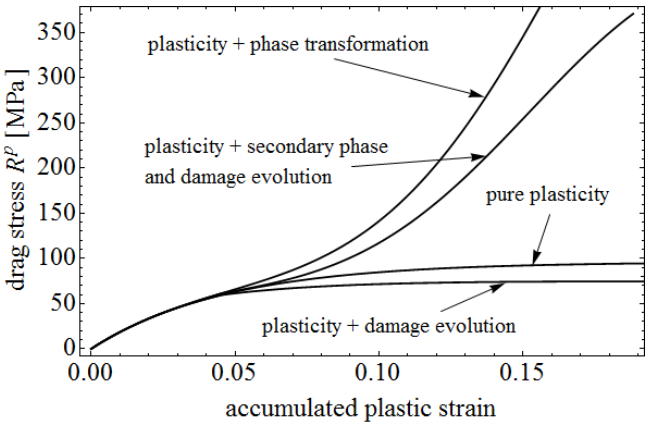

Fig. 6. Evolution of the drag stress

To examine the influence of the damage evolution and secondary phase content in the RVE on the isotropic (drag stress) and kinematic hardening (back stress) four cases are presented

DOI 10.1515/ama-2016-0020

in Fig. 6 and Fig. 7: (a) pure plasticity (neither damge evolution nor phase transformation is present); (b) plasticity and the damage evolutios were accounted for (no phase transformation); (c) only hardening effect of phase transformation was considered (damage development was neglected) and (d) both effects of damage evolution and phase transformation are included. The use of the total energy equivalnce principle allowed to obtain full coupling between damge evolution and plastic flow, meaningfully the damage content effects the plastic modulus (see Eq. 23 and 24) and the drop of force – like varibles due to damage can be observed (Fig. 6 and Fig. 7). The use of simple linear function Eq. 47 and 48 also allowed to take into account important phenomenon like the strong influence of seconadary phase content on the hardening process (see Fig. 6 and Fig 7).

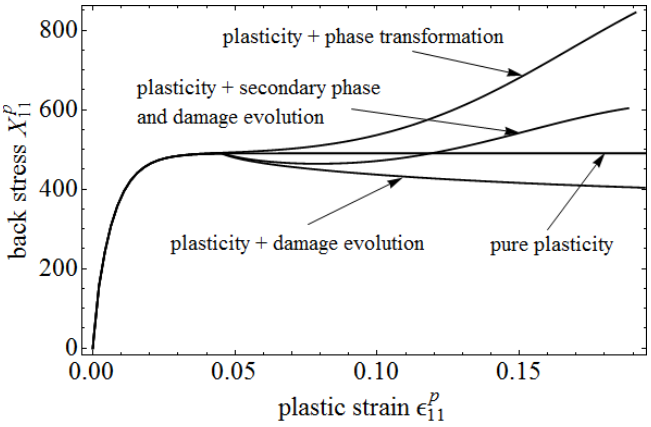

Fig. 7. Evolution of the back stress

Tab. 1. Material data for 316L stainless steel at the temperature of 4.2K

Young modulus [GPa]	206
Poisson ratio	0.3
Yield stress [MPa]	402.417
C_0^p [MPa]	82041.7
γ [MPa]	167
$R_{\infty,0}^p$ [MPa]	2104.24
b	22
h_C	1.03
h_R	7.3
Δv	0.02
D_0	0
D_C	0.8
α	200
n	4.5
S [MPa]	48.87
ξ^{max}	0.9
m	3.9
A	5.55

5. CONCLUSIONS

The constitutive model presented in the paper results from identification of two fundamental phenomena that occur in materials characterized by low stacking fault energy: plastic strain induced phase transformation and evolution of micro-damage reflected by decreasing elasticity modulus in the course of deformation. Non-associated theory was applied what allowed to obtain nonlinear isotropic and kinematic hardening. The influence of martensitic transformation on hardening process was modeled by introducing plastic moduli as functions of martensite content in the hardening laws. The total energy equivalence hypothesis is used to define the effective state variables. This approach enables: (1) the definition of internal state variables as well as the effective thermodynamic conjugated forces, which can be indifferently used in stress space and strain space by the use of the Legendre-Fenchel transformation; (2) obtaining symmetric physical properties of material (symmetric stiffness tensor, compliance tensor, strain hardening modules) even in the case of anisotropy induced by dissipative phenomena; (3) modeling of coupling between damage variable and other internal state variables in a natural way (Saanouni et. al., 1994). The average content of damage in the RVE (representative volume element) is described by one single scalar parameter. As was mentioned, this simplification is strong because martensitic phase is hard and behaves rather like rock-like material. Moreover, in brittle phases the stress state has the crucial influence on damage and anisotropic behavior of the material may take place. Thus, in the future work two separate scalar or tensorial type damage variable should be used (e.g. Kintzel et. al., 2010; Egner et. al., 2015).The model was validated through uniaxial tension test of 316L stainless steel, and a good agreement between the experimental and numerical results was obtained.

REFERENCES

1. **Abu Al Rub R.K, Voyiadjis G.Z.** (2003), On the coupling of anisotropic damage and plasticity models for ductile materials, *International Journal of Plasticity*, 40, 2611-2643.
2. **Baffie, N., Stolarz, J. and Magnin, T.** (2000), Influence of strain-induced martensitic transformation on fatigue short crack behaviour in an austenitic stainless steel, *Matériaux & Techniques*, 5-6, 57-64.
3. **Beese A.M, Mohr D.** (2011), Effect of stress triaxiality and lode angle on the kinetics of strain-induced austenite-to-martensite transformation, *Acta Materialia,* 59(7), 258-2600.
4. **Besson J., Cailletaud G., Chaboche J.-L., Forest S.** (2010), *Non-Linear Mechanics of Materials*, Springer.
5. **Bonora N.** (1997), A nonlinear CDM model for ductile failure, *Engineering Fracture Mechanics,* 58(1-2), 11-28.
6. **Chaboche, J. (**2008), A review of some plasticity and viscoplasticity constitutive theories, *International Journal of Plasticity,* 24, 1642-1693.
7. **Cherkaoui M., Berveiller M., Lemoine X.** (2000), Couplings between plasticity and martensitic phase transformation: overall behavior of polycrystalline TRIP steels, *International Journal of Plasticity*, 16, 1215-1241.
8. **Cherkaoui M., Berveiller M., Sabar H.** (1998), Micromechanical modeling of martensitic transformation induced plasticity (TRIP) in austenitic single crystals, *International Journal of Plasticity*, 14, 7, 597-628.
9. **Diani J.M, Sabar H., Berveiller M.** (1995), Micromechanical modelling of the transformation induced plasticity (TRIP) phenomenon in steels, *International Journal of Engineering Science*, 33, 1921-1934.
10. **Diani J.M., Parks D.M.** (1998), Effects of strain state on the kinetics of strain induced martensite in steels, *Journal of the Mechanics and Physics of Solids*, 46(9), 1613-1635.

DOI 10.1515/ama-2016-0020

11. **Egner H., Skoczeń B.** (2010), Ductile damage development in two-phase materials applied at cryogenic temperatures, *International Journal of Plasticity,* 26, 488-506.
12. **Egner H., Skoczeń B., Ryś M.** (2015a), Constitutive and numerical modeling of coupled dissipative phenomena in 316L stainless steel at cryogenic temperatures, *International Journal of Plasticity*, 64, 113-133.
13. **Egner H., Skoczeń B., Ryś M.** (2015b), Constitutive modeling of dissipative phenomena in austenitic metastable steels at cryogenic temperatures, *Inelastic Behavior of Materials and Structures Under Monotonic and Cyclic Loading, Advanced Structured Material*s, *57,* Springer International Publishing.
14. **Fischer F.D, Schlögl S.M.** (1995), The influence of material anisotropy on transformation induced plasticity in steel subject to martensitic transformation, *Mechanics of Materials*, 21, 1-23.
15. **Fischer F.D., Reisner G., Werner E., Tanaka K., Cailletaud G., Antretter T.** (2000), A new view on transformation induced plasticity (TRIP), *International Journal of Plasticity,* 16(1-8), 723-748.
16. **Fisher F.D., Reisner G.** (1998), A criterion for the martensitic transformation of a microregion in an elastic-plastic material, *Acta Materialia* 46, 2095-2102.
17. **Garion C., Skoczeń B.** (2003), Combined Model of Strain – Induced Phase Transformation and Orthotropic Damage in Ductile Materials at Cryogenic Temperatures, *International Journal of Damage Mechanics,* 12(4), 331-356.
18. **Hallberg H., Hakansson P., Ristinmaa M.** (2010), Thermo-mechanically coupled model of diffusionless phase transformation in austenitic steel, *International Journal of Solids and Structures,* 47, 1580-1591.
19. **Hallberg H., Hakansson P., Ristinmaa M.** (2007), A constitutive model for the formation of martensite in austenitic steels under large strain plasticity, *International Journal of Plasticity,* 23, 1213-1239.
20. **Heung N.H., Chang G.L, Chang-Seok O., Tae-Ho L., Sung-Joon K.,** (2004), A model for deformation behavior and mechanically induced martensitic transformation of metastable austenitic steel, *Acta Materialia*, 52(17), 5203-5214.
21. **Iwamoto T.** (2004) Multiscale computational simulation of deformation behavior of TRIP steel with growth of martensitic particles in unit cell by asymptotic homogenization method. *International Journal of Plasticity* 20(4-5), 841-869.
22. **Ju J.** (1989), On Energy – Based Coupled Elastoplastic Damage Theories: Constitutives Modelling and Computational Aspects, *International Journal of Solids and Structures*, 25(7), 803-833.
23. **Kachanov L.M.** (1958), *On rupture time under condition of creep*, Izvestia Akademi Nauk SSSR, Otd. Tekhn. Nauk., No. 8, 26-31 (in Russian).
24. **Kintzel O., Khan S., Mosler J.** (2010), A novel isotropic quasi-brittle damage model applied to LCF analyses of Al2024, *International Journal of Fatigue,* 32, 1984-1959.
25. **Kubler R.F., Berveiller M., Buessler P.** (2011), Semi phenomenological modeling of the behavior of TRIP steels, *International Journal of Plasticity*, 27, 299-327.
26. **Le Pecheur, A.** (2008), *Fatigue thermique d'un acier inoxydable austénitique: influence de l'état de surface par une approche multi-échelles*, PhD Thesis, École Centrale des Arts et Manufactures, École Centrale Paris.
27. **Lemaitre H.** (1992), *A course on damage mechanics.* Springer-Verlag, Berlin and New York.
28. **Levitas V.I., Idesman A.V., Olson G.B.** (1999), Continuum modeling of strain-induced martensitic transformation at shear band intersections, *Acta Materialia* 47(1), 219-233.
29. **Mahnken R., Schneidt A.** (2010), A thermodynamics framework and numerical aspects for transformation-induced plasticity at large strains, *Archives of Applied Mechanics,* 80, 229-253.
30. **Murakami S. (**2012), *Continuum damage mechanics: A continuum mechanics approach to the analysis of damage and fracture*, Springer: Dordrecht, Heidelberg, London, New York.
31. **Narutani T., Olson G.B., Cohen M.** (1982), Constitutive flow relations for austenitic steels during strain-induced martensitic transformation, *Journal de Physique*, Colloque C4, 12, 43, 429-434.
32. **Olson G.B., Cohen M**. (1975) Kinetics of strain-induced martensitic nucleation, *Metallurgical Transactions*, 6A, 791-795.
33. **Rabotnov Yu. N.** (1968), Creep rupture. In: Hetenyi M., Vincenti M. (eds) *Proceedings of applied mechanics conference*. Stanford University. Springer, Berlin, 342-349.
34. **Rabotnov Yu. N.** (1969), *Creep problems in structural members (North-Holland Series in Applied Mathematics and Mechanics).* North-Holland Publishing Company, Amsterdam/London.
35. **Ryś M.** (2014), Constitutive modelling and identification of parameters of 316L stainless steel at cryogenic temperatures, *Acta Mechanica et Automatica,* 8, 3, 136-140.
36. **Ryś M.** (2015), Modeling of damage evolution and martensitic transformation in austenitic steel at cryogenic temperature, *Archive of Mechanical Engineering,* LXII, 4.
37. **Saanouni K.** (1988), *On the cracking analysis of the elastoplastic media by the theory of continuum damage mechanics*, PhD Thesis (in French), Universite de Technologie de Compiegne, France.
38. **Saanouni K.** (2012), *Damage mechanics in metal forming: Advanced modeling and numerical simulation*, ISTE/Wiley, London.
39. **Saanouni K., Forster C., Ben Hatira F.** (1994) On the anelastic flow with damage, *International Journal of Damage Mechanics*, 3, 140–169.
40. **Santacreu P.O., Glez J.C., Chinouilh G., Frohlich T. (**2006), Behaviour model of austenitic stainless steels for automotive structural parts, *Steel Research International,* 77(9-10), 714.
41. **Skoczeń B., Bielski J., Tabin J.** (2014), Multiaxial constitutive model of discontinuous plastic flow at cryogenic temperatures, *International Journal of Plasticity, 55*, 198-218.
42. **Stolarz J., Baffie N., Magnin T.** (2001), Fatigue short crack behavior in metastable austenitic stainless steels with different grain size, *Materials Science and Engineering A,* 319-321, 521-526.
43. **Stringfellow, R.G., Parks, D.M., Olson, G.B.** (1992) Constitutive model for transformation plasticity accompanying strain-induced martensitic transformations in metastable austenitic steels. *Acta Metallurgica,* 40, 7, 1703-1716
44. **Suiker A.S.J., Turteltaub S.** (2006), Crystalline damage development during martensitic transformation, *European Conference on Computational Fluid Dynamics, ECCOMAS CFD 2006.*
45. **Suiker A.S.J., Turteltaub S.** (2007), Numerical modeling of transformation-induced damage and plasticity in metals. *Modeling and Simulation in Materials Science and Engineering,* 15, 147-166.
46. **Tomita Y, Iwamoto T.** (1995) Constitutive modeling of TRIP steel and its application to the improvement of mechanical properties. *International Journal of Mechanical Sciences,* 37, 1295–1305.
47. **Tomita Y., Iwamoto T.** (2001) Computational prediction of deformation behavior of TRIP steels under cyclic loading. *International Journal of Mechanical Sciences*, 43(9), 2017-2034.
48. **Ziętek G., Mróz Z.** (2011), On the hardening rule for austenite steels accounting for the strain induced martensitic transformation, *International Journal of Structural Changes in Solids,* 3, 3, 21-34.

Acknowledgments: This work has been supported by the National Science Centre through the Grant No 2015/17/N/ST8/01169 and UMO-2013/11/B/ST8/00332.

DE GRUYTER
OPEN

DOI 10.1515/ama-2016-0021 acta mechanica et automatica, vol.10 no.2 (2016)

TRANSIENT VIBRATIONS OF AN ELASTIC CYLINDER INSERTED IN THE ELASTIC MEDIUM

Heorgij SULYM[*], Imre TIMAR[**], Ihor TURCHYN[***]

[*]Faculty of Mechanical Engineering, Bialystok University of Technology, Wiejska Str., 45C, 15-351 Bialystok, Poland
[**]Faculty of Engineering, University of Pannonia, Egyetem str., 10, H-8200 Veszprem, Hungary
[***]Pidstryhach IAPMM, NANU, Naukova str., 3b, 79060 Lviv, Ukraine

sulym@pb.edu.pl, timari@almos.vein.hu, ihorturchyn@gmail.com

received 4 May 2015, revised 11 May 2016, accepted 16 May 2016

Abstract: Using method of Laguerre polynomials we have obtained the solution of the dynamic problem of the theory of elasticity for elastic cylinder inserted into massive body modeled as a space. The source of non-stationary processes in composite is high intensity force load of the inner surface of the cylinder. On the surface separation of materials of space and cylinder the conditions of ideal mechanical contact are satisfied. The solution is obtained as series of Laguerre polynomials, which coefficients are found from recurrent relations. The results of numerical analysis of transient stress-strain state in elastic space with cylindrical insertion might be used for the technological process of hydraulic fracturing during shale gas extraction.

Key words: Transient Wave Propagation, Nongomogeneous Medium, Analytical Solution, Laguerre Polynomials

1. INTRODUCTION

The common tendency of the development of modern technology and engineering is the elaboration and wide usage of new structural materials. Some of the most perspective new materials are composite materials, that are characterized by sheeting and significant discrepancy between mechanical features of structural sheets.

One of the most common methods of research of mechanical fields in composite bodies and spaces is homogenization of their features with further research of their behaviour as hypothetically homogeneous structures. With such approach we can simplify the general problem definition and use well-known methods of research of mechanical fields in homogeneous bodies. Still, using this approach we very often cannot authentically define qualitative and quantitative features of the processes in the very composite that are caused by its nonhomogeneity (Theotokoglou and Stampouloglou, 2008; Zhang and Hasebe, 1999).

The other approach in which an internal nonhomogeneity and interaction between separate parts of the composite are taken into account causes a consideration of separate problems for each composite element with further regard for their contact conditions (de Monte, 2006; Yin and Yue, 2002). Within this approach it is possible to account the real stress-strain state in every layer and define some peculiar features of the transformation of mechanical fields on the section surfaces. In case of flat-layered or sphere-layered body for solving the received problems the Laplace integral transform was successfully used (Liu and Qu, 1998, Sulym et al., 2013, Wang et al., 2002). However, for inhomogeneous cylindrical bodies the direct usage of this transformation creates great difficulties of the transition from transforms to originals (Lu, et al., 2006). Specially, it is about the cases when a cylinder is inserted in elastic space – because of the phenomenon of vibration damping we need to find complex roots of the complicated transcendental equation. Therefore, a lot of authors use either numerical methods of inversion of the Laplace integral transform (Dai and Wang, 2005;) or direct numerical methods (Onyshko and Senyuk, 2009; Savruk et al., 2008; Sladek et al., 2008).

This research aims at the elaboration of analytical method of finding the solution to dynamic axisymmetric problems of the theory of elasticity for cylinder included in elastic space, the investigation of transient stress-strain state in elastic space with cylindrical insertion, caused by impact load of its boundary surface. Method of solution based on the use to the problem of Laguerre integral transformation (Sulym and Turchyn, 2012; Turchyn and Turchyn, 2013).

2. PROBLEM FORMULATION

Now we consider the dynamic problem of the theory of elasticity for inserted into elastic space of cylinder with excellent mechanical properties of the medium (Fig. 1).

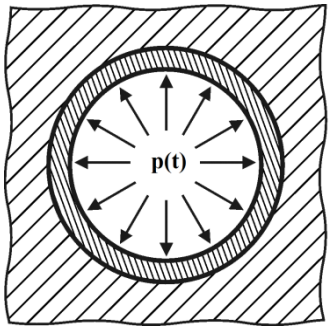

Fig. 1. Scheme of the problem

DOI 10.1515/ama-2016-0021

The source of non-stationary processes in composite is high intensity force load of the inner surface of the cylinder.

In order to identify the stress and strain field in the composite, assuming that on the surfaces of cylinder and elastic medium conditions of ideal mechanical contact are true, we should find the solution to the initial-boundary problem:

$$\rho^{-1}\partial_\rho(\rho\partial_\rho u^{(i)}) - \rho^{-2}u^{(i)} - \tilde{c}_i^2\partial_\tau^2 u^{(i)} = 0, \quad i = 1,2; \quad (1)$$

$$\sigma_{\rho\rho}^{(1)} = -p^*(\tau), \ \rho = \rho_0; \ \ u^{(2)} = 0, \ \rho \to \infty; \quad (2)$$

$$u^{(1)} = u^{(2)}, \ \sigma_{\rho\rho}^{(1)} = \sigma_{\rho\rho}^{(2)} \ \ \rho = 1; \quad (3)$$

$$u^{(i)} = \partial_\tau u^{(i)} = 0, \ \ \tau = 0, \ \ i = 1,2, \quad (4)$$

where: $\rho = r/R_1$ – non-dimensional radial variable of the cylindrical coordinate system; $\mathrm{R}_0, \mathrm{R}_1$ – accordingly, radiuses of the inner and the external surface of the cylinder, $u^{(i)}(\rho,\tau)$ – displacment to the radial motion ($i = 1$ – in cylinder, $i = 2$ – in elastic medium; $\tilde{c}_i = \frac{c_1}{c_{i,1}}$, $\tau = \frac{c_1 t}{R_1}$ – non-dimensional time; $c_{i,1}$ – the longitudinal waves propagation velocities in the material of cylinder other elastic medium; $\sigma_{\rho\rho}^{(i)}(\rho,\tau)$ – radial stresses in the cylinder other elastic medium, that are determined by Hook's law:

$$\sigma_{\rho\rho}^{(i)} = \mu_i\left[\kappa_i^2\partial_\rho u^{(i)} + (\kappa_i^2 - 2)\frac{u^{(i)}}{\rho}\right], \quad (5)$$

where: $\kappa_i^2 = \frac{\lambda_i + 2\mu_i}{\mu_i}$; λ_i, μ_i – elastic constants.

3. SOLUTION OF THE PROBLEM

We will search for the problem (1)-(4) solution in the class of functions that belong to the space $L_2(0,\infty; \ \ \lambda exp(-\lambda\tau))$, i.e. for which the condition:

$$\left\|u^{(i)}(\rho,\tau)\right\|^2 = \lambda\int_0^\infty exp(-\lambda\tau)\left|u^{(i)}(\rho,\tau)\right|^2 d\tau < \infty$$

is true, where $\lambda > 0$ some number (scaled multiplier). Then, the functions $u^{(i)}(\rho,\tau)$ can be showed as a series of Laguerre polynomials:

$$u^{(i)}(\rho,\tau) = \lambda\sum_{n=0}^\infty u_n^{(i)}(\rho)L_n(\lambda\tau), \quad (6)$$

where:

$$u_n^{(i)}(\rho) = \int_0^\infty exp(-\lambda\tau)\, u^{(i)}(\rho,\tau)L_n(\lambda\tau)d\tau\,, \quad (7)$$

and $\mathrm{L_n}(\lambda\tau)$ – Laguerre polynomials.

Further we will consider the formula (7) as integral transform of the function, and a series (6) – as the inversion formula of this transform.

Now we multiply the equation (1) on the conversion core $exp(-\lambda\tau)L_n(\lambda\tau)$ and integrate the obtained expression according the variable τ in the interval $[0, \ \infty)$. Accounting the equation (7) and the initial conditions (4), after the integration by parts we will obtain:

$$\rho^{-1}d_\rho(\rho d_\rho u_n^{(i)}) - \rho^{-2}u_n^{(i)} - \omega_i^2 u_n^{(i)} = \\ = \omega_i^2\sum_{m=0}^{n-1}(n-m+1)u_m^{(i)}, \ \ i = 1,2\,; \quad (8)$$

$$\sigma_{\rho\rho,n}^{(1)} = -p_n^*, \ \rho = \rho_0, \ u_n^{(2)} = 0, \ \rho \to \infty; \quad (9)$$

$$u_n^{(1)} = u_n^{(2)}, \ \sigma_{\rho\rho,n}^{(1)} = \sigma_{\rho\rho,n}^{(2)}, \rho = 1, \quad (10)$$

where $\omega_i = \lambda\tilde{c}_i$.

The solution to the triangular sequence of ordinary differential equations can be written as on algebraically convolution:

$$u_n^{(i)}(\rho) = \sum_{j=0}^n\left[C_{n-j}^{(i)}G_j(\omega_i\rho) + D_{n-j}^{(i)}W_j(\omega_i\rho)\right]. \quad (11)$$

Here are linearly independent fundamental solutions of the sequence (8), which we can represent as:

$$G_j(x) = \sum_{p=0}^{j} a_{j,p}\frac{(x)^p}{2^p p!}\mathrm{I}_{p+1}(x);$$
$$W_j(x) = \sum_{p=0}^{j} a_{j,p}\frac{(-x)^p}{2^p p!}\mathrm{K}_{p+1}(x), \quad (12)$$

where: $I_p(x)$ and $K_p(x)$ – Bessel's modified functions, and coefficients $\mathrm{a_{j,p}}$ satisfy recurrence relations:

$$a_{j,p+1} = \sum_{k=p}^{j-1}(j-k+1)a_{k,p}, \quad (13)$$
$$j = 1,2,\ldots, \ p = \overline{0,j-1}.$$

Accounting the conditions on infinity (2) and a view of fundamental solutions (12), we obtain that:

$$C_j^{(2)} \equiv 0, \ \ j = 0,1,2,\ldots. \quad (14)$$

The direct solutions stuffing (11) into conditions (9)-(10) leads to correlations, which after some transformations can be represented as recurrent sequences of systems of linear algebraic equations:

$$\begin{pmatrix} b_{1,1} & b_{1,2} & 0 \\ b_{2,1} & b_{2,2} & b_{2,3} \\ b_{3,1} & b_{3,2} & b_{3,3} \end{pmatrix}\begin{pmatrix} C_n^{(1)} \\ D_n^{(1)} \\ D_n^{(2)} \end{pmatrix} = \begin{pmatrix} H_{n,1} \\ H_{n,2} \\ H_{n,3} \end{pmatrix}, \quad (15)$$

where:

$$b_{1,1} = \kappa_1^2\omega_1 I_0(\omega_1\rho_0) - \frac{2}{\rho_0}I_1(\omega_1\rho_0); \ b_{1,2} = -\kappa_1^2\omega_1 K_0(\omega_1\rho_0) - \frac{2}{\rho_0}K_1(\omega_1\rho_0); \ b_{2,1} = I_1(\omega_1); \ b_{2,2} = K_1(\omega_1); \ b_{2,3} = -K_1(\omega_2);$$

$$b_{3,1} = \kappa_1^2\omega_1 I_0(\omega_1) - 2I_1(\omega_1); \ b_{3,2} = -\kappa_1^2\omega_1 K_0(\omega_1) - 2K_1(\omega_1); \ b_{3,3} = \tilde{\mu}_2\left(\kappa_2^2\omega_2 K_0(\omega_2) + 2K_1(\omega_2)\right), \ \tilde{\mu}_2 = \mu_2/\mu_1;.$$

$$H_{1,n} = -\frac{p_n}{\mu_1} - \sum_{j=1}^n C_{n-j}^{(1)}\left[\kappa_1^2 G_j'(\omega_1\rho_0) + (\kappa_1^2 - 2)G_j(\omega_1\rho_0)\right] - \sum_{j=1}^n D_{n-j}^{(1)}\left[\kappa_1^2 W_j'(\omega_1\rho_0) + (\kappa_1^2 - 2)W_j(\omega_1\rho_0)\right];$$

$$H_{2,n} = \sum_{j=1}^n\left[D_{n-j}^{(2)}W_j(\omega_2) - C_{n-j}^{(1)}G_j(\omega_1) - D_{n-j}^{(1)}W_j(\omega_1)\right]; \ H_{3,n} = \tilde{\mu}_2\sum_{j=1}^n D_{n-j}^{(2)}\left[\kappa_2^2 W_j'(\omega_2) + (\kappa_2^2 - 2)W_j(\omega_2)\right] -$$

$$- \sum_{j=1}^n C_{n-j}^{(1)}\left[\kappa_1^2 G_j'(\omega_1) + (\kappa_1^2 - 2)G_j(\omega_1)\right] - \sum_{j=1}^n D_{n-j}^{(1)}\left[\kappa_1^2 W_j'(\omega_1) + (\kappa_1^2 - 2)W_j(\omega_1)\right],$$

DOI 10.1515/ama-2016-0021

$$G_j'(\omega_i\rho)=\sum_{p=0}^{j}a_{j,p}\frac{(\omega_i\rho)^p}{2^p p!}\left[\omega_i I_p(\omega_i\rho)-\frac{I_{p+1}(\omega_i\rho)}{\rho}\right],\ W_j'(\omega_i\rho)=\sum_{p=0}^{j}a_{j,p}\frac{(-\omega_i\rho)^p}{2^p p!}\left[-\omega_i K_p(\omega_i\rho)-\frac{K_{p+1}(\omega_i\rho)}{\rho}\right]$$

From (15) obtain the recurrent solution:

$$D_n^{(2)}=\frac{(H_{n,1}b_{2,1}-H_{n,2}b_{1,1})(b_{1,2}b_{3,1}-b_{3,2}b_{1,1})-(H_{n,1}b_{3,1}-H_{n,3}b_{1,1})(b_{1,2}b_{2,1}-b_{2,2}b_{1,1})}{b_{1,1}\{b_{2,3}(b_{3,2}b_{1,1}-b_{1,2}b_{3,1})+b_{3,3}(b_{1,2}b_{2,1}-b_{2,2}b_{1,1})\}};\ D_n^{(1)}=\frac{H_{n,1}b_{2,1}-H_{n,2}b_{1,1}+b_{2,3}b_{2,1}D_n^{(2)}}{b_{1,2}b_{2,1}-b_{2,2}b_{1,1}};$$
$$C_n^{(1)}=\frac{H_{n,1}-b_{1,2}D_n^{(1)}}{b_{1,1}},\quad n=0,1,2,\ldots. \tag{16}$$

Having gradually defined with the help of recurrent solutions (16) all $C_{n-j}^{(i)}$, $D_{n-j}^{(i)}$, we will get the final problem solution as:

$$u^{(1)}(\rho,\tau)=\lambda\sum_{n=0}^{\infty}L_n(\lambda\tau)\sum_{j=0}^{n}\left[C_{n-j}^{(1)}G_j(\lambda\rho)+D_{n-j}^{(1)}W_j(\lambda\rho)\right]$$
$$u^{(2)}(\rho,\tau)=\lambda\sum_{n=0}^{\infty}L_n(\lambda\tau)\sum_{j=0}^{n}D_{n-j}^{(2)}W_j(\lambda\tilde{c}_2\rho) \tag{17}$$

Parameter λ serves as the scale multiplier in numerical summation of the series (17).

4. NUMERICAL ANALYSIS

For the purpose of approbation of the received results, a comparative analysis of numerical results obtained from the correlations (17) with known results for a homogeneous cylinder (6) received using the integral Laplace transform, was conducted.

A solution for a homogeneous cylinder can be obtained from the correlations (17) if to consider that the cylinder is in contact with space, constants and density of which are significantly lower than corresponding values of the cylinder material.

For the numerical analysis it was selected a cylinder with a relative radius of the inner surface $\rho_0=0.6$ and $\kappa_1^2=3.5$ which is affected by external load:

$$p^*(\tau)=p^*\times(1-exp(-\tau_0\tau))^2, \tag{18}$$

where p^* – dimensional value (Pa).

Dependance (18) makes it possible to agree well zero initial conditions with boundary ones, and in this case parameter τ_0 determines the time of the external load output on the stationary value.

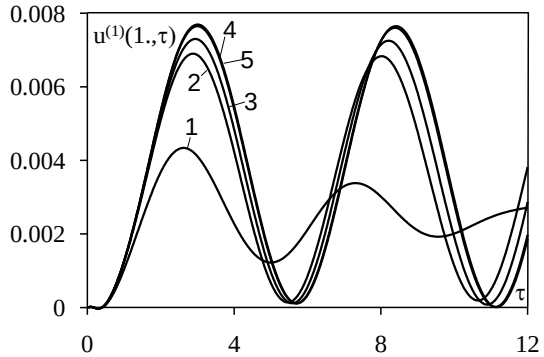

Fig. 2. Displacements the outer surface of the cylinder with different mechanical properties of elastic space

In the Fig. 2 there is the time distribution of dimensionless displacmenents $u^{(1)}(\rho,\tau)$ on the surface $\rho=1$ under $\kappa_2^2=2.5$ and different relative mechanical properties of space: $\tilde{\mu}_2=\tilde{c}_2=0.5,\ 0.1,\ 0.05,\ 0.01,\ 0.005$, correspondingly curves 1, 2, 3, 4, 5. Calculations were performed as $\tau_0=3$ and in the series according to the Laguerre polynomials 60 members were held.

As it is seen, the reduction of relative mechanical properties of the space leads to the increase in the amplitude of oscillation and the termination of the process of wave attenuation that agrees well with the physics of the phenomenon.

The results of calculation obtained for the value when were compared in their turn with the results obtained for a homogeneous cylinder using the Laplace transform (Sneddon, 1951). It was found out, that holding 60 members of the series according to the Laguerre polynomials the relative error between the results received using two methods does not exceed 0.5%.

Using the results obtained for the case of the cylinder and space it was also performed the calculation of the stress-strain state in the thin-walled steel cylinder ($\rho_0=0.9,\ \kappa_1^2=3.5$), inserted into the space of the sandstone ($\kappa_2^2=2.7$, $\tilde{c}_2=0.67$, $\tilde{\mu}_2=0.16$).

In this case it was considered that the load of the cylinder inner surface is a function of the impulsing tupe:

$$p(\tau)=p^*((1-\tau)^2-1)^2,\tau\le 2;\quad p(\tau)=0,\quad \tau>2. \tag{19}$$

In the Fig. 3 there is a time distribution of dimensionless radial stresses $\sigma_\rho=\sigma_{\rho\rho}^{(i)}(\rho,\tau)/p^*$ at different points of the cylinder and space. In this case, given the results of the comparative analysis above 60 members of the series according to the Laguerre polynomials were held.

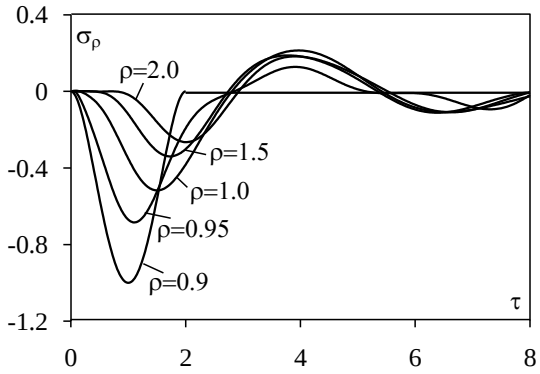

Fig. 3. Time distribution of radial stresses on different surfaces

According to the given results, the specified stresses reach the maximum modulo value on the surface where there is a load. On the division surface of cylinder materials and external space ($\rho=1$) during the load impulse action radial stresses make about 50% of its level and after the time moment $\tau=3$ thay change their sign and quickly attenuate. Approximately the same conclusions can be reached about the radial stresses in the material of the space.

DOI 10.1515/ama-2016-0021

Fig. 4 presents the displacements change at different point of the cylinder for $p^*/\mu_1 = 0.01$.

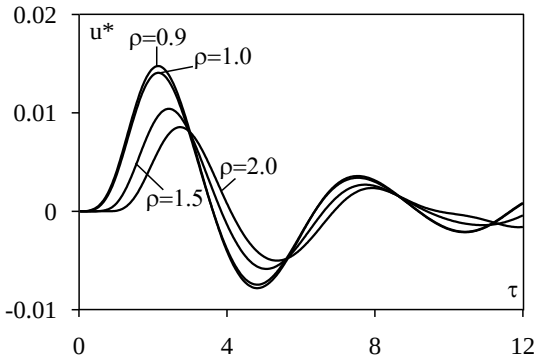

Fig. 4. Time distribution of radial displacements

As it is seen from the above, displacements of two boundary surfaces almost coincide that agrees well with small relative thickness of the cylinder and the malleability of the space.

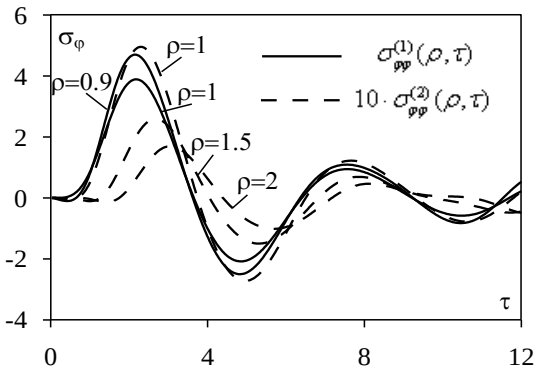

Fig. 5. Time distribution of radial stresses

The results of the calculation of dimensionless circular stresses $\sigma_\phi \equiv \sigma^{(i)}_{\phi\phi}/p^*$ are given presented in Fig. 5. At that stresses acting in the space were magnified 10 times.

According to the given results, circular stresses in the cylinder in absolute value exceed correspondent radial ones almost 5 times. In the space the level of these stresses slumps due to significantly poorer elastic properties of its material. Circular stresses reach the maximum value at the moments of time that follow immediately after the load impulse action termination and qualitatively repeat time distribution of radial displacements.

5. CONCLUSION

The paper proposes a new solution of the plane dynamic problem of elasticity theory for a elastic space with cylindrical tab. The solution is obtained as series of Laguerre polynomials, which coefficients are found from recurrent relations. The results of numerical analysis of transient stress-strain state in elastic space with cylindrical insertion might be used for the technological process of hydraulic fracturing during shale gas extraction.

REFERENCES

1. **Dai H., Wang X.** (2005), Thermo-electro-elastic transient responses in piezoelectric hollow structures, *International Journal of Solids and Structures,* 42, 1151-1171.
2. **Filippo de Monte** (2006), Multi-layer transient heat conduction using transition time scales, *International Journal of Thermal Science*, 45, 882–892.
3. **Liu G., Qu J.** (1998), Transient Wave Propagation in a Circular Annulus Subjected to Transient Excitation on Its Outer Surface, *Journal of the Acoustical Society of America*, 104, 1210–1220.
4. **Lu X., Tervola P., Viljanen M.** (2006), Transient analytical solution to heat conduction in composite circular cylinder, *International Journal of Heat and Mass Transfer*, 49, 341–348.
5. **Onyshko L.I., Senyuk M.M.** (2009), Stressed state of a hollow two-layer cylinder under dynamic loads, *Material Science*, 45, 55–61.
6. **Savruk M., Onyshko L., Senyuk M.** (2008), A plane dynamic axisymmetric problem for a hollow cylinder, *Materials Science*, 1-9.
7. **Sladek V., Sladek J., Zhang C.** (2008), Computation of stresses in non-homogeneous elastic solids by local integral equation method: a comparative study, *Computational Mechanics*, 41, 827–845.
8. **Sneddon I.** (1951), *Fourier transforms*, McCraw-Hill Book Company, New York.
9. **Sulym H., Hutsaylyuk V., Pasternak Ia., Turchyn I.** (2013), Stress-strain state of an elastic rectangular plate under dynamic load, *Mechanika*, 19, 620–626.
10. **Sulym H., Turchyn I.** (2014), Axisymmetric quasistatic thermal stressed state in a half space with coating, *Journal of Mathematical Science*, 198, 103–117.
11. **Theotokoglou E., Stampouloglou I.** (2008), The radially nonhomogeneous elastic axisymmentric problem, *International Journal of Solids and Structures*, 45, 6535–6552.
12. **Turchyn I., Turchyn O.** (2013), Transient plane waves in multilayered half-space, *Acta Mechanica et Automatica*, 7, 53-57.
13. **Wang X., Lu G., Guillow S.** (2002), Stress wave propagation in orthotropic laminated thick-walled spherical shells, *International Journal of Solids and Structures*, 39, 4027-4037.
14. **Yin X.C., Yue Z.Q.** (2002), Transient plane-strain response of multilayered elastic cylinders to axisymmetric impulse, *Journal of Applied Mechanics*, 69, 825–835.
15. **Zhang X., Hasebe N.** (1999), Elasticity solution for a radially nonhomogeneous hollow cylinder, *Journal of Applied Mechanics*, 66, 598–606.

DE GRUYTER
OPEN

DOI 10.1515/ama-2016-0022 acta mechanica et automatica, vol.10 no.2 (2016)

MODELLING THE MESHING OF CYCLOIDAL GEARS

Jerzy NACHIMOWICZ*, Stanisław RAFAŁOWSKI*

*Bialystok University of Technology, Department of Mechanical Engineering,
Faculty of Mechanical Engineering, ul. Wiejska 45C, 15-351 Białystok, Poland

j.nachimowicz@pb.edu.pl, s.rafalowski90@gmail.com

received 16 June 2015, revised 11 May 2016, accepted 16 May 2016

Abstract: Cycloidal drives belong to the group of planetary gear drives. The article presents the process of modelling a cycloidal gear. The full profile of the planetary gear is determined from the following parameters: ratio of the drive, eccentricity value, the equidistant (ring gear roller radius), epicycloid reduction ratio, roller placement diameter in the ring gear. Joong-Ho Shin's and Soon-Man Kwon's article (Shin and Know, 2006) was used to determine the profile outline of the cycloidal planetary gear lobes. The result was a scatter chart with smooth lines and markers, presenting the full outline of the cycloidal gear.

Key words: Cycloidal Drive, Modelling, Profile, Planetary Gear, Gear

1. INTRODUCTION

Analysis of the function of the cycloidal transmission indicates that it is a rolling transmission, in which all elements move along a circle (Rutkowski, 2014). Because of its specific design, cycloidal gears have many advantages, such as: a wide range single stage reductions (even up to 170), making the drive relatively small, high mechanical efficiency, and silent operation. Moreover, its minimal moment of inertia results in smooth start and allows fast change of movement direction. The drive also has a significant overload capacity and reacts quickly to change of load (Chmurawa, 2002; Bednarczyk, 2014).

Cycloidal gear stands out among all gears with its lower mass, smaller housing and its quietness. These are the advantages in machines that demand high gear ratio. In the current planetary gears, for getting enough reduction, three drive ratios are needed. It leads planetary gears to getting bigger and heavier with every drive ratio added. In cycloidal gears only two drive ratios are needed to get planetary gear reduction with three drive ratios. Moreover, inner clearances helps cycloidal gear to provide super precise movement in machinery.

Due to their advantages, cycloidal drives are becoming increasingly popular in modern industry, and are used in wood processing machines, CNC and machine tool workshops, technical head drives, as well as glass and textile machines.

The gears are also used in robot arm joints, hoists and turntables. However, the development and spread of cycloidal drives is not as dynamic as in the case of other similar devices. This is because constructing cycloidal drives is not an easy task – their design is highly complicated, and so is the technology of curved meshing of planetary gears. Also, producers of machinery which uses these type of drives do not share their designs (Chmuraa, 2002; Siczek and Warda, 2008; Yan and Lai, 2002; Feng and Litvin, 1996; Kabaca, 2013; Bednarczyk, 2013; Blagojevic et al., 2012; Hwang and Hsieh, 2007; Meng et al., 2007; Figliolinii et al., 2013; Sung and Tsai, 1997; Hong-Liu et al., 2013; Wand and Song, 2008).

Therefore, it was necessary to demonstrate the process of modelling a toothed gear with a cycloidal profile.

2. EQUATIONS DESCRIBING THE PROFILE OF A CYCLOIDAL GEAR

Modelling a cycloidal gear is possible with equations (1, 2) presented in an article by Shin and Kwon (2006):

$$\begin{aligned} B_x &= r \cdot cos(\varphi) - q \cdot \cos(\varphi + \Psi) - e \cdot cos(N\varphi) \\ B_y &= -r \cdot sin(\varphi) + q \cdot \sin(\varphi + \Psi) + e \cdot sin(N\varphi) \end{aligned} \quad (1)$$

where: r – distance between the ring gear rollers [mm]; q φ radius of the ring gear roller [mm]; N – number of rollers of the ring gear; e – eccentricity value [mm]; Ψ – contact angle between the roller and the lobe of the cycloid gear [°]; φ – angle between point B and the x axis in the central point of the coordinate system [°].

The contact angle between the roller and the lobe of the cycloid gear is determined from the following equation:

$$\Psi = atan\left[\frac{\sin[(1-N)\varphi]}{\frac{r}{eN} - \cos[(1-N)\varphi]}\right] \quad (2)$$

$(0° \leq \varphi \leq 360°)$

In order to determine the curvature profile of the cycloidal gear, the coordinates of multiple B points must be determined, which form the shape of the gear (Fig. 1). The equations (1, 2) make it possible to determine the coordinates of point b for any angle φ. The precision of the profile depends on the step value of angle φ the smaller the step is, the corresponding shape is more precise. What is characteristic about these equations is that there is always one less lobe of the cycloidal gear than there are rollers in the ring gear.

DOI 10.1515/ama-2016-0022

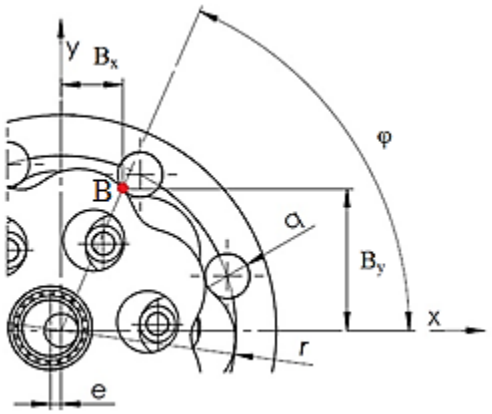

Fig. 1. Cycloidal gear parameters: r – radius of the ring gear; q – radius of the roller; e – eccentricity; φ – angle between point B and the x axis in the central point of the coordinate system; B – point on curvature profile of the lobe; Bx, By – coordinates of point B

3. GENERAL PROFILE OF THE LOBE OF THE CYCLOIDAL GEAR

Fig. 2 presents the outline of the lobe of the cycloidal gear. In order to form the shape of the lobe, the number of points was set at $k = 95$ with coordinates $B = (Bix\,, Biy)$. After determining the positions of all points against the beginning of the coordinate system, the points are connected with a spline.

As the profile of the cycloidal gear must be very precise, two additional points were added at both ends, whose position was determined for adjacent lobes of the gear.

This assumption is presented in equation:

$$\mathrm{w} \in < -2; \mathrm{k} + 3 > \in \mathrm{C} \tag{3}$$

where: w – number of point; k – number of points per each lobe of the gear; C – set of total numbers.

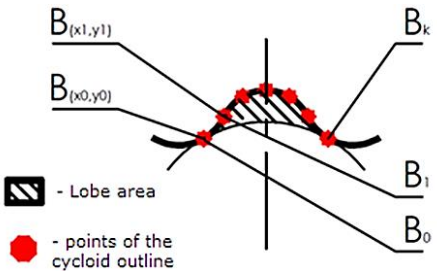

Fig. 2. Lobe profile outline: B_0, B_1, B_k - successive points creating the outline of the lobe; $\mathrm{B}(\mathrm{x}_0, \mathrm{x}_0)$, $\mathrm{B}(\mathrm{x}_1, \mathrm{y}_1)$ – coordinates for points B_0 and B_1 respectively

4. MODELLING THE PROFILE OF THE CYCLOIDAL GEAR

Microsoft Excel was used to make the necessary calculations in order to determine the profile of the cycloidal gear. The spreadsheet presents the basic parameters of a cycloidal drive (Fig. 3), which were then used to determine the additional parameters of the drive with the corresponding equations (Fig. 4).

	A	B	C	D
1	**Basic parameters of the cycloidal drive**			
2	Roller distance in the ring gear r [mm]	Eccentricity value e [mm]	Equidistant q [mm]	Number of lobes z1
3	**43,64**	**2**	**4**	**11**

Fig. 3. Basic parameters of the cycloidal drive required for the calculations

	E	F	G	H	I
1	**Additional parameters of the cycloidal drive**				
2	Q	k	N	reN>1	dφ
3	**24**	**95**	**12**	**1,818333333**	**0,344498**

Fig. 4. Additional parameters of the cycloidal drive required for the calculations

Equation formulas and the values in individual cells are presented in Tab. 1. When designing the profile of the gear, it is necessary to verify the condition necessary for the drive to work (cell H3), which was set for conditional formatting. When the condition is met, the background of the cell is green – when the condition is not met, it is red.

The next stage of the design is the determination of the lobe profile of the cycloidal gear. To do this, Tab. 2 was created in the spreadsheet which determined the coor-dinates of all points comprising the lobe outline of the cycloidal gear.

The first column of the table lists the indexes of the B points which created the profile of the lobe, beginning in cell A19.

The initial value of the index is -2, increased by 1 at each step, and the final value is $k + 2$, which in this case is 97. The second column contains the φ angle values in radians. The next column calculates the Ψ angle corresponding to angle φ. The coordinates of the points creating the profile of the lobe are presented in columns D and E.

Tab. 1. Formulas and their use in the calculations

Cell	E3	F3	G3	H3	I3
Definition	Q factor introduced in Shin and Know (2006), used in the calculations	k number of B points per each lobe of the gear	N number of rollers of the ring gear;	drive's functional condition (Shin and Know, 2006)	$d\varphi$ angle increase
Equation	$Q = e \cdot N$	(assumed value)	$N = z_1 + 1$	$r/(e \cdot N) > 1$	$d\varphi = 360/(z_1 \cdot k)$
Formula	$= B3 \cdot G3$	$= 95$	$= D3 + 1$	$= A3/(B3 \cdot G3)$	$= 360/(D3 \cdot F3)$

DOI 10.1515/ama-2016-0022

Tab. 2. Equation formulas for cycloidal points

	A	B	C	D	E
18	$\boldsymbol{k}$	$\boldsymbol{\varphi}$	$\boldsymbol{\Psi}$	$\boldsymbol{Bx}$	$\boldsymbol{By}$
19	-2	$RADIANS\ (A19 \cdot 0{,}344498$	$ATAN((SIN(-11 \cdot B19))/(1{,}818 - COS(-11 \cdot B19)))$	$43{,}64 \cdot COS(B19) - 4 \cdot COS(B19 + B20) - 2 \cdot COS(12 \cdot B19)$	$-43{,}64 \cdot SIN(B19) + 4 \cdot SIN(B19 + B20) + 2 \cdot SIN(12 \cdot B19)$

Tab. 3. Equation formulas for the full outline

	F	G	H	I	J
18	$\boldsymbol{\varphi}$ [o]	$\boldsymbol{\varphi}$ [rad]	$\boldsymbol{\Psi}$	$\boldsymbol{Bx(\varphi)}$	$\boldsymbol{By(\varphi)}$
19	0,2	$RADIANS(F19)$	$ATAN((SIN(-11 \cdot G19))/(1{,}818 - COS(-11 \cdot G19)))$	$43{,}64 \cdot COS(G19) - 4 \cdot COS(G19 + H19) - 2 \cdot COS(12 \cdot G19)$	$-43{,}64 \cdot SIN(G19) + 4 \cdot SIN(G19 + H19) + 2 \cdot SIN(12 \cdot G19)$

The results of the calculations were put in a scatter chart with smooth lines and markers, presenting the outline of the cycloidal gear lobe (Fig. 5).

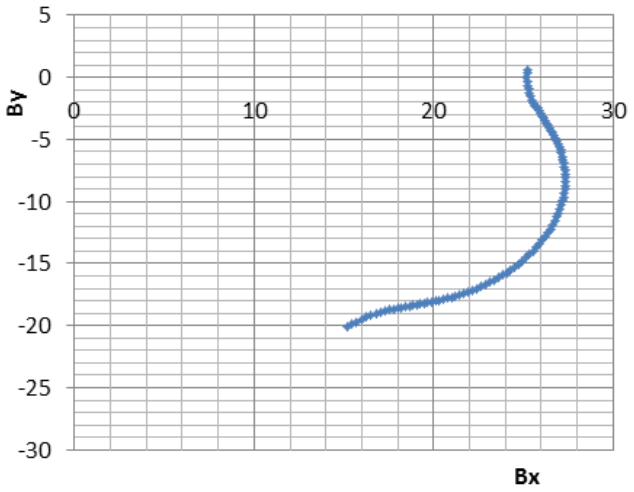

Fig. 5. Lobe profile in a coordinate system

The last stage of designing the cycloidal gear is determining its complete outline. Tab. 3 was created analogously to determining the position of the cycloidal gear lobe. The only difference is that the angle φ (columnt F), expressed in degrees, was used instead of the k point index.

The coordinates of the points on the outline curve were calculated for full 360°. To determine a very accurate contour of the cycloidal gear, the step angle of angle φ was 0.2°. Column G expresses the values from column F in radians. The next column presents the values of angle Ψ for corresponding angles from column G. The values of coordinates $Bx(\varphi)$ and $By(\varphi)$ were calculated and listed in columns I and J respectively.

The results of the calculations were put in a scatter chart with smooth lines and markers, presenting the full outline of the cycloidal gear (Fig. 6).

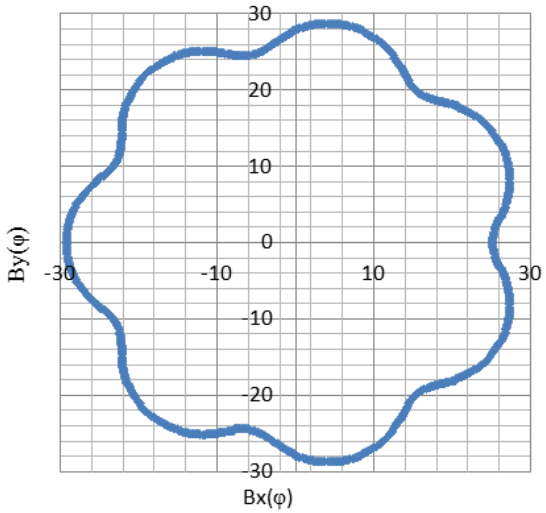

Fig. 6. Full outline of the cycloidal gear

5. CONCLUSIONS

Modelling the full outline of the cycloidal gear significantly facilitates the design process of the cycloidal drive. Because the cycloidal gear is an extremely important element of the drive, the precise outlining of the gear's profile is critical in designing the drive – it decides on the proper and stable functioning of the device.

Designing the profile of the cycloidal gear is complex. Due to the complexity of designing of the profile of the cycloidal gear it is necessary to use suitable spreadsheets, for example Microsoft Excel software or other computer aided engineering program like MathCad, Statistica or other 2D plots generators. After inputting all demanded data and assumptions they help getting adequate calculations. Furthermore, they are helpful in fast changing of parameters in prototypes, which is very comfortable and reduces amount of time needed to designing of cycloidal gear.

The main parameters that determine the profile are the eccentricity value, roller radius, as well as the epicycloid reduction ratio. The precision of the outline depends on the angle step of angle φ. Due to the complexity of the process it is best to do the calculations using computer software.

DOI 10.1515/ama-2016-0022

REFERENCES

1. **Bednarczyk S.** (2013), Cycloidal gear development focused on the transfer of efficiency of the machines, In: Idzikowski A.: *Efficiency of working machines and equipment in the industry*, Press WZ PCz, Czestochowa, 117-225.
2. **Bednarczyk S.** (2014), *Determination of the gear geometry of the of the cyclo gear*, Silesia University of Technology Scientific Notebooks, Gliwice, 29-39.
3. **Blagojevic M., Kocic M., Marjanovic N., Stojanovic B., Dordevic Z., Ivanovic L., Marjanovic V.** (2012), Influence of the friction on the cycloidal speed reducer efficiency, *Journal of the Balkan Tribological Association*, 18(2), 217-227.
4. **Chmurawa M.** (2002), *Cyclo gear meshing with modification*, Silesia University of Technology Scientific Notebooks, Gliwice, No. 1547, 21-39.
5. **Feng P. H., Litvin F. L.** (1996), Computerize design and generation of cycloidal gearing, *Mechanism and Machine Theory*, 31 (7), 891-911.
6. **Figliolinii G., Stachel H., Angeles J.** (2013), On Martin Disteli's spatial cycloidal gearing, *Mechanism and Machine Theory*, 60, 73-89.
7. **Hong-Liu Y., Jin-Hua Y., Xin H., Ping S.** (2013), Study on teeth profile modification of cycloid reducer based on non-Hertz elastic contact analysis, *Mechanics Research Communications*, 48, 87-92.
8. **Hwang Y.-W., Hsieh Ch.-F.** (2007), Determination of surface singularities of a cycliodal gear drive with inner meshing, *Mathematical and Computer Modelling*, 45, 340-354.
9. **Kabaca T.** (2013), A model teaching for the cycloid curves by the use of dynamic software with multiple represention approach, *Academic Journals*, Vol. 6(3), 40-50.
10. **Meng Y., Wu Ch., Ling L.** (2007), Mathematical modeling of the transmision performance of 2K-H pin cycloid planetary mechanism, *Mechanism and Machine Theory*, 42(7), 776-790.
11. **Rutkowski A.** (1986), *Machinery parts*, WSiP, Warsaw, 323-325.
12. **Shin J., Know S.** (2006), On the lobe profile design in a cycloid reducer using instant velocity center, *Mechanism and Machine Theory*, 41(5), 487-616.
13. **Siczek K., Warda B**. (2008), Using of cycloidal gear in car selfstarter, *Journal of KONES Powertrain and Transport*, 15(4), 509-516.
14. **Sung L. M., Tsai Y.C.** (1997), A study on the mathematical models and contact ratios of extended cycloid and cycloid bevel gear sets, *Mechanism and Machine Theory*, 32 (1), 39-50.
15. **Wang W.-S., Fong Z.-H.** (2008), A dual face-hobbing method for the cycloidal crowning of spur gears, *Mechanism and Machine Theory*, 43(11), 1416-1430.
16. **Yan H. S., Lai T. S.** (2002), Geometry design an elementary planetary gear train with cylindrical tooth-profiles, *Mechanism and Machine Theory*, 37(8), 683-686.

DE GRUYTER
OPEN

DOI 10.1515/ama-2016-0023 acta mechanica et automatica, vol.10 no.2 (2016)

COUPLED STATIC AND DYNAMIC BUCKLING MODELLING OF THIN-WALLED STRUCTURES IN ELASTIC RANGE REVIEW OF SELECTED PROBLEMS

Zbigniew KOŁAKOWSKI*, Andrzej TETER**

*Department of Strength of Materials, K12, Lodz University of Technology, ul. Stefanowskiego 1/15, 94-024 Lodz, Poland
**Department of Applied Mechanics, Lublin University of Technology, ul. Nadbystrzycka 36, 20-618 Lublin, Poland

zbigniew.kolakowski@p.lodz.pl, a.teter@pollub.pl

received 30 September 2015, revised 12 May 2016, accepted 17 May 2016

Abstract: A review of papers that investigate the static and dynamic coupled buckling and post-buckling behaviour of thin-walled structures is carried out. The problem of static coupled buckling is sufficiently well-recognized. The analysis of dynamic interactive buckling is limited in practice to columns, single plates and shells. The applications of finite element method (FEM) or/and analytical-numerical method (ANM) to solve interaction buckling problems are on-going. In Poland, the team of scientists from the Department of Strength of Materials, Lodz University of Technology and co-workers developed the analytical-numerical method. This method allows to determine static buckling stresses, natural frequencies, coefficients of the equation describing the post-buckling equilibrium path and dynamic response of the plate structure subjected to compression load and/or bending moment. Using the dynamic buckling criteria, it is possible to determine the dynamic critical load. They presented a lot of interesting results for problems of the static and dynamic coupled buckling of thin-walled plate structures with complex shapes of cross-sections, including an interaction of component plates. The most important advantage of presented analytical-numerical method is that it enables to describe all buckling modes and the post-buckling behaviours of thin-walled columns made of different materials. Thin isotropic, orthotropic or laminate structures were considered.

Key words: Interaction, Buckling, Thin-Walled Structures, FEM, Analytical-Numerical Method, Review

1. COUPLED BUCKLING OF THIN-WALLED STRUCTURES

The theory of coupled or interactive buckling of thin walled structures has been already developed widely for over sixty years. Thin-walled structures, especially plates, columns and beams, have many different buckling modes that vary in quantitative and qualitative aspects. In these cases, nonlinear buckling theory should describe all buckling modes from global (i.e., flexural, flexural-torsional, lateral, distortional and their combinations) to local and the coupled buckling as well as the determination of their load carrying capacity taking into consideration the structure imperfection. Coupling between modes occur for columns of such length where two or more eigenvalues loads of a structure are nearly identical (Fig. 1). The local buckling takes place for the short columns. On the other hand, the long columns are subject to global buckling.

The concept of coupled or interactive buckling involves the general asymptotic nonlinear theory of stability. Among all versions of the general nonlinear theory, the Koiter theory of conservative systems (Koiter, 1976; van der Heijden, 2009) is the most popular one, owing to its general character and development, even more so after Byskov and Hutchinson (1997) formulated it in a convenient way. The details descriptions of this method can be found in the monographs: van der Heijden (2009), Thompson and Hunt (1973) or Kubiak (2013). Applicability of an asymptotic expansion for elastic buckling problems with mode interaction was discussed in many papers, for instance: Tvergaard (1973a, 1973b), Koiter and Pignataro (1974), Byskov (1979, 1988), Sridharan (1983), Benito and Sridharan (1985a, 1985b), Pignataro and Luongo (1985, 1987a, 1987b), Casciaro et al. (1998), Goltermann and Mollman (1989a, 1989b), Garcea et al. (1999, 2009), Barbero et al. (2014).

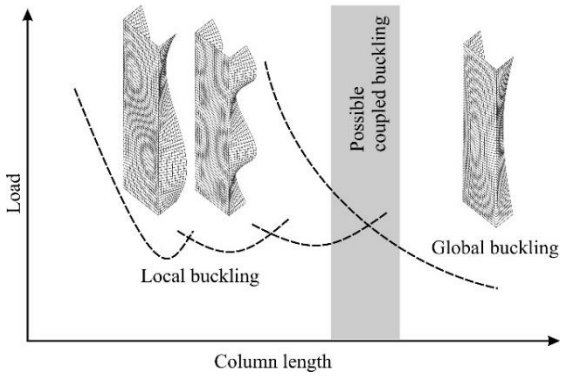

Fig. 1. Buckling modes vs. column length

The theory is based on asymptotic expansions of the post-buckling path and is capable of expanding the potential energy of the system in a series relative to the amplitudes of linear modes near the point of bifurcation. This theory is capable of considering many different buckling modes. The two uncoupled modes are symmetric and stable, but on coincidence they are found to give rise to a symmetric unstable mixed form (Fig. 2). The unstable coupled path will branch off the lower of the two uncoupled paths.

DOI 10.1515/ama-2016-0023

The coupled post-buckling path can be important in continuous systems and it have an important effect on the type of instability which occurs. It enables determination of post-buckling equilibrium paths for the imperfect structure and to determine on them secondary bifurcation points or/and the limit point. If one takes into account the second order approximation, one can determine the limit load capacity of a structure in the elastic range. An assumption of one of the "engineering" hypotheses of load carrying capacity allows for determination of the approximate estimation of load carrying capacity for the elastic-plastic range. This approach provides a lower bound of this load carrying capacity.

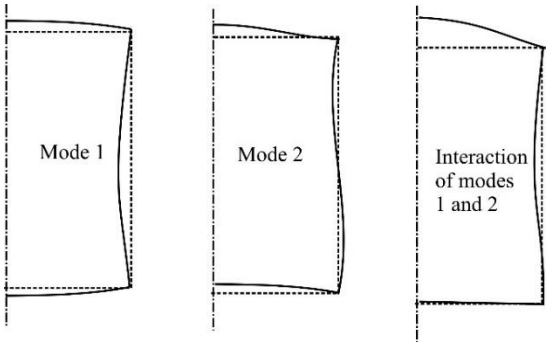

Fig. 2. Coupled buckling of two modes (view of cross sections) (Sridharan, 1983)

Although the problem of static coupled buckling can be treated as sufficiently well-recognized. Many scientists dealt with this problem, for instance: Sridharan and co-workers (1983, 1985a, 1985b, 1985c, 1986, 1988), Goltermann and Mollman (1989a, 1989b), Manevich (1981, 1982, 1985, 1988), Kolakowski (1987a, 1987b, 1988, 1989a, 1989b, 1989c, 1993a, 1993b, 1996).

The numerical calculations carried out by Kolakowski (1987a, 1987b, 1988, 1989a, 1989b, 1989c, 1993a, 1993b, 1996) have proven that the interaction of local modes having considerably different wavelengths is either very weak or does not occur at all. Moreover, one can see that the interaction of two global modes of buckling is very weak or even does not occur at all. According to the assumptions made in Byskov and Hutchinson's (1977) theory, local buckling modes do not interact explicitly. However, the interaction occurs through the interaction of each of them with the global mode. It can be noticed that the global flexural (Euler) buckling can interact with an even number of local modes that are symmetric or antisymmetric but the global flexural-torsional mode only with pairs of symmetric and antisymmetric modes. In some cases, an improper selection of the mode, even if a few of them are considered, may lead to an overestimation of the structure load carrying capacity; also the consideration of the two-mode approach may sometimes be misleading and yield false conclusions. This can be accomplished only by means of a non-linear analysis. The consideration of displacements and load components in the middle surface of walls within the first order approximation and precise geometrical relationships enabled the analysis of all possible buckling modes, including a mixed buckling. In thin-walled structures of open cross-sections, owning to their low rigidity, it is necessary to consider distortional deformations. The above factors have even led to the consideration of an interaction of a few modes - two global and some local ones. If the analysis of the stability problem of thin-walled structures is restricted to the first order approximation, where the theoretical limit load is always lower than the minimum value of the bifurcational load in the linear analysis, the imperfection sensitivity can only be obtained. The determination of the post-buckling equilibrium path requires the second order approximation to be taken into account. The structures where the local buckling precedes the global one are widely used because these perfect structures can carry a load higher than that referring to the bifurcation value of the local buckling. Therefore, it is necessary to consider the second order approximation, that is to say, the fourth order components of the potential energy. In general, the stability analysis with regard to the second non-linear approximation requires the solution of boundary value problems: for the second order global, local and mixed modes.

The analysis of dynamic interactive buckling is limited in practice single plates and shells. There are known the solutions of dynamic buckling problem for columns (Budiansky, 1966a; 1966b). But there are not many solutions for plate model of thin-walled structures (Sridharan, 1984; Kolakowski, 2007; Kolakowski and Kubiak, 2007; Kubiak, 2007; Teter, 2007, 2010, 2011, Teter and Kolakowski, 2013).

Dynamic buckling or dynamic response can be treated as a reinforcement of imperfections, initial displacements or stresses in the structure through dynamic loading in such a manner that a level of the dynamic response becomes very high (Ari-Gur and Simonetta, 1997; Lindberg, 1987; Strogne, 2000). For dynamic buckling of a perfect structure due to a pulse loading, there is no exact counterpart of the static characteristic bifurcation load. When the load is low, the thin-walled structure vibrates around the static equilibrium position. On the other hand, when the load is sufficiently high, then the structure can vibrate very strongly or can move divergently, which is caused by dynamic buckling. One should not confuse this case with vibration buckling where the loads are periodic and the transverse vibration becomes unacceptably large at critical combinations of amplitude, load frequency and damping. In this case one can get parametric resonance or ordinary resonance (Lindberg, 1987; Strogne, 2000; Simitses, 1990, 2006; Virgin, 2007; Warminski and Teter, 2012).

Chapters of monographs by Simitses (1990, 2006) and Virgin (2007) deals with the response of structures subjected to oscillating loads, leading to, so-called, vibration buckling. The periodically changing load produces periodically changing coefficients in the mathematical model. Then, in certain frequency intervals, the trivial solution loses its stability and, the parametric resonance occurs. In such a case transverse vibrations become unacceptably large at critical combinations of amplitude, load frequency and damping. The most essential and dangerous, from the practical point of view, is the principal parametric resonance. This phenomenon appears for sufficiently small values of the axial force, when the loading frequency equals twice the natural bending frequency of the system (the column in our case). Apart from the principal also case the fundamental resonances may also appear, when the loading frequency coincides with the natural bending frequency of the column. Moreover the secondary parametric resonances may also occur. So, vibration buckling corresponds to the buckling resulting from parametric excitations. In paper by Warminski and Teter (2012), the authors deals with aspects of the dynamic behaviour of thin-walled composite column under compression load, composed of static and periodic parts. The mathematical model of the structure considers geometrical nonlinear terms which couple considered global and local buckling modes of the column. The dynamic response is investigated around the principal parametric resonances.

DOI 10.1515/ama-2016-0023

In the analysis of dynamic stability of the thin walled structure under in-plane pulse loading, the following should be taken into account: shape of pulse loading, pulse duration and a magnitude of its amplitude (Kubiak, 2013; Lindberg, 1987; Strogne, 2000; Simitses, 1990, 2006; Bangash, 2009). The rectangular pulse is the most dangers (Kubiak, 2013). If the pulse duration is comparable to the period of natural vibrations, the dynamic pulse buckling occurs. If the pulse duration is longer, the problem becomes quasi-static. When the displacement growth is assessed with time for different amplitude of load, buckling occurs when the dynamic load reaches a critical value associated with a maximum acceptable deformation (strain) or stress, the magnitudes of which are defined arbitrarily. Thus, there is no perfect criterion so far for dynamic buckling and no general guidelines for the design. In the literature on this problem, various criteria concerning dynamic stability have been adopted (Kubiak, 2013; Simitses, 1990). One of the simplest is the criterion suggested by Volmir (Kubiak, 2013; Volmir, 1972).

Volmir (1972) analyzed the behaviour of a simply supported rectangular plate subjected to different pulse loads. He considered the buckling problem which can be described by a system with one degree of freedom and defined the Dynamic Load Factor as a ratio of the pulse amplitude of the critical load to the static critical load. Volmir proposed a criterion for the dynamic buckling, assuming that a loss of stability of the plate subjected to pulse load occurs when the maximum deflection of the plate is equal to the assumed constant value. Usually the critical deflection value was assumed to be equal to the thickness of the plate or half of its thickness.

The most widely used is the Budiansky-Hutchinson's criterion (Budiansky, 1966a; 1966b; Hutchinson and Budiansky, 1966), in which it is assumed that the loss of dynamic stability occurs when the displacement rate is the highest for a certain force amplitude. A dynamic load factor DLF has been defined as the quotient of the dynamic load amplitude and minimum critical stress (Kappos, 2002; Weller et al., 1989). In order to find the critical value of dynamic load factor DLFcr one should draw a graph of deflection amplitude as a function of dynamic load factor DLF (Fig. 3).

The equations of motion are solved for various load parameters to obtain the response of the system. When the motion of the system changes from small-amplitude oscillatory to large-amplitude oscillatory or becomes associated with distinctly removed positions from the undisturbed ones, the corresponding load parameter is called a dynamic critical load. Its disadvantage is an extremely large amount of computer time required to solve the equations of motion at different levels of the applied loads. In the case of uncoupled dynamic buckling, the curves suiting global modes in this graph are always unrestricted (Fig. 3b). The critical value of dynamic load factor is read off for the adopted restriction. It is worthy to add, when speaking about the local buckling mode, that in order to find critical value of dynamic load factor one has to find the point of inflection on the curve (Fig. 3a). The Budiansky-Hutchinson's criterion was used at many papers, for instance: Kolakowski and Kubiak (2007), Kubiak (2007), Teter (2007, 2010, 2011), Teter and Kolakowski (2013), Weller (1989), Hsu (1967, 1968), Tamura and Babcock (1975), Gilat and Aboudi (1995), Zhang et al. (2004), Mania (2005), Mania and Kowal-Michalska (2007).

Other criteria: Ari–Gur and Simonetta's criterion, Kleiber–Kotula–Saran criterion, Kubiak criterion, Petry–Fahlbusch criterion, phase plane criterion concept have been discussed in the papers (Ari-Gur and Simonetta, 1997; Petry and Fahlbusch, 2000; Cui et al., 1999, 2002) and the monograph (Kubiak, 2013).

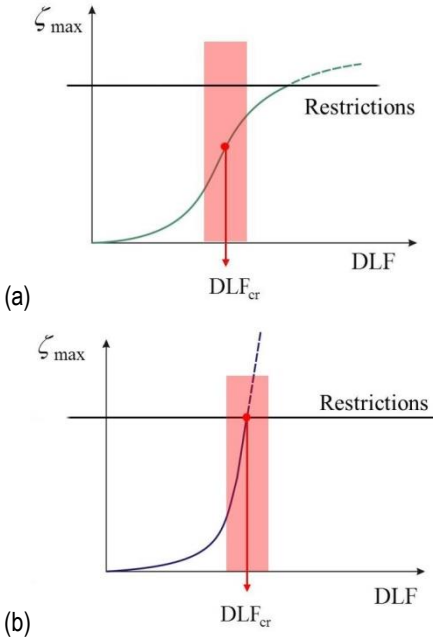

Fig. 3. The graphs of the dimensionless amplitude of deflection as a function of dynamic load factor DLF

Ari-Gur and Simonetta (1997) proposed four criteria. In this case, the dynamic buckling load was set as depending on deflection of the plate and load intensity defined as the force pulse amplitude or the shortening. They noted that for a perfectly plate, the pulse load, which would result in a loss of stability, was infinitely large.

A diversity of dynamic stability loss criteria follows from a lack of a generally accepted, accurate, explicit mathematical definition. One of a few exceptions, known to the authors, is the quasi-bifurcation criterion of dynamic buckling for step-like load (Heaviside's function) and the one concerning the critical pulse duration (so-called: the Kleiber-Kotula-Saran criterion (Kleiber et al., 1987)). This criterion was used at same papers: Kolakowski and Kubiak (2007), Kubiak (2007), Teter (2007, 2010, 2011), Teter and Kolakowski (2013). The latter criterion is based on a condition, that the tangent matrix of the system stiffness is zero. That is to say, all the Jacobian matrix are equal to zero.

Kubiak (2007, 2013) checked the values of the characteristic roots of the Jacobi matrix and proposed the dynamic buckling criterion that at the tracking time, the maximal radius calculated from the characteristic root of the Jacobi matrix was equal or greater than unity in the complex plane.

In the analysis of vibration the phase plane concept is often applied. Practically, the method of phase plane isn't used in the dynamic buckling. One can find only a few papers: Teter (2007, 2010, 2011), Hutchinson and Budiansky (1966), Hsu, (1967, 1968), Schokker et al. (1996) and monograph by Bazant and Cedolin (2010), which made use of the phase plane to determine the dynamic buckling load as an unbounded response for the uncoupled buckling. In the case of multimode buckling the method of phase plane was used in papers: Teter (2007, 2010, 2011), Teter and Kolakowski (2013). The phase plane criterion is formulated as: the dynamic buckling load for the tracing time of solutions has been defined as the minimum value of the pulse

Zbigniew Kołakowski, Andrzej Teter DOI 10.1515/ama-2016-0023

load, such that the phase portrait is an open curve. One should remember that phase planes for global buckling modes have a form of open and unbounded curves. The phase planes for local buckling modes have a form of open but bounded curve.

Petry and Fahlbusch (2000) were convince that the dynamic buckling load should be based on the stress state analysis. They have formulated the criterion of dynamic buckling as follows: the dynamic response of the structure is stable if the equivalent stress not exceed the assumed limit of stress.

2. METHODS OF SOLUTION

The differential equations of motion can be obtained from the Hamilton's Principle (Sridharan, 1983; Kolakowski and Kubiak, 2007; Kubiak, 2007; Teter, 2007, 2010, 2011, Teter and Kolakowski, 2013; Tamura and Babcock, 1975; Schokker et al., 1996). Basic dimensions of the plate (Fig. 4) are length parallel to the x direction (denote as l), width b (parallel to the y direction). and thickness h (parallel to the z direction).

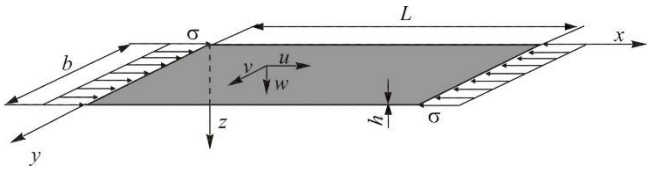

Fig. 4. The plate structure

In this case the Hamilton's Principle can be written as:

$$\delta\Psi = \delta\int_{t_0}^{t_1} \Lambda dt = \delta\int_{t_0}^{t_1}(K-\Pi)dt = 0 \tag{1}$$

where: Λ is a Lagrange's function, K is a kinetic energy, Π is a total potential energy.

The total potential energy is equal to:

$$\begin{aligned}&\Pi = U - W = 0.5\int_{\Omega}\left(\sigma_x\varepsilon_x + \sigma_y\varepsilon_y + \tau_{xy}\gamma_{xy}\right)d\Omega\\&-\{\int_0^b h\ \ [p^0(y)u + \tau_{xy}^0(y)\,v]dy\Big|\ \ {}^{x=\ell}_{x=0} +\\&\int_o^\ell h\ \ [p^0(x)\ \ v + \tau_{xy}^0(x)\ \ u]dx\Big|\ \ {}^{y=b}_{y=0} + \int_S qwdS\}\end{aligned} \tag{2}$$

where: $p^0(x)$, $p^0(y)$, $\tau_{xy}^0(x)$, $\tau_{xy}^0(y)$ are prebuckling in-plane load in the middle surface of the plate, q is transverse load, $\Omega = l\times b\times h = S\times h$ is a volume of the plate and u, v, w are components of the displacement in the x, y, z directions, $\sigma_x, \sigma_y, \sigma_z$ and $\varepsilon_x, \varepsilon_y, \varepsilon_z$ are stress and strain in the x, y, z directions, respectively.

The kinetic energy for the plate can be written as:

$$K = 0.5\int_{\Omega}\rho(\tilde{u}_{,tt}^2 + \tilde{v}_{,tt}^2 + \tilde{w}_{,tt}^2)d\Omega \tag{3}$$

where: ρ is density.

The kinematic conditions are assumed to be:

$$\begin{aligned}&\tilde{u}(x,y,z,t) = u(x,y,t) - zw_{,x}(x,y,t)\\&\tilde{v}(x,y,z,t) = v(x,y,t) - zw_{,y}(x,y,t)\\&\tilde{w}(x,y,z,t) \equiv w(x,y,t)\end{aligned} \tag{4}$$

The energy variation can be written as:

$$\begin{aligned}&\delta\Psi = \delta\int_{t_0}^{t_1}\Lambda dt =\\&\int_{t_0}^{t_1}\int_{\Omega}\rho(\tilde{u}_{,t}\delta\tilde{u}_{,t} + \tilde{v}_{,t}\delta\tilde{v}_{,t} + \tilde{w}_{,t}\delta\tilde{w}_{,t})d\Omega dt +\\&+\int_{t_0}^{t_1}\int_{\Omega}(\sigma_x\delta\varepsilon_x + \sigma_y\delta\varepsilon_y + \tau_{xy}\delta\gamma_{xy})\ \ d\Omega\,dt +\\&-\int_{t_0}^{t_1}\{\int_0^b h\ \ [p^0(y)\delta u + \tau_{xy}^0(y)\,\delta v]\ \ dy\Big|\ \ {}^{x=\ell}_{x=0} +\\&+\int_o^\ell h\ \ [p^0(x)\delta v + \tau_{xy}^0(x)\delta u]\ \ dx\Big|\ \ {}^{y=b}_{y=0} +\\&+\int_S q\delta w dS\}dt = 0\end{aligned} \tag{5}$$

Therese the middle surface strains and curvatures are equal (Fig. 4):

$$\begin{aligned}&\varepsilon_x^b = u_{,x} + \tfrac{1}{2}\ \ (w_{,x}^2 + v_{,x}^2 + u_{,x}^2)\\&\varepsilon_y^b = v_{,y} + \tfrac{1}{2}\ \ (w_{,y}^2 + u_{,y}^2 + v_{,y}^2)\\&2\varepsilon_{xy}^b = \gamma_{xy}^b = u_{,y} + v_{,x} + w_{,x}w_{,y} + u_{,x}u_{,y} + v_{,x}v_{,y}\\&\kappa_x = -w_{,xx}\qquad \kappa_y = -w_{,yy}\qquad \kappa_{xy} = -2w_{,xy}\end{aligned} \tag{6}$$

In the majority of publications devoted to stability of structures, the terms $(v_x^2 + u_x^2)$, $(u_y^2 + v_y^2)$ and $(u_{,x}u_{,y} + v_{,x}v_{,y})$ are neglected for $\varepsilon_x, \varepsilon_y, \gamma_{xy} = 2\varepsilon_{xy}$, respectively, in the strain tensor components, Eqs. (6). When the full tensor of membrane strains: $\varepsilon_{xi}, \varepsilon_{yi}, \gamma_{xy} = 2\varepsilon_{xy}$ is taken into account, then an analysis of all buckling modes can be carried out. The main limitation that results from the adopted theory was the assumption of a linear dependence between the curvatures and the second order derivatives of the displacement w.

The differential equations of motion corresponding to Eqs. (6) for the one plate can be written as follows:

$$\begin{aligned}&N_{x,x} + N_{xy,y} +\\&\{(N_x u_{,x})_{,x} + (N_y u_{,y})_{,y} + (N_{xy}u_{,x})_{,y} + (N_{xy}u_{,y})_{,x}\} +\\&+[-h\rho_0 u_{,tt} + h^2\rho_1 w_{,xtt}] = 0\\&N_{xy,x} + N_{y,y} +\\&\{(N_x v_{,x})_{,x} + (N_y v_{,y})_{,y} + (N_{xy}v_{,x})_{,y} + (N_{xy}v_{,y})_{,x}\} +\\&+[-h\rho_0 v_{,tt} + h^2\rho_1 w_{,ytt}] = 0\\&M_{x,xx} + M_{y,yy} + 2M_{xy,xy} + q +\\&(N_x w_{,x})_{,x} + (N_y w_{,y})_{,y} + (N_{xy}w_{,x})_{,y} +\\&+(N_{xy}w_{,y})_{,x} + [-h\rho_o w_{,tt} - h^2\rho_1(u_{,xtt} + v_{,ytt})\\&+h^3\rho_2(w_{,xxtt} + w_{,yytt})] = 0\end{aligned} \tag{7}$$

In the static case, the dynamic components of Eqs. (7) are neglected.The solution of these equations for each plate should satisfy: initial conditions, kinematic and static continuity conditions at the junctions of adjacent plates and the boundary conditions. The effects of damping can be neglected in practice. Its influence on the dynamic response is not greater than 1%. Kounadis et al. (1997) used a damper in their model and analyzed the damping influence on the dynamic response. The presented solution showed that the difference in the results for the structure with viscous Rayleigh damping and without damping was 0.2%. Additionally, wave propagation and in-plane effects can be neglected in the dynamic buckling study. The non-linear problem of stability has been solved with the asymptotic perturbation method in order to obtain an approximate analytical solution to the equations. The displacement fields and the sectional force fields were expanded in power series in the amplitudes of the buckling modes divided by the thickness of the first component plate. By substituting the

DOI 10.1515/ama-2016-0023

displacement fields and the sectional force fields into the equations of equilibrium, junction conditions and boundary conditions, the boundary value problems of the zero, first and second order can be obtained.

The displacements fields and the sectional force fields were defined as fallowed:

$$\mathbf{U} = \lambda\mathbf{U}^{(0)} + \zeta_i\mathbf{U}^{(i)} + \zeta_i\zeta_j\mathbf{U}^{(ij)} + \zeta_i\zeta_j\zeta_k\mathbf{U}^{(ijk)} + \cdots,$$

$$\mathbf{N} = \lambda\mathbf{U}^{(0)} + \zeta_i\mathbf{U}^{(i)} + \zeta_i\zeta_j\mathbf{U}^{(ij)} + \zeta_i\zeta_j\zeta_k\mathbf{U}^{(ijk)} + \ldots, \qquad (8)$$

The range of indexes was (l, N). The summation was supposed on the repeated indexes.

The differential equations of motion can be written as:

$$\frac{1}{\omega_{or}^2}\zeta_{r,tt}(t) + \left(1 - \frac{\sigma(t)}{\sigma_r}\right)\cdot\zeta_r(t) + a_{ijr}\zeta_i(t)\zeta_j(t) + b_{rrrr}\zeta_r^3(t) + \ldots = \zeta_r^*\frac{\sigma(t)}{\sigma_r} \qquad (9)$$

for $r = 1, \ldots, N$, where: ζ_r – the dimensionless amplitude of the r th buckling mode (the maximum deflection referred to the thickness of the first plate), σ_r, ω_{or}, ζ_r^* – the critical stress, the natural frequency of free vibrations and the dimensionless amplitude of the initial deflection corresponding to the r-th buckling mode, respectively, σ – the compressive stress. The coefficients: a_{ijr}, b_{rrrr} were determined with well-known formulae (see for example: Byskov and Hutchinson (1977), Kubiak (2013), Byskov (1988), Kolakowski et al. (1999), Teter and Kolakowski (2004)).

In Eqs. (9), the omission of the coefficients $\mathrm{b_{ijkr}}$ corresponding to the second order mixed mode was possible, because the post-buckling coefficients a_{ijr} (a three-mode approach) have been already included in the analysis. The secondary local buckling modes were analogous to the second order mixed modes. The admissibility of neglecting the mixed mode has been shown. In the static case, the dynamic components of Eqs. (9) were neglected.

For the ideal structure, the initial imperfections are equal to zero (in Eqs. (9) – $\zeta_r^* = 0$) and for the uncoupled problem, all indexes: i, j, r are equal to 1. The initial conditions were assumed that the no-dimensional displacements and velocities were equal to zero.

The static system of ordinary differential equations of equilibrium was solved by the modified numerical transition matrix method, in which the state vector of the final edge is derived from the state vector of the initial edge by the numerical integration of the differential equations along the circumferential direction formulae by means of the Godunov orthogonalization method. This method has allowed to find the post-buckling coefficients which can be used in description of post-buckling equilibrium path for static load and in Lagrange equations for dynamic load. Having Lagrange equations it's possible to analyze the transient dynamic response of thin-walled structures subjected to pulse loading. What is important using this method one can solve static simultaneous buckling problem as well as the dynamic one (Kubiak, 2013). The static interactive buckling of thin-walled structures have been discussed in the papers Kolakowski and co-workers (1987a, 1987b, 1988, 1989a, 1989b, 1993a, 1993b, 1995, 1996, 1999, 2000, 2002, 2003, 2004, 2005). The thin-walled closed and open (Fig. 5b) cross sections columns with or without stiffeners under compression were considered in detail. The columns were long and prismatic. The both ends were simple supported (Fig. 5a). The structures were composed of rectangular plates interconnected along longitudinal edges. In this case, a plate model was adopted in the analysis (Fig. 5c). The material of the structure was defined as isotropic, orthotropic or laminate.

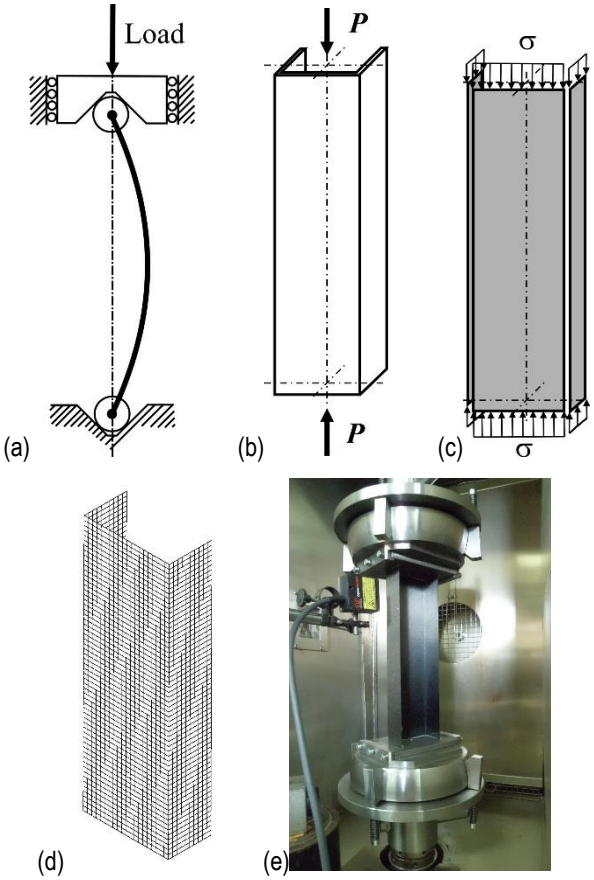

Fig. 5. Modelling of buckling thin-walled structure: (a) physical model; (b) calculation model; (c) ANM model; (d) FEM model; (e) experimental model

In the papers Teter and Kolakowski (2004, 2005), the static interactive buckling of columns with open sections, reinforced with intermediate stiffeners and with edge reinforcements, has been considered. The results discussed in the studies (Teter and Kolakowski, 2004) represent the most important results obtained by the authors in earlier investigations devoted to central intermediate stiffeners. Intermediate stiffeners are widely used in many types of structures. These stiffeners carry a portion of loads and subdivide the plate element into smaller sub-elements, thus increasing considerably the load carrying capacity. The shape, size and position of intermediate stiffeners and edge stiffeners in thin-walled structures exert a strong influence on the stability and the post-buckling behaviour of thin-walled structures. The importance of the minimum rigidity of the intermediate stiffeners required to restrict buckling to the plate elements was studied. The proposed estimation of the structure load carrying capacity for the second order approximation (Teter and Kolakowski, 2005) on the basis of the linear analysis complies with the FEM with the maximum error equaled to 25% in the whole over–critical range of the shortening. The method of determining the value of the frequencies of free vibrations was presented in the paper (Teter and Kolakowski, 2003). The buckling modes were the same as the vibration modes, so the solution to the eigenvalue problem is searched for various values of the r–th harmonic. For the free vibration, the axial load is equal to zero. At the point where the static load parameter reaches its maximum value for the imperfect structure

(secondary bifurcation or limit points), the Jacobian of the non–linear static system was equal to zero.

The problem of interactive dynamic buckling can be solved by means of the Runge-Kutta numerical method with differentiation formulas of variable order. The calculations were carried out for a settled imperfections (Kolakowski and Kubiak, 2007; Kubiak, 2007; Teter, 2007, 2010, 2011, Teter and Kolakowski, 2013; Tamura and Babcock, 1975; Kolakowski, 2009).

Computer codes to determine the post-buckling equilibrium paths within the second order approximation for structures made of isotropic, orthotropic materials, including orthotropy that varies along the plate width, gradient materials have been developed (Kolakowski (1987a, 1987b, 1988, 1989a, 1989b, 1989c, 1993a, 1993b, 1996). The codes has allowed to employ the analytical-numerical method to analyze elastic stability in thin-walled structures simply supported at both ends. Cases of complex loading of the structure and boundary reinforcements and changes in the plate thickness along its width can be analyzed. To extend the computing possibilities of this method, subroutines have been developed for determination of free vibration frequencies of thin-walled structures, taking into consideration all the inertia forces, including tangent and rotational inertia forces (Kolakowski and Kubiak, 2005). The presented analytical-numerical method provides very effective solutions to various types of thin-walled structures and it enables the statics and dynamic analysis of stability. It allows to analyze a dynamic response of complex thin-walled structures subjected to various shapes of the pulse loading and to calculate the critical dynamic buckling value using different dynamic buckling criteria. The analysis of dynamic stability with the analytical-numerical method renders the modal analysis of coupled and uncoupled dynamic buckling of thin-walled structures possible.

In the monograph by Kubiak (2013) has been analyzed a dynamic response of thin-walled structures under pulse loading, obtained with the finite elements method (the so-called: FEM) and, which should be noticed, with the ANM as well. The FEM has been used as a method to verify the calculations conducted with the ANM (Fig. 5c).

An application of finite elements method allows for analysis of nonlinear stability under static and dynamic loads in whole range. In order to analyze the post-buckling behaviour of the structure, calculations should be made in two stages. The linear analysis of buckling should be carried out in the first step in order to determine a few buckling modes that correspond to the lowest values of critical loads, both for local and global modes. Lanczos eigenvalue extraction methods can be used (Kirsch, 2004). In the second step, the non-linear analysis of stability for the model, in which the initial shape imperfections corresponding to the lowest modes of buckling are assumed, should be conducted. In case of the non-linear analysis of interactive buckling, the imperfections in shape corresponding to different buckling modes are assumed. Quite a serious problem lies in determination of the magnitude of imperfections for various modes in such a way that the relation between these imperfections should reflect the effect of one buckling mode on the other one (Kolakowski and Kubiak, 2005). A very important role in obtaining correct results is played by the proper modelling of boundary conditions. Modelling of boundary conditions, which correspond to the conditions assumed in other calculation methods (e.g., analytical models or analytical-numerical ones), is particularly difficult. The structural dynamic analysis using FEM, which has allowed us to find the response of a structure to the pulse loading, has been conducted using the Newmark's formula for the time integration and the Newton-Raphson scheme or arc-length method (Madenci and Guven, 2006; Morris, 2008). The applications of finite element method FEM to solve interaction buckling problems are on-going. FEM proved to be the most successful numerical method to analyze static or dynamic buckling of complex thin-walled structures. Such analyses involve a discretization of the structure and nonlinear solutions of large equation system. This method is very important in practice, because it is becoming standard practice to use FEM in conjunction with experiments in improving and preparing new engineering standards for thin-walled structures. Early 1970s papers (Barsoum and Gallagher, 2009; Powell and Klinger, 1970) described elastic global buckling using beam elements. The bifurcation analysis is described in papers (Rajasekaran and Murray, 1973; Toneff et al., 1987). The FEM plate models using plate or shell elements permitted analyses of coupling between local and global bucking in the elastic range (Bradford, 1990). There is no distinction between the analyses of plate and shell structures. In both case one can use shell elements in geometric and material nonlinear analyses (Lee et al., 1979, 1984; Dvorkin and Bathe, 1984; Fafard et al., 1987; White and Abel, 1990).

The finite element method was used by Bao et al. (1997) to analyze the critical stress for the plates and beam-columns made of anisotropic materials. Barbero and Tomblin (1993) dealt with a loss of global stability of thin-walled I-section beam-columns made of various fibre composites. Authors compared the experimental results with the FEM ones receiving a very good agreement. Gupta and Rao (1985) studied the stability of a thin cantilever beam with a Z-cross-section made of two (45/-45) or three- (0/45/0) layered laminates. The authors employed the finite element method and used two-node beam elements with three degrees of freedom at each node to build a discrete model of the beam under analysis.

Cui et al. (1999, 2002) presented the results of experimental results for rectangular plates with different boundary conditions subjected to pulse load. The authors performed a numerical analysis using the finite element method (Abaqus system). For the numerical analysis, they assumed that the dynamic critical load in the elastic–plastic range increased with an increasing material strengthening curve in the elastic–plastic state.

The experimental investigations on stability of thin-walled structures were presented in papers: Put et al. (1999), Hancock (2003), Kwon et al. (2007), Becque and Rasmusen (2009), Magnucka-Blandzi et al. (2012), Magnucki et al. (2010), Debski (2013). The experimental investigations of stability and carrying capacity if thin-walled box-sections beams (Krolak and Mlotkowski, 1996) and thin-walled multi-cell columns were made by Krolak et al. (2007). The results of FEM calculations have been compared to the theoretical and experimental investigations. Some composite structures were also taken into account (Debski, 2013; Turvey and Zhang, 2006; Wong and Wang, 2007; Parlapalli et al., 2007; Debski et al., 2013a, 2013b). A more experimental papers can be found in review papers: Chou and Rhodes (1997), Singer et al. (1998, 2002), Magnucka-Blandzi et al. (2011). Magnucki with his team (Magnucka-Blandzi and Magnucki, 2011) analyzed global and local stability of cold-formed thin-walled channel beams with open or closed cross-sections. The numerical FEM analysis and the laboratory tests of selected beams were performed. The numerical investigations of the optimization problem have been carried out.

DOI 10.1515/ama-2016-0023

3. FINAL REMARKS

The analytical-numerical method (ANM) provides very effective solutions to various types of thin-walled structures and it enables the dynamic analysis of buckling. It allows one to analyse a dynamic response of complex thin-walled structures subjected to various shapes of the pulse loading and to calculate the critical dynamic buckling value using different dynamic buckling criteria. The analysis of dynamic stability with the analytical-numerical method renders the modal analysis of coupled and uncoupled dynamic buckling of thin-walled structures possible.

The most important advantage of this analytical-numerical method is that it enables to describe a complete range of behaviour of thin-walled structures from all global (i.e., flexural, flexural-torsional, distortional bucklings and their combinations) to the local stability. In the solution obtained, a shear lag phenomenon, an effect of cross-sectional distortions, as well as an interaction between all the walls of structures are included.

Attention should be paid to the fact that the results obtained from the ANM are attained much faster and are less laborious if compared to the results from the FEM, and are characterized by satisfactory accuracy. Due to the application of the FEM, it has been possible to verify the results and moreover, to visualize better the results. Because the results obtained by both the methods are similar, it can be said that the proposed analytical-numerical method yields proper results.

REFERENCES

1. **Ali M.A., Sridharan S.** (1988), A versatile model for interactive buckling of columns and beam-columns, *International Journal of Solids and Structures*, Vol. 24, 481–486.
2. **Ari-Gur J., Simonetta S.R.** (1997), Dynamic pulse buckling of rectangular composite plates, *Composites Part B,* Vol. 28B, 301-308.
3. **Bangash M.Y.H.** (2009), *Shock. impact and explosion,* Structural analysis and design, Springer, Verlag, New York, USA.
4. **Bao G., Jiang W., Roberts J.C.** (1997), Analytic and finite element solutions for bending and buckling of orthotropic rectangular plates, *Int J Solid Struct,* Vol. 34, No. 14, 1797–1822.
5. **Barbero E., Tomblin J.** (1993), Euler buckling of thin-walled composite columns, *Thin-Walled Structures,* Vol. 17, 237–258.
6. **Barbero E.J., Madeo A., Zagari G., Zinno R., Zucco G.** (2014), Koiter asymptotic analysis of folded laminated composite plates, *Composites Part B: Engineering*, Vol.61, 267-274.
7. **Barsoum R.S., Gallagher R.H.** (2009), Finite element analysis of torsional and torsional-flexural stability problems, *Int. Journal for Numerical Methods in Engineering,* Vol. 2, 335-352.
8. **Bazant Z.P., Cedolin L.** (2010), *Stability of Structures. Elastic. Inelastic. Fracture and Damage Theories,* Oxford University Press, UK.
9. **Becque J., Rasmusen K.J.R.** (2009), Experimental investigation of local-overall interaction buckling of stainless steel lipped channel columns, *J. Constructional Steel Research,* Vol. 65, 1677–1684.
10. **Benito R., Sridharan S.** (1985), Mode interaction in thin-walled structural members*, Journal of Structural Mechanics,* Vol. 12, 517-542.
11. **Benito R., Sridharan S.** (1985). Interactive buckling analysis with finite strips*, International Journal for Numerical Methods in Engineering*, Vol. 21,145-161.
12. **Bradford M.A.** (1990), Lateral-distortional buckling of tee-section beams, *Thin-Walled Structures,* Vol. 10, 13-30.
13. **Budiansky B.** (1966), *Dynamic buckling of elastic structures: criteria and estimates*. Report SM-7, NASA CR-66072, USA.
14. **Budiansky B.** (1966), Survey of some buckling problem. *AIAA Journal,* Vol. 4, 1505-1510.
15. **Byskov E.** (1979), Applicability of an asymptotic expansion for elastic buckling problems with mode interaction*, AIAA Journal*, Vol. 17, 630-633.
16. **Byskov E.** (1988), Elastic buckling problem with infinitely many local modes*, Mechanics of Structures and Machines,* Vol. 15, 413-435.
17. **Byskov E., Hutchinson JW.** (1977), Mode interaction in axially stiffened cylindrical shells*, AIAA Journal*, Vol.15, 941-48.
18. **Casciaro R., Garcea G., Attanasio G., Giordano F.** (1998), Pertubative approach to elastic post-buckling analysis*, International Journal of Computer & Structure*, Vol. 66, 585-595.
19. **Chou S.M., Rhodes J.** (1997), Review and compilation of experimental results on thin-walled structures. *Computers & Structures*, Vol. 65 No. 1, 47–67.
20. **Cui S., Cheong H.K., Hao H.** (1999), Experimental study of dynamic buckling of plates under fluid-solid slamming. International *Journal of Impact Engineering,* Vol. 22, 675-691.
21. **Cui S., Hao H., Cheong H.K.** (2002), Theoretical study of dynamic elastic buckling of columns subjected to intermediate velocity impact loads, *International Journal of Mechanical Science,* Vol. 44, 687-702.
22. **Debski H.** (2013), Experimental investigation post-buckling behaviour of composite column with top-hat cross section, *Maintenance and Reliability,* Vol. 2, 105–109.
23. **Debski H., Kubiak T., Teter A.** (2013a), Buckling and postbuckling behaviour of thin-walled composite channel section column", *Composite Structures* Vol. 100, 195-204.
24. **Debski H., Kubiak T., Teter A.** (2013b), Experimental investigation of channel-section composite profiles' behaviour with various sequences of plies subjected to static compression, *Thin-Walled Structures,* Vol. 71, 147–154.
25. **Dvorkin E.N., Bathe KJ.** (1984), A continuum mechanics based four-node shell element for general nonlinear analysis, *Engineering Computations,* Vol. 1, 77-88.
26. **Fafard M., Beauleu D., Dhatt C.** (1987), Buckling of thin-walled members by finite elements, *Computers and Structures,* Vol. 25, 183-190.
27. **Garcea G., Madeo A., Zagari G. and Casciaro R.** (2009), Asymptotic post-buckling FEM analysis using correlational formulation, *International Journal of Solids and Structures,* Vol. 46, 377–397.
28. **Garcea G., Salerno G., Casciaro R.** (1999), Sanitizing of locking in Koiter perturbation analysis through mixed formulation*, Computer Methods in Applied Mechanics and Engineering*, Vol. 180,137-167.
29. **Gilat R., Aboudi J.** (1995), Dynamic buckling of nonlinear resin matrix composite structures, *Composite Structures,* Vol. 32, 81-88.
30. **Goltermann P., Mollman H.** (1989), Interactive buckling in thin-walled beams – II. Applications*, International Journal of Solids and Structures*, Vol. 25, 729-749.
31. **Gupta R.K., Rao K.P.** (1985), Instability of laminated composite thin-walled open-section beams, *Composite Materials,* Vol. 4, 299–313.
32. **Hancock G.J.** (2003), Cold-formed steel structures, *J. Constructional Steel Research,* Vol. 59, 473–487.
33. **Hsu C.S.** (1967), The effects of various parameters on the dynamic stability of shallow arch, *Journal of Applied Mechanics,* Vol. 34, 349-356.
34. **Hsu C.S.** (1968), On dynamic stability of elastic bodies with prescribed initial conditions, *International Journal of Non-Linear Mechanics*, Vol. 4, 1-21.
35. **Hutchinson J.W., Budiansky B**. (1966), Dynamic buckling estimates, *AIAA Journal,* Vol. 4, 525-530.
36. Kappos AJ. Dynamic Loading and Design of Structures, Spon Press, Taylor & Francis Group, 2002.
37. **Kirsch U.** (2004), *Design-oriented Analysis of Structures,* Unified Approach. Kluwer Academic Publishers, USA.
38. **Kleiber M., Kotula W., Saran M.** (1987), Numerical analysis of dynamic quasi-bifurcation, *Engineering Computations* Vol. 4, 48-52.
39. **Koiter WT.** (1976), *General theory of mode interaction in stiffened plate and shell structures*, WTHD Report 590, Delft.

40. **Koiter W.T., Pignataro M.** (1974), *An alternative approach to the interaction between local and overall buckling in stiffened panels*, Buckling of Structures/Proceedings of IUTAM Symposium. Cambridge, 133–148.
41. **Kolakowski Z.** (1987a), Mode interaction in thin-walled trapezoidal column under uniform compression, *Thin-Walled Structures*, Vol. 5, 329-342.
42. **Kolakowski Z.** (1987b), Mode interaction in wide plate with closed section longitudinal stiffeners under compression, *Engineering Transactions,* Vol. 35, 591-609.
43. **Kolakowski Z.** (1988), Some aspects of mode interaction in thin-walled stiffened plate under uniform compression, *Engineering Transactions,* Vol. 36, 167-179.
44. **Kolakowski Z.** (1989a), Interactive buckling of thin-walled beams with open and closed cross-section, *Engineering Transactions,* Vol. 37, 375-397.
45. **Kolakowski Z.** (1989b), Mode interaction in wide plate with angle section longitudinal stiffeners under compression, *Engineering Transactions,* Vol. 37, 117-135.
46. **Kolakowski Z.** (1989c), Some thoughts on mode interaction in thin-walled columns under uniform compression. *Thin-Walled Structures*, Vol. 7, 23-35.
47. **Kolakowski Z.** (1993a), Influence of modification of boundary conditions on load carrying capacity in thin-walled columns in the second order approximation, *International Journal of Solids and Structures*, Vol. 30, 2597-2609.
48. **Kolakowski Z.** (1993b), Interactive buckling of thin-walled beams with open and closed cross-sections, *Thin-Walled Structures,* Vol. 15, 159-183.
49. **Kolakowski Z.** (1996), Semi-analytical method for the analysis of the interactive buckling of thin-walled elastic structures in the second order approximation, *International Journal of Solids and Structures*, Vol. 33, 3779-3790.
50. **Kolakowski Z.** (2007), Some aspects of dynamic interactive buckling of composite columns, *Thin-Walled Structures,* Vol. 45, 866–871.
51. **Kolakowski Z.** (2009), Static and dynamic interactive buckling of composite columns, *Journal of Theoretical and Applied Mechanics,* Vol. 47, 177-192.
52. **Kolakowski Z. Mania R.J.** (2013), Semi-analytical method versus the FEM for analyzing of the local post-buckling of thin-walled composite structures, *Composite Structures,* Vol. 97, 99–106.
53. **Kolakowski Z., Krolak M.** (1995), Interactive elastic buckling of thin-walled closed orthotopic beam-columns, *Engineering Transactions,* Vol. 43, 571-590.
54. **Kolakowski Z., Krolak M.** (2002), Modal coupled instabilities of thin-walled composite plate and shell structures, *Composite Structures,* Vol. 76, 303-313.
55. **Kolakowski Z., Krolak M., Kowal-Michalska K.** (1999), Mode interactive buckling of thin-walled composite beam-columns regarding distortional deformations, *International Journal of Engineering Sciences,* Vol. 37, 1577-1596.
56. **Kolakowski Z., Kubiak T.** (2005), Load-carrying capacity of thin-walled composite structures, *Composite Structures,* Vol. 67, 417–426.
57. **Kolakowski Z., Kubiak T.** (2007), Interactive dynamic buckling of orthotropic thin-walled channels subjected to in-plane pulse loading, *Composite Structures,* Vol. 81, 222-232.
58. **Kolakowski Z., Teter A.** (1995), Influence of local postbuckling behaviour on bending of thin-walled elastic beams with central intermediate stiffeners, *Engineering Transactions,* Vol. 43, No. 3, 383-396.
59. **Kolakowski Z., Teter A.** (1995), Interactive buckling of thin-walled closed elastic column-beams with intermediate stiffeners, *International Journal of Solid and Structures,* Vol. 32, 1501-1516.
60. **Kolakowski Z., Teter A.** (2000), Interactive buckling of thin–walled beam–columns with intermediate stiffeners or/and variable thickness, *International Journal of Solid and Structures,* Vol. 37, 3323–3344.
61. **Kounadis A.N., Gantes C., Simitses G.** (1997), Nonlinear dynamic buckling of multi-dof structural dissipative system under impact loading, *International Journal Impact Engineering,* Vol. 19, 63-80.
62. **Krolak M., Kowal-Michalska K., Mania R.J., Swiniarski J.** (2007), Experimental tests of stability and load carrying capacity of compression thin-walled multi-cell columns of triangular cross-section, *Thin-Walled Structures,* Vol. 45, 883–887.
63. **Krolak M., Mlotkowski A.** (1996), Experimental analysis of post-buckling and collapse behaviour of thin-walled box-section beam, *Thin-Walled Structures,* Vol. 26, 287–314.
64. **Kubiak T.** (2007), Criteria of dynamic buckling estimation of thin-walled structures, *Thin-Walled Structures,* Vol. 45, 888–892.
65. **Kubiak T.** (2013), *Static and dynamic buckling of thin-walled plate structures,* Springer Verlag, London, UK.
66. **Kwon Y.B., Kim B.S., Hancock G.J.** (2007), Compression tests of high strength cold-formed steel channels with buckling interaction, *J. Constructional Steel Research,* Vol. 63, 1590–1602.
67. **Lee H.P., Harris P.J.** (1979), Post-buckling strength of thin-walled members, *Computers and Structures,* Vol. 10, 689-702.
68. **Lee H.P., Harris P.J., Cheng-Tzu T.H.** (1984), A nonlinear finite element computer program for thin-walled member, *Thin-Walled Structures,* Vol. 2, 355-376.
69. **Lindberg H.E. (ed.)** (1987), *Dynamic pulse buckling,* Kluwer Academic Publishers.
70. **Madenci E., Guven I.** (2006), *The finite element method and applications in engineering using ANSYS*. Springer, Verlag, New York, USA.
71. **Magnucka-Blandzi E., Magnucki K.** (2011), Buckling. and optimal design of cold-formed thin-walled beams: Review of selected problems, *Thin-Walled Structures,* Vol. 49, 554-561.
72. **Magnucka-Blandzi E., Paczos P., Wasilewicz P.** (2012), Buckling study of thin-walled channel beams with double box-flanges in pure bendin, *Strain,* Vol. 48, No. 4, 317-325.
73. **Magnucki K., Paczos P., Kasprzak J.** (2010), Elastic buckling of cold-formed thin-walled channel beams with drop flanges, *Journal of Structural Engineering,* Vol. 136, No. 7, 886-96.
74. **Manevich Al.** (1981), Interaction of buckling modes of stiffened plate under compression, *Stroitelnaya Mekhanika i Raschet Sooruzhenii*, Vol.1, 24-29.
75. **Manevich Al.** (1982), Theory of interaction buckling of stiffened thin-walled structures, *Prikladnaya Matematika i Mekhanika,* Vol.46, 337-345.
76. **Manevich Al.** (1985), Stability of shells and plates with T-section stiffeners, *Stroitelnaya Mekhanika i Raschet Sooruzhenii,* Vol. 2, 3 4-38.
77. **Manevich Al.** (1988), Interactive buckling of stiffened plate under compression, *Mekhanika Tverdogo Tela*, Vol. 5, 152-159.
78. **Mania R.** (2005), Buckling analysis of trapezoidal composite sandwich plate subjected to in-plane compression, *Composite Structures,* Vol. 69, 482–490.
79. **Mania R., Kowal-Michalska K.** (2007), Behaviour of composite columns of closed cross-section under in-plane compressive pulse loading, *Thin-Walled Structures,* Vol. 45, 902-905.
80. **Moellmann H. and Goltermann P.** (1989), Interactive buckling in thin-walled beams; Part I: Theory; Part II: Applications*, Inter. Journal of Solids and Structures*, Vol. 25, 715–749.
81. **Morris A.** (2008), *Practical guide to reliable finite element modelling*. John Wiley&Sons Inc, USA.
82. **Niezgodzinski T., Kubiak T.** (2005), The problem of stability of web sheets in box-girders of overhead cranes, *Thin-Walled Structures* Vol. 43, 1913-1925.
83. **Parlapalli M.R., Soh K.C., Shu D.W., Ma G.** (2007), Experimental investigation of delamination buckling of stitched composite laminates, *Composites: Part A*; Vol. 38, 2024–2033.
84. **Petry D. and Fahlbusch G.** (2000), Dynamic buckling of thin isotropic plates subjected to in-plane impact, *Thin-Walled Structures* Vol. 38, 267-283.

DOI 10.1515/ama-2016-0023

85. **Pignataro M., Luongo A.** (1987), Asymmetric interactive buckling of thin-walled columns with initial imperfection*, Thin-Walled Structures*, Vol. 3, 365–386.
86. **Pignataro M., Luongo A.** (1987), *Multiple interactive buckling of thin-walled members in compression,* Proceedings of the International Colloq. on Stability of Plate and Shell Structures. University Ghent, 235–240.
87. **Pignataro M., Luongo A., Rizzi N.** (1985), On the effect of the local overall interaction on the postbuckling of uniformaly compressed channels, *Thin-Walled Structures,* Vol. 3, 283-321.
88. **Powell G., Klinger R.** (1970) Elastic lateral buckling of steel beams, *Journal of Structural Engineering ASCE,* Vol. 96, No. 9, 1919-1932.
89. **Put B.M., Pi Y.L., Trahair N.S.** (1999), Lateral buckling test on cold-formed channel beams, *Journal of Structural Engineering ASCE,* Vol. 125, No. 5, 532–539.
90. **Rajasekaran S., Murray D.W.** (1973), Coupled local buckling in wide flange beam columns, Journal of Structural Engineering ASCE 1973;99(6):1003-23.
91. **Schokker A., Sridharan S., Kasagi A.** (1996), Dynamic buckling of composite shells. *Computers and Structures,* Vol. 59, 43-55.
92. **Simitses G.J.** (1990), *Dynamic stability of suddenly loaded structures,* Springer Verlag, New York, USA.
93. **Simitses G.J., Hodges D.H.** (2006), *Fundamentals of structural stability,* Butterworth-Heinemann, USA.
94. **Singer J., Arbocz J., Weller T.** (1998), *Buckling experiments. experimental methods in buckling of thin-walled structure. Basic concepts. columns. beams and plates*, Vol. 1, John Wiley & Sons Inc., New York, USA.
95. **Singer J., Arbocz J., Weller T.** (2002), *Buckling experiments. experimental methods in buckling of thin-walled structure. shells built-up structures. Composites and additional topics*, Vol. 2, John Wiley & Sons Inc., New York, USA.
96. **Sridharan S.** (1983), Doubly symmetric interactive buckling of plate structures*, International Journal of Solids and Structures*, Vol. 19, 625-641.
97. **Sridharan S., Ali M.A.** (1985), Interactive buckling in thin-walled beam-columns*, Journal of Engineering Mechanics, ASCE,* Vol. 111, 1470–1486.
98. **Sridharan S., Ali M.A.** (1986), An improved interactive buckling analysis of thin-walled columns having doubly symmetric sections*, International Journal of Solids and Structures*, Vol. 22, 429–443.
99. **Sridharan S., Benito R.** (1984), Columns static and dynamic interactive buckling, *Journal of Engineering Mechanics, ASCE,* Vol. 110, 49–65.
100. **Stronge W.J.** (2000), *Impact mechanics,* Cambridge University Press, Cambridge, New York, USA.
101. T**amura Y.S., Babcock C.D.** (1975), Dynamic stability of cylindrical shell under step loading, *Journal of Applied Mechanics,* Vol. 42, 190-194.
102. **Teter A.** (2007), Static and dynamic interactive buckling of isotropic thin–walled closed columns with variable thickness, *Thin–Walled Structures*, Vol. 45, 936–940.
103. **Teter A.** (2010), Dynamic. multimode buckling of the thin-walled columns with subjected to in-plane pulse loading, *Inter. J. Non-Linear Mechanics*, Vol. 45, 207-218.
104. **Teter A.** (2011), Dynamic critical load based on different stability criteria for coupled buckling of columns with stiffened open cross-sections, *Thin-Walled Structures*, Vol. 49, 589-595.
105. **Teter A., Kolakowski Z.** (2003), Natural frequencies of thin-walled structures with central intermediate stiffeners or/and variable thickness, *Thin–Walled Structures* Vol. 41, 291–316.
106. **Teter A., Kolakowski Z.** (2004), Interactive buckling and load carrying capacity of thin–walled beam–columns with intermediate stiffeners, *Thin–Walled Structures,* Vol. 42, 211–254.
107. **Teter A., Kolakowski Z.** (2005), Buckling of thin-walled composite structures with intermediate stiffeners, *Composite Structures* Vol. 69, 421-428.
108. **Teter A., Kolakowski Z.** (2013), Coupled dynamic buckling of thin-walled composite columns with open cross-sections, *Composite Structures,* Vol.95, 28–34.
109. **Thompson J.M.T., Hunt G.W.** (1973), *General Theory of Elastic Stability*, Wiley, New York, USA.
110. **Toneff J.D., Stiemer S.F. and Osterrieder P.** (1987), Local and overall buckling in thin-walled beams and columns. *Journal of Structural Engineering ASCE*, Vol. 113, No. 4, 769-786.
111. **Turvey G.J., Zhang Y.** (2006), A computational and experimental analysis of the buckling. postbuckling and initial failure of pultruded GRP columns, *Computers & Structures,* Vol. 84, 1527–1537.
112. **Tvergaard V.** (1973), Imperfections sensitivity of a wide integrally stiffened panel under compression, *International Journal of Solids and Structures*, Vol. 9,177-192.
113. **Tvergaard V.** (1973), Influence of post-buckling behaviour on optimum design of stiffened panels, *International Journal of Solids and Structures*, Vol. 9, 1519–34.
114. **van der Heijden A.M.A.** (ed.) (2009), *WT. Koiter's elastic stability of solids and structures,* Cambridge University Press, UK.
115. **Virgin L.N.** (2007), *Vibration of axially loaded structures,* Cambridge University Press, UK.
116. **Volmir S.A.** (1972), *Nonlinear dynamics of plates and shells,* Science, Moscow, Russia.
117. **Warminski J., Teter A.** (2012), Non-linear parametric vibrations of a composite column un-der uniform compression, *Proceedings of the Institution of Mechanical Engineers. Part C: Journal of Mechanical Engineering Science,* Vol. 226, 1921-1938.
118. **Weller T., Abramovich H., Yaffe R.** (1989), Dynamic buckling of beams and plates subjected to axial impact, *Composite Structures,* Vol. 37, 835-851.
119. **White D.W., Abel J.F.** (1990), Accurate and efficient nonlinear formulation of a nine-node shell element with spurious mode control, *Computers and Structures,* Vol. 35, 621-641.
120. **Wong P.M.H., Wang Y.C.** (2007), An experimental study of pultruded glass fibre reinforced plastics channel columns at elevated temperatures, *Computers & Structures,* Vol. 81, 84–95.
121. **Zhang T., Liu T., Zhao Y.** (2004), Nonlinear dynamic buckling of stiffened plates under in-plane impact load, *Journal of Zhejiang University Science*, Vol. 5, 609-617.

Acknowledgements: This paper was financially supported by the Ministerial Research Project No. DEC-2013/11/B/ST8/04358 financed by the Polish National Science Centre.

DOI 10.1515/ama-2016-0024

DIRECT CURRENT AND PULSED DIRECT CURRENT PLASMA NITRIDING OF FERROUS MATERIALS A CRITICAL REVIEW

Magdalena ŁĘPICKA*, Małgorzata GRĄDZKA-DAHLKE*

*Faculty of Mechanical Engineering, Department of Materials and Biomedical Engineering, Bialystok University of Technology, ul. Wiejska 45 C, 15-351 Bialystok, Poland

m.lepicka@pb.edu.pl, m.dahlke@pb.edu.pl

received 14 July 2015, revised 20 May 2016, accepted 25 May 2016

Abstract: Nowadays, the improvement of ferrous materials performance is a problem of high interest. One of well-known wear- and corrosion properties improving technique is plasma nitriding, in which elemental nitrogen is introduced to the surface of a metal part for subsequent diffusion into the material. As a result, a compound, "white" layer and a diffusion zone are formed at the detail's surface. Most of the authors positively describe the effects of surface ion nitiding. On the other hand, there are also reports on adverse effects of direct current and pulsed direct current plasma nitriding on ferrous materials performance. Therefore, an attempt to provide comprehensive summary on direct current and pulsed direct current ion nitriding and its influence on ferrous materials' mechanical and corrosion properties has been made. According to the results, some of the technique drawbacks are hard to avoid in mass production.

Key words: Plasma Nitriding, Ion Nitriding, Direct Current Plasma Nitriding, Pulsed Direct Current Plasma Nitriding, Edge Effect

1. INTRODUCTION

Used in industry for more than 30 years (Soltani Asadi and Mahboubi, 2012), plasma nitriding (PN), called also ion nitriding or plasma ion nitriding (Szilágyiné Biró, 2013), has become an acceptable alternative to conventional gas nitriding because it is a non-pollutant, energy-saving and easy time- and temperature control process (Olzon-Dionysio et al., 2010; Brühl et al. 2010; Szilágyiné Biró, 2013). Currently it is used in a great number of industry branches, e.g. in automotive in engine components (Sirin and Kaluc, 2012), in order to maximize performance and service life of various ferrous materials, e.g. ferritic and austenitic steels, bearing steels, martensitic steels, as well as non-ferrous metals, such as titanium (Musil et al., 2000).

Nowadays, the plasma nitriding process is carried out by variety of methods. The most popular one is the DC (direct current) plasma nitriding, referred also to cathodic nitriding or conventional plasma nitriding (Musil et al., 2010; Li et al., 2014), which is extensively used in commercial ion nitriding reactors (Baldwin et al., 1998).

2. GENERAL INFORMATION

According to Li et al. (2010), in the DC nitriding process the components to be treated act as a cathode, whereas the grounded walls of the furnace form the anode. The treated material is directly involved in the discharge process. Typically, the applied voltage between the anode and the cathode is from 400 to 700 V. The positive ions produced by glow discharge are accelerated near the cathode surface and bombard the surface of the treated specimen. Due to ion bombardment the active nitrogen is sputtered, the workpiece is heated and its surface is cleaned (Brühl et al., 2010; Sirin and Kaluc, 2012). As a result, the "white" layer and the diffusion layer with altered mechanical properties are formed. The "white" layer term originates from the white color on the microscopy of the compound layer after Nital etch application.

In particular, low-temperature plasma nitriding (<420°C) of austenitic stainless steels such as AISI 304 or 316L results in formation of a metastable austenite phase supersaturated with nitrogen atoms (nitrogen concentration is 20-30 at%) (Madjarov and Russeva, 2007; Li et al., 2008; Wang et al., 2009). This phase is usually called expanded austenite, S-phase or γ_N (Toshkov et al., 2007; Li et al., 2008; Wang et al., 2009) and exhibits significant improvement in substrate hardness while the wear resistance is enhanced by several orders of magnitude (Menthe et al., 2000). What is more, some authors attribute γ_N excellent anticorrosive properties (Fossati et al., 2006b). In temperatures exceeding 420°C, due to sufficient diffusivity of chromium in the austenite the precipitation of Cr_xN starts (Tab. 1, 2), resulting in depletion of Cr from austenitic matrix and, usually, decrease in corrosion resistance (Wang et al., 2009). Unfortunately, the rate of plasma nitriding processes and nitrogen diffusion in temperatures below 450°C is low and leads to a very long duration of the nitriding process for getting appropriate layer thickness (Wang et al., 2013). As a result, the process becomes ineffective and too expensive to apply in mass production. According to the literature (Tab. 1), in order to obtain a 5 µm nitride layer at least a 2 h lasting process must be applied (Li et al., 2008).

In martensitic stainless steels, the usually ca. 25 µm thick (Podgornik et al., 1998) outer, compound layer consists mainly of γ'-Fe_4N or ε-$Fe_{2,3}N$ intermetallic phases – iron nitrides (Sirin and Kaluc, 2012; Mashreghi et al., 2013). Study by Weber et al. (Weber et al., 1995) revealed that the corrosion rate of iron in an acidic solution can be reduced by one order of magnitude when the ε-$Fe_{2,6}N$ phases are formed, and reduced by three orders of magnitude by the formation of γ'-Fe_4N. Composition and thickness of the "white" layer highly depends on the used in the nitriding process gas composition, treatment time and temperature

DOI 10.1515/ama-2016-0024

(Tab. 1, 2), as well as the carbon content (Sirin and Kaluc, 2012). In general, the more homogenous and monolithic is the outer phase, the better. When nitriding martensitic steels, the homogenous monolayer can be obtained with elongation of treatment time (>15 h for AISI 4140) (Corengia et al., 2005). Nevertheless, temperature of 500°C must be applied. According to Corengia et al. (2004a), the single-phase γ'-Fe_4N layers exhibit better tribological properties than two-phase compound layers. In supermartensitic stainless steels, beside the γ'-Fe_4N and ε-$Fe_{2,3}N$ intermetallic phases, α_N, the "nitrogen expanded martensite" phase is also distinguished (Kurelo et al., 2015).

Tab. 1. Data on the direct current (DCPN) plasma nitriding collected from the literature; CD – case depth

Material	Parameters	Temp. (°C)	Time (h)	Nitride layer characteristics	Hardness	Ref.
AISI 1020	350 Pa N_2:H_2 4:1	400-480	3	γ'-Fe_4N + ε-$Fe_{2,3}N$ 2.5-5 µm CD: 30.3-58.5 µm	350-500 $HV_{0.05}$	(de Sousa et al., 2014)
AISI 304	2.67 Pa N_2:H_2 1:4	500	8	γ_N 4 µm	600 VHN_{25gf}	(Balusamy et al., 2013)
AISI 304	100 Pa N_2:H_2 1:3	400	8	γ_N CD: 51.7 µm	-	(Wang et al., 2013)
AISI 304	666-1332 Pa N_2:H_2 19:1	450-570	4	γ'-Fe_4N + ε-$Fe_{2,3}N$ + CrN	-	(Borges et al., 2000)
AISI 304	100 Pa NH_3	420	2-44	γ_N 3-27 µm	600-1200 $HV_{0.05}$	(Wang et al., 2006)
AISI 304	N_2	420	6	γ_N CD: 12 µm	15.4 GPa	(Raman and Jayaprakash, 2007)
AISI 304	500 Pa NH_3	400-500	2	γ_N 2-13 µm	440-1300 $HV_{0.1}$	(Liang et al., 2001)
AISI 304L	200-600 Pa N_2:H_2 1:4	350-480	4-8	γ_N + CrN + α_N	630-1200 $HV_{0.1}$	(Wang et al., 2009)
AISI 316	500 Pa N_2:H_2 1:3	450-550	5	γ_N + CrN 15-60 µm	1100-1500 $HV_{0.05}$	(Sun and Bell, 1998)
AISI 316	667 Pa N_2:H_2 1:3	450	5	γ_N + γ'-Fe_4N 6 µm	-	(Karimzadeh et al., 2013)
AISI 316L	500 Pa NH_3	520-560	1/12-2	γ_N + CrN + γ'-Fe_4N 1.5-12 µm	400-1200 $HV_{0.05}$	(Li et al., 2014)
AISI 316	500 Pa N_2:H_2 1:3	300-450	20	γ_N 2-20 µm	1400-1600 $HV_{0.05}$	(Bell, 2002)
AISI 316L	530 Pa N_2:H_2 1:4	400	4	γ_N + ε-$Fe_{2+x}N$ + γ'-Fe_4N 1.5-2.3 µm	183 $HV_{0.01}$	(Olzon-Dionysio et al., 2010)
AISI 316L	600 Pa N_2:H_2 1:4	350-480	2	γ_N + CrN 5 µm	740-1100 $HV_{0.1}$	(Li et al., 2008)
AISI 316L	250 Pa N_2:H_2 1:1	440	6	γ_N + CrN 3.5 µm	1200 $HV_{0.05}$	(Skolek-Stefaniszyn et al., 2010)
AISI 316L	N_2:H_2 1:1	440	6	γ_N 20 µm	1240 $HV_{0.05}$	(Borowski et al., 2010)
AISI 316L	1000 Pa N_2:H_2 4:1	430	1-5	γ_N 3-10 µm	300-1400 $HK_{0.1}$	(Fossati et al., 2006b)
AISI 316L	150-2000 Pa	430	5	γ_N + γ'-Fe_4N + CrN 9-15 µm	1380-1430 $HK_{0.01}$	(Borgioli et al., 2006)
AISI 316L	1000 Pa N_2:H_2 4:1	400-500	5	γ_N + γ'-Fe_4N + CrN 4-47 µm	373-1605 $HK_{0.1}$	(Fossati et al., 2006a)
AISI 316L	1000 Pa N_2:H_2 4:1	400-500	5	γ_N + γ'-Fe_4N + CrN 4-47 µm	800-1580 $HK_{0.01}$	(Borgioli et al., 2005)
AISI 316L	400 Pa N_2:H_2 1:3	425	12	γ_N 10 µm	1240 $HV_{0.01}$	(Dong et al., 2006)
AISI 316L	600 Pa N_2:H_2 1:4	400	2-7	γ_N + γ'-Fe_4N + ε-$Fe_{2,3}N$ + CrN +Cr_2N 8 µm	-	(Olzon-Dionysio et al., 2008)
AISI 316L	600 Pa N_2:H_2 1:4	400	2-7	γ_N + γ'-Fe_4N + CrN 6 µm	-	(de Souza et al., 2010)
AISI 410	500 Pa N_2:H_2 1:3	240-500	20	γ'-Fe_4N + ε-$Fe_{2,3}N$ + CrN + α_N 47-135 µm CD: 77-186 µm	1000-1200 $HK_{0.1}$	(Li and Bell, 2006)
AISI 420	650 Pa N_2:H_2 1:3	300	20	γ'-Fe_4N + ε-$Fe_{2,3}N$ + CrN	-	(Tuckart et al., 2007)
AISI 420	300-400 Pa N_2:H_2 1:4	530	20	γ'-Fe_4N + ε-Fe_3N + CrN CD: 61 µm	1300 $HV_{0.1}$	(Alphonsa et al., 2002)
AISI 4340	NH_3	500-540	2-16	γ'-Fe_4N + ε-Fe_3N 2.6-8.8 µm CD: 280-510 µm	500-640 $HV_{0.2}$	(Sirin et al., 2008; Sirin and Kaluc, 2012)
AISI CA6NM	400 Pa N_2:H_2 1:4	500	1-5	γ'-Fe_4N + ε-$Fe_{2,3}N$ + CrN 2-6 µm	1245-1309 $HV_{0.05}$	(Winck et al., 2013)
AISI H12	600 Pa N_2:H_2 1:4	500	1-6	γ'-Fe_4N + ε-$Fe_{2,3}N$ + α''-$Fe_{16}N_2$ CD: 38-85 µm	1240 HV_{70gf}	(Miola et al., 1999)
AISI HNV3	N_2:H_2	450-650	3-6	-	5.39-13.14 GPa	(Sobiecki et al., 2004)
HP13Cr	300 Pa N_2:H_2 1:4	350-450	6	γ'-Fe_4N + ε-$Fe_{2+x}N$ + CrN + α_N CD: 16-61 µm	12-14 GPa	(Kurelo et al., 2015)
UNS S31254	500 Pa N_2:H_2 1:4	400-500	5	γ_N + CrN + Cr_2N 10 µm	980-1380 $HV_{0.025}$	(Fernandes et al., 2010)

DOI 10.1515/ama-2016-0024

Tab. 2. Data on pulsed direct current plasma nitriding collected from the literature; CD – case depth

Material	Parameters	Temp. (°C)	Time (h)	Nitride layer characteristics	Hardness	Ref.
AISI 2205	300 Pa N_2:H_2:Ar 4-8:1-3:1-3	250-500	8-60	γ_N + γ'-Fe_4N + CrN 1.7 µm	-	(Larisch et al., 1999)
AISI 2205	250 Pa N_2:H_2 2:1	400	20	γ'-Fe_4N + ε-Fe_3N + CrN 12 µm	1420-1960 $HV_{0.01}$	(Kliauga and Pohl, 1998)
AISI 304	300 Pa NH_3	350-540	4	γ_N + γ'-Fe_4N + CrN 2-12 µm	3-14.7 GPa	(Liang, 2003)
AISI 304	400 Pa N_2:H_2 1:4	560	24	γ'-Fe_4N + ε-Fe_3N + CrN CD: 40-90 µm	900-1100 $HV_{0.1}$	(Singh et al., 2006)
AISI 304	400 Pa N_2:H_2 4:1	560	24	γ'-Fe_4N + ε-Fe_3N + CrN CD: 50-110 µm	1000-1300 $HV_{0.1}$	(Singh et al., 2006)
AISI 304	250 Pa N_2:H_2 1:2	-	-	γ_N + CrN CD: 22 µm		(Michler, 2008)
AISI 304L	600 Pa N_2:H_2 1:4	450	1/2-16	γ_N + CrN	1500-1600 $HK_{0.01}$	(Menthe and Rie, 1999)
AISI 316L	250 Pa N_2:H_2 1:3	400-550	12	γ_N + γ'-Fe_4N + ε-$Fe_{2,3}N$ + CrN + Cr_2N	1450-1500 $HV_{0.025}$	(Mingolo et al., 2006)
AISI 316L	250 Pa N_2:H_2 3:1	400-550	12	γ_N + γ'-Fe_4N + ε-$Fe_{2,3}N$ + CrN + Cr_2N	1400-1500 $HV_{0.025}$	(Mingolo et al., 2006)
AISI 316L	173 Pa N_2:H_2 1:1	400	-	γ_N 3.4-4.8 µm	1245 $HV_{0.025}$	(Díaz-Guillén et al., 2015)
AISI 316L	533 Pa N_2:H_2 4:1	400-500	5	γ_N + γ'-Fe_4N + CrN 5-70 µm	1115-1315 $HV_{0.1}$	(Jeong and Kim, 2001)
AISI 321	300 Pa N_2:H_2:Ar 4-8:1-3:1-3	250-500	8-60	γ_N + γ'-Fe_4N + CrN 2.5 µm	3305-8292 $HV_{0.0001}$	(Larisch et al., 1999)
AISI 410	600 Pa N_2:H_2 1:3	350-500	20-28	γ'-Fe_4N + ε-$Fe_{2,3}N$ + CrN + α_N CD: 30 µm	1150-1400 $HV_{0.025}$	(Corengia et al., 2004b)
AISI 420	600 Pa N_2:H_2 1:3	350-550	15	ε-Fe_3N + γ'-Fe_4N + α_N CD: 90-130 µm	1000-1200 $HK_{0.025}$	(Xi et al., 2008a; Xi et al., 2008b)
AISI 420	250 Pa N_2:H_2 3:1	480-560	4	γ'-Fe_4N + ε-$Fe_{2,3}N$ + CrN CD: 80 µm	1525 $HV_{0.025}$	(Pinedo and Monteiro, 2004)
AISI 430	300 Pa N_2:H_2:Ar 4-8:1-3:1-3	250-500	8-60	γ_N + γ'-Fe_4N + ε-$Fe_{2,3}N$ + CrN 14.6 µm	-	(Larisch et al., 1999)
AISI 4140	500 Pa N_2:H_2 17:3	570-620	5	γ'-Fe_4N + ε-$Fe_{2,3}N$ CD: 42 µm	-	(Fattah and Mahboubi, 2010)
AISI 4140	600 Pa N_2:H_2 1:3	500	2-28	γ'-Fe_4N + ε-$Fe_{2,3}N$ 3-7.5 µm CD: 220-600 µm	650-850 $HV_{0.1}$	(Corengia et al., 2005)
AISI 4340	173 Pa N_2:H_2 1:1	540	4	γ'-Fe_4N 7.5-14.5 µm CD: <350 µm	700-825 $HV_{0.05}$	(Díaz-Guillén et al., 2009)
AISI 52100	500 Pa N_2:H_2 7:13	450-560	1-5	ε-$Fe_{2,3}N$ + γ'-Fe_4N	-	(Basu et al., 2008)
AISI CA6NM	532 Pa N_2:H_2 1:4	500	2	γ'-Fe_4N + ε-$Fe_{2,3}N$ + CrN CD: 25 µm	1240 $HV_{0.5}$	(Allenstein et al., 2013)
AISI H12	600 Pa N_2:H_2 1:4	500	1-6	γ'-Fe_4N + ε-$Fe_{2,3}N$ + α''-$Fe_{16}N_2$	-	(Miola et al., 1999)
AISI L2	666 Pa N_2:H_2 3:7	450-550	6-9	γ'-Fe_4N + ε-Fe_3N CD: 110-330 µm	480-510 $HV_{0.02}$	(Soleimani et al., 2012)
AISI M2	400 Pa N_2:H_2 4:1	50-570	5	4-6 µm	-	(Jeong and Kim, 2001)
AISI P21	600 Pa N_2:H_2 1:3	475-525	10	γ'-Fe_4N + ε-$Fe_{2,3}N$ 2.8-5 µm CD: 100-200 µm	640-710 $HV_{0.05}$	(Wen, 2009)
Corrax	N_2:H_2 1:4	360	10	γ_N 10-12 µm	1290 $HV_{0.05}$	(Brühl et al., 2010)
M340	N_2:H_2 1:4	360	10	γ_N + CrN + $M_{23}C_6$ 9-10 µm	1100 $HV_{0.05}$	(Brühl et al., 2010)
N695	N_2:H_2 1:4	360	10	γ_N + CrN + $M_{23}C_6$ 14-15 µm	1130 $HV_{0.05}$	(Brühl et al., 2010)

Because of the different unit cell parameters of the cited γ' and ε phases, the mixture of crystalline structures can generate stress at the boundaries of the grains, increasing the fragility of the layer (Sirin and Kaluc, 2012). Delayed cracking of the nitride layers on AISI 420 martensitic stainless steel has been reported by Tuckart et al. (2007). After 24 months incubation time, without any external disturbance, the cracks were formed in the nitrided specimens. According to O'Brien and Goodman (1991), the weak bonding at the interphases or different thermal expansion coefficients of the phases can be the cause of this phenomena.

In the plasma nitrided workpieces, beneath the compound layer, the diffusion layer is formed. The diffusion layer consists mainly of interstitial atoms in solid solution and fine and coherent nitride precipitates (Sirin and Kaluc, 2012; Mashreghi, 2013). The hardness and wear resistance of the diffusion layer depends on the time and temperature of the treatment, the gaseous mixture composition, the concentration of the alloying elements on the steel, the amount of precipitated nitrides and the initial microstructure of the material (Sirin and Kaluc, 2012). In order to determine the nitrogen influence depth, the effective depth case

DOI 10.1515/ama-2016-0024

is measured (Tab. 1, CD). It is the thickness of the hardened layer of a specimen, understood as the depth up to a further point for which a specified level of hardness is maintained. As can be seen in Tab. 1, in the case of ion nitrided materials, the layer thickness is not identical as the effective depth case.

The mechanisms of conventional DC plasma nitriding have been extensively studied and discussed by many authors, but the consensus has not been reached up to date. The dominant mechanisms for nitrogen mass transfer are claimed to be: nitrogen implantation (Xu and Zhang, 1986), low energetic $N_mH_n^+$ bombardment (Hudis, 1973), nitrogen adsorption (Tibbetts, 1974), neutral and ion adsorption (Szabo and Wilhelmi, 1984).

According to Zlatanowić and Popović (2010), a significant advance in plasma surface engineering, as well as in control and stability of the processing, was provided with introduction of pulsed DC power supply in plasma deposition techniques. In pulsed DC supply, the number of parameters which determine the quality of obtained surface, process characteristics and operating procedure is greater than in conventional DC process. Properties of the surface are directly affected by the power supply pulse frequency, duty cycle and output voltage, while the process stability and control are significantly improved (Zlatanowić and Popović, 2010). Pye (2003) claims that in plasma nitriding systems, the DC supply power is adjusted as required to the component geometry and chamber configuration. In conventional DC plasma nitriding technique, it is difficult to provide proper process temperature when the user has a mixed load of different part geometries and sizes. The pulsed technique enables operator adaption of the minimum power input necessary for the abnormal glow discharge (Pye, 2003).

3. INFLUENCE ON PERFORMANCE OF FERROUS MATERIALS

The influence of DC and pulsed DC plasma nitriding on ferrous materials performance has been extensively described in numerous studies. In this paper, the effect of ion nitriding on corrosion resistance, as well as on wear and fatigue, will be described.

3.1. Corrosion resistance

In recent years, many studies have been performed in order to improve corrosion resistance of austenitic stainless steels by ion nitriding and extend its industrial applications. In contrast, relatively few studies have been conducted so far on low temperature plasma nitriding of martensitic and supermartensitic stainless steels.

In general, many authors have been very positive about the influence of ion nitriding on corrosion resistance of austenitic and superaustenitic steels. In the research by Fossati et al. (2006a; b) it has been stated that the anodic current density in potentiodynamic scans becomes smaller with increase of nitriding treatment time. The authors pointed that in comparison with the untreated samples, the modified AISI 316L is less prone to pitting corrosion. According to the researchers, the repassivation capability of stainless steels is enhanced with γ_N formation due to its high nitrogen concentration. Moreover, in the study by Borgioli et al. (2006) it has been proven that the treatment pressure has a significant influence on performance of AISI 316L steel in 5% NaCl aerated solution. If the pressure exceeds 1.5 hPa, the chromium nitride precipitates or, if the pressure is extremely high (2.5 hPa), treated samples are unable to form homogenous protective passive layer. In addition, Olzon-Dionysio et al. (2008) demonstrated that treatment time pays an important role for the corrosion resistance. According to the authors, the higher the ε/γ' ratio, the better. Similar findings were obtained by de Souza et al. (2010). Fernandes et al. (2010) reported that plasma nitriding is beneficial also for UNS S31254 superaustenitic stainless steel, regardless of the process temperature ranging from 400 to 500°C.

As mentioned before, plasma nitriding process of austenitic stainless steels is conducted in temperatures below 420°C in order to prevent the chromium nitrides precipitation. It is believed that formation of γ_N phase with enough thickness depends on the temperature (<480°C) and duration of the process (Li et al., 2014a). In study by Li et al. (Li et al., 2014a) nitriding of austenitic AISI 316L steel was carried out at high temperatures (520-560°C) for times ranging from 5 to 120 min. Although the layers obtained in the research consisted of γ_N and a small amount of CrN and iron nitrides, the pitting corrosion resistance of substrate material has been improved even after 5 minutes of treatment.

Nevertheless, there are also some critical voices on performance of ion nitrided austenitic stainless steels. In the electrochemical impedance spectroscopy study by Borowski et al. (2010) it was exhibited that impedance of DC nitrided specimen was reduced by two orders of magnitude with respect to the untreated material. What is more, the polarization curves exhibited that DC nitriding of AISI 316L resulted in increase of corrosion current and shift of corrosion potential towards less noble materials. Liang (2003) reported that nitriding of AISI 304 steel only in temperatures below 450°C resulted in improvement in corrosion resistance, especially pitting corrosion. Samples nitrided at 465°C exhibited poor corrosion resistance, having lower corrosion potential and higher corrosion current density compared to the untreated specimens. In research by Liang et al. (2001) the DC plasma nitrided AISI 304 steel was characterized by low corrosion potential and very high corrosion current density (7.15 $\mu A \times cm^{-2}$), indicating high dissolution rates. As authors suggested, low pressure plasma arc source nitriding provided better substrate material performance than DC nitriding. Reduced corrosion resistance of PN AISI 316L stainless steel has also been reported by Karimzadeh et al. (2013). Inferior corrosion resistance has been attributed to the existence of sliding bands, created as a consequence of γ_N formation. According to the authors, the mentioned sliding bands can provide active sites for corrosion processes development. Menthe et al. (1995) stated that the passive layer obtained in the nitriding process is similar to the one naturally existing on AISI 304L steel by the means of corrosion resistance. Thus, the corrosion performance is not severely affected by surface modification. The corrosion performance of AISI 316L DC nitrided steel did not significantly improve in comparison with the untreated material in the study by Skolek-Stefaniszyn et al. (2010).

In terms of enhancing corrosion resistance, DC and pulsed DC plasma nitriding seems much more efficient when applied on martensitic, supermartensitic and bearing steels. Li and Bell (2006) demonstrated that the corrosion resistance of AISI 410 steel significantly improved after direct current plasma nitriding; in potentiodynamic tests in 3,5% $NaCl_{aq}$, the passivation region occurred only for nitrided samples. What is more, the pitting potential of surface modified specimens shifted towards positive potentials. The nitrided samples exhibited also lower weight loss in immersion tests in 1% HCl solution than untreated material. The

DOI 10.1515/ama-2016-0024

authors claim that superior corrosion resistance of ion nitrided AISI 410 steel was due to ε and γ' iron nitrides precipitation on the material surface. In the research by Corengia et al. (2004b) the positive influence of plasma nitriding on martensitic stainless steels has been proven. However, the authors pointed that samples nitrided for 20 h in 400 and 500°C exhibited decrease in corrosion resistance. Similar findings were obtained by Xi et al. (2008a) for DC-pulsed nitrided AISI 420 steel. The improvement in corrosion resistance was observed for samples treated in 350°C. According to the authors, the beneficial effect could be related to the solid solution of Cr and the ε and α_N phases present in the outer layer. However, corrosion resistance of specimens nitrided in 450 and 550°C has been reduced due to CrN formation and Cr depletion in the solid solution. In other study by these authors (Xi et al., 2008b), resistance to erosion and erosion-corrosion of AISI 420 steel has been examined. According to the results, in both neutral and acidic environment, the erosion-corrosion resistance of investigated steel was improved by means of 350°C nitriding, but decreased through 550°C nitriding for reasons provided earlier in the text. Basu et al. (2008) observed significant improve in corrosion properties of plasma nitrided AISI 52100 bearing steel. The authors attribute good corrosion resistance in aqueous medium to presence of ε and γ' nitrides in the modified layer. The higher temperature and longer time of nitriding process, the greater volume of nitride fraction at the surface.

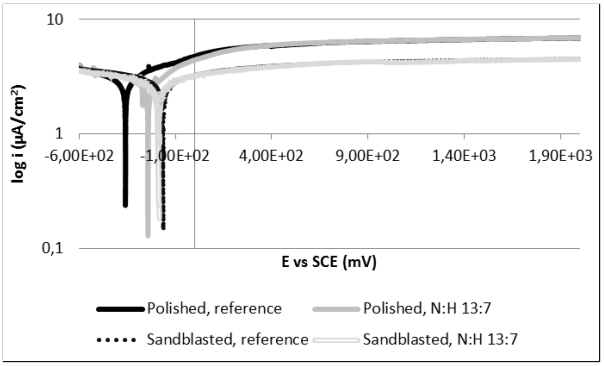

Fig. 1. Potentiodynamic curves of DC plasma nitrided (N_2:H_2 13:7, 400°C, 200 Pa, 2 h) and reference specimens

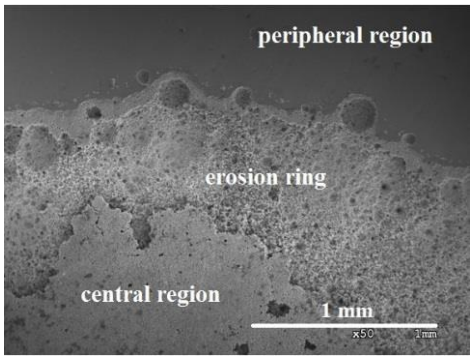

Fig. 2. Corroded surface morphology of DC plasma nitrided specimen, 35% H_2:65% N_2, SEM photograph, magnification 50×

Negative effect of ion nitriding on corrosion performance of martensitic stainless steels was observed by some authors. In research by Wierzchoń et al. (2006), AISI 420F steel nitrided in 530°C in the glow discharge assisted process exhibited slight decrease in corrosion resistance. Potentiodynamic curves of DC nitrided AISI 410 steel presented by Sobiecki et al. (2004) unequivocally indicate reduction in corrosion resistance of material treated in temperatures exceeding 450°C.

The effect of nitriding on martensitic stainless steel corrosion resistace has also been investigated by the authors of this review. Fig. 1 presents potentiodynamic curves of sandblasted and polished DC plasma nitrided (N_2:H_2 13:7, 400°C, 200 Pa, 2 h) AISI 440B steel. Taking into account provided results, it may seem that plasma nitriding does not significantly affect corrosion resistance of sandblasted material and slightly improves corrosion properties of polished specimens. Unfortunately, some specimens DC nitrided in slightly different conditions, e.g. nitrogen to hydrogen ratio 7:13, 400°C process temperature, 200 Pa pressure and 2 h lasting process exhibited severe damages after potentiodynamic tests (Fig. 2).

According to Baldwin et al. (1998), the conventional method of plasma nitriding is effective when nitriding low-alloy or tool steels, but is considered less successful with austenitic stainless or high alloy steels. The process is characterized by some inconvenience especially when workpieces of complex geometry are treated (Olzon-Dionysio et al., 2010). Numerous problems have been encountered arising from the direct plasma applied to the specimens. The reports show that the edge effect, arcing, hollow cathode effect, inhomogeneity of the workpiece temperature are observed (Szilágyiné Biró, 2013), as well as problems with treating parts of different dimensions within one batch (Saeed et al., 2013).

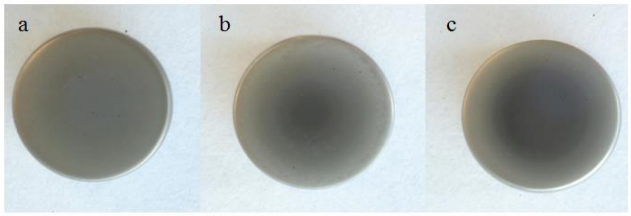

Fig. 3. Plasma nitrided specimens; a – 50% H_2:50% N_2, b – 35% H_2:65% N_2, c – 20% H_2:80% N_2; macro photographs (Łępicka i Grądzka-Dahlke, 2013)

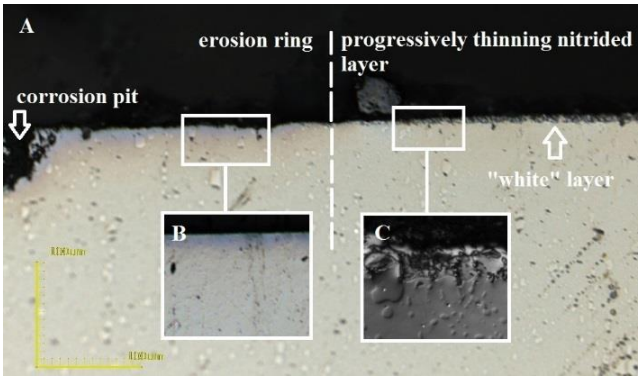

Fig. 4. Cross section of plasma nitrided (N_2:H_2 1:1) AISI 440B sample after potentiodynamic test. Confocal microscope photograph in: A - 216×, B, C - 2160× magnification

In the edge effect, the nitrogen supersaturated solution is formed on the edges of cylindrical specimens, leading to production of a non-uniform surface with different colors in the central and peripheral regions (Olzon-Dionysio et al., 2010; Szilágyiné Biró, 2013). As mentioned before, in DC plasma nitriding samples

DOI 10.1515/ama-2016-0024

are submitted to a high cathodic potential and the plasma is produced on their surface. In such case, the distortions in the electric field occur around the corners and the edges of the workload and the shape of the plasma sheath, which determines ion flux distribution, create erosion rings characterized by different colors and discontinuous hardness (Alves Jr. et al., 2001; 2006). The edge effect and its influence on corrosion resistance of stainless steels has also been observed by the authors of this review. Fig. 3 presents DC plasma nitrided AISI 440B specimens in three different gaseous mixture compositions. As it can be seen, the less nitrogen, the smaller the erosion ring. According to Figs. 2 and 4, the edge effect deteriorates the corrosion resistance of AISI 440B martensitic stainless steel. The affected by the edge effect area becomes the progressively dissolved anode, whereas tightly covered with inhomogenous nitride layer peripheral and central regions act as cathodes (Fig. 4). Detailed results from our studies on influence of DC plasma nitriding on corrosion resistance of AISI 440B martensitic stainless steel can be found in our previous work (Łępicka and Grądzka-Dahlke, 2013; 2014).

The influence of the edge effect on corrosion resistance of stainless steel has also been investigated by Olzon-Dionysio et al. (2010). The AISI 316L samples affected by the edge effect showed poorer corrosion resistance than those without erosion rings. Nevertheless, all investigated specimens exhibited improvement in corrosion resistance with reference to untreated material. According to de Sousa et al. (2014), the edge effect can be eliminated by using cathodic cage ion nitriding.

3.2. Wear and fatigue

Phases obtained in the DC and pulsed DC ion nitriding processes – γ_N, γ'-Fe_4N and ε-$Fe_{2,3}N$ – are known for their superior hardness and anti-wear properties. In research by Li et al. (2008) the effect of DC plasma nitriding on dry-sliding wear properties of AISI 316L stainless steel has been evaluated. The ring-on-block dry wear test exhibited significant reduction of wear rate in comparison with unnitrided material. It should be noted, however, that the wear rate of nitrided specimens enhanced with increase of treatment temperature, and, as a consequence, Cr nitrides volume in the modified layer. Wear of the DCPN treated AISI 316L steel was dominated by plastic deformation, slight abrasion and frictional polishing. Nevertheless, microcracking of layers with high CrN content has been observed. Similar findings were obtained by Sun and Bell in ball-on-disc tribosystem (Sun and Bell, 1998) – with increasing nitriding temperature, the wear volume of nitrided surface increased. What is more, the higher was nitriding temperature, the greater was friction coefficient. The positive influence of DC ion nitriding on wear resistance of AISI 316L steel has also been noted by Borowski et al. (2010) and Skolek-Stefaniszyn et al. (2010). Foerster et al. (2007) noticed that in dry sliding tests with WC-Co ball as a counter sample glow discharge ion nitriding reduced the friction coefficient with respect to untreated sample. According to Wang et al. (2009), the DC plasma nitriding significantly improves dry-sliding wear resistance also of AISI 304L steel. In the block-on-ring configuration friction test, the minimum value of wear rate was observed for γ_N-rich specimens. As the other authors, Wang et al. (2009) stressed that increasing concentration of Cr_xN in the reaction layer results in decrease in dry-sliding wear resistance. Reduction of AISI 304L wear rate after nitriding was also emphasized by Menthe et al. (2000).

A significant advance in wear rate was also observed in martensitic, duplex, tool and precipitation hardenable steels.

Xi et al. (2008a) conducted dry ball-on-disc tests on AISI 420 steel nitrided in 350 and 550°C. According to the authors, the anti-wear properties of material nitrided in lower temperature overachieve the 550°C ones. After nitriding the abrasive wear behavior occurred. In other work by the same authors (Xi et al., 2008b) the same data dependency was acknowledged regarding erosion resistance. Sobiecki et al. (2004) stated that glow-discharge assisted nitriding conducted in temperatures ranging from 450 to 650°C remarkably improved frictional wear resistance of AISI HNV3 steel. The harder the surface, the better the anti-wear properties. Similar conclusions were obtained by Kliauga and Pohl (1998) for ion nitrided AISI F51 duplex steel. In research by Wen (2009) friction- and wear tests of AISI P21 DC nitrided steel were conducted under dry conditions on a block-on-ring tribotester. A significant reduction in the wear and friction coefficient was observed. As the author noticed, greater compressive stress and higher hardness of the nitrided specimen translates into its better wear resistance. The anti-wear properties of investigated steel were related to the increase in the thickness of diffusion layer.

Fatigue strength study of AISI 4340 steel conducted by Sirin et al. (2008) demonstrated that in comparison with untreated steel the fatigue strength of nitrided material increased up to 91%. A linear relationship between the case depth and the fatigue strength was obtained. The fatigue behavior after ion nitriding was also observed for AISI L2 cold work tool steel by Soleimani et al. (2012). The fatigue strength of nitrided in 550°C for 6 h samples improved by about 67%. As in research by Sirin et al. (2008) the dominant fatigue crack initiation mechanism was subsurface “fish eye” type crack formation which originated from nonmetallic inclusions.

The beneficial influence of plasma nitriding on fatigue limit of ferrous materials was also reported by Winck et al. (2013). According to the authors, after just 1 h of nitriding in 500°C the fatigue life of CA6NM type steel increased by 23.67% at 2 million cycles. Fractographic analysis of fracture surfaces showed that the fractured surfaces resembled the structure referred to as “fish eye”.

Additionally, the researchers stated that in low stress level (250 MPa) fatigue tests, the fatigue life of nitrided AISI 304L steel is raised by a factor of 10.

However, there are also studies concerning negative effect of plasma nitriding on fatigue life of austenitic steels. In research by Raman and Jayaprakash (2007) the plasma nitrided AISI 304 exhibited inferior plain fatigue and fretting fatigue lives compared with the unmodified material. As the authors claim, this was caused by chromium segregation at the grains boundaries of ion nitrided specimens. The chromium nitrides precipitation might have weakened the grain boundaries, resulting in early crack initiation and its accelerated propagation.

3.3. Direct Current Plasma Nitriding: other shortcomings

As mentioned in the previous paragraphs, beside the edge effect, DC plasma nitriding is characterized also by inconvenience as arcing and hollow cathode effect.

Arcing, caused mainly by degassing in localized area of the specimen surface, leads to local heat up of the part to extreme temperatures and, as an effect, melting or sputtering material from its surface (Szilágyiné Biró, 2013). Severe arcing of the component results in necessity of scraping the metallic part. In order to

DOI 10.1515/ama-2016-0024

prevent arcing, the batch must be thoroughly cleaned from oil, grease and rust in relatively expensive cleaning routine (Gallo and Dong, 2009). According to Sharma et al. (2006) arcing can also be avoided by optimizing duty factor of the pulse in plasma deposition method.

The hollow cathode effect occurs when nitrided parts are of complex shape or contain deep holes, especially the blind ones (Szilágyiné Biró, 2013). During the ionization process, the gas is trapped in the hollow cavities and immobilized. This causes local heating of the product and can result in structure or property changes that affect the part's performance in service (Szilágyiné Biró, 2013). Soltani Asadi and Mahboubi (Soltaniet al., 2012) have conducted research in which the effect of the sample geometry on the DC plasma nitrided steel was investigated. According to the authors, the hollow cathode effect was observed at the sample with 2 mm width groove. The microhardness tests results revealed that the sample was overheated during the plasma nitriding process, whereas samples with grooves of 4, 6, 8 and 10 mm width were not overheated. What is more, the hollow cathode effect led to large in size and prone to coursing nitrides formation.

Surprisingly, the hollow cathode effect found its application in variety of plasma processing techniques, e.g. thin film depositions and surface treatment. For example, in the research by Li et al. (2014c) the hollow cathode discharge effect was used to easily heat batch and working space.

In order to avoid described above common problems attributed with DC nitriding, many efforts have been made over past few years to develop high productive plasma nitriding methods. The same type of complex nitrided layer can be produced by numerous nitriding methods, e.g. RF nitriding (Baldwin et al., 1998), plasma immersion ion implantation (Blawert et al., 1998; Saklakoglu et al., 2007), plasma source ion nitriding (Liang et al., 2001), anodic nitriding (Psyllaki et al., 2008), laser nitriding (Psyllaki et al., 2008), cyclic plasma nitriding catalyzed by rare earth metals (We et al., 2010), cathodic cage plasma nitriding (de Sousa et al., 2007; Ribeiro et al., 2008) or nitrogen ion-beam implantation combined with pulsed plasma nitriding (Ochoa et al., 2005). Due to promising results from numerous studies by many researchers, the influence of mentioned nitriding techniques on ferrous materials performance will be described in the next paper.

4. CONCLUSIONS

The aim of the review was to provide comprehensive summary on direct current and pulsed direct current plasma nitriding of ferrous materials. Used in a great number of industry branches, ion nitriding is an attractive method that maximizes performance and service life of metallic materials.

According to the results, DC and pulsed DC plasma nitriding is an effective surface hardening, anti-wear and anti-corrosion method applied on austenitic, superaustenitic, martensitic, supermartensitic, duplex, tool, valve, precipitation hardened steels. Nevertheless, there are also well documented cases of deteriorating effect of this surface modification method on tribological and corrosion properties of ferrous materials.

The discussed technique has also its drawbacks, e.g. the edge effect, arcing and hollow cathode effect, which result in inhomogeneity of obtained layer. The occurrence of mentioned disadvantages is virtually impossible to prevent in DC method, especially on small details.

REFERENCES

1. **Allenstein A.N., Lepienski C.M., Buschinelli A.A., Brunatto S.F**. (2013), Plasma nitriding using high H_2 content gas mixtures for a cavitation erosion resistant steel, *Applied Surface Science*, Vol. 277, 15-24.
2. **Alphonsa I., Chainani A., Raole P.M., Ganguli B., John P.I.** (2002), A study of martensitic stainless steel AISI 420 modified using plasma nitriding, *Surface and Coatings Technology*, Vol. 150, 263-268.
3. **Alves Jr. C., da Silva E.F., Martinelli A.E.** (2001), Effect of workpiece geometry on the uniformity of nitrided layers, *Surface and Coatings Technology*, Vol. 139, 1-5.
4. **Alves Jr. C., de Araújo F.O., Ribeiro K.B., da Costa J.P., Sousa R.M., de Sousa R.S.** (2006), Use of cathodic cage in plasma nitriding, *Surface and Coatings Technology*, Vol. 201, 2450-2454.
5. **Baldwin M.J., Fewell M.P., Haydon S.C., Kumar S., Collins G.A., Short K.T., Tendys J.** (1998), Rf-plasma nitriding of stainless steel, *Surface and Coatings Technology*, Vol. 98, 1187-1191.
6. **Balusamy T., Sankara Narayanan T.N., Ravichandran K., Park I.S., Lee M.H.** (2013), Plasma nitriding of AISI 304 stainless steel: Role of surface mechanical attrition treatment, *Materials Characterization*, Vol. 85, 38-47.
7. **Basu A., Majumdar J.D., Alphonsa J., Mukherjee S., Manna, I.** (2008), Corrosion resistance improvement of high carbon low alloy steel by plasma nitriding, *Materials Letters*, Vol. 62, 3117-3120.
8. **Bell T.** (2002), Surface engineering of austenitic stainless steel, *Surface Engineering*, Vol. 18, 415-422.
9. **Blawert C., Mordike B.L., Collins G.A., Short K.T., Tendys, J.** (1998), Influence of process parameters on the nitriding of steels by plasma immersion ion implantation, *Surface and Coatings Technology*, Vol. 103-104, 240-247.
10. **Borges C.M., Hennecke S., Pfender E.** (2000), Decreasing chromium precipitation in AISI 304 stainless steel during the plasma-nitriding process, *Surface and Coatings Technology*, Vol. 123, 112-121.
11. **Borgioli F., Fossati A., Galvanetto E., Bacci T.** (2005), Glow-discharge nitriding of AISI 316L austenitic stainless steel: influence of treatment temperature, *Surface and Coatings Technology*, Vol. 200, 2474-2480.
12. **Borgioli F., Fossati A., Galvanetto E., Bacci T., Pradelli G.** (2006), Glow discharge nitriding of AISI 316L austenitic stainless steel: Influence of treatment pressure, *Surface and Coatings Technology*, Vol. 200, 5505-5513.
13. **Borowski T., Kamiński J., Trojanowski J., Wierzchoń T.** (2010), Analysis of the structure and properties plasma nitrided 316L steel in different zones of plasma discharge (in polish), Archives of Machine Technology and Automatization, Vol. 30, 69-77.
14. **Brühl S.P., Charadia R., Simison S., Lamas D.G., Cabo A.** (2010), Corrosion behavior of martensitic and precipitation hardening stainless steels treated by plasma nitriding, *Surface and Coatings Technology*, Vol. 204, 3280-3286.
15. **Corengia P., Traverso M.G., García Alonso-García D., Egidi D.A., Ybarra G., Moina C., Cabo A.** (2004a), DC-Pulsed plasma nitriding of 4140: microstructure and topography, *Matéria*, Vol. 9, 111.
16. **Corengia P., Ybarra G., Moina C., Cabo A., Broitman E.** (2004b), Microstructure and corrosion behaviour of DC-pulsed plasma nitrided AISI 410 martensitic stainless steel, *Surface and Coatings Technology*, Vol. 187, 63-69.
17. **Corengia P., Ybarra G., Moina C., Cabo A., Broitman E.** (2005), Microstructural and topographical studies of DC-pulsed plasma nitrided AISI 4140 low-alloy steel, *Surface and Coatings Technology*, Vol. 200, 2391-2397.
18. **de Sousa R.M., de Araújo F.O., Ribeiro K.B., Mendes M.D., da Costa J.P., Alves Jr. C.** (2007), Cathodic cage nitriding of

DOI 10.1515/ama-2016-0024

samples with different dimensions, *Materials Science and Engineering A*, Vol. 465, 223-227.

19. **de Sousa R.M., Moura Y.L., de Sousa P.O., Neto J.M., Costa T.C., Alves Jr. C.** (2014), Nitriding of AISI 1020 Steel: Comparison Between Conventional Nitriding and Nitriding with Cathodic Cage, *Materials Research*, Vol. 17, 708-713.
20. **de Souza S.D., Olzon-Dionysio M., Basso R.O., de Souza S.** (2010), Mössbauer spectroscopy study on the corrosion resistance of plasma nitrided ASTM F138 stainless steel in chloride solution, *Materials Characterization*, Vol. 61, 992-999.
21. **Díaz-Guillén J.C., Campa-Castilla A., Pérez-Aguilar S.I., Granda-Gutiérrez E.E., Garza-Gómez A., Candelas-Ramírez J., Méndez-Méndez R.** (2009), Effect of duty cycle on surface properties of AISI 4340 using a pulsed plasma nitriding process, *Superficies y Vacío*, Vol. 22, 1-4.
22. **Díaz-Guillén J.C., Granda-Gutiérrez E.E., Vargas-Gutiérrez G., Díaz-Guillén M.R., Aguilar-Martínez J.A., Álvarez-Contreras L.** (2015), Effect of Nitriding Current Density on the Surface Properties and Crystallite Size of Pulsed Plasma-Nitrided AISI 316L, *Journal of Materials Science and Chemical Engineering*, Vol. 3, 45-51.
23. **Dong H., Qi P.Y., Li X.Y., Llewellyn R.J.** (2006), Improving the erosion–corrosion resistance of AISI 316 austenitic stainless steel by low-temperature plasma surface alloying with N and C, *Materials Science and Engineering A*, Vol. 431, 137-145.
24. **Fattah M., Mahboubi F.** (2010), Comparison of ferritic and austenitic plasma nitriding and nitrocarburizing behavior of AISI 4140 low alloy steel, *Materials and Design*, Vol. 31, 3915-3921.
25. **Fernandes F.P., Heck S.C., Pereira R.G., Picon C.A., Nascente P.P., Casteletti L.C.** (2010), Ion nitriding of a superaustenitic stainless steel: Wear and corrosion characterization, *Surface and Coatings Technology*, Vol. 204, 3087-3090.
26. **Foerster C.E., Serbena F.C., da Silva S.R., Lepienski C.M., de M. Siqueira C. J., Ueda M.** (2007), Mechanical and tribological properties of AISI 304 stainless steel nitrided by glow discharge compared to ion implantation and plasma immersion ion implantation, *Nuclear Instruments and Methods in Physics Research B*, Vol. 257, 732-736.
27. **Fossati A., Borgioli F., Galvanetto E., Bacci T.** (2006a), Corrosion resistance properties of glow-discharge nitrided AISI 316L austenitic stainless steel in NaCl solutions, *Corrosion Science*, Vol. 48, 1513-1527.
28. **Fossati A., Borgioli F., Galvanetto E., Bacci T.** (2006b), Glow-discharge nitriding of AISI 316L austenitic stainless steel: influence of treatment time, *Surface and Coatings Technology*, Vol. 200, 3511-3517.
29. **Gallo S.C., Dong H.** (2009), Study of active screen plasma processing conditions for carburising and nitriding austenitic stainless steel, *Surface and Coatings Technology*, Vol. 203, 3669-3675.
30. **Hudis M.** (1973), Study of ion-nitriding, *Journal of Applied Physics*, Vol. 44, 1489-1496.
31. **Jeong B.Y., Kim M.H.** (2001), Effects of pulse frequency and temperature on the nitride layer and surface characteristics of plasma nitrided stainless steel, *Surface and Coatings Technology*, Vol. 137, 249-254.
32. **Jeong B.Y., Kim M.H.** (2001), Effects of the process parameters on the layer formation behavior of plasma nitrided steels, *Surface and Coatings Technology*, Vol. 141, 182-186.
33. **Karimzadeh N., Moghaddam E.G., Mirjani M., Raeissi K.** (2013), The effect of gas mixture of post-oxidation on structure and corrosion behavior of plasma nitrided AISI 316 stainless steel, *Applied Surface Science*, Vol. 283, 584-589.
34. **Kliauga A.M., Pohl M.** (1998), Effect of plasma nitriding on wear and pitting corrosion resistance of X2CrNiMoN22-5-3 duplex stainless steel, *Surface and Coatings Technology*, Vol. 98, 1205-1210.
35. **Kurelo B.E., de Souza G.B., da Silva S.R., Serbena F.C., Foerster C.E., Alves Jr. C.** (2015), Plasma nitriding of HP13Cr supermartensitic stainless steel, *Applied Surface Science*, Vol. 349, 403-414.
36. **Larisch B., Brusky U., Spies H. J.** (1999), Plasma nitriding of stainless steels at low temperatures, *Surface and Coatings Technology*, Vol. 116–119, 205–211.
37. **Łępicka M., Grądzka-Dahlke M.** (2013), Effect of Heat Treatment and Corrosion Resistance of AISI 440B Martensitic Stainless Steel, *Acta Mechanica et Automatica*, Vol. 7, 155-159.
38. **Łępicka M., Grądzka-Dahlke M.** (2014), Effect of Plasma Nitriding Conditions on Corrosion Resistance of AISI 440B Martensitic Stainless Steel, *Acta Mechanica et Automatica*, Vol. 8, 156-159.
39. **Li C.X., Bell T.** (2006), Corrosion properties of plasma nitrided AISI 410 martensitic stainless steel in 3.5% NaCl and 1% HCl aqueous solutions, *Corrosion Science*, Vol. 48, 2036-2049.
40. **Li G.J., Peng Q., Li C., Wang Y., Gao J., Chen S.Y., Shen B.L.** (2008), Effect of DC plasma nitriding temperature on microstructure and dry-sliding wear properties of 316L stainless steel, *Surface and Coatings Technology*, Vol. 202, 2749-2754.
41. **Li Y., Wang L., Shen L., Zhang D., Wang C.** (2010), Plasma nitriding of 42CrMo low alloy steels at anodic or cathodic potentials, *Surface and Coatings Technology*, Vol. 204, 2337-2342.
42. **Li Y., Wang Z., Wang L.** (2014a), Surface properties of nitrided layer on AISI 316L austenitic stainless steel produced by high temperature plasma nitriding in short time, *Applied Surface Science*, Vol. 298, 243-250.
43. **Li Y., Xu H., Zhu F., Wang L.** (2014b), Low temperature anodic nitriding of AISI 304 austenitic stainless steel, *Materials Letters*, Vol. 128, 231-234.
44. **Li Y., Zhang S., He Y., Zhang L., Wang L.** (2014c), Characteristics of the nitrided layer formed on AISI 304 austenitic stainless steel by high temperature nitriding assisted hollow cathode discharge, *Materials and Design*, Vol. 64, 527-534.
45. **Liang W.** (2003), Surface modification of AISI 304 austenitic stainless steel by plasma nitriding, *Applied Surface Science*, Vol. 211, 308-314.
46. **Liang W., Juncai S., Xiaolei X.** (2001), Low pressure plasma arc source ion nitriding compared with glow-discharge plasma nitriding of stainless steel, *Surface and Coatings Technology*, Vol. 145, 31-37.
47. **Mashreghi A.R., Soleimani S.Y., Saberifar S.** (2013), The investigation of wear and corrosion behavior of plasma nitrided DIN 1.2210, *Materials and Design*, Vol. 46, 532-538.
48. **Menthe E., Bulak A., Olfe J., Zimmermann A., Rie K.T.** (2000), Improvement of the mechanical properties of austenitic stainless steel after plasma nitriding, *Surface and Coatings Technology*, Vol. 133-134, 259-263.
49. **Menthe E., Rie K.T.** (1999), Further investigation of the structure and properties of austenitic stainless steel after plasma nitriding, *Surface and Coatings Technology*, Vol. 116-119, 199–204.
50. **Menthe E., Rie K.T., Schultze J.W., Simson S.** (1995), Structure and properties of plasma-nitrided stainless steel, *Surface and Coatings Technology*, Vol. 74-75, 412-416.
51. **Michler T.** (2008), Influence of plasma nitriding on hydrogen environment embrittlement of 1.4301 austenitic stainless steel, *Surface and Coatings Technology*, Vol. 202, 1688-1695.
52. **Mingolo N., Tschiptschin A.P., Pinedo C.E.** (2006), On the formation of expanded austenite during plasma nitriding of an AISI 316L austenitic stainless steel, *Surface and Coatings Technology*, Vol. 201, 4215-4218.
53. **Miola E.J., de Souza S.D., Olzon-Dionysio M., Spinelli D., dos Santos C.A.** (1999), Nitriding of H-12 tool steel by direct-current and pulsed plasmas, *Surface and Coatings Technology*, Vol. 116-119, 347-351.
54. **Musil J., Vlcek J., Ruzicka M.** (2000), Recent progress in plasma nitriding, *Vacuum*, Vol. 59, 940-951.
55. **O'Brien J.M., Goodman D.** (1991), Heat treating, plasma (ion) nitriding, 240-242, in: Davis W.J.R., Metals Handbook. 9th ed., Vol. 4, ASM, Ohio.
56. **Ochoa E.A., Figueroa C.A., Alvarez F.** (2005), The influence of the ion current density on plasma nitriding process, *Surface and Coatings Technology*, Vol. 200, 2165-2169.

57. **Olzon-Dionysio M., Campos M., Kapp M., de Souza S., de Souza S.D.** (2010), Influences of plasma nitriding edge effect on properties of 316L stainless steel, *Surface and Coatings Technology*, Vol. 204, 3623-3628.
58. **Olzon-Dionysio M., de Souza S.D., Basso R.O., de Souza S.** (2008), Application of Mössbauer spectroscopy to the study of corrosion resistance in NaCl solution of plasma nitrided AISI 316L stainless steel, *Surface and Coatings Technology*, Vol. 202, 3607-3614.
59. **Pinedo C.E., Monteiro W.A.** (2004), On the kinetics of plasma nitriding a martensitic stainless steel type AISI 420, *Surface and Coatings Technology*, Vol. 179, 119–123.
60. **Podgornik B., Vizintin J., Leskovsek V.** (1998), Tribological properties of plasma and pulse plasma nitrided AISI 4140 steel, *Surface and Coatings Technology*, Vol. 108-109, 454-460.
61. **Psyllaki P.P., Griniari A., Pantelis D.I.** (2008), Parametric study on laser nitriding of 1.5919 steel, *Journal of Materials Processing Technology*, Vol. 195, 299-304.
62. **Pye D.** (2003), Practical Nitriding and Ferritic Nitrocarburizing, ASM International, Materials Park.
63. **Raman S.S., Jayaprakash M.** (2007), Influence of plasma nitriding on plain fatigue and fretting fatigue behaviour of AISI 304 austenitic stainless steel, *Surface and Coatings Technology*, Vol. 201, 5906-5911.
64. **Ribeiro K.B., de Sousa R.M., de Araújo F.O., de Brito R.A., Barbosa J.P., Alves Jr. C.** (2008), Industrial application of AISI 4340 steels treated in cathodic cage plasma nitriding technique*, Materials Science and Engineering A*, Vol. 479, 142–147.
65. **Saeed A., Khan A.W., Jan F., Abrar M., Khalid M. Zakaullah M.** (2013), Validity of "sputtering and re-condensation" model in active screen cage plasma nitriding process, *Applied Surface Science*, Vol. 273, 173–178.
66. **Saklakoglu I.E., Saklakoglu N., Short K.T., Collins G.A.** (2007), Characterization of austenitic stainless steel after plasma immersion nitrogen and carbon implantation, *Materials and Design*, Vol. 28, 1657-1663.
67. **Sharma M.K., Saikia B.K., Phukan A., Ganguli B.** (2006), Plasma nitriding of austenitic stainless steel in N_2 and N_2–H_2 dc pulsed discharge, *Surface and Coatings Technology*, Vol. 201, 2407-2413.
68. **Singh G.P., Alphonsa J., Barhai P.K., Rayjada P.A., Raole P.M., Mukherjee S.** (2006), Effect of surface roughness on the properties of the layer formed on AISI 304 stainless steel after plasma nitriding, *Surface and Coatings Technology*, Vol. 200, 5807–5811.
69. **Sirin S. Y., Sirin K., Kaluc E.** (2008), Effect of the ion nitriding surface hardening process on fatigue behavior of AISI 4340 steel, *Materials Characterization*, Vol. 59, 351-358.
70. **Sirin S.Y., Kaluc E.** (2012), Structural surface characterization of ion nitrided AISI 4340 steel, *Materials and Design*, Vol. 36, 741-747.
71. **Skolek-Stefaniszyn E., Kaminski J., Sobczak J., Wierzchon T.** (2010), Modifying the properties of AISI 316L steel by glow discharge assisted low-temperature nitriding and oxynitriding, *Vacuum*, 85, 164-169.
72. **Sobiecki J. R., Mańkowski P., Patejuk A.** (2004), Improving the performance properties of valve martensitic steel by glow discharge-assisted nitriding, *Vacuum*, Vol. 76, 57-61.
73. **Soleimani S.Y., Mashreghi A.R., Ghasemi S.S., Moshrefifar M.** (2012), The effect of plasma nitriding on the fatigue behavior of DIN 1.2210 cold work tool steel, *Materials and Design*, Vol. 35, 87-92.
74. **Soltani Asadi Z., Mahboubi A.** (2012), Effect of component's geometry on the plasma nitriding behavior of AISI 4340 steel, *Materials and Design*, Vol. 34, 516-521.
75. **Sun Y., Bell T.** (1998), Sliding wear characteristics of low temperature plasma nitrided 316 austenitic stainless steel, *Wear*, Vol. 218, 34-42.
76. **Szabo A., Wilhelmi H.** (1984), The mechanisms of nitriding of steel surfaces in a D. C. glow discharge, *Haerterei Technische Mitteilungen*, Vol. 39, 148-151.
77. **Szilágyiné Biró A.** (2013), Trends of Nitriding Processes, *Production Processes and Systems*, Vol. 6, 57-66.
78. **Tibbetts G. G.** (1974), Role of nitrogen atoms in "ion-nitriding", *Journal of Applied Physics*, Vol. 45, 5072-5073.
79. **Toshkov V., Russev R., Madjarov T., Russeva E.** (2007), On low temperature ion nitriding of austenitic stainless steel AISI 316, *Journal of Acheivements in Materials and Manufacturing Engineering*, Vol. 25, 71-74.
80. **Tuckart W., Forlerer E., Iurman L.** (2007), Delayed cracking in plasma nitriding of AISI 420 stainless steel, *Surface and Coatings Technology*, Vol. 202, 199–202.
81. **Wang J., Xiong J., Peng Q., Fan H., Wang Y., Li G., Shen B.** (2009), Effects of DC plasma nitriding parameters on microstructure and properties of 304L stainless steel, *Materials Characterization*, Vol. 60, 197-203.
82. **Wang L., Ji S., Sun J.** (2006), Effect of nitriding time on the nitrided layer of AISI 304 austenitic stainless steel, *Surface and Coatings Technology*, Vol. 200, 5067-5070.
83. **Wang L., Ji S., Sun J.** (2006), Effect of nitriding time on the nitrided layer of AISI 304 austenitic stainless steel, *Surface and Coatings Technology*, Vol. 200, 5067-5070.
84. **Wang S., Cai W., Li J., Wei W., Hu J.** (2013), A novel rapid D.C. plasma nitriding at low gas pressure for 304 austenitic stainless steel, *Materials Letters*, Vol. 105, 47–49.
85. **Weber T., de Wit L., Saris F.W., Koniger A., Rauschenbach B., Wolf G.K., Krauss S.** (1995), Hardness and corrosion resistance of single-phase nitride and carbide on iron, *Materials Science and Engineering A*, Vol. 199, 205-210.
86. **Wen D.C.** (2009), Plasma nitriding of plastic mold steel to increase wear- and corrosion properties, *Surface and Coatings Technology*, Vol. 204, 511–519.
87. **Wierzchoń T., Psoda M., Skołek E., Rudnicki J., Sobiecki J.R.** (2006), Glow discharge assisted nitriding of chromium steel 3H13, *Maintenance Problems*, Vol. 2, 53-64.
88. **Winck L.B., Ferreira J.A., Araujo J.A., Manfrinato M.D., da Silva C.M.** (2013), Surface nitriding influence on the fatigue life behavior of ASTM A743 steel type CA6NM, *Surface and Coatings Technology*, Vol. 232, 844-850.
89. **Wu K., Liu G.Q., Wang L., Xu B.F.** (2010), Research on new rapid and deep plasma nitriding techniques of AISI 420 martensitic stainless steel, *Vacuum*, 870-875.
90. **Xi Y.T., Liu D.X., Han D.** (2008a), Improvement of corrosion and wear resistances of AISI 420 martensitic stainless steel using plasma nitriding at low temperature, *Surface and Coatings Technology*, Vol. 202, 2577-2583.
91. **Xi Y.T., Liu D.X., Han D.** (2008b), Improvement of erosion and erosion–corrosion resistance of AISI 420 stainless steel by low temperature plasma nitriding, *Applied Surface Science*, Vol. 254, 5953-5958.
92. **Xu B., Zhang Y.** (1986), Collision dissociation model in ion-nitriding, 5th International Congress on Heat Treatment of Materials, 1086-1093.
93. **Zlatanović M., Popović I.** (2010), Gas discharge static characteristics in pulse regime, *Contemporary Materials*, Vol. 1, 138-143.

Acknowledgement: This scientific work was supported by the Faculty of Mechanical Engineering, Bialystok University of Technology, project No S/WM/1/2014.

ABSTRACTS

Peter Jankejech, Peter Fabian, Jozef Broncek, Yuriy Shalapko
Influence of Tempering on Mechanical Properties of Induction Bends below 540°C

The article describes basic principles of induction bending and the change of mechanical properties from as received (straight) pipe made from HSLA steel to induction bend. The main purpose of this article is to experiment with tempering temperatures below 540°C. After tempering at 540°C which is the lowest recommended temperature for post bend heat treatment (PBHT) according to CSA specifications (Canadian Standards Association) the induction bend area in many cases does not achieve the minimum required mechanical properties and therefore it is not accepted for usage. In this article mechanical properties such as tensile, toughness, hardness are evaluated. Also the article contains microstructural analyses and comparison of bended and heat treated samples.

Jarosław Szrek, Artur Muraszkowski, Przemysław Sperzyński
Type Synthesis, Modelling and Analysis of the Manipulator for Wheel-Legged Robot

The aim of this article is to present the concept of wheel-legged mobile manipulator, which is a combination of mobile platform with specially selected suspension system and a manipulator. First, a literature review was performed and own solution proposed. The kinematic structure of manipulator, selected simulation results, physical model and the concept of the control system has been presented. Geometry synthesis was used to design basic dimension. Structural synthesis was performed according to the intermediate chain method. Simulations were performed using the multibody dynamics simulation software. New approach in the field of the mobile manipulators was presented as a result.

Cezary Kownacki
Multi-UAV Flight on the Basis of Virtual Structure Combined with Behavioral Approach

Implementations of multi-UAV systems can be divided mainly into two different approaches, centralised system that synchronises positions of each vehicle by a ground station and an autonomous system based on decentralised control, which offers more flexibility and independence. Decentralisation of multi-UAV control entails the need for information sharing between all vehicles, what in some cases could be problematic due to a significant amount of data to be sent over the wireless network. To improve the reliability and the throughput of information sharing inside the formation of UAVs, this paper proposes an approach that combines virtual structure with a leader and two flocking behaviours. Each UAV has assigned different virtual migration point referenced to the leader's position which is simultaneously the origin of a formation reference frame. All migration points create together a virtual rigid structure. Each vehicle uses local behaviours of cohesion and repulsion respectively, to track its own assigned point in the structure and to avoid a collision with the previous UAV in the structure. To calculate parameters of local behaviours, each UAV should know position and attitude of the leader to define the formation reference frame and also the actual position of the previous UAV in the structure. Hence, information sharing can be based on a chain of local peer-to-peer communication between two consecutive vehicles in the structure. In such solution, the information about the leader could be sequentially transmitted from one UAV to another. Numerical simulations were prepared and carried out to verify the effectiveness of the presented approach. Trajectories recorded during those simulations show collective, coherence and collision-free flights of the formation created with five UAVs.

Adam Niesłony, Michał Böhm, Tadeusz Łagoda, Filippo Cianetti
The Use of Spectral Method for Fatigue Life Assessment for Non-Gaussian Random Loads

The well-known problem with the fatigue lifetime assessment of non-Gaussian loading signals with the use of spectral method has been presented in the paper. A correction factors that transform the non-Gaussian signal into an equivalent Gaussian signal proposed by Bracessi et al. (2009) has been used for the purpose of lifetime calculations together with Palmgren-Miner Hypothesis. The calculations have been performed for the 10HNAP steel under random non-Gaussian load with four dominating frequencies. The signal has been generated on the test stand SHM250 for random tension-compression tests. The results with zero and non-zero mean stresses have been used to calculate the fatigue life with the frequency domain method based on Dirlik's model and with a time domain method with the use of the rainflow cycle counting algorithm. The obtained calculation results have been compared with experimental results.

Viorel Ungureanu, Dan Dubina
Influence of Corrugation Depth on Lateral Stability of Cold-Formed Steel Beams of Corrugated Webs

The beams of thin corrugated web afford a significant weight reduction compared with hot-rolled or welded ones. In the initial solutions, the flanges are made of flat plates, welded to the sinusoidal web sheet, requiring a specific welding technology. A new solution is proposed by the authors, in which the beam is composed by a web of trapezoidal cold-formed steel sheet and flanges of back-to-back lipped channel sections. For connecting flanges to the web self-drilling screws are used. The paper summarizes the experimental and numerical investigations carried out at the CEMSIG Research Centre (www.ct.upt.ro/centre/cemsig/) of the Politehnica University of Timisoara and, at the end, presents the influence of corrugation depth of web on the lateral stability of the beams.

Petr Baron, Jozef Dobránsky, Martin Pollák, Marek Kočiško, Tomáš Cmorej
The Parameter Correlation of Acoustic Emission and High-Frequency Vibrations in the Assessment Process of the Operating State of the Technical System

The article describes application of selected methods of technical diagnostics for assessing the operating status of precision gearboxes. Within the confines of experimental measurements in the field of physical metallurgy materials of diagnosed system were being examined while taking into account the process of degradation of material properties during operation of monitored gearboxes. Measurements and collecting of dynamic data were realized on 4 selected gearboxes where a high-frequency vibrations and acoustic emission (noise) measurements were carried out. Retrieved values were subsequently used for mutual correlation and verification of applied methods. Results of both selected methods underlined unsatisfactory operation status with 3 inspected gearboxes. Measured values were identified as being above suggested caution limit of Alarm 2, representing a level of danger.

Dmytro Fedorynenko, Serhii Sapon, Sergiy Boyko
Accuracy of Spindle Units with Hydrostatic Bearings

The work is devoted to the research of precision regularities in a spindle unit by the trajectory of the spindle installed on hydrostatic bearings. The mathematical model of trajectories spindle with lumped parameters that allows to define the position of the spindle with regard the simultaneous influence of design parameters, geometrical deviations of form, temperature deformation bearing surfaces, the random nature of operational parameters and technical loads of hydrostatic bearings has been developed. Based on the results of numerical modeling the influence of shape errors of bearing surface of hydrostatic bearing on the statistical characteristics of the radius vector trajectories of the spindle by varying the values rotational speed of the spindle and oil pressure in front hydrostatic bearing has been developed. The obtained statistical regularities of precision spindle unit have been confirmed experimentally. It has been shown that an effective way to increase the precision of spindle units is to regulate the size of the gap in hydrostatic spindle bearings. The new design of an adjustable hydrostatic bearing, which can improve the accuracy of regulation size gap has been proposed.

Maciej Ryś
Constitutive Modelling of Damage Evolution and Martensitic Transformation in 316L Stainless Steel

In this work, the constitutive model, derived with the use of thermodynamic of irreversible processes framework is presented. The model is derived under the assumption of small strains. Plastic strain induced martensitic phase transformation is considered in the austenitic matrix where the volume fraction of the martensite is reflected by a scalar parameter. The austenitic matrix is assumed as the elastic-plastic material and martensitic phase is assumed as randomly distributed and randomly oriented inclusions. Both phases are affected by damage evolution but there is no distinction in the model between damage in austenite and martensite.

Heorgij Sulym, Imre Timar, Ihor Turchyn
Transient Vibration of an Elastic Cylinder Inserted in the Elastic Medium

Using method of Laguerre polynomials we have obtained the solution of the dynamic problem of the theory of elasticity for elastic cylinder inserted into massive body modeled as a space. The source of non-stationary processes in composite is high intensity force load of the inner surface of the cylinder. On the surface separation of materials of space and cylinder the conditions of ideal mechanical contact are satisfied. The solution is obtained as series of Laguerre polynomials, which coefficients are found from recurrent relations. The results of numerical analysis of transient stress-strain state in elastic space with cylindrical insertion might be used for the technological process of hydraulic fracturing during shale gas extraction.

Jerzy Nachimowicz, Stanislaw Rafałowski
Modelling the Meshing of Cycloidal Gears

Cycloidal drives belong to the group of planetary gear drives. The article presents the process of modelling a cycloidal gear. The full profile of the planetary gear is determined from the following parameters: ratio of the drive, eccentricity value, the equidistant (ring gear roller radius), epicycloid reduction ratio, roller placement diameter in the ring gear. Joong-Ho Shin's and Soon-Man Kwon's article (Shin and Know, 2006) was used to determine the profile outline of the cycloidal planetary gear lobes. The result was a scatter chart with smooth lines and markers, presenting the full outline of the cycloidal gear.

Zbigniew Kołakowski, Andrzej Teter
Coupled Static and Dynamic Buckling Modelling of Thin-Walled Structures in Elastic Range - Review of Selected Problems

A review of papers that investigate the static and dynamic coupled buckling and post-buckling behaviour of thin-walled structures is carried out. The problem of static coupled buckling is sufficiently well-recognized. The analysis of dynamic interactive buckling is limited in practice to columns, single plates and shells. The applications of finite element method (FEM) or/and analytical-numerical method (ANM) to solve interaction buckling problems are on-going. In Poland, the team of scientists from the Department of Strength of Materials, Lodz University of Technology and co-workers developed the analytical-numerical method. This method allows to determine static buckling stresses, natural frequencies, coefficients of the equation describing the post-buckling equilibrium path and dynamic response of the plate structure subjected to compression load and/or bending moment. Using the dynamic buckling criteria, it is possible to determine the dynamic critical load. They presented a lot of interesting results for problems of the static and dynamic coupled buckling of thin-walled plate structures with complex shapes of cross-sections, including an interaction of component plates. The most important advantage of presented analytical-numerical method is that it enables to describe all buckling modes and the post-buckling behaviours of thin-walled columns made of different materials. Thin isotropic, orthotropic or laminate structures were considered.

Magdalena Łępicka, Małgorzata Grądzka-Dahlke
Direct Current and Pulsed Direct Current Plasma Nitriding of Ferrous Materials – a Critical Review

Nowadays, the improvement of ferrous materials performance is a problem of high interest. One of well-known wear- and corrosion properties improving technique is plasma nitriding, in which elemental nitrogen is introduced to the surface of a metal part for subsequent diffusion into the material. As a result, a compound, "white" layer and a diffusion zone are formed at the detail's surface. Most of the authors positively describe the effects of surface ion nitiding. On the other hand, there are also reports on adverse effects of direct current and pulsed direct current plasma nitriding on ferrous materials performance. Therefore, an attempt to provide comprehensive summary on direct current and pulsed direct current ion nitriding and its influence on ferrous materials' mechanical and corrosion properties has been made. According to the results, some of the technique drawbacks are hard to avoid in mass production.